Numerical modelling of production-induced stress changes and seismicity in fault-compartmentalized reservoirs of the North German Basin

Dissertation

Vom Fachbereich Material- und Geowissenschaften
der Technischen Universität Darmstadt
zur Erlangung des akademischen Grades
Doktor-Ingenieur (Dr.-Ing.)

TECHNISCHE UNIVERSITÄT DARMSTADT

vorgelegt von
M. Sc. Constantin Haug
geboren am 09.12.1985 in Tübingen, Baden-Württemberg

Referent: **Prof. Dr. Andreas Henk**
Korreferent **Prof. Dr.-Ing. Michael Alber**

Darmstadt, November 2018

Haug, Constantin: Numerical modelling of production-induced stress changes
and seismicity in fault-compartmentalized reservoirs of the North German Basin
Darmstadt, Technische Universität Darmstadt,
Jahr der Veröffentlichung der Dissertation auf TUprints: 2019
Tag der mündlichen Prüfung: 19.12.2018
Tag der Einreichung: 12.11.2018

Vorsitzender der Prüfungskommission:	Prof. Dr. Christoph Schüth
Referent:	Prof. Dr. Andreas Henk
Korreferent:	Prof. Dr.-Ing. Michael Alber
Prüfer:	Prof. Dr. Eva Schill
Prüfer:	Prof. Dr.-Ing. Matthias Becker

Abstract

Natural gas production from some Rotliegend reservoirs in the Netherlands and North Germany has triggered seismic events after the affected sites had undergone a significant decrease in pore pressure. Recent seismic events in North Germany have caused negligible structural damage but major public concern in a region of low historic seismicity. In a first order approach, the pore pressure depletion of deep reservoirs is accompanied by stress changes that superimpose on pre-production and far-field stresses and potentially question the strength of pre-existing fault planes. Basic analytic models can explain how first, the production-induced differential increase of effective vertical and horizontal stress components within the reservoir, and second the compensation of reservoir contraction by compatibility stresses in the reservoir surroundings, can lead to the reactivation of pre-existing faults during depletion. These analytic approaches fail however to account for the mechanical stratigraphy and structural complexities occurring in reality.

In this study, general characteristics of Rotliegend gas fields were depicted in 2D Finite element models in order to improve the quantitative understanding of production-induced seismicity and identify geological parameters that may favour the occurrence of seismicity in North Germany. The tendency towards normal faulting was investigated for a parameter space of reservoir depth, reservoir thickness, mechanical and hydraulic properties and compartment geometries. Distinct features of the local geology such as a varying thickness of viscoelastic salt in the overburden and offset reservoir compartments were addressed by three basic model settings whereby a graben setting served as a reference scenario. The consolidation procedure of the FE- multiphysics tool ABAQUS was used to solve the fully coupled poroelastic equations, requiring the establishment of a modelling strategy first. Herein the Biot-coefficient, that commonly assumes values inferior to one in solid rocks, constituted a crucial model parameter. In the numerical procedure, the evaluation of failure and output of Terzaghi effective stress ignored the Biot-coefficient at first glance. It is however shown that the coefficient scales with total stresses and governs the magnitudes of both effective stress concepts, the Biot-Willis effective stress, reflecting the direct poroelastic stress-strain relation, and Terzaghi effective stress determining the yield of porous rock formations under large confining pressures. A second crucial feature, the deterministic model fault was depicted by contact surfaces that capture the discontinuous character of real faults and allow for relative displacements. In the poroelastic modelling, sealing faults invoke continuity constraints that, along with an inconvenient definition of failure stress, lead to the introduction of the fault-loading parameter *SSR,* used for the comparative evaluation of fault-loading in different model variations. Identified critical fault-loading patterns were in a second modelling campaign allowed to dissipate by means of dynamic slip, whereby the

implementation of slip-rate weakening friction and the consideration of dynamic stresses in ABAQUS explicit captured essential characteristics of dynamic rupture.

Several factors that may favour production-induced seismicity in North Germany were identified in the modelling. First, individual parameters such as large reservoir thickness, large Biot-coefficients of the reservoir, shallow reservoir position, a large stiffness contrast between caprock and reservoir and in particular the effect of viscoelastic evaporites in the overburden, exerting a non-homogeneous load and inhibiting stress redistribution, are factors favouring the reactivation of the graben-bounding fault. Second, intra-field compartmentalizing faults are found a more likely location for seismic events than the graben boundary. Particularly production scenarios that deplete either both of two offset compartments, or the footwall compartment, exert a strong loading on the fault. Furthermore, partly-juxtaposed reservoir compartments constitute a preferential geometric setting for fault reactivation. A favoured reactivation of steeply dipping faults (> 60°) in all models reflects a dominant contribution of compaction-strains to fault-loading and contrasts with tectonic concepts. The fault reactivation potential on the graben boundary is found to be highest at the upper reservoir level and a narrow interval above it. For the intra-field setting, rupture initiates at the lower level of the fault section bounding the footwall compartment. Rupture generally propagates either downwards or simultaneously up– and downwards. Thereby, the interplay of the overall stress state and the initial acceleration can favour or inhibit slip propagation but the isotropic stress state within the salt and the tendency for reverse faulting below the reservoir pose ultimate geologic barriers to the propagation of rupture. The final rupture pattern depends predominantly on the geological setting and its local stress state, whereas the effect of the simulated depletion scenarios is hardly distinguishable.

Bulk formation strain is shown to be ambiguously expressed by two different effective stress concepts, moreover, the modelling results reveal a strong sensitivity on the representation of the fault. These findings of the study highlight specific challenges of the modelling of reservoir geomechanical problems. Reviewing the model results, a single dominant parameter for seismic hazard cannot be derived as fault criticality is predominantly governed by a complex interplay of initial stresses, pore pressure and fault strength. The investigated parameters revealed the potential to enhance or mitigate critical tendencies in an interfering manner. In consequence, more detailed prediction models require more detailed structural and field data. Nevertheless, the FE models enhance the understanding of processes and influential parameters for induced seismicity and are able to investigate scenarios and define limiting cases in the planning and operation of fields. The presented two-step approach, encompassing the prioritized identification of critically stressed faults and the separate simulation of rupture can be extended to case investigations addressing for example problems of caprock integrity.

Zusammenfassung

Die Förderung von Erdgas aus diversen Rotliegend-Gaslagerstätten in den Niederlanden und Norddeutschland hat Erdbeben ausgelöst, die mit einer signifikanten Porendruckabsenkung im Untergrund korrelieren. Für die betroffene Region in Norddeutschland wird die Erdbebengefährdung als vernachlässigbar eingeschätzt. Entsprechend haben die induzierten Erdbeben, ungeachtet ihrer sehr geringfügigen Oberflächenauswirkungen, große Besorgnis in der Bevölkerung hervorgerufen. Ein vereinfachter Erklärungsansatz für die induzierten Erdbeben sieht Porendruck-induzierte Spannungsänderungen vor, die mit dem vorherrschenden tektonischen Spannungszustand interferieren und dabei die Integrität von vorhandenen Störungen infrage stellen. Analytische Ansätze beschreiben erstens, wie die Porendruckabnahme zu einer differentiellen Zunahme der effektiven vertikalen und horizontalen Spannungskomponenten innerhalb des Reservoirs führen und zweitens, wie die kompressiven Verformungstendenzen des Reservoirs Kompensationsspannungen in umliegenden Gesteinsformationen hervorrufen. Die analytischen Modelle können die Reaktivierung von Störungen durch Porendruckabsenkungen grundsätzlich erklären, realistische mechanische Stratigraphien und die strukturelle Komplexität der Lagerstätten aber nur unzureichend abbilden.

Die vorliegende Arbeit abstrahiert grundlegende geologischen Gegebenheiten der norddeutschen Rotliegend-Gasfelder in zweidimensionale Finite Elemente (FE) Modelle. Mithilfe der numerischen Modellierung soll das quantitative Verständnis der induzierten Erdbeben verbessert und der Einfluss verschiedener Parameter, die das Auftreten von induzierten Erdbeben in Norddeutschland potenziell begünstigen, evaluiert werden. Ein Parameterraum, der die Tiefe und Mächtigkeit des Reservoirs, die mechanischen und hydraulischen Modelleigenschaften sowie die Geometrie der Reservoirhorizonte entlang kompartmentbildender Verwerfungen variiert, wurde im Hinblick auf das jeweilige Reaktivierungspotenzial der Störung als Abschiebung analysiert. Charakteristische geologische Merkmale wie die lateral variierende Mächtigkeit von Evaporiten und kompartmentbildende Verwerfungen innerhalb der Gasfelder wurden in drei unterschiedlichen Modell-settings untersucht und der Grabenrand als Referenzszenario herangezogen. Die bodenmechanische Konsolidationsanalyse des FE-Programms ABAQUS wurde für die Lösung der voll gekoppelten poroelastischen Gleichungen verwendet und dafür zunächst ein Modellierungsansatz konzipiert. Hierbei ist der Biot-Koeffizient zentraler Inputparameter und nimmt für Festgesteine normalerweise Werte kleiner eins an. In der numerischen Prozedur war er in der Berechnung von Versagensspannungen und der Ausgabe von Terzaghi-Spannungen zunächst scheinbar nicht berücksichtigt. Es wird aber gezeigt, dass der Biot-Koeffizient den totalen Spannungszustand determiniert und damit die Magnituden beider abgeleiteter Effektivspannungskonzepte bestimmt. Biot-Willis Effektivspannungen beschreiben das Spannungs-Verformungs-Verhalten des

poroelastischen Materials in direkter Weise, Terzaghi Effektivspannungen determinieren die Festigkeits- bzw. Fließgrenze von porösen Gesteinen unter hohem Umgebungsdruck. Eine weitere zentrale Bedeutung kommt der deterministischen Darstellung von Störungen als Kontaktflächen im numerischen Modell zu. Kontaktflächen bilden den diskontinuierlichen Charakter von realen Störungen ab und erlauben kleinräumige Relativverschiebungen innerhalb des FE-Netzes. In der poroelastischen Modellierung führt die Repräsentation einer abdichtenden Störung durch Kontakt zusätzliche Kontinuitätsbedingungen ein, die zusammen mit der kontroversen numerischen Versagensspannung die Einsetzung der Störungsbelastungsgröße *SSR* erforderten. Der Parameter *SSR* quantifiziert die Belastung der Störung im Sinne des Mohr-Coulomb Kriteriums und erlaubt eine vergleichende Bewertung verschiedener Parametervariationen. Ein zweiter Simulationslauf in *ABAQUS explicit* analysiert die Dissipation der vorhergehend identifizierten, kritischen Belastungsfälle in Form von dynamischem Versatz auf der Modellstörung. Das implementierte Reibungsgesetz verschreibt der Störung einen abnehmenden Reibungswiderstand mit zunehmender Gleitgeschwindigkeit und bildet in Kombination mit den dynamischen Spannungen Grundzüge der dynamischen Bruchausbreitung bei der seismischen Reaktivierung von Störungen ab.

In der Modellierung wurden verschieden Faktoren identifiziert, die das Auftreten von produktions-induzierten Erdbeben begünstigen. Einzelne Parameter, wie eine geringe Tiefenlage des Reservoirs, eine große Reservoir-Mächtigkeit, große Biot-Koeffizienten sowie ein großer Steifigkeitskontrast zwischen Deckgestein und Reservoir begünstigen die Reaktivierung von Randstörungen des Reservoirhorizontes. Viskoelastische Evaporite im Hangenden spielen eine besondere Rolle für die Kritikalität der Störung, da sie eine lateral inhomogene Auflast auf das Reservoir ausüben und die räumliche Dissipation der produktions-induzierten Spannungen einschränken. Im Vergleich zum Grabenrand wurden Verwerfungen, die die Lagerstätte in interne Kompartimente unterteilen, als wahrscheinlichere Lokation für Erdbeben identifiziert. Hier erfahren Störungen, vor allem durch Produktionsszenarien, die den Porendruck entweder in beiden gegeneinander versetzten Kompartimenten oder nur im Liegenden Kompartiment absenken, eine besondere Belastung. Dabei kontrolliert der Versatz der Kompartimente entlang der Störung eine, durch die Geometrie bedingte, differenzielle Kompaktion der Kompartimente. Die bevorzugte Reaktivierung von steil einfallenden Störungen (> 60°) spiegelt in allen Modellen einen essentiellen Beitrag der elastischen Reservoirkompaktion zur kritischen Belastung der Störung wider, die im Kontrast zu tektonischen Modellen steht. Das größte Reaktivierungspotenzial der Grabenstörung wurde in den Modellen im oberen Bereich des Reservoirs und einem schmalen Abschnitt darüber beobachtet, an den kompartmentbildenden Verwerfungen tritt die Bruchinitiierung im unteren Bereich des Liegenden Reservoirhorizontes auf. Die Bruchausbreitung erfolgt entweder abwärts oder gleichzeitig auf- und abwärts entlang der Störung, wobei der übergeordnete heterogene Spannungszustand und die initiale

Beschleunigung die Bruchausbreitung entweder begünstigen oder dämpfen können. Der isotrope Spannungszustand im Salz und die Aufschiebungstendenz unterhalb des Reservoirs stellen ultimative geologische Barrieren für die Bruchausbreitung dar. Die Bruchlänge und der maximale Versatz hängen dabei vorwiegend vom tektonischen Spannungszustand und seiner Modifikation durch die Porendruckabsenkung ab und spiegeln nur sekundär die simulierte Porendruckabsenkung wider.

Die mögliche Abbildung der Reservoirverformung durch zwei unterschiedliche Effektivspannungskonzepte sowie die starke Sensitivität der Ergebnisse gegenüber verschiedenen Möglichkeiten der Störungsdarstellung heben fachspezifische Herausforderungen der numerischen Modellierung hervor. Aus den Modellierungsergebnissen lässt sich zusammenfassend kein einzelner, isolierter Parameter als Indikator für eine wahrscheinliche produktions-induzierten Reaktivierung von Störungen ableiten, weil das Reaktivierungspotenzial vor allem durch eine komplexe Wechselwirkung aus Anfangsspannungszustand, der Porendruckänderung und der Festigkeit von Störungen determiniert wird. Um die beobachtete Wechselwirkung verschiedener Parameter im Sinne einer Verstärkung oder Abschwächung des Reaktivierungspotenzials zu limitieren, muss der Parameterraum für detaillierte Vorhersagemodelle durch Struktur- und fallspezifische Daten weiter eingeschränkt werden. Nichtsdestotrotz liefert die vorgestellte FE- Modellierung ein grundlegendes Prozess- und Parameterverständnis und ermöglicht die Betrachtung von Szenarien und Grenzfällen in der Planung und dem Betrieb von Gaslagerstätten. Der präsentierte zweistufige Ansatz erlaubt zunächst die Identifizierung von kritischen Störungen und Belastungsfällen und evaluiert in einem zweiten Schritt die potenziellen Konsequenzen des kritischen Belastungsfalles in Form von dynamischer Bruchausbreitung. Hierbei stellt der vorgestellte Modellierungsansatz auch für andere geomechanische Problemstellungen, wie der Integrität von Deckgesteinen, ein vielversprechendes Werkzeug dar.

Acknowledgements

First and foremost, I like to thank Prof. Dr. Andreas Henk for giving me the opportunity to engage in this project and his trust in me to accomplish this study. I am grateful for his scientific support, his helpful feedback and for providing pragmatic advice in the course of this project. Furthermore, I very much appreciated to always find an open ear when there were questions.

Funding of this project was provided by Deutsche Erdoel AG (DEA), their support is gratefully acknowledged both in financial terms as well as for providing constructive criticism and helpful comments. Moreover, I'm grateful for the opportunity to work on an exciting topic and to gather a glance into the E&P industry. Namely I thank Dr. Jens-Alexander Nüchter, Dr. Thomas Bartels, Dr. Christian Bücker and Dr. Hanna-Maria Rumpel. In particular Dr. Jens-Alexander Nüchter was involved in the project with contagious enthusiasm, provided ideas and input and I always enjoyed far-reaching discussions with him. Dr. Thomas Bartels provided the data and could be approached at any time for background information. I want to thank both of them for the good atmosphere during project meetings, the uncomplicated communication and their cooperation within this project.

At this point I also have to emphasize my gratitude to Dr. Fengming Zhou of ABAQUS. Coming from a civil engineering background, he reacted with great interest, openness and professional excellence to issues that were encountered in ABAQUS from a geological point of view. His input laid the base for understanding and pointing out the validity and implications of different effective stress concepts and allowed me to deal with the prevailing issues in ABAQUS.

Moreover, I am sincerely grateful to Prof. Dr.-Ing. Michael Alber for taking on the second examination of this thesis and to Prof. Dr.-Ing. Matthias Becker and Prof. Dr. Eva Schill for co-examining.

I thank the entire staff of the Institute of Applied Geosciences in Darmstadt for the agreable work environment and for the good times at common events such as *TU meet and move*. In particular, I want to thank the group of engineering geology for the good atmosphere and cooperation, thank you Stefanie Kollmann, Reimund Rossmann, Karsten Reiter, Tobias Hergert, Clairet Guerra, Muhammad Zain-Ul-Abedin, Torben Treffeisen, Steffen Ahlers, Xianri Li, Christoph Wagner, Dennis Laux, visiting scientist Ilmir Nugmanov and the two Master students Stefan Wewior and Georg Schulz.

I look back with a smile to great times spent with colleagues of the hydrogeology group, Nils Michelsen, Sahand Farhang, Inga Schreiter, Stephan Schulz, Tom Schiedek, Aili Li and Christos Pouliaris and want to thank them for advice, motivation, coffee break, and professional discussions during Friday's *Schoppestund* at Ratskeller.

Great thanks go to my parents, Chris and my brother Johannes for backing me in any respect during the last years. At last, infinite thanks go to my love Antonella for being my shining light during stressful times.

Table of Contents

List of Figures

List of Tables

List of Symbols and Abbreviations

$1/K_p$	Drained pore compressibility
$1/K_\emptyset$	Unjacketed pore compressibility
[K]	Stiffness matrix
{u}	Displacement vector
a	Coefficient of rate- and –state friction
A	Area
A_i	Prefactor of the empiric creep law
b	Coefficient of rate- and –state friction
B	Skempton's coefficient
c	Diffusivity
c_g	Isothermal gas compressibility
C_{ijkl}	Stiffness tensor
C_0	Uniaxial compressive strength
CEBS	Central European Basin System
d	Decay coefficient for exponential friction-weakening
D	Darcy (unit)
D	Constitutive law
d_L	Characteristic rupture length
DEA	Deutsche Erdöl AG
det	Determinant
E	(Drained) Young's Modulus
ESPB	European South Permian Basin
erfc	Error function
F_i	Sum of applied forces, including body forces
$\vec{F}$	Force vector
FE	Finite element
FEM	Finite element method
FD	Finite difference
g	Gravitational acceleration
g(x)	Subfunction of Rudnicki's analytic solution
G	Shear modulus
h	Piezometric head
h, h_0	Contact clearance
H	Poroelastic expansion coefficient

I	Identity matrix
K	Bulk modulus
K_d	Drained bulk modulus
k_f	Hydraulic conductivity
K_g	Bulk modulus of single grain constituents
K_f	Bulk modulus of fluid
K_i	Intrinsic permeability
K'	Effective ratio of horizontal to vertical stress
K_u	Undrained bulk modulus
L	Characteristic length
L_e	Length
LSB	Lower Saxony Basin
m	Exponent of grain size in the empiric creep law
Δm_f	Change in fluid mass content per reference volume
M	Biot modulus
M	Earthquake magnitude (unspecified)
M_L	Richter earthquake magnitude
M_w	Seismic moment magnitude
n	Stress exponent in the empiric creep law
$\vec{n}$	Normal vector
p	Hydrostatic pressure
p	Contact pressure
Pa	Pascal (unit for pressure)
P_c	Confining pressure
P_d	Difference between confining and pore pressure
P_f	Pore pressure
P_{fovp}	Abnormal pore pressure (overpressure)
P_{fhyd}	Hydrostatic pore pressure
q	Deviatoric stress
q	Pumping rate in Rudnicki's analytic solution
$\vec{q}$	Specific discharge
q_d	Differential stress in the empiric creep law
Q	Activation enthalpy
Q	Volumetric flow
R	Universal gas constant

R	Specific storage coefficient
r	Radius
SSR	Shear stress ratio
T	Temperature
T_0	Uniaxial tensile strength
t	Time
t_c	Characteristic time
$\vec{u}$	Nodal displacement
$u(x)$	Shape function
v	Instantaneous slip velocity
V	Volume
v_0	Reference slip velocity
V_p	Pore Volume
V_f	Fluid volume
V'_f	Expelled fluid volume
vs	Slip rate
$\vec{x}$	Position vector
Z	Z-factor for real gases
α	Biot-coefficient
β	Subfunction of Rudnicki's analytic solution
$\Delta\sigma_{rad}$	Radial total stress change
$\Delta\sigma_{tan}$	Tangential total stress change
$\gamma_{ij}(x,y)$	2D stress arching parameter
δ_{ij}	Kronecker delta
$\dot{\varepsilon}_{dash}$	Viscous strain rate
ε_{ij}^{e}	Elastic strain
ε_{ij}^{p}	Plastic strain
ε	Total strain (ABAQUS specific)
ε'	Effective strain (ABAQUS specific)
ε_{ij}	(Cauchy) Strain tensor
ε_{vol}	Volumetric strain
ε_{kk}	Volumetric strain
η	Dynamic viscosity

θ	Counterclockwise angle between the normal of an arbitrary section and the Cartesian x-direction
θ_1	Clockwise angle between the first principal axis and the Cartesian x-direction
θ_2	Counterclockwise angle between the first principal axis and the normal of an arbitrary section
θ_s	State variable of rate- and state friction
κ	Mobility coefficient
λ	(Drained) first Lamé parameter
$\lambda_1, \lambda_2, \lambda_3$	Eigenvalues
λ_i	Scalar factor
λ_u	Undrained first Lamé parameter
μ	Coefficient of (internal) friction
μ_s	Static coefficient of friction
μ_d	Dynamic coefficient of friction
∇	Nabla operator
ν	Poisson's ratio
ν_u	Undrained Poisson's ratio
ξ	Increment in fluid content
ρ	Density
ρ_{dry}	Dry rock density
ρ_{wet}	Wet rock density including the fluid weight in the pore space
ρ_f	Fluid density
ρ_g	Density of the solid phase
$\vec{\sigma}$	Stress vector
$\sigma_1, \sigma_2, \sigma_3$	Maximum, intermediate and minimum principal stress
$\sigma'_1, \sigma'_2, \sigma'_3$	Effective maximum, intermediate and minimum principal stress
σ_D	Differential stress
σ_{ij}^{dev}	Deviatoric stress tensor
σ_i	Principal stress tensor
σ'_i	Effective principal stress tensor
σ_{ij}	Stress tensor
σ'_{ij}	Effective stress tensor
σ_m	Mean, hydrostatic stress
σ_{kk}	Normal components of the stress tensor

σ_n	(Total) normal stress
σ'_n	Effective normal stress
σ'_{Biot}	Effective Biot-Willis stress
σ'_{Terz}	Effective Terzaghi stress
$\sigma_V, \sigma_H, \sigma_h$	Tectonic vertical, maximum and minimum principal stress
$\sigma'_V, \sigma'_H, \sigma'_h$	Effective tectonic vertical, maximum and minimum principal stress
τ	Shear stress on an arbitrary plane
τ_{max}	Maximum shear stress
τ_{ij}	Shear stress components of the stress tensor (non-diagonal components)
$\emptyset$	Porosity
χ	Angle of dilatancy
ψ	Angle of (internal) friction

Preliminary Definitions

- Principal stresses are ranked in decreasing order as maximum, intermediate and minimum principal stress, referring to their absolute magnitude instead of their sign.

- The sign convention of stresses follows the convention of continuum mechanics; i.e. compressive stresses have a negative sign. Pressure, encountered as confining pressure in chapter 3 has a positive sign for the effect of reducing the volume of a rock specimen. The positive pressure results thus in compressive stresses of negative sign within the specimen.

- The term *compaction* is in some disciplines reserved for the non-linear deformation and irreversible loss of porosity in rocks or soils. In this study it addresses the thickness-reduction of reservoir sediments resulting from pore pressure depletion and is hence used in a more general sense.

- The *reservoir stress path* refers to the coupled change of total horizontal stress and pore pressure in laterally extensive reservoir horizons. This parameter governs the build-up of differential effective stress as the total vertical stress remains constant.

- The *stress path* refers to the representation of stress changes in the Mohr-diagram, illustrating the evolution of shear and normal stresses along a path that may converge with, or diverge from the failure line.

- Faults in the earth's crust are commonly inclined with respect to the vertical direction. The *hanging wall block* is defined by its position atop of the inclined fault plane, while the *footwall block* refers to the block below the fault plane.

1 Introduction

The work of this study was accomplished in the framework of the bilateral research project: '*Production-Induced Stress Redistribution and Fault Reactivation in Compartmentalized Reservoirs – Principle and Parameter Studies'* between TU Darmstadt and Deutsche Erdöl AG (DEA).

The project idea arose from the recent issue of production-induced seismicity in northern German Rotliegend gas fields. The numerical study was designed to improve the understanding of processes and factors potentially leading to seismic reactivation of faults. The data provided, comprised a generalized 2D reservoir and burden geometry, initial reservoir pore pressure, a bottom-hole depletion magnitude and material properties that mimic general features of northern German Rotliegend gas fields whereby reference to any particular field is not intended.

Scientific progress was documented by conference contributions (EAGE Conference and Exhibition Paris 2017, DGMK Frühjahrstagung Celle 2017, EAGE Sustainable Earth Science Conference & Exhibition Celle 2015) a mid-term report and recurrent presentations at the headquarter of the project partner. Parts of the outcome of the project were furthermore published in the open-access article 'Assessment of geological factors potentially influencing production-induced seismicity' (Haug et al. 2018). Several figures and text blocks of which the author claims pivotal intellectual authorship were adopted from this publication and appear in sections 1.3, 4.3, 8, 9, 10.4, 11 of this thesis.

1.1 Motivation and objectives

Induced seismicity is an increasing challenge to deep subsurface operations, such as the extraction of hydrocarbons, geothermal energy exploitation and gas storage. Both, injection and extraction of fluids from permeable reservoirs have induced seismicity at the affected sites (Foulger et al. 2018, Suckale, van der Baan & Calixto 2017, van Wees et al. 2014). In recent years, hydrocarbon extraction from some Rotliegend reservoirs of northern Germany (Fig. 1-1) and the Netherlands has triggered seismic events (e.g. Buijze et al. 2017) in populated areas, raising major public concern.

In Groningen, production started in the early 1960's, and first seismicity was recorded in 1991. Since then, 271 seismic events with $M_w > 1.5$ have been recorded until 2016 (DeDontney et al. 2016). This lead to a production cut in 2014 (Waal et al. 2015) and more recent events were followed by announcements of further production constraints along with a final exit from gas production in 2030.

In Lower Saxony 77 seismic events with magnitudes between $M_L \approx 0.5$ and probably up to $M_L \approx 4.3$-4.4 associated to active gas fields have been recorded hitherto (Uta 2017). Since tectonic seismicity is

scarcely documented in North Germany preceding gas production, these events had a strong impact on public perception of hydrocarbon production. From a scientific point of view, important questions concern the superposition of pre-existing far-field tectonic stresses by local pore pressure depletion and the mechanisms that locally drive long-term stable faults towards criticality.

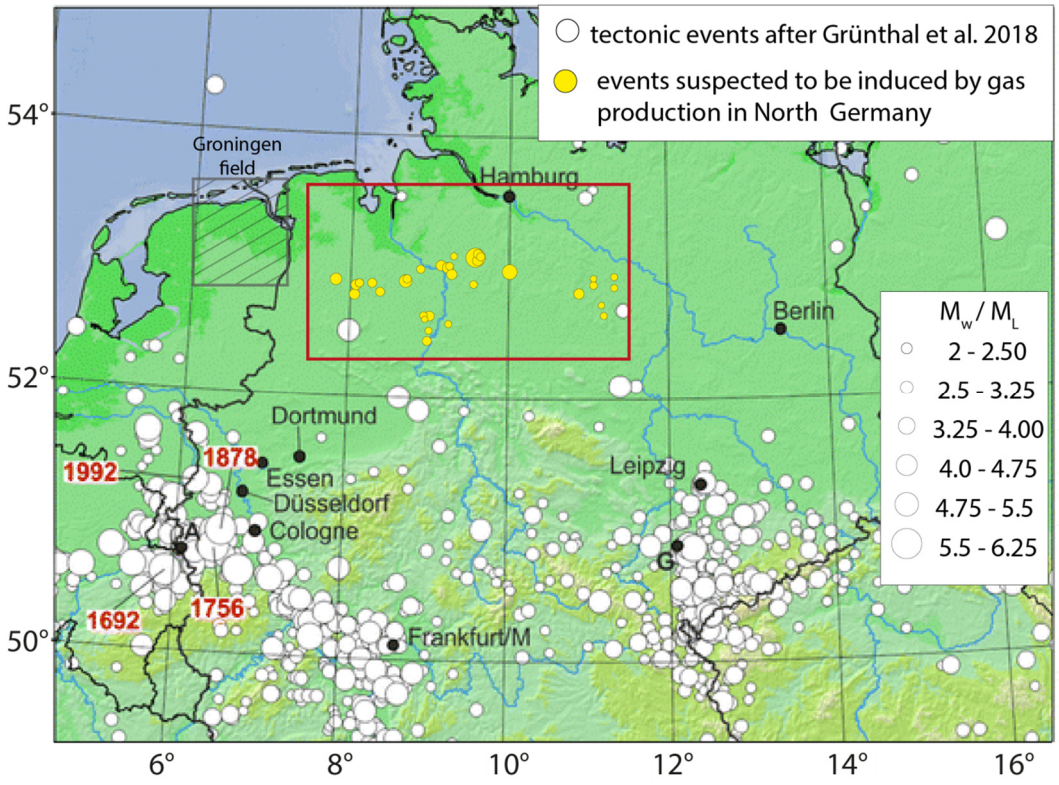

Fig. 1-1: Map of middle Europe showing tectonic events (taken from Grünthal et al. 2018) and earthquakes induced by gas production in North Germany (red frame) (after Bischoff et al. 2012). The linkage of the 1977 Soltau earthquake (located on 10° degrees longitude) to gas production has been controversial (Dahm et al. 2007) and the event was recently reclassified to tectonic origin by Uta (2017). The location of the Groningen field is indicated by the hatched frame.

Production-induced seismicity has been observed in different hydrocarbon fields worldwide (e.g. Foulger et al. 2018) but recurring events have only been recorded in a small number of basins in which only few fields are pertained. The large majority of producing gas fields on global scale as well as within the North German gas province, remain seismically quiet (Grasso 1992, McGarr et al. 2002, Suckale 2009, Uta 2017).

Basic concepts of production-induced stress changes and seismicity explain how pore pressure reduction may eventually cause fault failure within the reservoir (Altmann et al. 2010, Chan & Zoback 2002, Zoback & Zinke 2002) or in the hosting rocks surrounding the reservoir (Segall 1989, Segall & Fitzgerald 1998, Soltanzadeh & Hawkes 2008). However, all available analytical solutions are restricted to simple reservoir geometries and limited by assumptions of zero lateral strain or homogeneous

distribution of material properties. Such solutions are incapable to solve for the production-induced strain field that arises from interaction with structural complexities in compartmentalized reservoirs.

Seismicity in the Dutch gas fields has been addressed by an increasing number of studies, thereby geomechanical modelling has proven to be a valuable tool for the study of production-induced stress redistribution in complex reservoir geometries (e.g. Mulders 2003, Orlic & Wassing 2013). Presumably due to the significantly greater recurrence intervals of seismic events, i.e. larger time span between two events of similar magnitude (BVEG 2017, Uta 2017), similar scientific effort has not been undertaken for the North German gas fields.

This study aims on fundamentally increasing the understanding of production-induced stress changes and fault reactivation in compartmentalized reservoirs of the North German Basin. Therefore, geological factors that may explain the occurrence of seismicity in specific fields and compartments are assessed in numerical models. The generic models aim on capturing essential geological features of North German Rotliegend gas fields but reference to a particular field is not intended. For the comparative evaluation of different parameters, a suitable modelling workflow in the Finite Element (FE-) software ABAQUS has to be established first.

1.2 Study Outline

The introductory chapter of this thesis concludes with a review of essential literature on fluid-induced seismicity and introduces basic models of depletion-induced stress changes. The review is followed by a theoretical part that encompasses first, the fundamentals of rock mechanics (chapter 2) and second, principles and moduli associated to fluid infiltrated porous solids representing the factual material behaviour within the upper earth's crust (chapter 3). The latter chapter lays the base for the understanding of two different effective stress concepts encountered in the numerical modelling with ABAQUS.

Chapter 4 focusses on stress changes predicted by analytic models for pore pressure depletion and illustrates applicability and limitations of their employment on realistic geometries and compartmentalized reservoirs.

Chapter 5 briefly describes principles of the well-established Finite Element method (FEM), its application in consolidation analysis and important aspects of contact modelling and element selection.

A characteristic modulus for the mechanical behaviour of fluid infiltrated reservoir sandstones is the Biot-coefficient that in modelling is often presumed to be 1 but actually is much smaller for solid rocks. Chapter 6 explains and discusses issues encountered when introducing the Biot-coefficient inferior to one into the soil mechanical procedure of ABAQUS. Directly linked to the Biot-coefficient is an undocumented change from Terzaghi to Biot-Willis effective stress output in ABAQUS versions released during the project. Emerging from this issue, implications of two complementary effective stress concepts in the modelling of geomechanical problems are discussed.

Chapter 7 deals with the establishment of the FE modelling workflow for the case-specific study of seismicity in North Germany. It encompasses the implementation of different physical model properties such as initial stress, the pore pressure field and faults. The preliminary studies aim on the creation of a generic but deterministic reservoir model serving as a suitable. base for the comparison of the effect of a large range of parameters on production-induced fault-loading. Important properties of the deterministic reservoir model encompass sealing faults, overpressured reservoir horizons, strong stiffness contrasts and a non-critical stress state prior to production.

Chapter 8 and 9 apply the workflow and findings of the preliminary studies to the modelling of production-induced stresses and present the effect of different parameters on fault-loading in the North German basin. The Rotliegend reservoirs are located within staggered Permian graben and Horst structures (Fig. 1-2) and firstly their detailed geological setting is introduced. Based on the geological background three generic model series are defined. Model series I addresses the loading of a graben-fault, bounding a single reservoir compartment. Model series II investigates the stress state below a viscoelastic salt diapir. Model series III deals with the production-induced loading of a sealing intra-field fault that offsets two reservoir compartments.

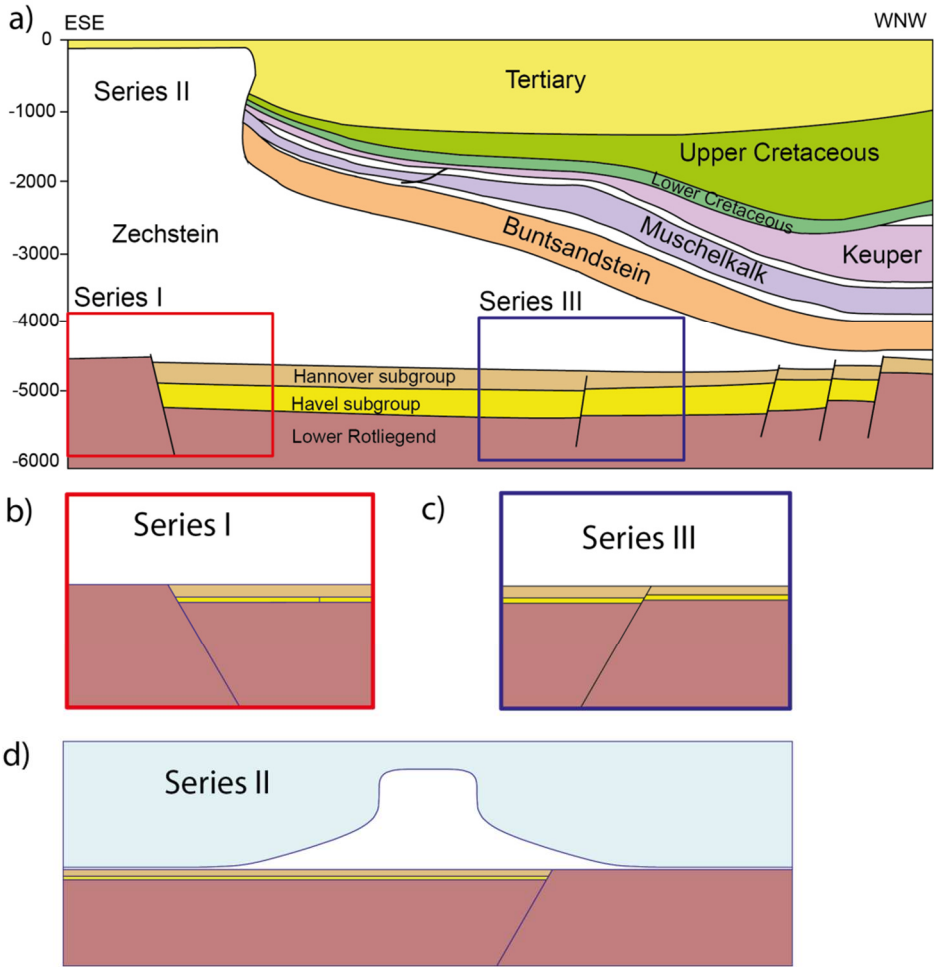

Fig. 1-2: a) Characteristic geological profile of North German Rotliegend gas field. b-d) abstracted model geometries representing a single reservoir at the graben boundary (b), intra-field reservoir horizons compartmentalized and offset by a sealing fault (c), and d) Evaporite layers in the overburden exhibiting significant lateral variation in thickness due to diapirism.

In the second part of chapter 8, a modelling workflow is introduced that evaluates the previously determined fault loading patterns with respect to their dissipation in the dynamic rupture of faults. The results of the dynamic rupture study, shedding light on potential earthquake locations and boundaries for the propagation of slip, are presented in the second part of chapter 9.

Chapter 10 summarizes the findings of the 2D parameter study and discusses the realization of model properties such as the sealing faults and the used effective stress concept with respect to their impact on the modelling results. This is followed by a detailed discussion of the parameter study and dynamic rupture analysis, a comparison of the findings to other studies, and recommendations for future studies.

The final chapter 11 formulates short conclusions. Implications of the most important results for production-induced seismicity in North Germany are articulated and general conclusions on the study results and modelling approach are drawn.

1.3 Literature review – Part I: Induced seismicity and depletion-induced stress changes

Fluid-induced seismicity results from mechanical disequilibria, build-up by pore pressure driven differences in deformation and stresses inside the reservoir and its surrounding, ultimately compensated by the reactivation of faults (e.g. Grasso 1992, van Thienen-Visser & Breunese 2015, Shapiro 2015, Segall 1989). Both, injection and extraction of fluids from permeable reservoirs have induced seismicity at the affected sites (Suckale 2009, van der Baan & Calixto 2017, van Wees et al. 2014). Injection-induced seismicity driven by an increase in pore pressure has been documented for a variety of subsurface operations including (1) waste water disposal in deep formations (Walsh & Zoback 2015), (2) pressure maintenance in oil and gas fields (Ellsworth 2013), (3) pore pressure diffusion in the framework of hydraulic fracturing (Deng et al. 2016, Rubinstein & Mahani 2015, Shapiro 2015), (4) injection into storage facilities (Ruiz-Barajas et al. 2017), and (5) stimulation (Evans et al. 2012) and operation of geothermal reservoirs (Majer et al. 2007). Mechanisms leading to injection-induced seismicity include the decrease in effective normal stresses caused by the increase in pore pressure (P_f) (e.g. Cappa & Rutqvist 2011, Rubinstein & Mahani 2015, Shapiro & Dinske 2009), more complex models relate injection-induced seismicity to changes in total stress attributed to pore pressure stress coupling (e.g. Altmann et al. 2010, Rutqvist & Tsang 2005, Rutqvist et al. 2008) or propagation of Coulomb stress perturbations (e.g. Rozhko 2010, Segall & Lu 2015). Seismicity caused by the withdrawal of oil or gas from deep permeable reservoirs, i.e. by a reduction in P_f has until recently received significantly less scientific attention and mechanisms may differ significantly with respect to injection-induced seismicity (Candela et al. 2018).

Ground subsidence is a most obvious mechanical effect resulting from pressure depletion (e.g. Doornhof et al. 2006, Ferronato et al. 2008). Prominent historic examples are the Goose Creek oil field in Louisiana (Pratt & Johnson 1926) and the Wilmington oil field (Nagel 2001) in California. Moreover, small earthquakes were felt close to Wilmington and Goose Creek oil fields after having undergone significant compaction. Reservoir compaction, tracing to the surface as subsidence (Bardainne et al. 2008, Ferronato et al. 2008, Fokker & van Thienen-Visser 2015) serves as a first order explanation of the currently most prominent example of production-induced seismicity, the Groningen gas field of the Netherlands (Muntendam-Bos et al. 2015, Sanz et al. 2015).

For production-induced stresses and fault reactivation, important theoretical, analytic and analogue models were proposed in the last three decades. For instance Pennington et al. (1986) proposed that the production-induced elastic reservoir strain accumulates along fault segments bounding reservoir compartments due to compaction of the reservoir rocks. Segall 1985, 1992) proposed that stress

changes within the reservoir and reservoir strain may destabilize faults at some distance to the reservoir and presented analytic solutions to the stressing of the reservoir surrounding rock by reservoir contraction as a possible explanation for seismicity in the Lacq gas field, France. Baranova et al. (1999) successfully applied Segall's (1985) model to demonstrate that the October 1996, *M* = 3.9 event associated to the Strachan gas field, Alberta, Canada was induced by hydrocarbon extraction. Analogue experiments by Odonne et al. (1999) confirmed the general validity of Segall's (1989) model albeit suggesting some deviations in the preferred geometry of the faults. Bardainne et al. (2008) emphasize that the misfit between Segall's (1989, 1992) predictions and seismicity in the Lacq gas field derive mainly from the fault-bound deformation pattern as opposed to the circular pattern of the analytic models.

Segall & Fitzgerald (1998) demonstrated that fault-loading and reactivation within the reservoir or in the hosting rocks depends strongly on the geometry of the reservoir, and on the rock mechanical parameters controlling the ratio of stress and pore pressure changes within the reservoir. For the reservoir centre, Segall & Fitzgerald's (1998) inclusion model yields a total horizontal stress change that is in accordance with predicted horizontal stress change from the uniaxial strain model (cp. section 4.2). This coupled change of total horizontal stress and pore pressure results in the build-up of differential stress, as effective horizontal and vertical stresses increase at different rates (e.g. Schutjens et al. 2007, Teufel et al. 1991) and the differential stress has been reasoned to cause seismic reactivation of faults (Zoback & Zinke 2002). The coupling of pore pressure to total stress change is commonly referred to as the *reservoir stress path* and has been observed in worldwide field data (Addis 1997, Goulty 2003, Salz 1977, Santarelli et al. 1998, Teufel et al. 1991). The observed scatter in the field data is interpreted by Altmann et al. (2010) as a consequence of a spatio-temporal variation of the coupling factor. Moreover, Altmann et al. (2014) postulate that the complete principal stress tensor is coupled to pore pressure changes, resulting for example in enhanced production-induced loading in normal faulting stress regimes, as both, total vertical and horizontal stresses undergo coupled pore pressure-stress changes.

Several authors have attempted to reconcile the in-situ *reservoir stress path* parameter with results from rock-testing (Hettema et al. 1998, Schutjens et al. 1998, Spiers et al. 2017) and field scale compaction and subsidence models, but the Groningen field for example, subsides in a non-linear and delayed manner (Hettema et al. 2000, Marketos et al. 2016, Waal et al. 2015, van Thienen-Visser & Fokker 2017).

On reservoir-scale, inelastic deformation of sandstones prevails for large confining pressures (Santarelli et al. 1998, Teufel et al. 1991) and nonlinear compaction may lead to reactivation of faults

in spite of a stable stress path during the elastically recoverable part of consolidation (Chan & Zoback 2002, Ozan et al. 2011).

Addressing finite reservoir geometries, surrounded by an undepleted sideburden, Soltanzadeh & Hawkes (2008) extended Segall & Fitzgerald's (1998) elliptical model to rectangular reservoir geometries and replaced the *reservoir stress path* by a general arching parameter (section 4.3) that accounts for vertical and horizontal stress changes in and around the reservoir. Further geomechanical studies use numerical methods to compute the stress arching parameter as a function of different factors such as reservoir size, reservoir aspect ratio or stiffness contrasts of reservoir and burden (Khan et al. 2000, Alassi et al. 2006, Segura et al. 2011, Gheibi et al. 2017, Holt et al. 2004).

In order to account for complex geometries and strain fields, Finite element methods have been increasingly applied to assess the effect of pore pressure depletion on model scenarios addressing Dutch Rotliegend gas fields (Mulders 2003, Nagelhout & Roest 1997, Roest & Mulders 2000).

Orlic & Wassing (2013) simulated stress changes and fault slip in faulted reservoirs and such overlain by elastic and viscoelastic caprocks in the Dutch part of the North German basin. Their models along with earlier numerical studies by Mulders (2003) suggest that differential compaction and offset along intra-field faults along with superposition of induced stress changes play a key role for fault reactivation in production-induced seismicity. The Production from offset reservoir horizons induces non-continuous strain fields and moments across the fault, in the simplest case due to offset along the fault. However, differences in displacement, frequently referred to as 'differential compaction' (Doser et al. 1991, Mulders 2003, van Wees et al. 2014, Yerkes & Castle 1976) can relate either to differences in total production, in production rates, reservoir thicknesses, elastic and poroelastic properties, or a combination of these parameters.

Geomechanical FE modelling has furthermore been successfully applied for instance in the assessment of a potentially induced M_L*=5.8* earthquake in the Emiglia-Romana region in 2012. By means of a large scale FE geomechanical model of the Cervone area, Juanes et al. (2016) prove that pore pressure-induced stress perturbations did not suffice to trigger the devastating event.

Addressing different levels of abstraction, the previously introduced models and concepts provide a basic understanding of the mechanisms that may lead to production-induced seismicity. Difficulties in establishing detailed correlations between model results and earthquakes arise among others from uncertainties with respect to localization, kinematics and statistical distribution of induced seismic events. Frohlich et al. 2016) and Hauksson et al. (2015) review induced seismic activity during the last century in the producing areas of the Texas Permian basin and the greater Los Angeles area, California.

Frohlich et al. (2016) point out on one hand that past induced seismic events are difficult to assess as a consequence of the development of the installed seismic monitoring network. That is, poorly located earthquakes can hardly be associated to particular operations of a certain field as the production of hydrocarbons commonly comprises both, injection and fluid withdrawal (Frohlich et al. 2016). On the other hand, faults critically stressed from tectonic forces cannot be precluded for some affected areas such as lower California (e.g. Hauksson et al. 2015, Hough & Page 2016) northwestern Texas (Frohlich et al. 2016) as well as for the Strachan (Baranova et al. 1999) and Lacq (Bardainne et al. 2008) fields located in close proximity to seismically active mountain ranges.

The initial, i.e. the far-field stress state is of crucial importance for production-induced seismicity as it determines the distance to failure to be overcome by stress changes (e.g. van Wees et al. 2014). Thereby pre-production stresses in gas reservoirs can be very complex, even in regions of low tectonic activity (e.g. Fischer & Henk 2013, van Wees et al. 2014).

With respect to the northern German gas fields, Uta (2017) and Brandes et al. (2015) argue that the deglaciation of large parts of northern Europe may have resulted in recent changes of the stress field that render some faults under a more critical stress, as inferred from the virtual absence of seismicity in this region during times covered by historic records. Moreover, stress changes associated to ongoing salt tectonics (Lohr et al. 2007, Mohr et al. 2007) may have had a strong influence on the local stress field (e.g. Cornet & Röckel 2012).

1.4 Literature Review Part II: Recent developments spurred by seismicity in the Groningen gas field

Zöller & Holschneider (2016) call the Groningen gas field a *"natural laboratory for production-induced earthquakes*" reasoning that tectonic background seismicity can be neglected and an abundant number of induced events can be observed. The Groningen field is one of the world's largest onshore gas fields (Sijacic et al. 2017) and compared to the Lower Saxony fields, represents superlatives with respect to produced volume, economic relevance and seismic activity. Given the comparatively shallow depth of earthquakes, magnitudes that have reached a maximum of M_L*=3.6* close to Huizinge in 2012 (Waal et al. 2015) question the integrity of local infrastructure whose building code could not foresee an induced seismic hazard.

In consequence, available data and scientific effort, both, by operators and public institutions surpass the venture for the North German gas fields for which the focus has so far been laid on the expansion of the seismic monitoring network (e.g. BVEG 2017, Mokelke et al. 2016). During the period of this

project a number of studies have been published on induced seismicity in the Groningen field that will briefly be introduced in the following.

The question of whether production-induced surface subsidence and seismicity of the Groningen field can be managed is raised by (Waal et al. 2015). They report that production cuts in the area of largest compaction, i.e. the centre of the Groningen field, have already lead to reduced seismicity rates and subsidence rates there. This supposedly results from a transformation of the brittle deformation pattern to ductile deformation at slower loading rates (Muntendam-Bos et al. 2015). Furthermore, the authors review prediction efforts on reservoir compaction which is identified to be the driving mechanism for the seismicity in the Groningen field and state the difficulty of compaction prediction, i.e. compaction models had to be revised constantly ever since seismicity started (Muntendam-Bos et al. 2015).

Sijacic et al. (2017) investigate the correlation between production and seismicity by statistic methods, in order to estimate prospects of success of the production cuts since 2014. They find a correlation between production rates and seismicity for example in the yearly swing in gas production whose maximum is reflected by an outburst of seismic events some 4–8 months later.

Van Wees et al. (2017) address the onset and evolution of seismicity in generic FE reservoir models in the light of the 2014 imposed decreases in production rate. Their models predict an increase in seismic moment with continuing production but imply that the production stop leads to a significant slowing of the seismic moment increase. Continuing compaction after the production stop is accounted for by Kelvin-creep in their model and the seismic event is represented by an instantaneous drop in frictional resistance to its dynamic value once slip initiates.

Muntendam-Bos et al. 2015 present a guideline for seismic risk assessment of the Groningen field. The first level of risk assessment comprises among others three key risk factors, 1) pressure drop, 2) fault density and 3) stiffness ratio between reservoir and reservoir seal identified by van Eijs et al. (2006) in a statistical analysis of field properties and seismicity. Assessment level two and three apply to fields for which induced seismicity has already been recorded, comprising classic seismic hazard analysis, quantitative seismic risk assessment and a managing plan. Thereby the largest risk is posed by large ground-accelerations associated to maximum possible magnitudes (e.g. Bommer & van Elk 2017, Bourne et al. 2018, Zöller & Holschneider 2016) that occur at a low probability.

A full-scale numerical model of the Groningen field is presented by Sanz et al. (2015) and Lele et al. (2016). The model is calibrated on subsidence data and uses reservoir simulation to map the pore

pressure field. They find a good correlation of fault friction-dissipated energy and the cumulative radiated energy released in seismic events, providing a base to evaluate future production scenarios.

The *Shell* report on production-induced seismicity, authored by van den Bogert (2015) investigates different FE modelling options and their impact on the onset of fault slip and slip magnitude. The author finds that stiffness contrasts, compartment offsets of less than the reservoir height and contemporaneous depletion of fault-juxtaposed reservoir horizons show distinctively different stress paths and slip patterns. Moreover, they suggest that fault slip and formation strain energy i.e. compaction, compete for the same energy source, concluding that modelling static fault slip can be correlated to recorded seismic events but more sophisticated rupture models that account for co-seismic energy radiation should be set up in the future.

Wassing et al. (2016) introduce slip-dependent friction weakening into generic models to account for post-failure dynamic rupture and a more realistic evaluation of moment magnitudes. The friction weakening behaviour is here characterized by a critical slip length during which frictional resistance drops linearly to the dynamic value and results, similar to real seismic events, in a shear stress drop on the fault. Further findings comprise the similarity of modelling results for both, dynamic and static modelling of friction-weakening fault slip.

Wassing et al. (2017) investigate the impact of a viscoelastic caprock on dynamic fault rupture, stating that the favourable pre-production stress state associated to the presence of salt leads to a comparatively earlier reactivation of the fault on which significantly smaller slip magnitudes can be observed for this case.

Buijze et al. (2017) model seismic rupture in 2D models that encompass an increasingly realistic abstraction of the Groningen gas field in terms of fault geometry, lithology-specific fault friction, and material properties, based on field data and the study of outcrop analogues. The authors model dynamic rupture by means of cohesion-weakening friction and account for the radiation of elastic waves from their simulated seismic events. Similar to van den Bogert (2015), Buijze et al. (2017) emphasize the influence of compartment offset on the nucleation of earthquakes. For zero offset, fault reactivation occurs at comparatively large pore pressure depletion magnitudes, which in turn result in large seismic events. Reservoir offset on the other hand favours rupture nucleation at much lower depletion magnitudes. Downward propagation of fault rupture is inhibited by the heterogeneous stress state associated to the offset geometry, leading ultimately to smaller event magnitudes.

Zbinden et al. (2017) simulate different depletion and mitigation scenarios for two offset reservoir horizons. The models include two-phase flow by fully coupling the mechanical simulator to an external flow simulator. Their results reflect the influence of fault zonation and semi-permeable hydraulic properties producing a distinct pore pressure evolution and a non-linear stress path within the fault zone. A mitigation strategy for production-induced seismicity is proposed, stipulating pressure maintenance by injection into the depleting horizons.

Ter Heege et al. (2018) review the applicability of numerical reservoir models in the assessment of production-induced seismicity. They propose the usage of static models to analyse the localization and likelihood of reactivation during injection or depletion. In order to assess characteristics of seismicity on the other hand, dynamic rupture models, accounting for the radiation of seismic waves are recommended. The authors conclude that the combination of both modelling approaches may allow for the optimization of production strategies and mitigation of seismicity.

The production cuts of 2014 initially appeared to constitute a successful mitigation strategy for seismicity in the Groningen field. In January 2018 however, the region was hit by its overall third largest and biggest event since Huizinge 2012.

2 Basics of Geomechanics

This chapter gives a brief overview over essential theories and aspects of rock deformation under conditions of the brittle upper crust. It starts from the description of stress and strain, sheds light on deformation regimes in the earth's crust and reviews constitutive laws for the description of stress and strain in rocks and soils on different time and length scales. At last concepts of rock and fault strength are introduced, providing criteria and limiting load cases for the assessment of fault reactivation, potentially leading to dynamic rupture and seismic events.

The term geomechanics comprises concepts and theories from different theoretical and applied disciplines (Cornet 2014), such as continuum mechanics, rock and soil mechanics, structural geology and petroleum engineering. In the context of oil and gas operations, geomechanical problems comprise borehole stability, fault stability, shear-enhanced compaction, land subsidence, hydraulic fracturing, induced seismicity and the planning of wellbores close to salt domes (e.g. Zoback 2007).

In reality, most of these problems encompass the effect of fluids in the subsurface. Here, the basic concepts are explained irrespective of pore pressure. The stress-strain relationship and failure of rocks under fluid-saturated conditions is separately addressed in chapter 3.

2.1 Cauchy Stress and Strain

A continuous body at rest, subject to an external load or body force, can be fictively cut by an arbitrary plane *A*, in order to retrieve the stress vector $\vec{\sigma}$. The plane $A(\vec{n})$ is determined by its unit normal vector $\vec{n} = n_1, n_2, n_3$. The stress vector $\vec{\sigma}(\vec{x}, \vec{n})$ depends on its location $P(\vec{x}) = (x_1, x_2, x_3)$, and its relative orientation to the cutting plane's normal vector $\vec{n}$. The stress vector at point *P* measured in Pa [kg/ms^2] is then given by (e.g. Zang & Stephansson 2010):

$$\vec{\sigma}(\vec{x}, \vec{n}) = \lim_{\Delta A \to 0} \frac{\Delta \vec{F}}{\Delta A} \qquad 2.1$$

Extending the consideration of a certain plane and point to any arbitrary cutting plane within the body, the stress vector $\vec{\sigma}$ is then related by the Cauchy stress tensor σ_{ij} to an arbitrary plane of unit normal vector $\vec{n}$ (e.g. Jaeger et al. 2007)

$$\vec{\sigma} = \sigma_{ij}\vec{n}_j \, . \qquad 2.2$$

The Cauchy stress tensor is a second rank tensor whose diagonal *(index i=j)* contains the normal stresses to three orthogonal cutting planes, determined by the given coordinate system (Fig. 2-3). Within the Cartesian coordinate system (n_1=x, n_2=y, n_3=z), Equation 2.2 can be written as:

$$\sigma_{ij} = \begin{pmatrix} \sigma_{11} & \sigma_{12} & \sigma_{13} \\ \sigma_{21} & \sigma_{22} & \sigma_{22} \\ \sigma_{31} & \sigma_{32} & \sigma_{33} \end{pmatrix} = \begin{pmatrix} \sigma_{xx} & \sigma_{xy} & \sigma_{xz} \\ \sigma_{yx} & \sigma_{yy} & \sigma_{yz} \\ \sigma_{zx} & \sigma_{zy} & \sigma_{zz} \end{pmatrix} \qquad 2.3$$

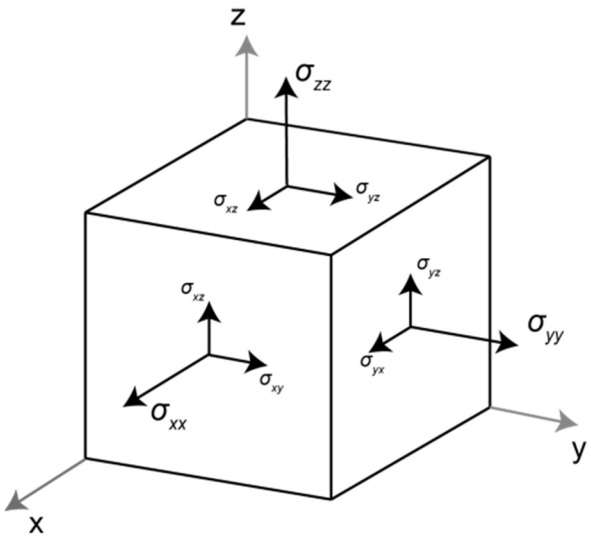

Fig. 2-3: Graphical representation of the stress tensor in the Cartesian coordinate system and its index convention that denotes normal stress (*i=j*) and shear stresses (*i≠j*).The first index governs the direction and sign of the stress component.

The condition of the body at rest, i.e. the balance of momentum of the system requires that shear stresses occupying the non-diagonal components of the tensor *(i≠j)* are equilibrated and the stress tensor becomes symmetric (*ij=ji*).

In accordance with the sign convention of the FE-software ABAQUS, compressive stresses are negative in this study.

2.2 **Principal Stresses**

The stress tensor can be expressed in any rectangular coordinate system but for any given stress state, there is one particular system, that spans the base to shear-free cutting planes, the principal system. The principal stress tensor comprises thus only three diagonal normal stress components (e.g. Zang & Stephansson 2010)

$$\sigma_i = \begin{pmatrix} \sigma_1 & & \\ & \sigma_2 & \\ & & \sigma_3 \end{pmatrix}. \qquad 2.4$$

The components are ordered by magnitude $\sigma_1 > \sigma_2 > \sigma_3$. Mathematically, the transfer of the stress tensor from one coordinate system to another is executed by multiplying the tensor with the transformation matrix and its transpose (Jaeger et al. 2007).

The normal vectors $\vec{n}'$ of the shear free sections are co-linear to the stress trajectories $\vec{\sigma}$, according to the scalar factor λ_i (Eqs. 2.15-2.19 Zang & Stephansson 2010)

$$\vec{\sigma} = \sigma_{ij}\vec{n} = \lambda_i \vec{n}\,'. \qquad 2.5$$

Multiplication by the identity matrix yields the following Eigen-value problem

$$(\sigma_{ij} - \lambda_i I)\vec{n} = 0 \qquad 2.6$$

that has a non-trivial solution for the determinant being zero

$$det(\sigma_{ij} - \lambda_i I) = 0 \qquad 2.7$$

leading to the polynomial

$${\lambda_i}^3 - I_1{\lambda_i}^2 + I_2\lambda_i - I_3 = 0 \qquad 2.8$$

where $\lambda_1, \lambda_2, \lambda_3$ are Eigenvalues of Equation 2.6, representing the magnitude of the principal stresses. Using λ_i in Equation 2.6 returns the Eigen-vectors n_j for the orientations of the principal axes. The coefficients I_1, I_2, I_3 are tensor invariants; they are independent of the coordinate system considered (e.g. Jaeger et al. 2007).

2.3 Deviatoric, hydrostatic and differential stress

Decomposition of the stress tensor into a hydrostatic part for volumetric deformation and a deviatoric part is useful (Zang & Stephansson 2010), for instance in the formulation of yield hypotheses (section 2.7). The hydrostatic stress is a third of the first invariant $\frac{1}{3}I_1$ and corresponds to a mean stress

$$\sigma_m = \frac{\sigma_{kk}}{3} = \frac{\sigma_{11} + \sigma_{22} + \sigma_{33}}{3}. \qquad 2.9$$

The deviatoric part is obtained by subtracting the hydrostatic stress from the stress tensor whereby the *Kronecker Delta* indicates that only the diagonal elements are subject to the operation:

$$\sigma_{ij}^{dev} = \sigma_{ij} - \frac{\sigma_{kk}}{3}\delta_{ij} \qquad 2.10$$

δ_{ij}: Kronecker returning 0 for i=j and 1 for i≠j

In the vector space that is spanned by the three principal axes, the hydrostatic stress is represented by a line, oriented at equal angle to all principal axes and represents the normal vector to the deviatoric plane. In critical state soil mechanics, the hydrostatic stress is often referred to as *p* and the deviatoric stress as *q*. These two variables span a plane that allows for the 2D illustration of yield hypotheses such as the Cam-clay or modified Drucker-Prager model.

Another important characteristic value of the principal stress tensor, sometimes confused with deviatoric stress (Engelder 1994), is the differential stress, i.e. the difference between maximum and minimum principal stress

$$\sigma_D = \sigma_1 - \sigma_3 \,. \qquad 2.11$$

Differential stress determines the maximum shear stress (Eq. 2.12) and governs failure of macroscopically intact rock, subjected to a confining and an axial pressure, conditions applied for example in triaxial rock testing (e.g. Zoback 2007)

$$\tau_{max} = \frac{\sigma_1 - \sigma_3}{2}. \qquad 2.12$$

2.4 Strain Tensor

The deformation of a body due to external forces can be expressed by the dimensionless variable strain. In the simplest, 1D case of a rod under axial tension, the dimensionless Cauchy strain is the change in length per unit length (Fjaer 2008)

$$\varepsilon = \frac{L_{e1} - L_{e2}}{L_{e1}} = \frac{\Delta L_e}{L_e}. \qquad 2.13$$

For the continuum description, i.e. the displacement of an infinite number of single material points relative to one another, infinitesimal strain is addressed in this section. This strain-approach assumes only small relative displacements with respect to the original geometry. Displacements and strain are related by the following formulation (Fjaer 2008):

$$\varepsilon_{ij} = \frac{1}{2}\left(\frac{\delta u_i}{\delta x_j} + \frac{\delta u_j}{\delta x_i}\right) \qquad 2.14$$

And the resulting strain tensor can be written as:

$$\varepsilon_{ij} = \begin{pmatrix} \varepsilon_{11} & \varepsilon_{12} & \varepsilon_{13} \\ \varepsilon_{21} & \varepsilon_{22} & \varepsilon_{23} \\ \varepsilon_{31} & \varepsilon_{32} & \varepsilon_{33} \end{pmatrix}. \qquad 2.15$$

The strain tensor has analogue properties to the stress tensor, i.e. a principal system exists for which shear strains vanish. The first invariant of the strain tensor is volumetric strain (Fjaer 2008)

$$\varepsilon_{vol} = \frac{\Delta V}{V} = \varepsilon_1 + \varepsilon_2 + \varepsilon_3 = \varepsilon_{kk}\,. \qquad 2.16$$

While hydrostatic strain describes an isometric change in volume (Fig. 2-4 a), the deviatoric strain addresses changes of the shape of a body at constant volume (Fig. 2-4 b).

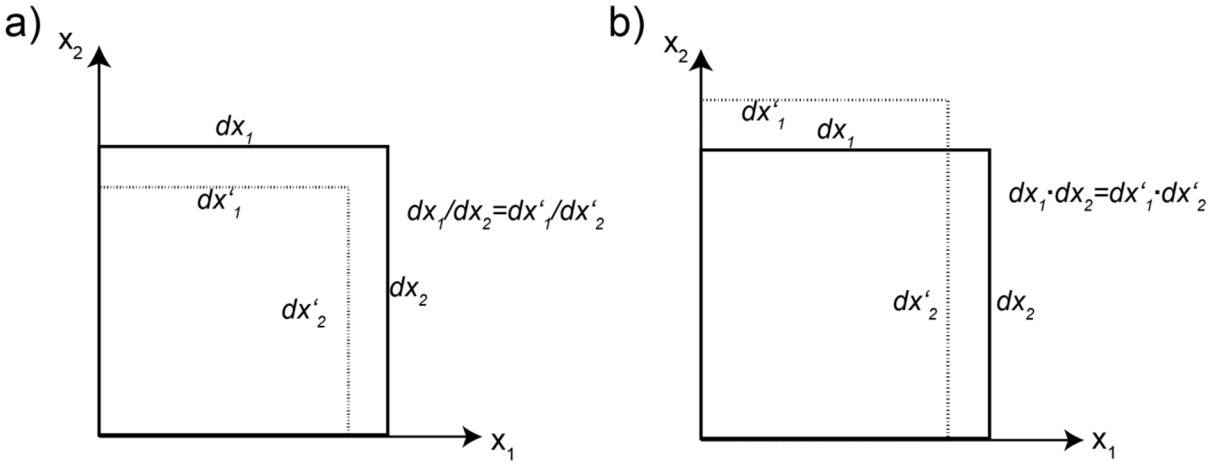

Fig. 2-4: a) Hydrostatic strain resulting in an isometric volume change b) Deviatoric strain describing a change in shape (after Zoback 2007, Katzenbach et al. 2012).

2.5 2D plane strain and stress transformations

Many geotechnical engineering problems are essentially 2D problems, for example dams, composite walls or railroad tracks (Katzenbach et al. 2012). The evaluation of stresses in 2 dimensions requires assumptions in order to reduce the real 3D problem in a physical sound way. The 2D plane-strain approach sets the out-of-plane deformation to zero (Jaeger et al. 2007). Plane strain conditions are justified when the loading or displacement boundary conditions are applied orthogonally to one or two of the coordinate axes independently of the third axes, essentially requiring that properties do not change in the third direction (Katzenbach et al. 2012).

When dealing with fault reactivation, the shear and normal stresses on the fault plane are consulted to evaluate the loading of the fault or to identify preferential fault orientations for reactivation within the given stress field (e.g. Sibson 1985). Here the Mohr-Plot allows deriving graphically the orientation of the principal axis and shear and normal stresses on cutting planes of arbitrary orientations.

Normal and shear stress on a plane whose normal is rotated by a counterclockwise angle θ with respect to the x_{11}-axis can be computed by (Eqs. 2.31, 2.32 Jaeger et al. 2007):

$$\sigma_n = \frac{1}{2}(\sigma_{xx} + \sigma_{yy}) + \frac{1}{2}(\sigma_{xx} - \sigma_{yy})cos2\theta + \tau_{xy}sin2\theta \qquad 2.17$$

$$\tau = \frac{1}{2}(\sigma_{yy} - \sigma_{xx})sin2\theta + \tau_{xy}cos2\theta \qquad 2.18$$

Figure 2-5 a) shows one of the shear-free sections associated to the principal coordinate system in 2 dimensions. The first principal axis is thereby rotated by θ_1 with respect to the Cartesian x_{11}-axis. Figure 2-5 b) illustrates shear and normal stress on an arbitrary section whose normal is rotated by θ with respect to the x_{11}-axis and equations 2.17, 2.18 apply for the computation of shear and normal stress on this plane. Figure 2-5 c) illustrates the pre-defined shear plane in the given principal stress field, the angle θ_2 describes the counterclockwise radial distance between the normal of the section and the first principal direction. Shear and normal stress on the given plane can be computed as a function of the principal stresses according to equations. 2.20, 2.21 and under consideration of the angle θ_2. The Transform relations can be expressed in the Mohr-domain (Fig. 2-5 d). Coordinates on the Mohr circle represent shear and normal stress magnitudes of a given stress state, for a range of shear plane orientations 0°< ϑ< 180°. The sign convention for shear stress in this study is illustrated in Figure 2-5 c.

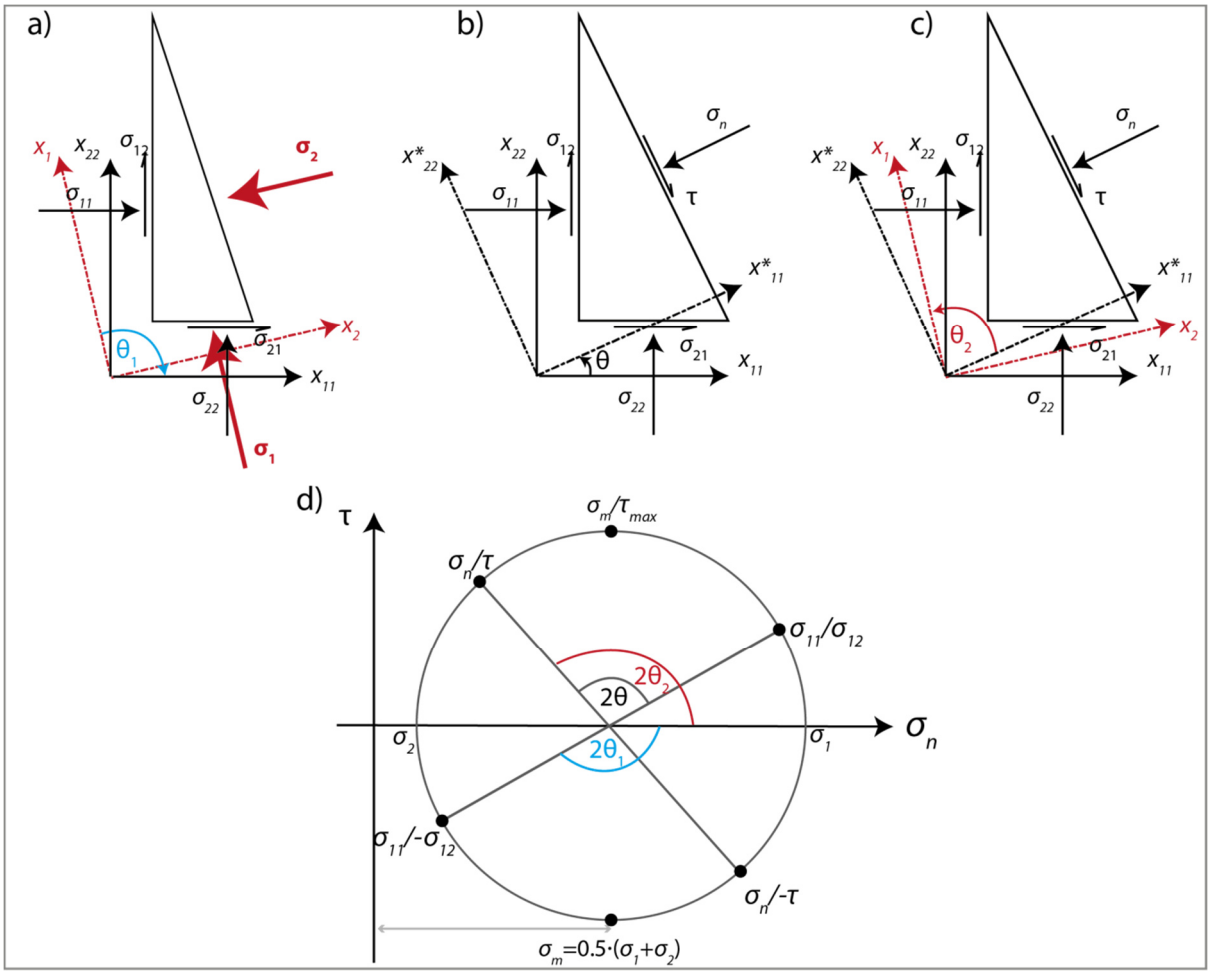

Fig. 2-5: Stress components and angular transformation relations in 2D for a given stress state. a) Normal stress on a principal plane. θ_1 defines the clockwise angle between the first principal stress and the normal of the plane. b) Normal and shear stress on an arbitrary section, defining the coordinate system *x**, that is rotated counter clockwise by an angle θ with respect to x_{11}. c) θ_2 defining the counter clockwise angle between the first principal axis and the normal to the arbitrary cutting plane. d) Schematic representation of shear and normal stresses from (a-c) in the Mohr domain, for the given stress state.

Setting shear stress in Equation 2.18 to zero, allows to solve for the orientation of the first principal stress axis with respect to the x_{11} direction (Eq. 2.53 Jaeger & Cook)

$$tan\theta_1 = \frac{2\tau_{xy}}{(\sigma_{xx} - \sigma_{yy}) + \sqrt{\left[4\sigma_{xy}^2 + (\sigma_{xx} - \sigma_{yy})\right]}}. \qquad 2.19$$

Shear and normal stress on an arbitrary plane can also be computed in terms of the principal stresses but the angle θ_2 defines here the counter clockwise angle between first principal axis and the normal of the cutting plane (Fig. 2-5 c):

$$\sigma_n = \frac{\sigma_1 + \sigma_2}{2} + \frac{\sigma_1 - \sigma_2}{2} cos2\theta_2 \qquad 2.20$$

$$\tau = -\frac{\sigma_2 - \sigma_1}{2} sin2\theta_2 \qquad 2.21$$

Equations 2.20 and 2.21 are commonly cited in literature to determine shear and normal stress on a fault. This is because in earth sciences one principal axis is often considered to be vertical and the problem reduces to a simple one in which the principal orientations have a fixed angle with respect to the given fault plane. As subsurface principal stress orientations can deviate locally from the assumption of a vertical principal axis (Fig. 9-44), the Cartesian formulation (2.17 and 2.18) was applied to compute shear and normal stress on a deterministic fault plane in this study.

2.6 Tectonic stress regime

Given the earth's shear free surface and the vertical gravitational load, the principal stress tensor within the upper crust is commonly assumed to have one sub-vertical principal component (e.g. Zang & Stephansson 2010). Among others based on this assumption, Anderson (1951) proposed three different brittle deformation patterns and kinematics with respect to the relative magnitudes of principal stresses (Fig. 2-6). The tectonic stress tensor denoted as $\sigma_V, \sigma_h, \sigma_H$ in Figure 2-6 arises from the mentioned assumption of fixed principal stress orientations and comprises two horizontal and a vertical stress component. In reality, the principal stress tensor often deviates from the tectonic stress tensor (e.g. Lund & Townend 2007) but the tectonic stress tensor is still commonly used for first order descriptions of tectonic processes (e.g. Twiss & Moores 2007).

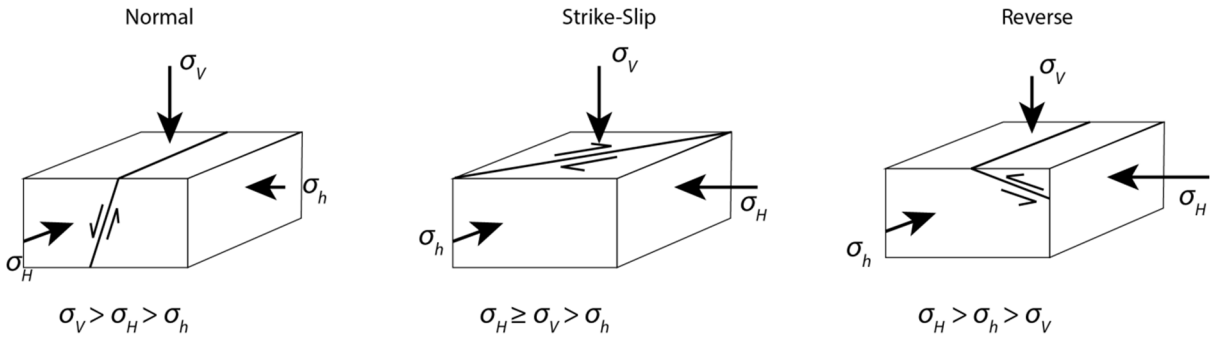

Fig. 2-6: Anderson's faulting regimes (after Zoback 2007) that propose the occurrence of conjugate faults at an angle of less than 45° with respect to the maximum principal stress. Created fractures and fault planes pass through the intermediate stress. Anderson's concept thereby represents a large scale representation of Mohr's concept for shear failure (section 2.8.1).

The Anderson' tectonic regime in a strict sense refers to the brittle creation of new faults and fractures, overcoming compressive and tensile rock strength. As rock strength is governed by inhomogenities on any scale (e.g. Adey & Pusch 1999) Anderson's approach has to be considered a conceptual one. The concept of the critically stressed crust (Townend & Zoback 2000) on the other

hand proposes that the intraplate strength of the crust is on a large scale governed by frictional strength of predefined zones of weakness.

2.7 Constitutive Laws

The constitutive laws correlate stresses to deformation. The coefficients of the constitutive laws have to be derived from material testing while the mathematical formulation has to obey thermodynamical principles (e.g. Fjaer 2008). Three basic models of material behaviour show unique features. In elastic material, loading causes recoverable elastic strain; plastic strain on the other hand is characterized by irreversible deformation. The stress-strain relationship in elastic and plastic material is independent of time whereas viscoelastic deformation depends on time and the corresponding loading rate (Jaeger et al. 2007).

The realistic behaviour of rocks is scale-dependent and widely governed by the presence of fractures and microcracks (Lawn & Marshall 1998, Singh et al. 2002) the cementation and compaction-grade and the confining pressure (Zoback 2007). The material response comprises thus different processes, such as grain rearrangement, propagation of fractures, elastic closure of fractures, creeping dislocation or slip occurring on different scales. These processes influence the overall stiffness of rock (e.g. Hoek & Brown 1997) and determine a linear or nonlinear stress-strain relationship.

In general, different materials expose a combination and sequence of material behaviour in response to an increasing applied load. Figure 2-7 shows the typical loading-strain curve of a rock specimen subjected to a uniaxial compression test.

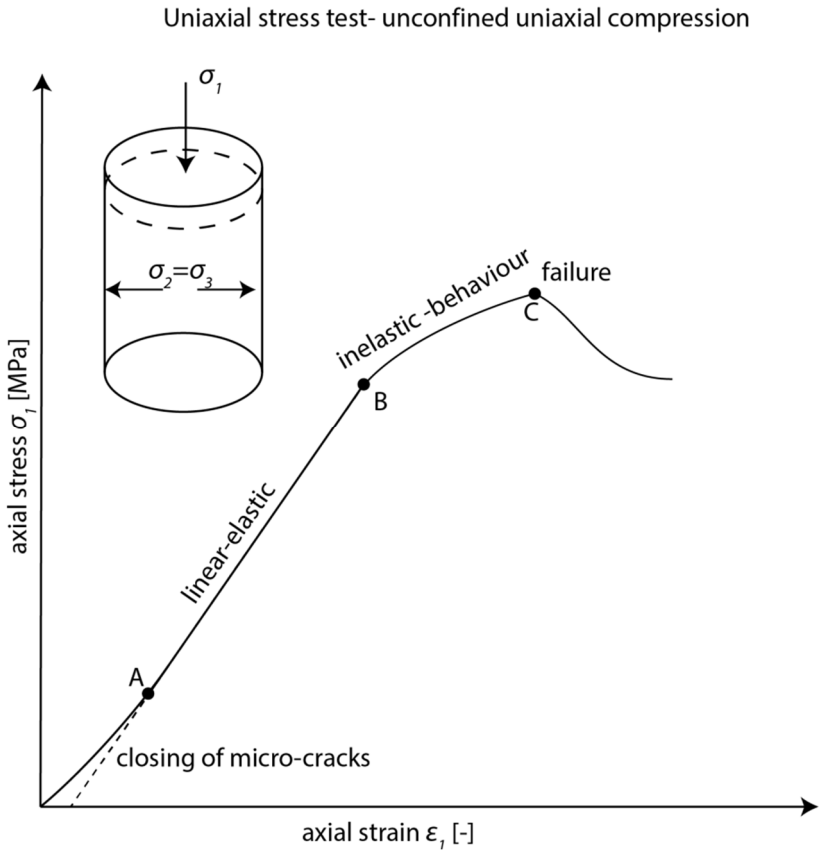

Fig. 2-7: Typical stress-strain curve of a uniaxial compression test. The initial closure of microcracks results first in a nonlinear stress-strain relation. The slope between the points A and B expresses linear elastic behaviour and allows for the derivation of Young's modulus. Point B indicates the yield strength of the sample that is the onset of non-recoverable deformation. In the given example the sample can still bear loading above point B, corresponding to strain hardening behaviour, before abrupt failure at point C. Failure is characterized by a drop in stress-bearing capacity.

2.7.1 Elasticity and stress-strain relationship

Linear elasticity as indicated by the section A-B in Figure 2-7 poses a single valued, i.e. linear function connecting stress and strain:

$$\sigma_{ij} = C_{ijkl}\varepsilon_{kl} \qquad 2.22$$

C_{ijkl}: Elasticity tensor [Pa]

The current strain depends only on the current stress, rendering the relationship independent of the time rate of change (e.g. Jaeger et al. 2007). However, nonlinear elasticity relationships introduce a dependence of strain also on the previous load increment but in opposition to other constitutive laws, the strain remains fully recoverable. Consideration of isotropic materials render the elasticity tensor

C_{ijkl} a symmetric one for which *Einstein* notation applies, the stress-strain law according to Hooke is then expressed by:

$$\sigma_{ij} = \lambda \varepsilon_{kk} \delta_{ij} + 2G\varepsilon_{ij} \qquad 2.23$$

λ: First Lamé's parmater [Pa] *G*: Second Lamé's parameter, shear modulus [Pa]

And the strain tensor can be written as:

$$\varepsilon_{ij} = \frac{1+\nu}{E}\sigma_{ij} - \frac{\nu}{E}\sigma_{kk}\delta_{ij} \qquad 2.24$$

Relation 2.24 can also be decomposed into volumetric stress and strain, described by the Bulk modulus *K* and a deviatoric response expressed in terms of the shear modulus *G*. Transformation equations between the different elastic moduli can be looked up in standard textbooks.

2.7.2 Elastoplasticity

This section deals with plastic deformation occurring for stress states that lie on or above the yield surface. Elastoplasticitiy comprises the differentiation of two strain components, the elastic and a plastic one (Eq. 2.60, Fjaer 2008):

$$d\varepsilon_{ij} = d\varepsilon_{ij}^{e} + d\varepsilon_{ij}^{p} \qquad 2.25$$

$d\varepsilon_{ij}^{p}$: Plastic strain rate

The relation between plastic strain increment and stress increment is described by the flow rule. Three basic types of plastic strain-stress relations are differentiable (Fig. 2-8):

1. Ideal plasticity

At yielding, the material cannot bare additional load and deforms at constant stress, during re- und unloading cycles the yield stress is identical.

2. Hardening

The material withstands further loading beyond the yield point. After unloading, the yield strength increases to the previous maximum load.

3. Softening

At yielding the material cannot carry any further load, instead the load-bearing capacity decreases. After unloading, reduced yield strength persists.

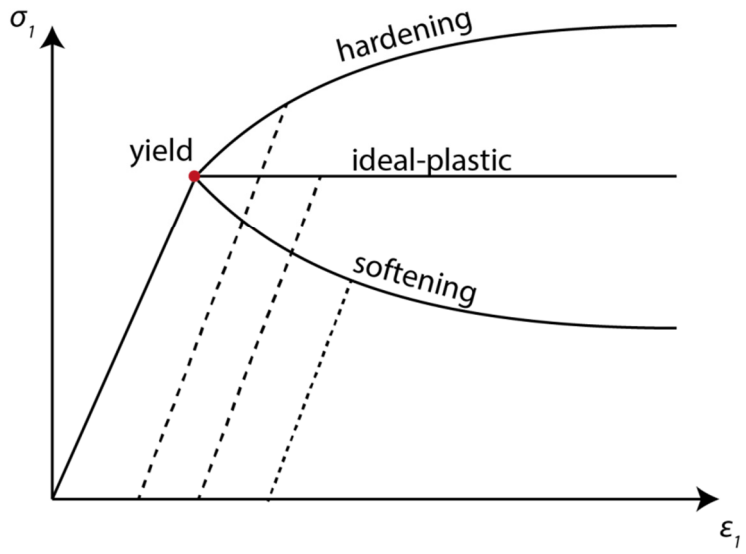

Fig. 2-8: Schematic illustration of the three basic plasticity models (after Zilch et al. 2013) at stresses above yield strength. During reloading, ideal plastic behaviour is characterized by a constant yield strength while for hardening and softening material plastic deformation occurs at higher and lower stress respectively.

Elastoplastic behaviour can be observed in soils and poorly cemented sediments due to grain rearrangement (e.g. Zoback 2007) while at large confining pressures all rock types undergo irreversible plastic deformation (Jaeger et al. 2007).

The loading of a material point is unambiguously determined by the three principle stresses. Most yield criteria consider the influence of the all three principal stresses in their formulation of strength, e.g. *von Mises*, *Drucker-Prager*, *Cam clay*, *Lade*, but the Mohr Coulomb-criterion takes only the maximum and minimum principal stress into account (Haimson & Rudnicki 2010). Plastic deformation can proceed as associated flow or non-associated flow with respect to the yield surface. In terms of the Mohr-Coulomb criterion, non-associated flow is indicated by a difference in friction and dilation angle, resulting in a volume increase at shear failure, referred to as dilation (Katzenbach et al. 2012).

2.7.3 Viscoelastic Creep

Some rocks show rate-dependent stress-strain behaviour under certain Pressure-Temperature conditions or during a constant long-term loading (Jaeger et al. 2007). For example the upper earth's mantle, given high temperature and high pressure conditions is postulated to show viscoelastic behaviour according to the Maxwell model (Jaeger et al. 2007). Under conditions of the brittle crust, rock salt, in particular halite is most prominently encountered to show viscous rheology. The viscous behaviour of rock salt affects the opening of boreholes (Weijermars et al. 2014) and cavities (Munson

1997) and the subsurface topograhy as viscous flow is activated when subjected to differential loading (Weijermars et al. 1993).

In a conceptual approach, viscous strain is represented by dashpots (Newton Element) (Eq. 9.92 Jaeger et al. 2007):

$$\sigma = \eta\left(\frac{d\varepsilon}{dt}\right) = \eta\dot{\varepsilon}_{dash} \qquad 2.26$$

η: Dynamic Viscosity in [Pa s]

Viscoelastic material behaviour can be described by a selection of rheological models idealized by different combinations of spring (elastic behaviour) and dashpot elements (e.g. Maxwell, Kelvin, Kelvin-Voigt, St-Venant).

In practice, the damping behaviour of viscoelastic material can be derived by a creep test series, i.e. the material experiences a slow constant force and creep parameters are determined (Haupt 1991). For this load case the material response is not limited by an ultimate deformation state. In relaxation tests on the other hand material is loaded instantaneously and allowed to relax while the applied load is held constant or released (Lee & Ehgartner 2001), whereby the time for reaching a determined stress and deformation state is governed the viscosity of the material.

Creep behaviour following a stress change commonly occurs in three stages, transient, steady state and accelerating, characterized by different deformation rates. It is important to note that even steady state creep may lead to failure at stresses below yield strength (Fjaer 2008) but for strain rates of salt in the crust, brittle failure is not stipulated (van Keken et al. 1993, Weijermars et al. 2014,).

Viscoelastic behaviour of salt is governed by different processes at micro-scale, e.g. dislocation creep (power-law creep), pressure diffusion creep (Newtonian Creep), and processes of dynamic recrystallization (Li & Urai 2016, Urai & Spiers 2007) that can be accounted for by exponents and prefactors in the constitutive creep law (Weijermars et al. 2014):

$$\frac{d\varepsilon}{dt} = A_i q_d^n d^m \exp\left(\frac{-Q}{RT}\right) \qquad 2.27$$

A_i: Prefactor from material tests n: Stress exponent m: Exponent of grain size Q: Activation Enthalpy [J]
q_d: Differential stress [Pa] R: Universal Gas constant [kg m^2/(s^2 mol K)] T: Temperature[K]

In rock salt engineering, dislocation creep (n>1) is postulated to constitute the main deformation mechanism (Urai & Spiers 2007, van Keken et al. 1993) whereby diffusion creep (n=1) is assigned a more dominant role in 'wet' salt at low, typical crustal strain-rates. Here, a characteristic grain size of the salt layer is not available an m is set to zero, neglecting diffusion creep.

Instead, a constant Newton viscosity of 1×10^{17} Pa s for halite, as proposed by van Keken et al. (1993) is used in this study (section 8). By choosing the pre-factors in the ABAQUS creep law accordingly, the creep strain rate can be related directly to the intended linear viscosity. Treating the viscous material as a Newton fluid, it is obvious, that the deformation is shear-rate dependent, i.e. shear stresses cannot be carried by fluids and are relaxed as a function of the viscosity.

2.8 Rock strength and failure

Failure is represented by an abrupt change in deformation mode, which in the earth's crust is often associated to brittle behaviour. The brittle domain in geo-materials is characterized by shear, tensile or compaction failure (Zoback 2007) and the term failure refers to a severe drop in load bearing capacity. Considering failure as the material's deficiency to carry any further load (Fig. 2-7 negative slope), failure can be considered a plastic strain-softening behaviour at yield. The strength of a rock is governed by the maximum load that can be carried prior to brittle failure. For instance the maximum load determining the uniaxial compressive strength is simply the maximum principal stress. In an engineering context the term strength may be used in a more general sense and coincide with the yield stress of the material, if the associated plastic deformation questions the integrity of the engineered structure. Mentioned yield strength hypotheses (section 2.7.2) express limiting load cases in terms of the principal stresses. In structural geology, the Mohr-Coulomb criterion is popularly consulted to determine shear failure of a pre-existing fault plane (e.g. Morris et al. 1996). For problems of plastic reservoir compaction, initiation of new fractures and borehole stability, different plasticity models than Mohr-Coulomb are commonly consulted (Zoback 2007). In supplementation to the yield hypotheses largely arising from soil mechanics, the Hoek-Brown (Hoek & Brown 1997) criterion poses a strength criterion for solid rock masses, considering a combination of maximum and minimum principal stresses, uniaxial compressive strength, strength of the undisturbed rock pieces and macroscopic properties of the rock mass.

2.8.1 Shear failure

Brittle shear failure in rock under compression occurs when shear stress along a plane becomes sufficiently high. In unconfined uniaxial compression this may occur as a function of the applied confining pressure. In triaxial tests, applied differential stress governs shear failure whereby the resistance i.e. the rock's shear strength increases with increasing lateral pressure (Fjaer 2008). While the simplest approach, the Tresca criterion considers shear stress only, Mohr's hypothesis states that failure is in fact a function of the normal stress on the shear plane (Eq. 4.25 Jaeger et al. 2007)

$$|\tau_{max}| = f(\sigma_n)\,. \qquad 2.28$$

Plotted in the Mohr diagram, the linear increase of shear and frictional strength with normal stress can be evaluated in terms of the Mohr-Coulomb criterion

$$\tau_{max} = \mu\sigma_n + C\,. \qquad 2.29$$

μ is here the coefficient of internal friction and *C* is the cohesion of the rock or the soil. The failure line thus separates the Mohr domain into a critical and non-critical area (Fig. 2-9) whereby stress states above the failure line cannot exist (Jaeger et al. 2007). Fitting data from rock-mechanical testing Mohr's failure envelope is often nonlinear and flattening towards higher normal stresses (Zoback 2007), adapting to a number of critical stress states.

2.8.2 Fault reactivation

In reservoir geomechanics the Mohr-Coulomb criterion is commonly used to assess the stress state on pre-existing discontinuities being a function of shear (τ) and normal stress (σ_n). In opposition to the previous section which dealt with failure of macroscopic intact rock, i.e. cohesive granular material, the cohesion of faults is commonly assumed negligible (Fig. 2-9) (Marone 1995). The reactivation and onset of sliding on a pre-existing fault plane is governed by its frictional strength expressed by the static coefficient of friction μ_s (Zoback 2007). In analogy to the coefficient of internal friction μ, the coefficient of friction determines the slope of the linear Mohr-Coulomb criterion alternatively expressed by the friction angle ψ(Fig. 2-9).

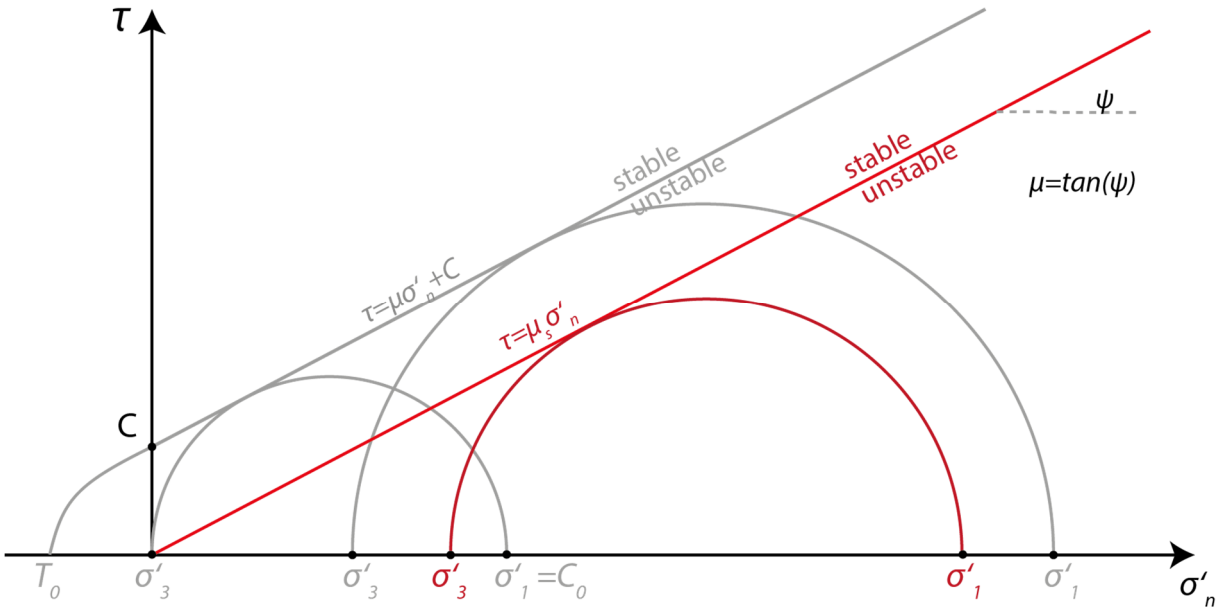

Fig. 2-9: Failure envelope of the Mohr-Coulomb criterion separating a stable and unstable stress state. The red failure line and Mohr-circles indicate the reactivation of a cohesionless fault whose frictional strength is reflected by the slope of the failure line. In opposition to that, the light grey envelope considers cohesion, applying for macroscopically intact rock. The maximum principal stress σ_1 corresponds to the uniaxial compressive strength C_0 for the omission of a lateral confinement. Under tensional normal stresses the uniaxial tensional strength T_0 cuts off the failure line. This study considers normal faulting stress regimes for which $\sigma'_1=\sigma'_v$ and $\sigma'_3=\sigma'_h$ applies (Fig. modified after Fjaer 2008, Labuz & Zang 2012).

The angle ψ (Fig. 2-9) determines the favourable orientation of fault planes (Eq.2.3)) with respect to the first principal stress. For macroscopically intact rock, ψ determines the preferred orientation of newly created fractures (e.g. Fjaer 2008). The correlation between friction and optimum fault or fracture orientation with respect to the maximum principal stress is given by (Eq. 4.42 Zoback 2007):

$$\psi = \frac{\pi}{2} - artan(\mu) \qquad 2.30$$

Seismicity is associated to an instantaneous displacement, i.e. slip of a significant area and has long been recognized as a frictional phenomenon of pre-existing fault planes (Brace & Byerlee 1966). Thereby brittle failure assumes only a secondary role for example in the extension of faults and fault wear (e.g. Angelier 1990, Scholz 1998). The frictional resistance to initiate sliding of one rock against another was experimentally investigated by Byerlee (1978) finding that the static coefficient of friction sμ is widely independent of rock type at elevated normal stress, but depends strongly on the magnitude of normal stress. Using Byerlee's (1978) data collection, Zoback (2007) proposed a typical range of friction coefficients for normal stresses encountered at reservoir depth:$0.6<\mu_s<1$. However, high clay contents of fault zones may lower the frictional resistance significantly (Kohli & Zoback 2013).

2.8.3 Tensile failure, Griffith criterion and shear enhanced compaction

As the subsurface stress state at depth is overall compressive, natural tensile failure is rare but may occur in the framework of dynamic stress changes at constant pore pressure or sudden pore pressure changes (e.g. Engelder & Lacazette 1990, Tingay et al. 2008). In order to increase reservoir permeability, the method of hydraulic fracturing takes advantage of the comparatively low tensile strength of rocks (e.g. Haimson & Cornet 2003) (Fig. 2-9). Once pore pressure exceeds the minimum principal stress, tensile fractures normal to σ_3 may develop.

In fact, the strength of materials is directly or indirectly governed by imperfections and stress concentrations around them. The propagation of pre-existing cracks is described by Griffith's concept and bases on the thermodynamical principle of minimizing free energy. The growth of cracks is then determined by a favourable or less favourable configuration between surface energy, increasing with crack length, and free energy (e.g Scholz 2002). Macro-scale failure and faulting is potentially governed by propagation of micro-scale cracks. The modified Griffith criterion considers both, the compressive and tensile strength of rocks, accounting for failure by propagation of cracks at lower confining pressures and Mohr-Coulomb frictional behaviour at higher confining pressures (e.g. Jaeger & Cook, Fjaer 2008).

The depletion of pore pressure during gas production leads to an increase in compressive vertical effective stress and a decrease in reservoir thickness, i.e. reservoir compaction. This vertical deformation may proceed in a nonlinear and irreversible manner within weak sediments (Boutéca et al. 2000, Goulty 2003, Teufel et al. 1991) at sufficient stress. High-porosity sediments compact in a nonlinear manner even under hydrostatic loads, this process is called pore collapse. It is associated to the reorientation of grains or shear slip on intergrain contacts (Hettema et al. 1998, Boutéca et al. 2000). The volume reduction and irreversible deformation below factual shear strength (Zoback 2007) can thereby be described by a capped yield surface encompassing large hydrostatic stress magnitudes in the *p*-*q* space (section 2.3). Along the cap, strain hardening occurs as the process of porosity loss results eventually in an increase in load bearing capacity. Common yield criteria that encompass a capped yield surface are the modified Drucker Prager and the cam-clay model (e.g. Fjaer 2008).

2.9 Friction, rupture and unstable sliding

According to Scholz (1998), earthquake phenomena largely depend on the temporal evolution of fault friction rather than the frictional strength μ_s of the fault. Stick-slip behaviour as observed in spring-slider experiments (Fig. 2-10 a) have long been acknowledged to expose an analogous behaviour the

cycle of earthquakes and interseismic calm periods (Marone 1998, Scholz 1998). Thereby the actual seismic event corresponds to instantaneous slip acceleration, i.e. a sliding instability over a defined fault patch for which time and length scale are crucial parameters. These parameters lack however a causal description and complicate the formulation of predictive mathematical tools (Ampuero & Rubin 2008, Rubin & Ampuero 2005).

The evolution of friction in stick-slip experiments, being a function of slip rate, slip or stress history, exposes characteristic patterns as displayed in Fig. 2-10 b) (Ruina 1983, Scholz 1998, Segall et al. 2010). Considering shear stress, the frictional instability is characterized by a sudden increase of the frictional resistance during steady state sliding. On a record of slip velocity, this is associated to a sudden increase in sliding velocity (e.g. Beeler et al. 1994) and a following decay of frictional resistance to sliding over a characteristic rupture length (Fig. 2-10 b). Finally, the frictional surfaces 'heal' and return to the steady state friction coefficient (Scholz 1998). The complex interplay of friction, slip velocity, slip distance and slip history can be phenomenologically described by rate-and-state friction laws as constituted for example by Ruina (1983):

$$\tau = \sigma'_n \left(\mu_s + a \ln\left(\frac{v}{v_0}\right) + b \ln\left(\frac{v_0 \theta_s}{d_L}\right)\right) \qquad 2.31$$

μ_s: Coefficient of friction at reference slip velocity v_0 v: Instantaneous slip velocity [m/s]

d_L: Characteristic rupture length [m] θ_s: State variable of rate and state friction

Herein the commonly known static and dynamic friction coefficients μ_s, μ_d are replaced by a continuous function for frictional resistance. Figure 2-10 b) illustrates the meaning of the rate-and -state coefficients *a, b* and d_L. Coefficients *a,b* can be determined experimentally (McClure & Horne 2011). The change in friction with slip rate ($\mu = a\left(\frac{v}{v_0}\right)$) (Eq. 2.31) is called the *direct effect* of rate- and -state friction. Opposing to this, an evolutionary effect, also referred to as *state effect* ($\mu = b \ln\left(\frac{v_0 \theta_s}{d_L}\right)$) (Eq. 2.31) follows the change in sliding velocity. A prerequisite for unstable sliding is the domination of the state effect over the direct effect, whereby the two effects are scaled by parameters a and b respectively (Beeler et al. 1994). The state variable θ_s on the other hand is very complex and evolves with d_L/v (Segall et al. 2010). Rate and state friction allows for the discrimination between seismic or aseismic slip (McClure & Horne 2011). The former is characterized by a stable sliding regime and the latter by instantaneous unstable sliding, accompanied by a stress drop. From a causal point of view, aseismic slip within the rate-and -state model can prevail for instance for pore volume dilation within fluid infiltrated faults (Segall & Rice 1995, Segall et al. 2010).

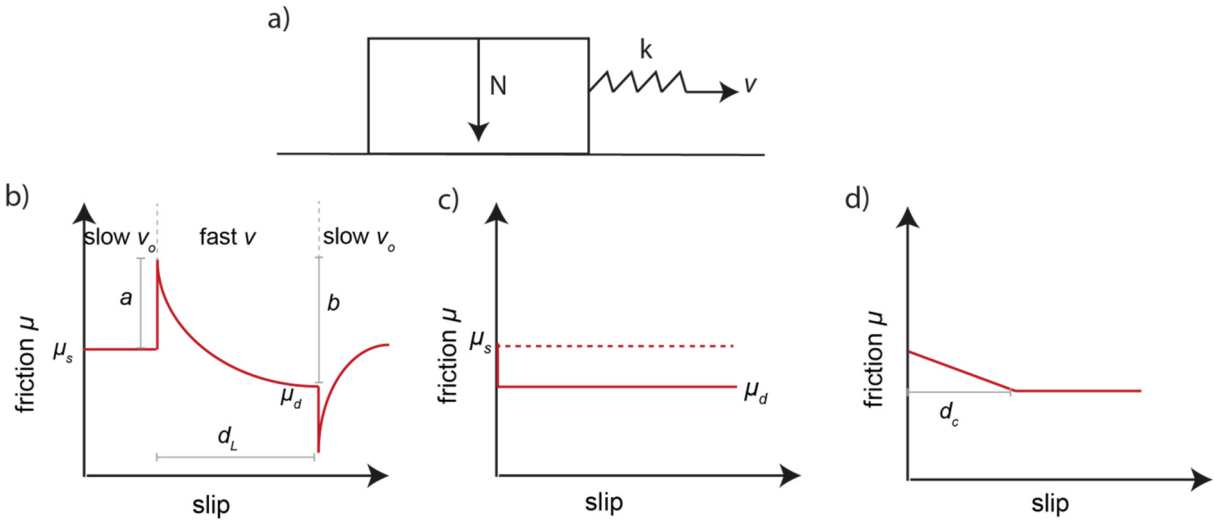

Fig. 2-10: a) Schematic sketch of a spring-slider used to investigate frictional phenomena. The spring slider exposes stick slip behaviour for a constant pull corresponding to a velocity *v*. b) Idealized experimental observation of the frictional response to an instantaneous increase and decrease in slip velocity. The pattern is mathematically described by the rate- and -state friction model (Eq. 2.31). c) Constant static friction, as used by default in ABAQUS (dashed line), simple physical models assume an instantaneous drop to dynamic friction at the onset of sliding (solid line). d) Linear decrease in frictional resistance to its dynamic value over a critical distance d_c (Fig. inspired by Daub & Carlson 2010, Scholz 1998).

Figure 2-10 c) shows the friction model invoked by default in contact modelling (section 7.2.3) and the more realistic instantaneous drop to dynamic friction at failure. More sophisticated slip- or cohesion-weakening approaches (Fig. 2-10 d) were used in recent models on production-induced seismicity (Buijze et al. 2017, Ter Heege et al. 2018, van Wees et al. 2017, Wassing et al.2016, 2017, Zbinden et al. 2017) and have previously been applied for the modelling of dynamic rupture (e.g. Bizzarri et al. 2001, Cappa & Rutqvist 2012). The fundamental property of the majority of slip-weakening models is the degradation of the frictional resistance to sliding to its dynamic value over a characteristic slip distance d_c. This approach implies that the fault ruptures seismically anytime the frictional fault strength is overcome. Seismic and aseismic slip are consequently not discriminated (e.g. McClure & Horne 2011, Wassing et al. 2017). Nevertheless, the slip produced from slip-weakening model faults captures important characteristics of earthquakes (Wassing et al. 2017), as for instance the propagation of slip from unstable to stable or conditionally stable regions at sufficiently large dynamic stresses (Scholz 1998).

With respect to rate- and -state friction, Ampuero & Rubin (2008) argue that no (rate-and state) friction law is hitherto able to reproduce all available experimental data. Correspondingly the poor constraining of the constitutive equations poses a severe obstacle to the modelling of real earthquakes.

3 Poroelasticity

Deformation of a fluid filled porous medium is sometimes successfully condensed to a simple concept of load decomposition between solid phase and pore pressure referred to as 'effective stress'. Adding a term for fluid content or pore pressure to the already introduced elastic stress-strain relationship (Eq. 2.23) leads to the 'Biot-Willis' effective stress that has proven to provide an accurate stress-strain relationship for fluid saturated porous rocks (Nur & Byerlee 1971). However, the numerical tool applied in this study, ABAQUS, used Terzaghi's definition of effective stress in earlier releases. The extensive description of poroelastic compressibilities in this section arises from the fact that the Biot-coefficient cannot be specified directly in ABAQUS. That means that the physical properties of the coefficient had to be translated into available material properties of the ABAQUS soils procedure and this required first an understanding of the respective poroelastic moduli and compressibilities. In sum, this chapter is meant to provide the basis to understand the application of the ABAQUS soil mechanical procedure in a rock mechanical problem and to accurately capture the stress-strain behaviour of the investigated reservoir sandstone that exhibits a typical Biot-coefficient $\alpha = 0.7$ (Zimmerman 1991).

3.1 General Concepts and phenomena of poroelasticity

Fluid saturated porous material is encountered in the majority of earth science and geological engineering problems. Poroelastic behaviour applies to both 1) unconsolidated granular material constituting building ground or aquifers and 2) cemented granular material composing solids with interconnected pores, as for example in hydrocarbon reservoirs and deep aquifers (Cheng 2016).

Poroelasticity comprises two fundamental physical phenomena:

1) Solid-to-fluid coupling - a change in total applied stress results in a change in fluid pressure, if the fluid is prevented from escaping the pore network, or a change in fluid mass, if drainage is possible.
2) Fluid-to-solid coupling - a change in pore pressure or fluid mass content results in volume change and dilation or compression of the bulk porous material (Detournay & Cheng 1993, Wang 2000).

Full coupling of stress, strain and pore pressure can be explained by starting with a pore pressure gradient induced for example by injecting fluid into an underground reservoir. The gradient leads to time dependent fluid flow and the associated transient pore pressure field and seepage forces induce stresses and strains that couple back to the pore pressure field (Wang 2000). In general the magnitude of coupling depends on several compressibilities (Wang 2000) introduced in section 3.3.

Terzaghi (1925) experimentally investigated the consolidation of fluid-saturated soils that are loaded under undrained conditions, i.e. fluid is prevented from escaping (Fig. 3-11 b) and excess pore pressure builds up. Subsequently, the excess pore pressure is allowed to dissipate and the load is transferred to the solid skeleton resulting in settlement of the soil sample associated to a bulk volume and pore volume reduction. For loose sediments comprising relatively incompressible single grains and fluid, the total stress can be decomposed into pore pressure and a solid stress, the Terzaghi (1936) effective stress

$$\sigma_{ij} = \sigma'_{ij} - \delta_{ij} P_f \, . \qquad 3.1$$

3.2 Volumetric and deviatoric strain-stress relationship

The general theory of three-dimensional consolidation was presented by Biot (1941), the theory assumes a coherent solid, soil or rock skeleton and a mobile fluid in an entirely interconnected pore space. In this two- phase medium, two strain quantities (Detournay & Cheng 1993) are introduced accounting for first, bulk strain, expressed by the infinitesimal strain tensor ε_{ij} (section 2.4, Eq. 2.15) and second, the increment in fluid content ξ (Eq. 3.25, Cheng 2016):

$$\xi = \frac{\Delta m_f}{\rho_f} = -\frac{\Delta V'_f}{V} \qquad 3.2$$

Δm_f: Change in fluid mass [kg] per reference volume [m^3] ρ_f: Fluid density [kg/m^3]

$\Delta V'_f$: expelled fluid volume [m^3] V_f: Control volume [m^3]

For fluid withdrawal, the increment in fluid content ξ assumes negative values. In the theory of poroelasticity, the total stress tensor and pore pressure P_f are the force quantities (Detournay & Cheng 1993). Pore pressure is a scalar variable and acts isotropically in the control volume, provided that seepage forces (e.g. Rozhko 2010) can be neglected. The constitutive strain-stress equations for isotropic poroelastic material can be formulated by several sets of permutations of independent and dependent poroelastic variables (Wang 2000). Equation 3.3 and 3.4 denote the mutual relation of the four basic variables $\sigma, \varepsilon, \xi, P_f$ in volumetric deformation (Eqs. 12.17, 12.18 Cornet 2014):

$$\varepsilon = \frac{1}{3}\frac{\sigma_{kk}}{K_d} + \frac{P_f}{H} \qquad 3.3$$

$$\xi = \frac{1}{3}\frac{\sigma_{kk}}{H} + \frac{P_f}{R} \qquad 3.4$$

K_d: Drained bulk modulus [Pa] H: Poroelastic expansion coefficient [Pa] R: Coefficient of unconstrained specific storage [Pa]

$\sigma_{kk}/3$ is the applied hydrostatic load on the control volume and the coefficients K_d, H, R constitute poroelastic constants treating the fluid filled material as a whole. The response of the isotropic material to deviatoric stress is independent of pore pressure and determined by the dry, elastic shear modulus (Eq. 7 Detournay & Cheng 1993)

$$\varepsilon_{ij} = \frac{1}{2G}\sigma_{ij} \,. \qquad 3.5$$

The complete mechanical response of a poroelastic material to loading is thus composed of a poroelastic volumetric component and a 'dry' deviatoric component. The strain tensor can be stated in the 'pure compliance' formulation (Eq. 2.36, Wang 2000) as follows:

$$\varepsilon_{ij} = \frac{1}{2G}\sigma_{ij} - \frac{1}{2G}\frac{\nu}{1+\nu}\sigma_{kk}\delta_{ij} + \frac{1}{3H}P_f\delta_{ij} \qquad 3.6$$

Considering principal coordinates, shear strains ε_{ij} $(i \neq j)$ vanish and the strain tensor simplifies to (Eqs. 2.11-2.13, Wang 2000):

$$\varepsilon_1 = \frac{\sigma_1}{E} - \frac{\nu}{E}\sigma_2 - \frac{\nu}{E}\sigma_3 + \frac{P_f}{3H} \qquad 3.7$$

$$\varepsilon_2 = -\frac{\nu}{E}\sigma_1 + \frac{\sigma_2}{E} - \frac{\nu}{E}\sigma_3 + \frac{P_f}{3H} \qquad 3.8$$

$$\varepsilon_3 = -\frac{\nu}{E}\sigma_1 - \frac{\nu}{E}\sigma_2 + \frac{\sigma_3}{E} + \frac{P_f}{3H} \qquad 3.9$$

3.3 Moduli and coefficients of the volumetric response

The poroelastic moduli and their relation to the four basic variables $(\sigma_{ij}, \varepsilon_{ij}, P_f, \xi)$ are most easily explained by referring to schematic rock mechanical testing.

Figure 3-11 a) illustrates a fluid infiltrated rock volume that is jacketed by an impermeable membrane and subjected to an incremental hydraulic confining pressure P_c. Pore pressure in the specimen is balanced with atmospheric pressure by a tube that allows fluid to escape under loading. For a given load increment ΔP_c fluid continues to flow out of the sample until the pore pressure has equilibrated with the atmospheric pressure ($\Delta P_f = 0$) (e.g. Cheng 2016). This constant pore pressure boundary condition is called the *drained condition* and the ratio of volumetric deformation to applied confining pressure at constant pore pressure is defined by the drained bulk modulus K_d (Eq. 1.8 Wang 2000):

$$\frac{1}{K_d} = \frac{\Delta\varepsilon}{\Delta\sigma_{kk}} \quad \Delta P_f = 0 \qquad 3.10$$

The fully drained condition in combination with slow incremental loading allows the fluid to escape the decreasing pore volume. The fluid does hence not participate in the load bearing process and the observed stiffness corresponds to the stiffness of the porous solid frame (e.g. Fjaer 2008, Nur & Byerlee 1971) that is also referred to as rock skeleton (e.g. Cheng 2016, Wang 2000).

In a second setup, the fluid is prevented from escaping the specimen and the pore pressure change for each load increment is registered within the sample, this is the undrained condition. The ratio of volumetric deformation to applied confining pressure at constant fluid content defines the undrained bulk modulus K_u (Eq. 1.8 Wang 2000):

$$\frac{1}{K_u} = \frac{\Delta\varepsilon}{\Delta\sigma_{kk}} \quad \Delta\xi = 0 \qquad 3.11$$

The undrained material response is a composite response of the solid frame, the single grain constituents and the entrapped fluid. For relatively incompressible fluids the undrained stiffness is larger than the drained stiffness, affecting for example the determination of elastic moduli by wave propagation which reflects the stiffness of subsurface material under undrained conditions (e.g. Fjaer 2008).

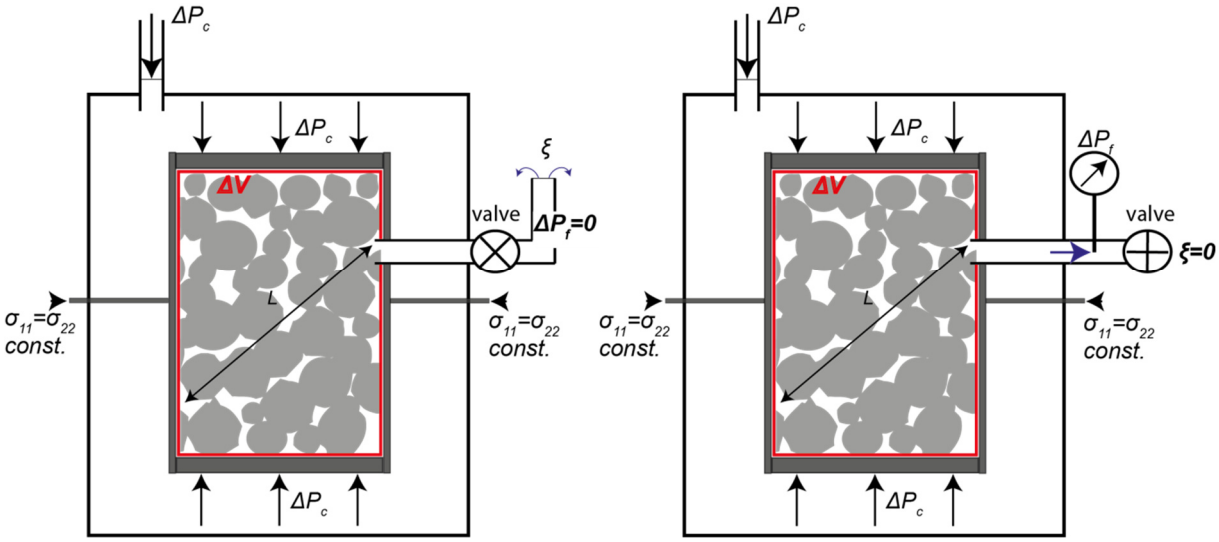

Fig. 3-11: a) Applied confining pressure ΔP_c on a drained specimen whose pore pressure is in balance with the atmospheric pressure. Given the constant pore pressure condition, fluid is allowed to escape under loading. The arrow *L* determines the characteristic length of the quasi-static modelling approach. b) Illustration of the undrained condition, that is, fluid is not allowed to escape and all components, the fluid compressibility, the single grain compressibility and the skeleton's compressibility participate in the load bearing process. The reduction in pore space thereby leads to an increase in pore pressure (Fig. inspired by Detournay & Cheng 1993, Cheng 2016).

Further poroelastic moduli, the poroelastic expansion coefficient *H* and the unconstrained specific storage coefficient *R* are defined as ratios of two basic variables (section 3.2) while keeping a third one constant, for more details consult (pp. 18-19, Wang 2000).

The Biot-coefficient characterizes the drained response of fluid saturated porous material, it is the ratio of increment of fluid content to change in bulk volume at constant pore pressure (Eqs. 1.24, 2.26, Wang 2000):

$$\alpha = \frac{K}{H} = \frac{\Delta\xi}{\Delta\varepsilon} \quad \Delta P_f = 0 \qquad 3.12$$

In basic terms, the Biot-coefficient is the expelled fluid volume relative to the total volume change resulting from an applied increment of confining pressure at constant pore pressure (Detournay & Cheng 1993):

$$\alpha = \frac{\Delta V'_f}{\Delta V} \qquad 3.13$$

For the undrained response of soil and rock, Skempton's coefficient *B* describes the change in pore pressure relative to applied stress at constant fluid content.

The value of the coefficients *B* and *α* range between 0 and 1. For the Skempton coefficient *B,* the pore pressure change cannot be larger than the applied stress and the Biot coefficient α cannot account for a change in bulk volume that is larger than the change in fluid volume (Cheng 2016).

Petrophysical considerations put similar limits on the two parameters. The Biot coefficient scales particularly with in-situ stress and porosity (e.g. Ingraham et al. 2017, Zoback 2007), and low porosity rocks tend to have smaller Biot-coefficients (Zoback 2007).

The last Modulus introduced here is the specific storage coefficient, also called the Biot-modulus *M*, that has the unit Pascal. It's reciprocal determines the increment in fluid content with respect to a change in pore pressure at constant strain (Eq. 2.27 Wang 2000):

$$\frac{1}{M} = \frac{\xi}{\Delta P_f} \quad \Delta\varepsilon = 0 \qquad 3.14$$

It must be noted that *1/M* is not identical to the fluid compressibility as the pore volume can change also under a constant strain condition (Cheng 2016).

3.3.1 Load cases and time dependence

The perfectly drained ($\Delta P_f = 0$) and undrained conditions ($\xi = 0$) are limiting cases of poroelastic behaviour (Detournay & Cheng 1993). Given the viscosity and compressibility of the fluid and the permeability of the medium, a specific time is required for a fluid 'particle' to move a finite distance *L* (Fig. 3-11) to equilibrate the pore pressure gradient between two pores. When loading is applied rapidly, fluid is trapped within the pore space and the bulk response is undrained, independently of the superordinate drainage condition. However, with ongoing time, fluid will be expelled, expanding the remaining fluid and relieving pore pressure. The volume under consideration will approach the drained condition, i.e. equilibrium between pore pressure and the atmospheric pressure. Consequently, the poroelastic material has an apparent time-dependent stiffness, at small times it is stiffer (undrained condition) and softens during large times. This behaviour scales with relative time instead of physical time. The relative time is defined by the completion of the given physical process and depends on the size and geometry of the problem (Cheng 2016).

In practice the characteristic time t_c can be defined as the time that the pressure relief front travels throughout the complete sample or control volume to render a significantly drained condition. Then 'Small times' are considered $t \ll t_c$, and 'large times' are considered to correspond to $t \gg t_c$ (Cheng 2016). Given the restriction that pore pressure needs to be equilibrated over the characteristic length *L*, the analysis of coupled deformation and fluid flow according to Biot (1942, 1957) is quasi-static (Detournay & Cheng 1993) but can be extended to the dynamic range (Biot 1962).

3.3.2 Micromechanics and unjacketed test

This section explains the individual contribution of the solid constituents to the stress-strain response of the two-phase bulk material. Up to this stage, the loading of the poroelastic material comprised two components, the confining pressure P_c and the pore pressure P_f. The difference between the confining and the pore pressure (Eq. 3.1, Wang 2000) corresponds to Terzaghi's effective stress

$$P_d = P_c - P_f \,. \qquad 3.15$$

With respect to the continuum mechanics sign convention it must be noted here that a confining pressure of positive sign causes compression of the medium and results in negative compressive stresses within the medium.

The total change of volume ΔV and pore volume change ΔV_p can be expressed as (Eqs. 3.2, 3.3 Wang 2000):

$$\frac{\Delta V}{V} = -\frac{1}{K_d} P_d - \frac{1}{K_g} P_f \qquad 3.16$$

$$\frac{\Delta V_p}{V_P} = -\frac{1}{K_p} P_d - \frac{1}{K_\emptyset} P_f \qquad 3.17$$

$1/K_d$: Drained bulk compressibility $1/K_p$: drained pore compressibility $1/K_\emptyset$: unjacketed Pore compressibility

V_p: Pore Volume [m^3]

In the unjacketed test (Fig. 3-12) the specimen is immersed in confining fluid that can permeate the pore space of the specimen. In consequence, an increment in confining pressure produces an equal increment in fluid pressure within the pores ($P_c = P$ and $P_d = 0$).

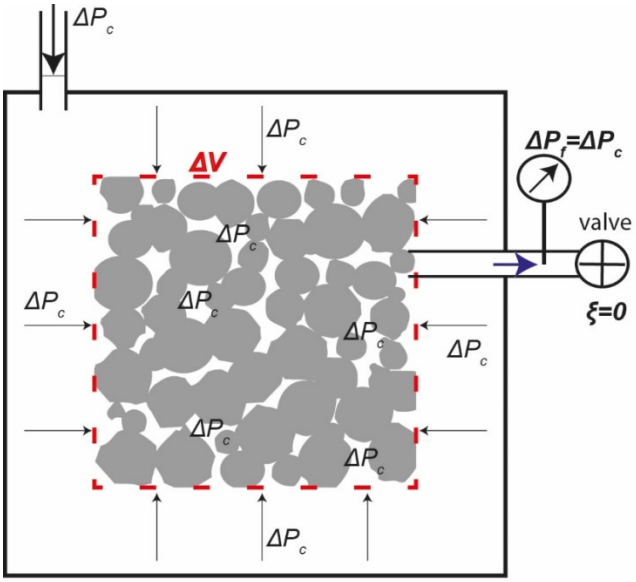

Fig. 3-12: In the unjacketed test pore pressure P_f and confining pressure P_c are identical and the bulk strain corresponds to the effect of the fluid pressure on the single constituents of the specimen that make up the pore space. The stress-strain relation reflects hence the stiffness of the single grain constituents (K_g) (Fig. inspired by Detournay & Cheng 1993, Cheng 2016).

The volumetric change of the specimen is now exclusively governed by the deformation of the single grain constituents or 'internal structure' and the bulk strain correlates with its compressibility. Rewriting 3.16 leads to (Eq. 3.7 Wang 2000):

$$\frac{1}{K_g} = -\frac{1}{V}\frac{\Delta V}{\Delta P_f} \quad \Delta P_d = 0 \qquad 3.18$$

For the ideal case of a solid phase composed of a single constituent, the pores preserve their geometry in the unjacketed test and the porosity remains constant. In the natural case of cemented rocks this does not apply and the compressibility of the single grain constituents $1/K_g$ differs from the pore compressibility $1/K_P$.

The unjacketed bulk compressibility is commonly used for the micromechanical description of the Biot-coefficient weighting the stiffness of the rock skeleton and the 'internal stiffness' facing the pore pressure load (Eq. 3.12 Wang 2000)

$$\alpha = 1 - \frac{K_d}{K_g}. \qquad 3.19$$

Conversion of the Biot-coefficient into the already introduced poroelastic moduli and vice versa is given for example by (Eq. 3.66 Wang 2000):

$$\frac{1}{K_g} = \frac{1}{K_d} - \frac{1}{H} = \frac{1}{K_d} - \frac{\alpha}{K_g} \qquad 3.20$$

3.4 Effective stress, coefficients and failure stress

3.4.1 Effective stress for volumetric deformation

The effective stress concept postulates that volumetric strain in fluid saturated porous rocks is governed by the sum of confining pressure and pore pressure. In the example of the drained test (section 3.3.1) ($\Delta P_f = 0$), it is obvious that the applied load is carried completely by the solid frame resulting in a volumetric deformation ΔV. Applying a load to a fluid saturated sample in which the pore volume is pressurized above ambient pressure, the deformation will be smaller (Nur & Byerlee 1971) as the pore pressure counteracts an applied load P_c and reduces the 'effective' load supported by the solid frame. The concept of effective stress that was initially proposed and experimentally confirmed by Terzaghi (Eq. 3.1) yields a congruent effective stress-strain relation only, if the single constituents of porous material are incompressible compared to the bulk or frame modulus, i.e. $K_g \gg K_d$ and thus $\alpha = 1$.

A more general definition of the effective stress can be derived by reformulating the volumetric part of Equation 3.6. The volumetric strain deriving from confining and pore pressure can be expressed by means of the Biot-coefficient α (Eq. 3.12) and the drained bulk modulus K_d

$$\varepsilon = \frac{\Delta V}{V} = -\frac{1}{K_d}\left(\Delta P_c - \alpha \Delta P_f\right). \qquad 3.21$$

The effective load reduction in the solid, caused by the pore pressure is weighted by α (Eq. 1.33 Cheng 2016)

$$P' = P_c - \alpha P_f \qquad 3.22$$

or expressed by the effective stress tensor (e.g. Eq. 2.68 Wang)

$$\sigma'_{ij} = \sigma_{ij} + \alpha P \delta_{ij} \,. \qquad 3.23$$

Equations 3.22 and 3.23 yield an 'exact' (Nur & Byerlee 1971, Wang 2000) effective stress that applies also for cemented solid rocks that expose a relative compressibility of their internal structure compared to the compressibility of the skeleton ($K_d/K_g > 0$) and the Biot-coefficient α is consequently smaller than one.

Equation 3.23 simplifies the stress-strain relation of fluid saturated rocks in a convenient manner and finds application in many problems of reservoir geomechanics (e.g. Aruffo et al. 2014). However, Equation 3.23 can be replaced by alternative effective stress concepts, addressing problems other than volumetric deformation (e.g. Garg & Nur 1973, Lade & Boer 1997).

The 'correct' Biot-Willis effective stress law was confirmed in experiments on Weber sandstone and Westerley granite by (Nur & Byerlee 1971). These experiments were conducted by controlling both, the increment of confining pressure and the increment of pore pressure within the samples, providing a 12-hour period for pore pressure to equilibrate. In this experimental setup, the overall boundary condition is still drained, i.e. fluid can escape, however the maintained pore pressure is larger than the ambient pressure and contributes to the load bearing process.

3.4.2 Effective stress for pore collapse

Several experimental studies provide strong evidence that the ultimate strength of fluid filled porous rock is in fact governed by Terzaghi effective stress, for example in sandstone (Byerlee 1975, Dropek et al. 1978, Handin et al. 1963, Garg & Nur 1973), limestone and granite (Schmitt & Zoback 1989, Vincké et al. 1998). Failure is here explained by the destruction of pore space, referred to as pore collapse. This irreversible modification of the pore structure is alternatively referred to as pore crushing (Wong et al. 1997) or shear-enhanced compaction (Zoback 2007). In analogy to the lower Hashin-Shtrikman bound, one can argue that the strength of the pore structure is always less than that of the solid component (Cheng 2016) and it is likely that the pore structure is destroyed first before the strength of the single constituents is reached. Failure is thus associated to a change in porosity reflecting a stronger change of pore volume compared to the change of total volume (Eq. 1.38 Cheng 2016):

$$\Delta\phi = \Delta(V_P/V) \qquad 3.24$$

ϕ: Porosity [-]

The porosity change is shown to be controlled by Terzaghi effective stress (e.g. Eq. 3.17 herein, e.g. Eq. 3.43 in Cheng 2016), stated as the simple difference between pore and confining pressure, P_d, in the following Equation (Eq. 3.43 Cheng 2016):

$$\frac{\Delta\phi}{1-\phi} = -\frac{P_d}{K_\phi} = -\left[\frac{1}{K} - \frac{1}{1-\phi}\frac{1}{K_g}\right]P_d \qquad 3.25$$

The failure-associated disproportional change of porosity is in conclusion governed by Terzaghi effective stress (Cheng 2016).

3.5 Darcy's law

Studying the flow of water through a sand column, Darcy found that the flow rate is directly proportional to the piezometric head and inversely proportional to the length of the column. In generalized three dimensional form, Darcy's law states as (Cheng 2016):

$$\vec{q} = -k_f \nabla h \qquad 3.26$$

$\vec{q}$: Specific discharge [m/s] k_f: Hydraulic conductivity [m/s] h: piezometric head [m]

where $\vec{q}$ is the volume of fluid crossing a unit area per unit time, called the specific discharge, the Nabla (∇) operator indicates the spatial gradient in piezometric head h, i.e. the difference in head between two points at distance x_i. The piezometric head is the potential energy of the fluid per unit weight, composed of a pressure head P_f and the elevation *z* above the geodetic datum (Wang 2000):

$$h = \frac{P_f}{\rho_f g} + z \qquad 3.27$$

g: gravitational acceleration [m/s^2]

Flow in groundwater occurs typically at low velocities and the kinetic energy can be neglected in the fluids total energy content. In this case the general variable *hydraulic head* corresponds to the *piezometric head* (Eq. 3.27*)*.

Hydraulic conductivity k_f, is the empirical proportionality coefficient of Darcy's law and as a second rank tensor accounts for directional variability of the medium's permeability. The statement of hydraulic conductivity reflects the original application of Darcy's law in hydrogeology. However the capacity of rock or loose sediments to prevent fluid from flowing along a gradient scales with the density and viscosity of the permeating fluid which is different for oil and gas. In petroleum

engineering the intrinsic permeability K_i is typically stated. The relation between the general intrinsic permeability K_i and hydraulic conductivity k_f is stated as (Wang 2000):

$$K_i = \frac{k_f \eta}{\rho_f g} \qquad 3.28$$

η: Dynamic viscosity [Pa s]

Intrinsic permeability is measured in m^2 while in petroleum engineering the commonly used unit is Darcy $(1\mathrm{D} = 9{,}869 \cdot 10^{-13} m^2)$.

The empirical relation given by Darcy is in fact limited to laminar flow, incompressible fluid and one-phase flow, foreseen in the general theory of poroelasticity. These assumptions do not necessarily apply for the flow of gas in geological reservoirs, but alternative options to model non-laminar flow are not pursued further in this study.

3.6 Governing equations

The constitutive equations introduced in section 3.2 relate forces to the deformation of the porous, fluid-infiltrated material whereby fluid flow is governed by Darcy's law. In a more general manner, the poroelastic problem is expressed by partial differential equations comprising fewer variables.

Seven equations are available up to this stage; six equations for stress or strain and one for either pore pressure or increment in fluid content (section 3.2), in order to solve for three displacement components u_i, the pore pressure P_f, the increment in fluid content ξ and six stress components σ_{ij},.

Here, three additional force equilibrium equations (Eq. 4.10 Wang 2000) are introduced

$$\frac{\partial \sigma_{ji}}{\partial x_j} = -F_i \qquad 3.29$$

ensuring that internal stresses are in overall equilibrium with the gravitational body force and external forces. Substituting the constitutive stress-strain relations (section 3.2) into the force equilibrium equations (Eq. 3.29) and expressing strains as derivatives of displacements leads to partial differential equations that provide a displacement formulation of the mechanical equilibrium (Eq.4.15 Wang 2000)

$$G\nabla^2 u_i + \frac{G}{1-2\nu}\frac{\delta^2 u_k}{\delta x_i \delta x_k} - \alpha \frac{\delta P_f}{\delta x_i} = -F_i\,. \qquad 3.30$$

Further formulations of the governing mechanical equations in terms of stress, strain and considering increment in fluid content instead of pore pressure as coupling factor are available for instance in Wang (2000) (p. 74-77), Rutqvist & Stephansson (2003), Lewis & Schrefler (1999), Zienkiewicz (1982).

Fluid continuity or conservation of fluid mass requires that the fluid mass in the system is constant or in balance with an external sink or source (Eq. 4.63 Wang 2000):

$$\frac{\partial \xi}{\partial t} + \nabla \vec{q} = Q \qquad 3.31$$

Q: Volumetric flow [m^3/s]

Combining Darcy's law with an Equation for increment in fluid content (Eq. 3.2) and applying the continuity requirement yields the inhomogeneous partial differential Equation for fluid diffusion(Eq. 4.63 Wang 2000, Eq. 54 Rutqvist & Stephansson 2003)

$$\frac{\alpha}{K_d B}\left[\frac{B}{3}\frac{\sigma_{kk}}{\partial t} + \frac{\partial P_f}{\partial t}\right] - \frac{K_i}{\eta}\nabla^2 P_f = Q\,. \qquad 3.32$$

where $\alpha/(K_d B)$ is the specific storage at constant stress, alternatively named *1/R*. The quotient of the intrinsic permeability K_i and the dynamic viscosity η is the mobility coefficient *κ [m^4/(Ns)]* and introduces an expression for the permeability, commonly found in petroleum related literature (Cheng 2016, Rudnicki 1986).

It is obvious that the poroelastic coupling derives from the fact that pore pressure appears in both equations (3.30) and (3.32). In general, the governing equations are directly solvable for simple geometries, boundary and initial conditions. The direct solution playing a major role in this study is the uniaxial strain case. Otherwise numerical methods can be applied for solving the partial differential equations, namely the boundary element method (Wang 2000) or the Finite Element method used in this study.

4 Induced stress changes - analytical models

This chapter gives an overview of production-induced stress changes that can be expected from analytical prediction models. In the light of the effective stress issue (section 6 and 10.2), differences in the evaluation of failure stress using Biot-Willis and Terzaghi stress are illustrated (section 4.2. Moreover, models that serve for the description of injection-induced seismicity are discussed with respect to their applicability in production-induced seicmicity. This chapter contains figures and text blocks that appear in a similar manner in the open-access publication Haug et al. (2018).

4.1 Coupled vs uncoupled stress changes for injection and depletion

Systematic triggering of seismicity by fluid-injection at the Rangely field (Raleigh et al. 1976), lead to the conclusion that the increase of pore pressure results in a decrease of the effective normal stresses on faults, resulting thus in a reduced frictional resistance to shear reactivation. In the Mohr-Coulomb space this mechanism corresponds to a shift of the Mohr circle to the left (Fig. 4-13). At the same time it is clear that a simple shift towards higher normal stresses, i.e. to the right, associated to a pore pressure decrease cannot serve as explanation for production-induced failure. The simple shift of the Mohr circle describes uncoupled stress changes, that is, a pore pressure change at constant total stress and corresponding constant shear stress.

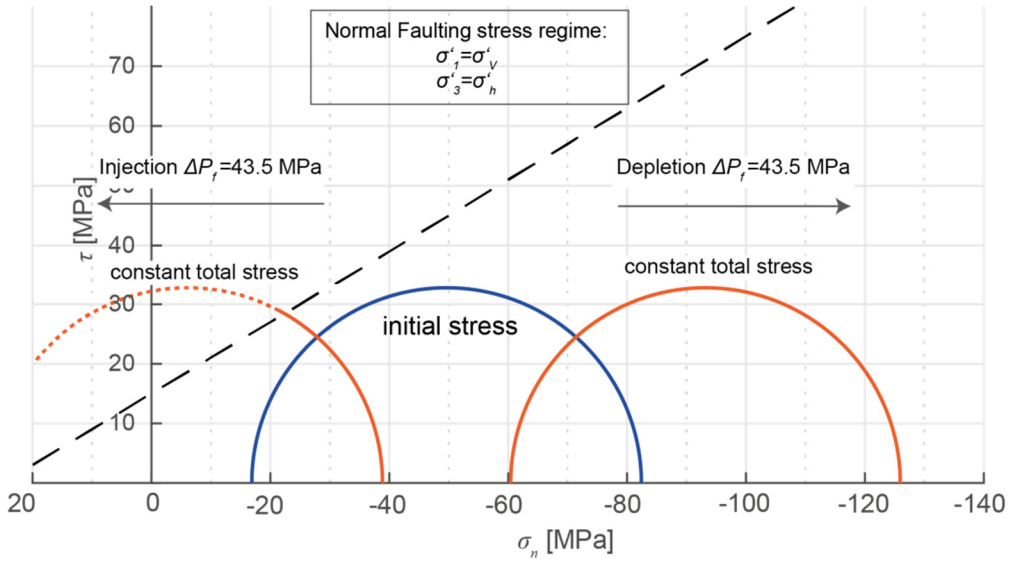

Fig. 4-13: Schematic illustration of uncoupled stress change for injection and depletion. Depletion shifts the Mohr circle to the right, to a greater distance to failure. Injection decreases the effective normal stress and shifts the Mohr circle to the left, to an unstable domain. Due to the constant total stress state, shear stress remains also constant. The dashed line represents the Mohr-Coulomb failure criterion and separates a stable and unstable domain, whereby the existence of unstable stress states is forestalled by failure.

The theory of poroelasticity mainly formulated by Biot (1941) predicts coupled changes of total stress with changes in pore pressures P_f. The coupling of pore pressure and stress is obvious from series of in-situ stress measurements by hydraulic fracturing tests (Addis 1997, Santarelli et al. 1998, Tingay et al. 2003) performed at different stages of depletion, as, for instance compiled by (Altmann et al. 2010). Apart from in-situ measurements, coupling factors can be derived by differentiation of Equation 4.1 which relates total horizontal stresses σ_h to the total vertical load σ_v, the Poisson ratio ν of the rocks, and to P_f under the prerequisite of uniaxial strain conditions ($\varepsilon_h = 0$)

$$\sigma_h = \left[(\sigma_V + \alpha P_f)\frac{\nu}{1-\nu}\right] - \alpha P_f \mid \varepsilon_h = 0\,. \qquad 4.1$$

From Equation 4.1, the coupling of pore pressure and stress changes can be described as follows

$$\Delta\sigma_h = -\alpha\frac{1-2\nu}{1-\nu}\Delta P_f \mid \varepsilon_h = 0 \qquad 4.2$$

whereby ΔP_f is positive for injection and negative for production. The total vertical stress remains constant under the assumption of a lateral extensive reservoir

$$\Delta\sigma_V = 0 \mid \varepsilon_h = 0\,. \qquad 4.3$$

Reducing the total stresses to effective values according to (Eq. 3.1 and 3.22), the change in effective stress is expressed by Equations 4.4 and 4.5. Note that for the case of $\alpha < 1$ the effective stress definition is rather controversial (section 6 and 10.2), in consequence effective stress changes are evaluated in terms of both, Terzaghi and Biot-Willis effective stress here.

The Biot-Willis effective stress change as a function of total stress and pore pressure change is

$$\Delta\sigma'_{ij} = \Delta\sigma_{ij} + \alpha\Delta P_f\,. \qquad 4.4$$

For the evaluation of failure and fracturing, Terzaghi effective stress is commonly considered and its change is given by

$$\Delta\sigma'_{ij} = \Delta\sigma_{ij} + \Delta P_f\,. \qquad 4.5$$

Using Equations 4.4 in 4.2, changes in effective horizontal and effective vertical stresses, can be expressed as:

$$\Delta\sigma'_h = \left[-\left(\frac{1-2\nu}{1-\nu}\right) + 1\right]\alpha\Delta P_f \qquad 4.6$$

$$\Delta\sigma'_V = \alpha\Delta P_f \qquad 4.7$$

The horizontal and vertical effective stress change in terms of Terzaghi effective stresses can be derived by inserting Eq. 4.5 into Eq. 4.2, yielding:

$$\Delta\sigma'_h = \left[\left(-\alpha\frac{1-2\nu}{1-\nu}\right)+1\right]\Delta P_f \qquad 4.8$$

$$\Delta\sigma'_V = \Delta P_f \qquad 4.9$$

Equations 4.2 and 4.3 predict an increase in differential stress and an increase in effective stresses during depletion of a reservoir, which, illustrated in the Mohr Diagram results in an increase in the diameter of the Mohr circle and a shift of the Mohr circle towards higher effective normal stresses (i.e. to the right in Figure 4-14). In case that the increase rate in diameter exceeds the increase in frictional resistance with normal stress of a fault, the Mohr circle approaches the Coulomb frictional failure envelope, and the fault may become instable (Fig. 4-14).

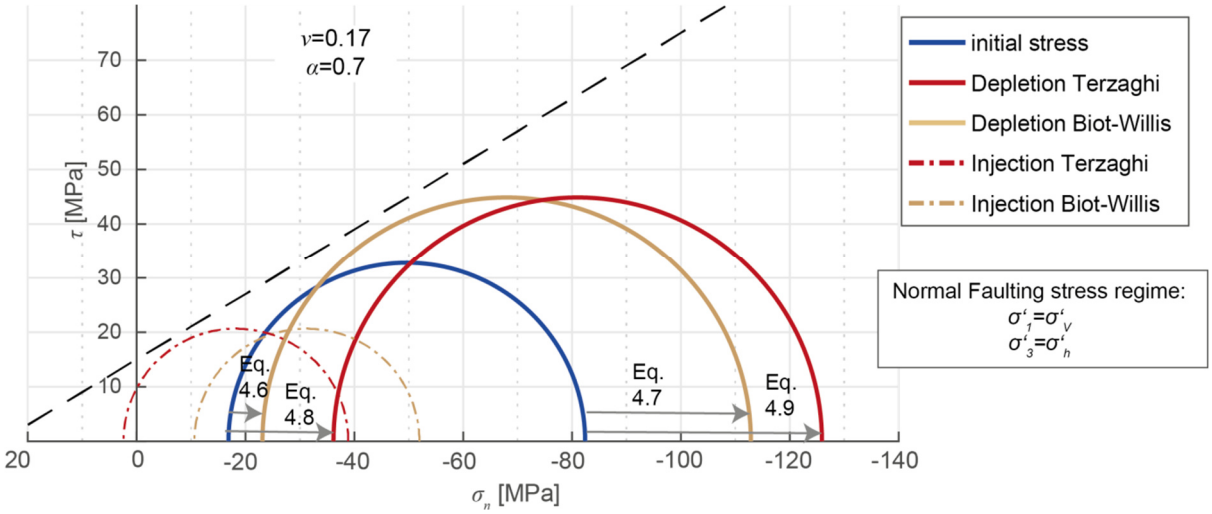

Fig. 4-14: Schematic illustration of the consequences of a coupled change of pore pressure and total stress, evaluated in terms of effective stresses in the Mohr-domain. Production results in an increase of the diameter of the circle and a shift to the right. Injection returns a decrease of the diameter of the circle and a shift to lower effective normal stresses. The dashed line represents the Mohr-Coulomb failure criterion and separates a stable and unstable domain.

Figure 4-14 illustrates that the evaluation of fault reactivation risk in terms of Biot-Willis effective stress is a conservative approach for production and a non-conservative approach for injection. The inverse applies for the evaluation of Terzaghi effective stress.

4.2 The depletion-induced stress path

In case that the increase rate in diameter exceeds the increase in frictional resistance with normal stress on a fault, the Mohr circle approaches the Coulomb frictional failure envelope. The stress path indicated in red arrows can thus be considered critical if its slope is larger than the slope of the failure

line. Figure 4-15 shows the depletion-induced increase in diameter of the Mohr circle as a function of the Biot-coefficient for the evaluation of Biot-Willis and Terzaghi effective stress.

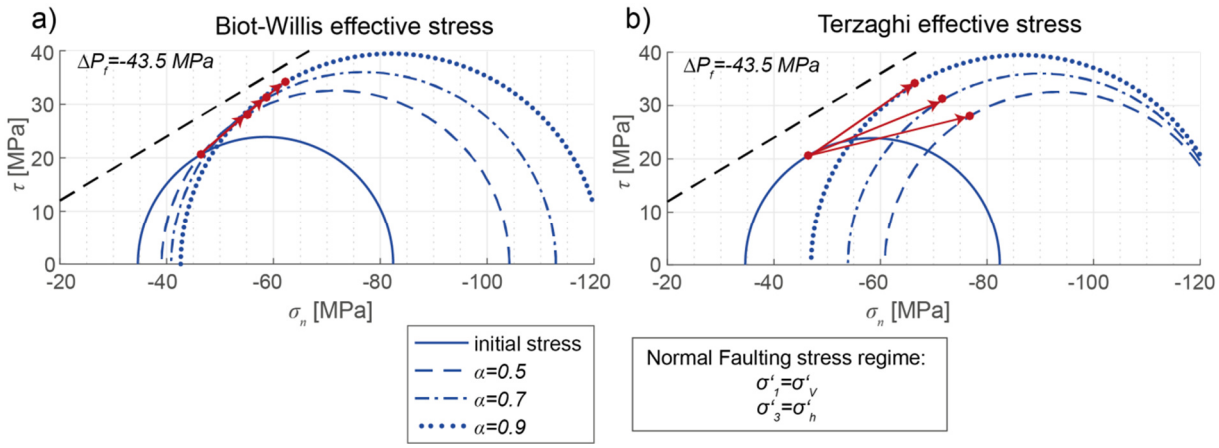

Fig. 4-15: Schematic illustration of total stress changes (Eqs. 4.2, 4.3) for different Biot-coefficients, evaluated in terms of Biot-Willis effective stress (a) and Terzaghi effective stress (b). For Biot-Willis effective stress, the Biot-coefficient controls the effect of pore pressure change along a stress path that is predefined by Poisson's ratio (Eq. 4.12). For Terzaghi effective stress, the slope of the stress path is governed by both, Poisson's ratio and Biot-coefficient.

Considering a typical friction coefficient of $\mu_s=0.6$, two limiting cases for the critical slope of the stress path can be distinguished:

- Zoback (2007) defines a limiting maximum value of the coupling factor

$$\frac{\sigma_h}{\Delta P_f} = -\alpha \frac{1-2\nu}{1-\nu} = -0.67 \qquad 4.10$$

  based on the frictional equilibrium formulated in terms of Terzaghi effective stress. According to Zoback (2007) low Poisson ratios and large Biot-coefficients result in a steep stress path ultimately leading to failure.

- Considering Biot-Willis effective stress, Eq. 4.6 can be rearranged to:

$$\Delta\sigma'_h = \frac{\nu}{1-\nu}\alpha\Delta P_f. \qquad 4.11$$

  Along with Equation 4.7, the Biot-coefficient affects vertical and horizontal principal stresses equally, build-up of differential stress is thus a mere function of Poisson's ratio. For a Poisson's ratio inferior to 0.25, the following identity signals an unstable stress path:

$$\frac{\Delta\sigma'_h}{\Delta\sigma'_V} = \frac{\nu}{1-\nu} < 0.32 \qquad 4.12$$

While the slope of the stress path depends exclusively on Poisson's ratio; the Biot-coefficient turns out to determine the required pore pressure depletion magnitude to reach the failure line (cp. Fig. 4-15 a).

In the following, stress paths for characteristic reservoir properties of the North German basin are investigated. Figure 4-16 shows the stress path evaluated for Biot-Willis and Terzaghi effective stress, illustrating the influence of fault dip, Poisson's ratio and the Biot-coefficient on the slope of the stress path. The pre-production stress state is computed from a typical overburden load of $\sigma_1 = \sigma_V = -119\ \mathrm{MPa}$ corresponding to

- An overburden density of ρ = 2530 and a reservoir depth of z = 4800 m
- hydrostatic pore pressure at a depth of z = 4800 m
- A Biot-coefficient of the reservoir $\alpha = 0.7$
- $K' = \sigma'_3/\sigma'_1 = \sigma'_h/\sigma'_V = 0.42$ (cp. section 7.1.2).

The resulting vertical effective stress magnitude is $\sigma'_V = -82.4\ \mathrm{MPa}$ and the horizontal effective stress magnitude is $\sigma'_h = -34.6\ \mathrm{MPa}$. For the investigated scenarios, the stress path approach of Figure 4-16 cannot explain fault reactivation as the required pore pressure change to reach the failure line is out of scale.

If Terzaghi effective stress is evaluated for failure, a critical slope prevails for low Poisson's ratios and large Biot-coefficients. For Biot-Willis effective stress, the slope of the stress path depends exclusively on Poisson's ratio, but absolute pore pressure magnitudes in order to reach the failure line scale with the Biot–coefficient. Apart from the simple stress path considerations, Figure 4-16 reveals the crucial role of the pre-production stress state, determining the distance and required depletion magnitude to failure.

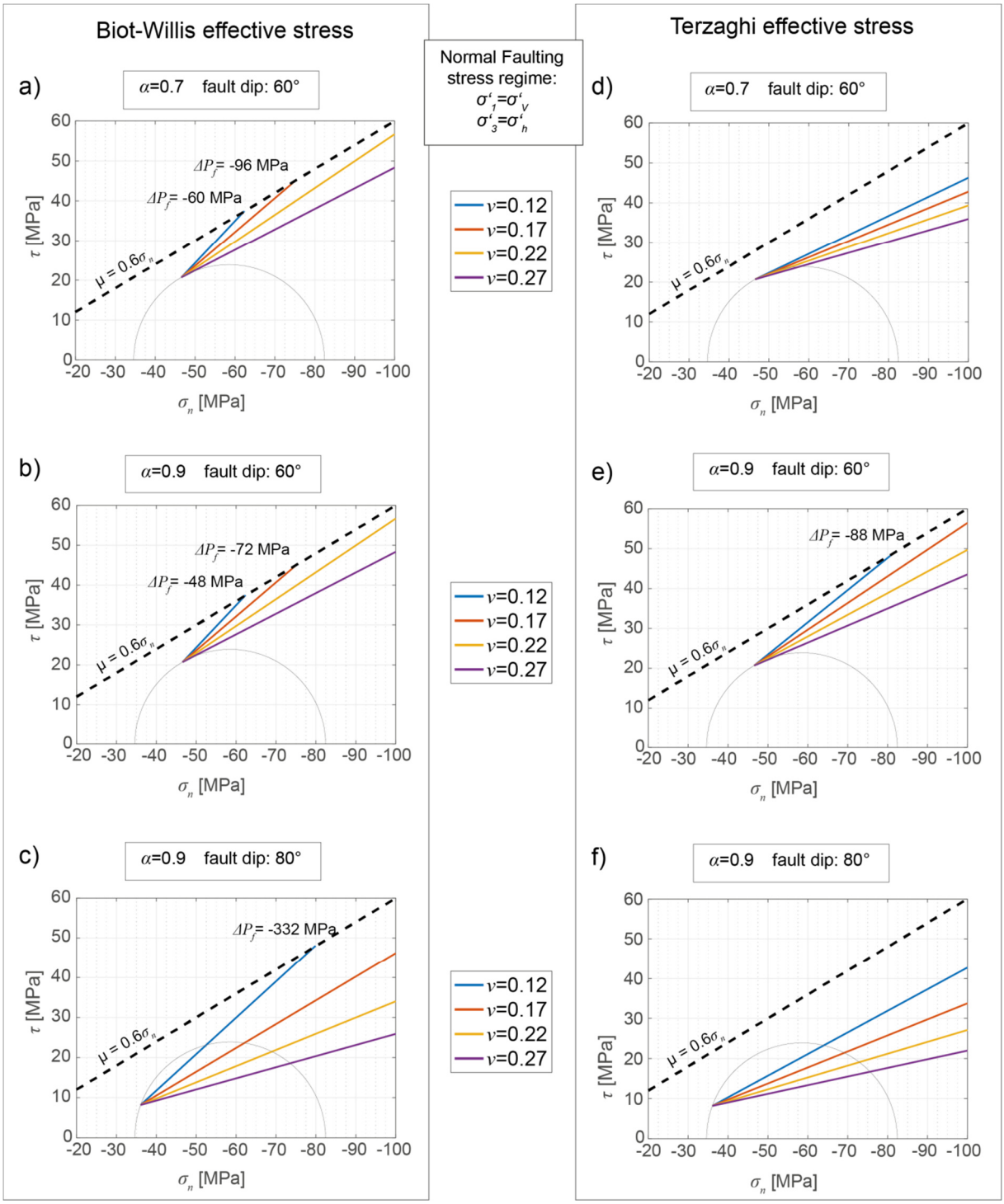

Fig. 4-16: Stress path and required depletion magnitude to failure for different, typical reservoir parameters, evaluated in terms of (a-c) Biot-Willis effective stress and (d-f) Terzaghi effective stress.

4.3 Inclusion models

Segall & Fitzgerald (1998) published a more sophisticated analytic poroelastic model that considers an elliptic reservoir inclusion hosted in an elastic full space. Their solutions allow for computing changes of horizontal and vertical principal stresses inside and around the reservoir inclusion, whose tendency

to compact with pore pressure depletion is counteracted by the surrounding rock. Soltanzadeh & Hawkes (2008) extended this approach to rectangular reservoir geometries and defined a general stress arching parameter $\gamma_{(ij)}$ to describe total stress changes in and around a depleting reservoir (Fig. 4-17 a,b)

$$\gamma_{ij}(x,y) = \frac{\Delta\sigma_{ij}}{\alpha\Delta P_f \delta_{ij}}. \qquad 4.13$$

Accordingly, effective stress changes inside the reservoir may be written as:

$$\Delta\sigma'_{ij\ in} = \big(\gamma_{ij}(x,y) + \delta_{ij}\big)\alpha\Delta P_f \delta_{ij} \qquad 4.14$$

Stress changes in the rocks surrounding the reservoir are given by:

$$\Delta\sigma'_{ij\ out} = \Delta\sigma_{ij\ out} = \gamma_{ij}(x,y)\alpha\Delta P_f \delta_{ij} \qquad 4.15$$

In the undepleted surrounding rock, the total stress change corresponds to an effective stress change provided the deformation occurs under drained conditions. A detailed numerical study showing also the perturbation of the arching parameter across model faults, was recently presented by Gheibi et al. (2017). In Figure 4-17 a) and b) stress changes according to the base model proposed by Soltanzadeh & Hawkes (2008) are illustrated schematically. Along a horizontal profile at mid-reservoir height, total vertical stresses decrease towards the lateral reservoir boundary and increase directly outside the reservoir (Fig. 4-17 b). Total horizontal stresses are reduced during production but their rate of reduction decreases with increasing proximity to the lateral reservoir boundary (Fig. 4-17 b). Since stress changes at the reservoir boundary must be balanced on opposite sides of the pore pressure discontinuity, poroelastic stress changes in the reservoir are transferred into the host rocks, as schematically illustrated in Figure 4-17 c) and d). The stress transfer is referred to as arching effect, and controls fault-loading during production. At the reservoir boundary, changes in normal stresses $\Delta\sigma_n$ are continuous (Fig. 4-17 b,d) while the tangential component $\Delta\sigma_v = \Delta\tau$ is discontinuous (Fig. 4-17 a,c). Note that stress changes in the reservoir centre correspond to the predictions of the uniaxial strain model (Eqs. 4.1-4.3). At the reservoir boundary, stress changes are controlled by the pore pressure discontinuity, the geometry of the boundary, and by rock mechanical contrasts across the bounding fault; thus, stress paths at the reservoir centres must differ from those at reservoir boundaries. This means that time series of *in-situ* stress measurements during depletion as, for instance, published by Teufel et al. (1991) cannot directly predict the loading of reservoir-bounding faults.

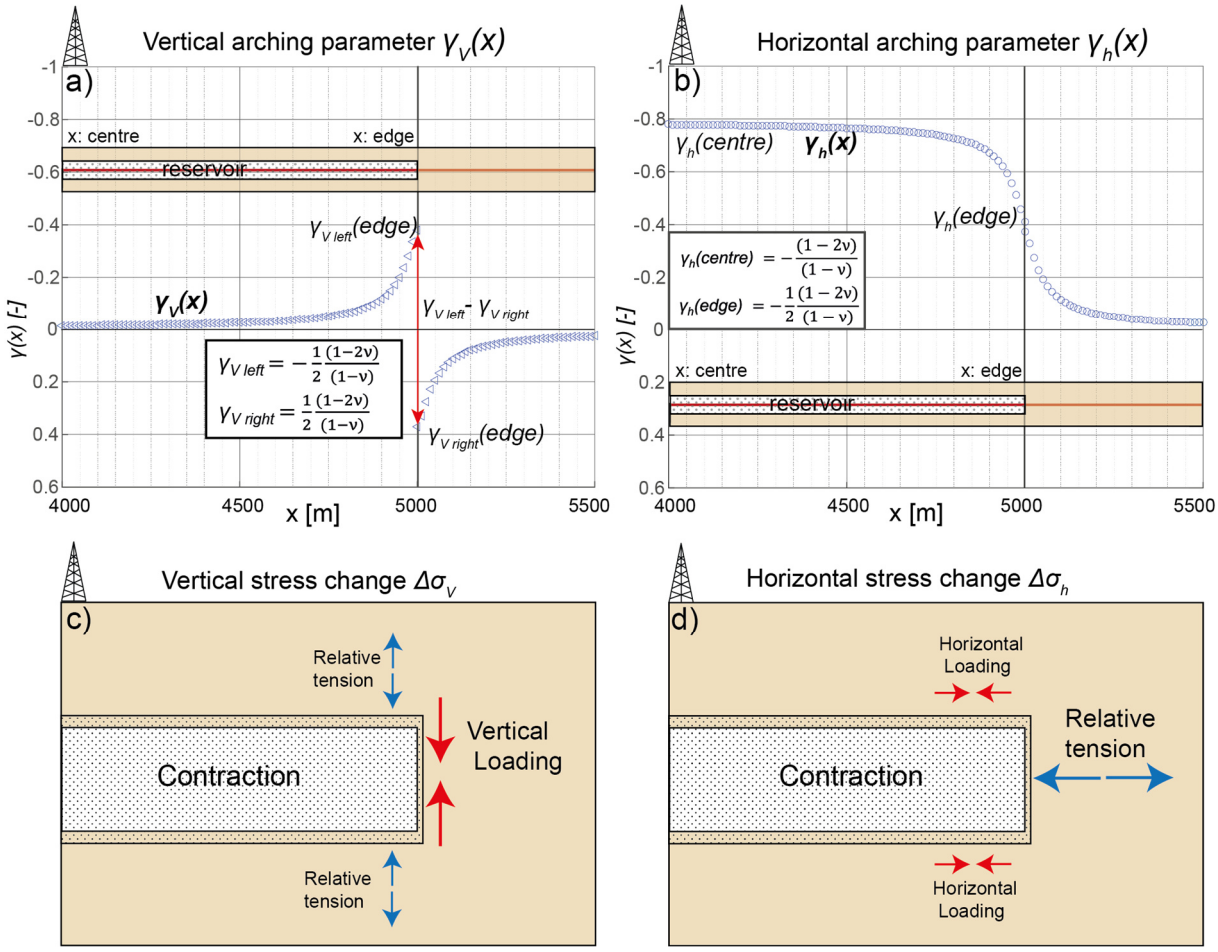

Fig. 4-17: a-b) Stress arching parameters indicating the ratio of total stress change to pore pressure change along a horizontal midline through a rectangular depleted reservoir inclusion. c-d): induced loading in the adjacent formations as a consequence of reservoir contraction. a) The total vertical stress change $\Delta\sigma v$ is discontinuous while the total horizontal stress change $\Delta\sigma_h$ (b) is continuous across the pore pressure discontinuity. c-d) Effective stress changes are largest within the reservoir (Eq. 4.14), as effective stresses become more compressive with pore pressure depletion. Loading also occurs in the surrounding rock: c) The vertical stress increases at the reservoir flanks and decreases above the reservoir (Eq. 4.15). d) The reservoir contraction leads to relative horizontal tension at the flanks of the reservoir and a slight horizontal loading above and below the reservoir.

4.4 Spatio-temporal effects

Analytic and reservoir stress path approaches considered so far have assumed a steady state pore pressure field that affects reservoir stress in a one-directional sense, fault reactivation results from 'direct' pore pressure changes in the affected region (e.g. Deng et al. 2016). In this case, the time period until potential fault reactivation depends on the diffusion of the pore pressure change as a function of production-rate, permeability and distance to the well.

In opposition to that, the spatio-temporal poroelastic effect accounts for the initial dominance of stress changes transmitted within the solid rock over the slower diffusion of the pore pressure front (Segall & Lu 2015). High injection or production rates exerted to low permeability rocks cause an initial volume change in the immediate surrounding of the well. This near-field strain stresses in turn rock formations far beyond the pore pressure front for which the diffusive advance is limited by the given medium's permeability (e.g. Rozhko 2010, Segall & Lu 2015). In consequence, Coulomb stress perturbations ahead of the pore pressure front may trigger earthquakes after short injection times on far-distant faults (e.g. Goebel et al. 2017).

Based on the observation of *reservoir stress path* data scattering around the values predicted by the uniaxial strain model, Altmann et al.(2010, 2014) showed that the coupling ratios of the *reservoir stress path* vary in time and space before approaching the 'long-term' limit according to Eq. 4.2. Moreover, due to the suggested coupling of all stress tensor components to the pore pressure change, the build-up of differential stress, before reaching the long-term limit becomes complex.

Herein, Rudnicki's (1986) analytic solution (cp. section 6.5) is applied to simulate pore pressure and stress changes for typical reservoir properties of the North German basin. The production time is 22 years at a production rate of 0.23 m^3/s; the fluid and material properties are listed in Table 3, section 8.2.2.

The temporal evolution of stress is picked in 1000 m radial distance to the production point (Fig. 4-18). The results displayed in Figure 4-18 confirm basic findings of previous authors. Decreasing permeability results in the radial stress signal arrive prior to the pore pressure signal, furthermore the radial and tangential stress components change at different rates (Fig. 4-18 a-c) resulting in an intermediate differential stress build-up before reaching the long-term limits.

Dependent on the permeability of the medium, the coupling ratio converges after several days (Fig. 4-18 a), or years (Fig. 4-18 b), with the long term limit that is, for the radial stress component, defined by the r*eservoir stress path* (Eq. 4.2). The long term limit of tangential stress components according to (Altmann et al. 2014) assume:

$$\alpha\gamma_{22} = \frac{\Delta\sigma_{22}}{\Delta P_f} = -\frac{1}{2}\alpha\frac{1-2\nu}{1-\nu} \qquad 4.16$$

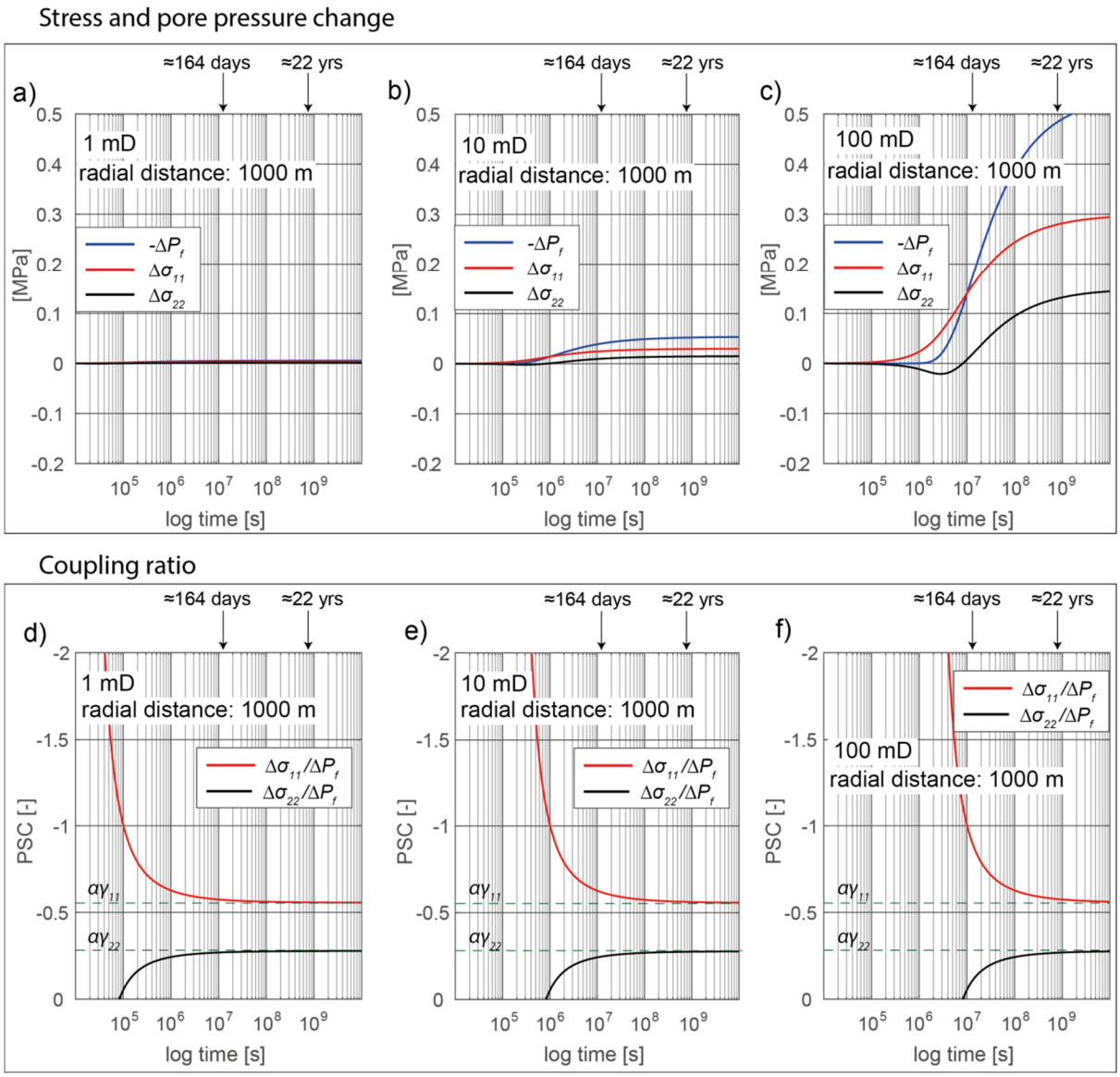

Fig. 4-18: a-c) Stress and pore pressure changes computed with Rudnicki's (1986) equations (section 6.5), in 1000 m radial distance to the well. Following the x-axis from the well, radial stress changes correspond to the x-component of the stress tensor $\Delta\sigma_{rad}=\Delta\sigma_{11}$. The tangential stresses correspond to the y- and z- components of the tensor respectively $\Delta\sigma_{tan}=\Delta\sigma_{22}=\Delta\sigma_{33}$. Plots (d-f) show the coupling ratios of radial and tangential total stress to pore pressure as a function of the permeability of the reservoir.

In the context of production-induced seismicity, strong reservations on the role of spatio-temporal effect have to be stated. First, the onset of seismicity in prominent examples of production-induced seismicity, the Groningen, the North German gas fields and the Lacq gas field show a temporal correlation of depletion magnitude and seismicity (e.g. Bardainne et al. 2008, Muntendam-Bos et al. 2015, Uta 2017). The registration of seismic events started as late as after several decades of production and seemingly correlates with ongoing compaction (van Thienen-Visser & Breunese 2015). Thus, at the stage that seismic events were registered, diffusive perturbations of the pore pressure field had most likely reached compartment boundary faults.

Second, the assumption of an infinite full space, as considered in Rudnicki's (1986) approach, does not reflect common reservoir geometries that exhibit a significantly larger lateral extension compared to their thickness. Hence, a coupling of all stress tensor components to the pore pressure change is limited to the stress arching effect and in consequence, a change of vertical stress (section 4.3) can only be observed on the lateral reservoir boundary of the herein presented models (section 9).

5 Finite Element simulation

The numerical modelling in this study is executed by means of the Finite Element method. In quick terms the Finite Element method allows for the approximate solution of partial differential equations in time and space and the addressing of complex geometries as well as elaborate initial and boundary conditions. It can be applied to a wide range of physical problems, but in the following, an introduction to the theory is first undertaken on static problems of structural mechanics, before the formulation of the coupled flow-displacement formulation is presented. For a more detailed review on the general mathematical background, refer to Zienkiewicz et al. (2013), the application of the FE method in the analysis of consolidation can be looked up in Lewis & Schrefler (1999). In the last section of this chapter, schemes to solve the coupled equations in a fully coupled manner or by applying specialized mechanical and flow simulators are presented.

5.1 The Displacement Finite Element Method

In order to introduce the matrix formulation of the displacement based FE method, the example of a statically determined truss structure can be considered first. The truss structure comprises 1D rod elements connected to each other by nodes. If a force is applied to any of the nodes, reaction forces at all nodes, the supports and nodal displacements can be computed. Searching the nodal displacements, their relation to applied loads can be formulated in the stiffness matrix *K*. The stiffness matrix summarizes all possible force-displacement interactions of the single elements building the entire structure (Merkel & Öchsner 2010)

$$\{F\} = [K]\{u\}\,. \qquad 5.1$$

The stiffness matrix is occupied in a manner that nodal displacement degrees of freedom are compatible with each other and the sum of all forces yields zero.

Considering the response of an arbitrary elastically deformable continuum to loading, the displacement of every single infinitely small point of the body is described by a solution of the partial differential equation of motion at that point. The infinite number of displacement degrees of freedom is reduced in the FE method by discretization of the continuum into finite elements. From the element's respective nodal displacements, the stress state within the element can be retrieved via the constitutive law (Gawehn & Funk 2017).

A combination of two principles, the principle of total potential energy and the principle of virtual work can be applied to solve Equation 5.1 (Gawehn & Funk 2017).

The total potential energy of the system can be subdivided into the internal strain-energy and the potential energy of the external load to the system. The internal strain energy derives from the work conducted on the deforming body. The virtual work concept, comprises virtual nodal displacements that allow the derivation of approximate stresses along the elements' edges (Merkel & Öchsner 2010).

Combining the principles of virtual work and total potential energy, nodal displacement functions whose best-fit approximate solutions render the potential energy at a minimum can be investigated. The discretization of the continuum leads to a linear equation system containing displacement functions for all nodes whereby the accuracy of the approximate solution naturally depends on the mesh resolution (Gawehn & Funk 2017).

The continuous description of displacements along the edge of elements is described by element-specific displacement functions. Eqs. 5.2 and 5.3 show the linear (first-order) and quadratic (second-order) displacement function along the x-axis of a given element:

$$u(x) = a_0 + a_1 x \tag{5.2}$$

$$u(x) = a_0 + a_1 x + a_2 x^2 \tag{5.3}$$

The displacement function *u(x)* whose approximated result aims on minimizing the total potential energy, can also be expressed as function of the element's shape. The allowed local displacements (*N1, N2*) lead to the element specific shape function

$$u(x) = [N_1(x), N_2(x)] \begin{pmatrix} u_1 \\ u_2 \end{pmatrix}. \tag{5.4}$$

In order to find the best-fit approximate solution for the differential equation, the Ansatz-function is derivated (*u'*) and its approximate solution is inserted into the differential Equation of motion to evaluate the *Residuum*. The Residuum is weighted by another function and in order to satisfy a given convergence tolerance (Gawehn & Funk 2017), is supposed to fade when integrating over the entire domain.

5.1.1 Element Integration and nonlinearity

The stiffness matrix of single elements $\tilde{k}_e$ is composed of the derivative of the shape-function (*u')* and the constitutive law *D* (Eq. 10.2 Katzenbach et al. 2012)

$$\tilde{k}_e = \int u'^T D u' dV \,. \qquad 5.5$$

The Ansatz function is most correctly integrated at the integration points and stress is interpolated therefrom. Integration points are discrete points within the element whose relative position with respect to the nodes is fixed.

Nonlinearities in the FE model derive from different sources, namely nonlinear constitutive laws, large deformations, contact constraints and contact slip. In the present study the *nonlinear geometry option*, invoking the iterative Newton-Ritz solution method is used in all models.

5.1.2 FE Formulation for consolidation

The formulation of the consolidation problem is more complex than for the elastostatic example (Eq. 5.1). Equation 5.6 exemplarily shows the FE formulation of fully coupled poroelasticity according to (Eq. 3.18 Lewis & Schrefler 1999), but various formulations can be found in the literature (Zhou 1997).

$$\begin{bmatrix} 0 & 0 \\ 0 & H \end{bmatrix} \begin{Bmatrix} \bar{u} \\ \bar{p} \end{Bmatrix} + \begin{bmatrix} K & L \\ L^T & S \end{bmatrix} \frac{\delta}{\delta t} \begin{Bmatrix} \bar{u} \\ \bar{p} \end{Bmatrix} = \begin{Bmatrix} \delta \bar{F} \\ \bar{Q} \end{Bmatrix} \qquad 5.6$$

K, H, L and *S* are coefficient matrices of properties like permeability, compressibilites, element volume, shape and transformation functions (Rutqvist & Stephansson 2003). In functional terms, *K* is still the stiffness matrix and *L* is a coupling coefficient matrix (Settari & Walters 2001). The primary unknown variables are the nodal displacements $\vec{u}$ and the pore pressure $\bar{p}$ (Eq. 5.17,5.18, Zhou 1997).

Within the ABAQUS consolidation procedure, the mesh is attached to the solid phase of the rock, while the fluid flows through the mesh. Along with the displacement degrees of freedom, pore pressure is a nodal variable, while stress is evaluated at the integration points. Thereby the number of pore pressure degrees of freedom, does not require conformity with the total number of nodes. The herein described FE approach to the consolidation problem is only one option out of several, a review can be consulted in Zhou (1997, p. 60-62).

5.1.3 Short note on time and dynamics

The transient consolidation procedure used in ABAQUS is a quasi-static one, i.e. pore pressure changes are transient leading to time-dependent stress states, but the overall static equilibrium is ensured during any time increment. In opposition to dynamic procedures, inertia, the acceleration of a moving mass is not considered. Dynamic considerations are of interest in comparably fast processes such as crash simulations or earthquakes (e.g. Templeton et al. 2009). Dynamic stress-displacement procedures, are available both in ABAQUS standard/implicit and explicit (*ABQ 2016 Analysis Guide 6.3.1*), but exclude poroelasticity. The earthquake as consequences of stress changes can however be simulated individually (e.g. Kroll et al. 2017). The explicit integration scheme is commonly used for dynamic problems, solution quantities are known at the beginning of an increment and are computed by a forward-marching direct solution scheme which omits iterations and matrix inversion (*ABQ 2016 Analysis Guide 6.3.1*). As the achievement of a global equilibrium is not required at any time, incrementing is fast and computationally cheap but convergence and equilibrium checks are dropped. The results from a user-defined time-stepping scheme must hence be carefully scrutinized for plausibility (*ABQ 2016 Analysis Guide 6.3.1*).

5.1.4 Element selection and discretization

The element type and mesh resolution determines the accuracy of the solution, particularly in model areas of large stress and pore pressure gradients. In general, the element selection and discretization is a trade-off between accuracy and computational cost. The improved accuracy arising from the use of higher order, –full integration elements comes at the cost of computation time and may be compensated for example by refining a mesh of lower-order elements.

The majority of modelling in this study considers two-dimensional geometries. Basic 2D element shapes are triangular and quadrilateral. Furthermore, one can discriminate the element order: First order elements have nodes only at element corners, second order elements have additional midside nodes along the edge of the element. The additional node and associated nonlinear shape function allow for an accurate bending of elements, a deformation mode that is observed to cause *shear-locking* in first order quadrilateral elements.

As a general rule, discretization by first order tetrahedral elements is not recommended as these elements comprise only one integration point and benchmark models show large inaccuracies (*ABQ 2016 Benchmark Guide 2.1*). Second order elements on the other hand have additional integration

points and their computational performance can be enhanced by using their reduced integration version, for reduced integration however, issues of *hourglassing* may occur.

For plane strain computations of coupled pore pressure-displacement problems, a limited element selection is available in ABAQUS. The second order triangular type (CPE6HP) revealed severe numerical oscillations and was discarded. Second order quadrilateral elements (CPE8P) comprise an additional displacement degree of freedom on the midside of their edge, but only four pore pressure degrees of freedom exist on the corner nodes. This distribution of pore pressure and displacement degrees of freedom results in interpolation-related numerical oscillations of contact pressure. In consequence first order quadrilateral elements (CPE4P) were predominantly deployed in this study.

Table 1 shows the computation times for different models, encompassing different numbers of elements and element types. Due to the larger number of degrees of freedom, 3D simulations revealed a particularly longer computation time for only slightly larger element numbers compared to the 2D variants.

Tab. 1: Discretization of different models and computation time

Model and size	**Element type**	**Element number**	**Computation time for X CPUS**
Reference model (section 8.2.2) 2D 8 km	CPE4P	90000	23 min 4 CPUS
Salt Diapir 2D 26 km	CPE4 and CPE4P	260000	4.5 hrs 6CPUS
Reference model (section 8.2.2) 2D 8 km - contact constraint enforcement	CPE4P	90000	53 min 6CPUS
Reference model 3D reduced size: Y:950m Z:1500 X:3300	C3D8P	130000	4.4 hrs 6CPUS
Reference model 3D: Y: 1400 Z:3000 X:4000	C3D8P	500000	~1.5 days 6CPUS

5.2 Coupling within the numerical model

In a mathematical sense, an uncoupling of stress or strain from pore pressure occurs if the mean stress coupling term in Eq. 3.32 is omitted. In this case, a change in pore pressure or fluid increment does produce stress or strain but changes of the stress or strain do not affect pore pressure and the fluid flow can be computed independently of the transient stress or strain field.

For particular simulation approaches like steady state, uniaxial strain, or a highly compressible fluid (Wang 2000), the diffusion Equation (3.32) is forcibly uncoupled from the mechanical equilibrium Equation (3.30). As pore pressure in the uniaxial strain model is predefined, the *reservoir stress path* derived from uniaxial strain conditions is essentially uncoupled in a mathematical sense. Nevertheless, in a physical sense, these models do capture the coupling of fluid to solid and reflect coupled changes of pore pressure and stress. The approach of using external pore pressure as input for the consolidation analysis is often referred to as one-way coupling and according to Dean et al. (2006) is capable of addressing many problems of reservoir geomechanics in a sufficiently accurate manner.

The requirement of coupling a reservoir flow simulator to a mechanical simulator arises from the limited mechanical capacities of the reservoir simulator and in turn the common deficiency of mechanical simulators to account for two-phase fluid flow and for complex flow patterns within the subsurface model. Thereby the format of the reservoir model is commonly compatible with the Finite Difference (FD) reservoir simulator (e.g. Settari et al. 2005, Settari & Sen 2007).

Several strategies to pass variables between mechanical and flow computations can be differentiated subsumed under the term *partial coupling schemes*:

One-way coupling signifies that pore pressure is computed separately in a reservoir simulator. It can then be mapped as pore pressure boundary condition or applied load to the mechanical simulator at defined times (Gutierrez & Lewis 2002).

A two way coupling scheme provides the mechanical simulator with pore pressure, the mechanical simulator feeds back an updated porosity (Dean et al. 2006) and an updated ‘pseudo compressibility’ (Inoue & Da Fontoura 2009a, Lautenschläger et al. 2013). Sometimes an intermediate module is used to evaluate porosity, permeability and pseudo-compressibility from the effective stress output (Rutqvist & Stephansson 2003). The passed variable between the two simulators is the change in pore volume (Rutqvist & Stephansson 2003).

In an explicit (two-way) coupling scheme, the two codes are executed sequentially and pore pressure, porosity and pore compressibility are exchanged either at the beginning of predefined time steps (Inoue & Da Fontoura 2009b), at any time step (Samier et al. 2003), or when an external module invokes exchange due to significant changes in one of the variables (Dean et al. 2006). In this scheme, only one iteration including the updated parameter is done per time step (Settari & Walters 2001) and the solution is advanced within the mechanical simulator (Dean et al. 2006).

In the iterative two-way coupling scheme, the flow and stress equations are continuously iterated over the time step (Settari & Walters 2001), during each iteration the simulators perform sequential

computations of flow and displacement. The coupling parameter is again the pore volume (Dean et al. 2006). If convergence tolerances are similarly tight, the iterative approach yields the same results as a fully coupled simulator (e.g. Bostrom 2009, Vilarrasa et al. 2016).

In distinction to the previous partial schemes, in the full coupling scheme the flow and displacement calculations are performed in one code solving for flow and displacement variables simultaneously (Longuemare et al. 2002) offering unconditional numerical stability (Dean et al. 2006, *ABQ 2016 Analysis Guide 6.8.1*). The FE-software ABAQUS used in this study provides the fully coupled procedure, whose detailed handling is explained in section 7.4.

5.3 Contact in FE Modelling

5.3.1 General principles

Contact mechanics incorporated in the FE-method allows for the computation of contact area and generated contact pressures between two interacting bodies (*ABQ 2016 Analysis guide 36.1*). In opposition to the standard continuum approach, contact represents a discontinuity in the model and is thus a popular option for the deterministic modelling of faults (e.g. Fischer & Henk 2013, Hergert et al. 2015, Reiter & Heidbach 2014). In numerical terms, contact introduces nonlinearities into the model and the stiffness matrix changes if components come in contact (*ABQ 2016 Analysis guide 6.16*). Most important contact constraints in mechanical terms are the normal and the tangential contact behaviour. In the normal direction the pressure-overclosure relationship, determines how normal stresses evolve as a function of contact clearance and penetration (Fig. 5-19). The tangential contact constraint is defined by various available friction models.

In ABAQUS, two basic contact algorithms were eligible for this study, General Contact and Contact Pairs, differing mainly in their default constraint enforcement methods, general range of available options and their approach to identify surfaces in contact.

Contact constraints can be enforced by three different numerical methods:

- The direct method ensures exact enforcement of contact constraints but is expensive in terms of computational cost and provides rather poor prospects of convergence.
- The Penalty method approximates the *hard* contact constraint by reducing the penalty stiffness.
- The augmented Lagrange method uses augmented iterations for a better approximate solution of the penalty method.

Furthermore, Lagrange Multipliers can be added to the penalty methods (Weyler et al. 2012) to accurately enforce tangential and normal constraints, accompanied however by a higher computational cost.

Figure 5-19 shows principles of surface-to-surface contact that include the assignment of a Master and Slave role in contact interaction. The surface on stiffer or coarser underlying elements is commonly assigned the Master-role.

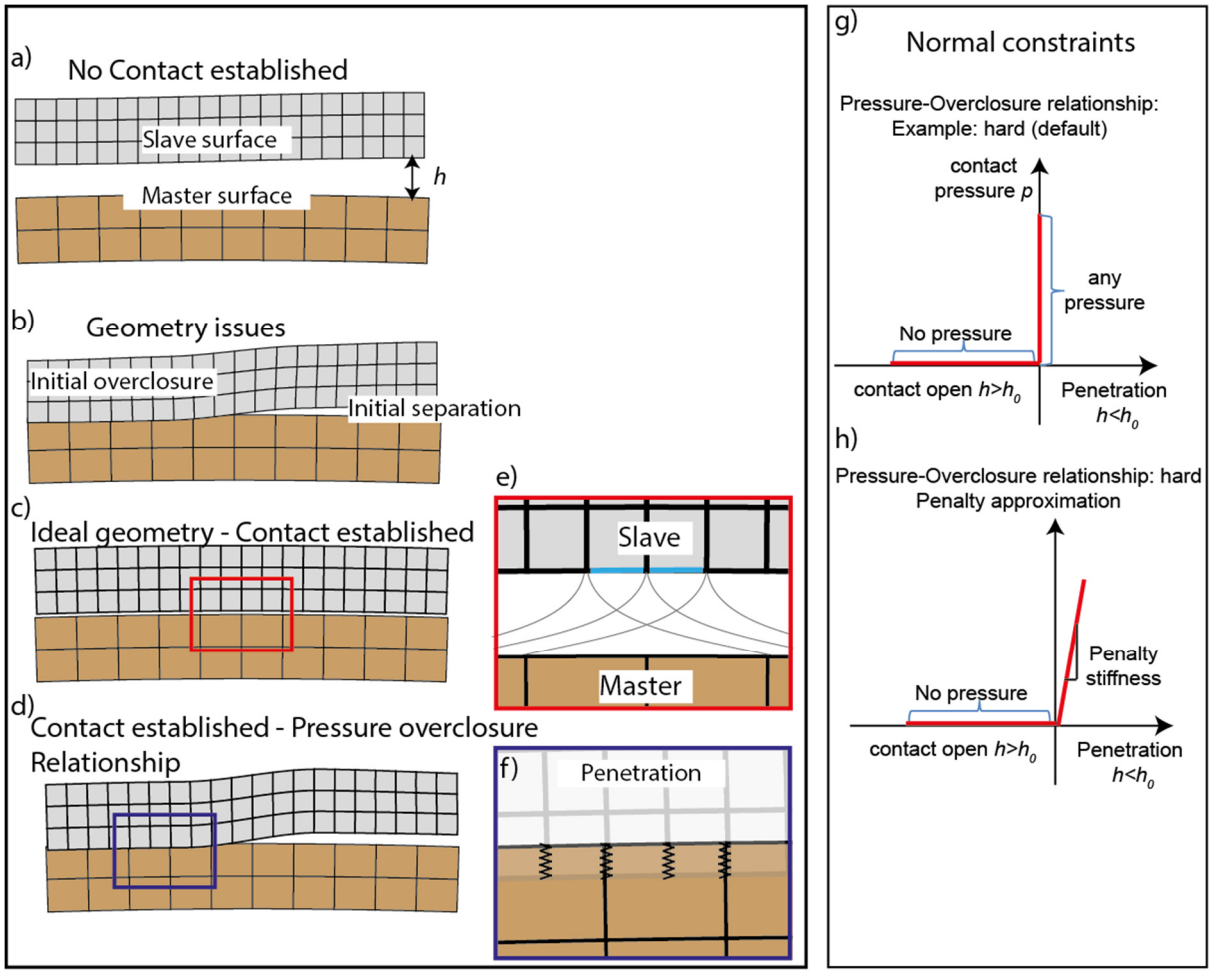

Fig. 5-19: a-d) Different modes of normal contact interaction: a) open contact, b) initial penetration, c) ideal establishment of contact, d) penetration and separation during the simulation. e) The Master and Slave principle attributes different roles to the surfaces and determines the constraint enforcement of one surface with respect to degrees of freedom of the other. f) The pressure penetration relationship is governed by the contact stiffness and ABAQUs allows to specifiy different approaches for computing the pressure relationship. *Hard* contact represents a strict approach (g) but is approximated by the penalty method (h).

5.3.2 Tangential constraint

Modelling fault slip with contact, the accurate enforcement of the tangential constraint is particularly crucial. The penalty method allows penalty slip for non-critical shear stress in order to facilitate the solution procedure. In this case, penalty slip adds up to the total slip output, irrespective of whether slip occurs at failure or not. Default tolerances and penalty stiffnesses are designed for much lower pressures than prevailing at 5000 m depth and must hence be modified. A stricter enforcement of the frictional constraint at the cost of penalty slip can be imposed by using Lagrange multipliers or by increasing the contact's so-called *sticking stiffness* Figure 5-20 b) These modifications of the default contact settings inhibit the steady assimilation of compaction-strain on the contact at subcritical stresses.

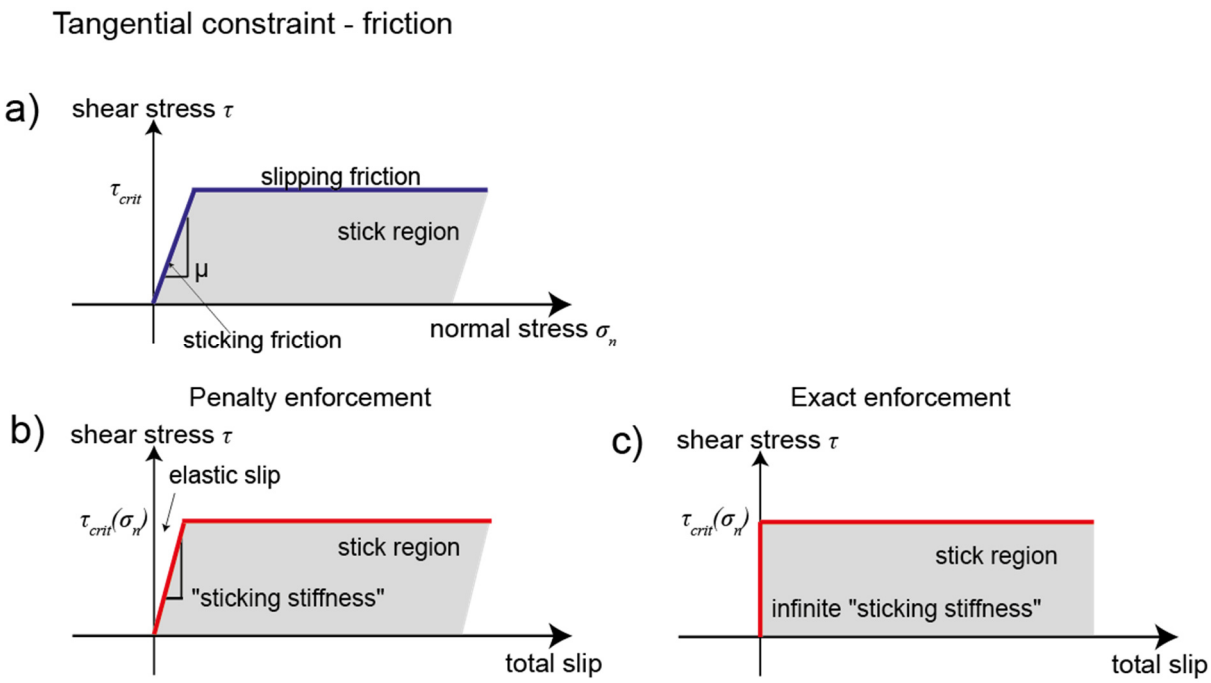

Fig. 5-20: a) Sticking friction is a function of shear and normal stress according to the Mohr-Coulomb model (section 2.8). b) Slip vs shear stress diagram for which the critical shear stress value is a linear function of normal stress. Slip occurs also for subcritical shear stress within the penalty enforcement method. c) Illustration of the exact enforcement of the tangential frictional constraint that that allows slip only at failure.

5.3.3 Mesh refinement

For various purposes, contact surfaces can be tied together, the tie option assigns displacements of the master nodes to that of the slave nodes. In general, the implementation of contact allows for abrupt changes in mesh resolution as elements on either side of the contact are not required to match in element size and node position (Fig. 5-21).

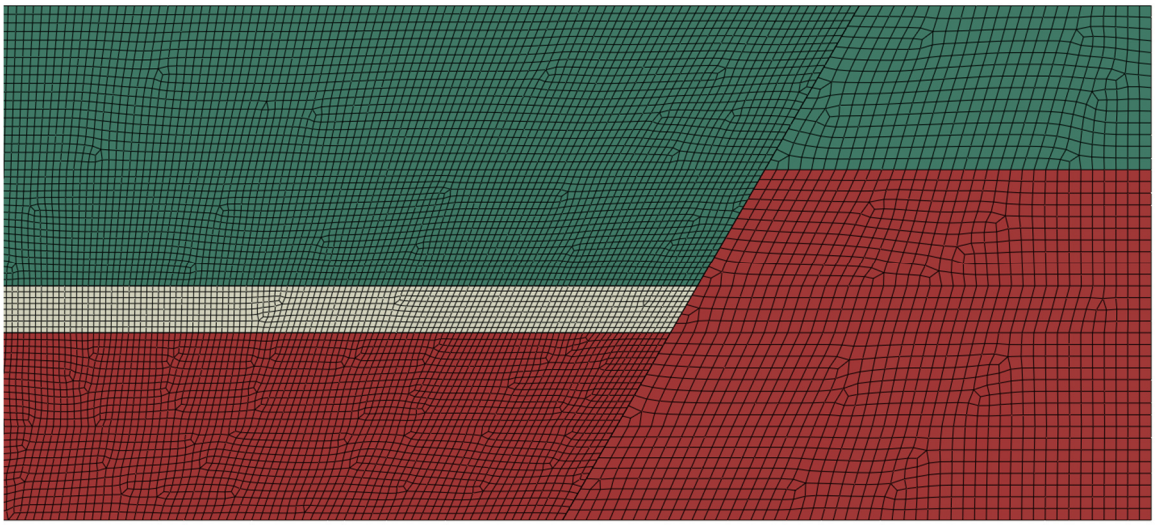

Fig. 5-21: Example of a graben fault represented by contact. The contact approach allows for a significantly lower mesh resolution of the graben shoulder (red colour) compared to the reservoir (white colour). The reservoir was initially expected to require a high mesh resolution encompassing the largest stress changes and fluid flow.

5.3.4 Stress rotations with penalty slip

Figure 5-22 shows fault-loading and slip due to pore pressure depletion of a homogeneous reservoir model. The frictional strength of the fault is defined by the common value μ_d*=0.6* (e.g. Zoback 2007) but for the default penalty stiffness, slip occurs at stresses below the frictional strength of the fault (Fig. 5-22 b). A detailed description of the fault-loading parameter SSR is provided in section 8.3.

An increased sticking stiffness guarantees that numerical slip does not occur below a critical stress *SSR=0.6* (Fig. 5-22 c) resulting in a more distinct loading of the fault. Figure 5-22 d) and e) show the rotation of the maximum principal stress with depletion. Reservoir depletion results in counterclockwise stress rotations above the lateral edge of the reservoir (Fig. 9-44) and assumes an antagonist role to numerical fault slip that aligns the maximum principal stress along the fault plane. Fig. 5-22 e) illustrates the stronger sub-critical stress rotations for the increased sticking stiffness.

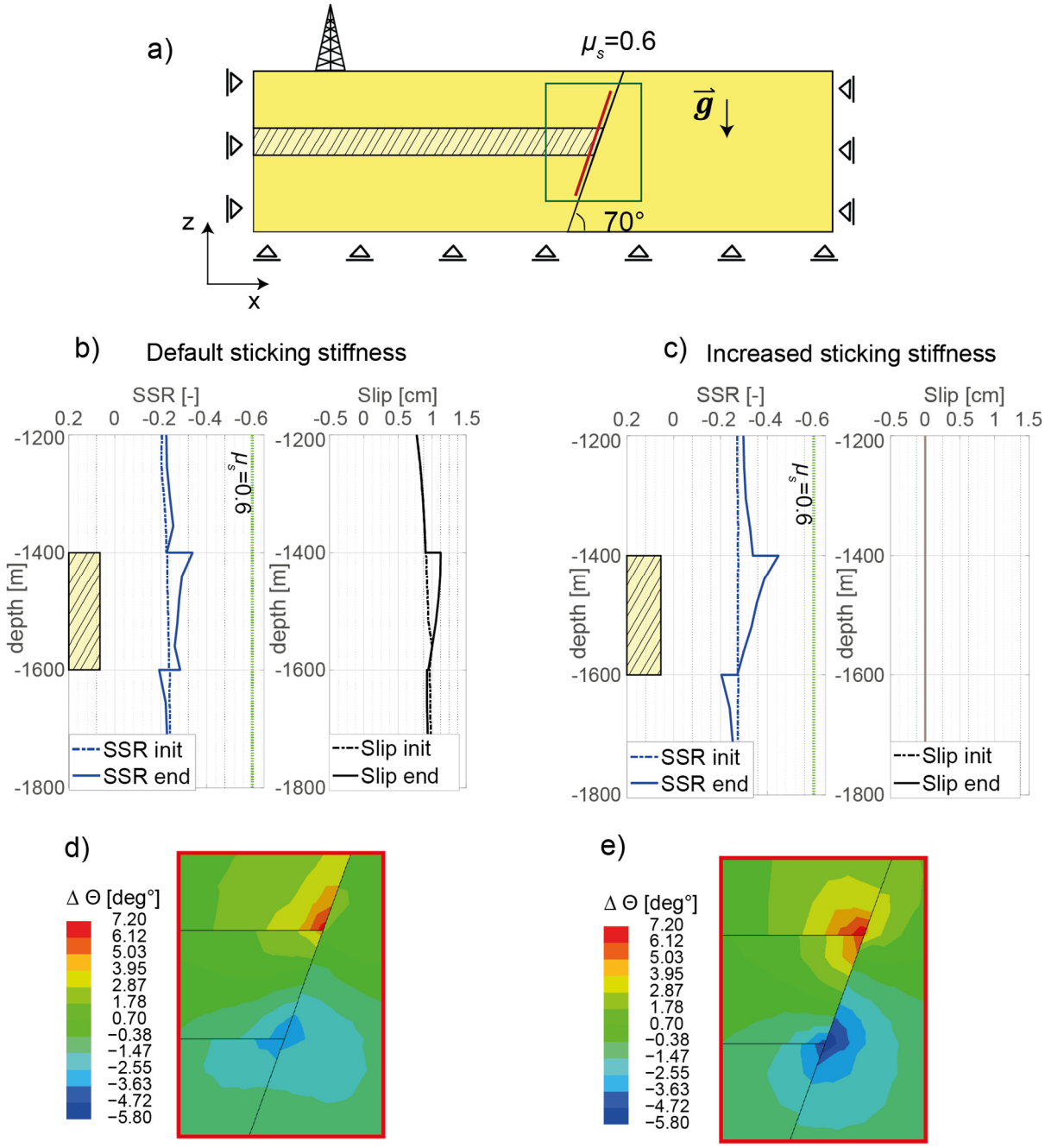

Fig. 5-22: a) Model geometry and boundary conditions of a homogeneous reservoir model, bounded by a graben fault of 70° dip that experiences a pore pressure decrease. b) Fault-loading and fault slip for the case that penalty slip is allowed. c) Fault-loading and fault slip for the modification of the sticking stiffness that impedes subcritical slip. Rotation of the maximum principal stress during the production step, influenced by numerical penalty slip d) and for the more accurate imposition of the frictional constraint e).

6 Applying Poroelasticity in ABAQUS

The ABAQUS fully coupled pore pressure-displacement analysis *soils* originally addresses the consolidation of loose rocks. In opposition to software packages specialized in reservoir geomechanics, ABAQUS does not provide a pre-established user guided interface for the modelling of rock deformation, pore pressure and stresses within deep reservoirs and the surrounding rocks.

The following chapter deals with the modelling of reservoir rocks that commonly have Biot-Willis coefficients smaller than unity. In simple words the chapter can be summarized as an answer to the statement: “If effective stress governs deformation, why do two different effective stress laws alternately implemented in ABAQUS produce identical strain?”.

6.1 Poroelastic material in ABAQUS

6.1.1 Biot-coefficient

In spite of the common application of ABAQUS in reservoir geomechanics, (e.g. Bostrom & Skomedal 2004, Capasso & Mantica 2006, Monaco et al. 2011, Rueda et al. 2014, Sanz et al. 2015, Zielonka et al. 2014) the Biot-coefficient α receives no mentioning in the ABAQUS documentation. This is surprising as the Biot-coefficient is a major poroelastic constant and weights the influence of pore pressure on the solid effective stress (Zoback 2007).

The ABAQUS Theory Guide introduces the effective stress formulation of Terzaghi (1936) that was originally constituted for soils of high bulk compressibility compared to the compressibility of their single grain constituents ($\alpha = 1$). However, well-consolidated reservoir sandstones, as encountered in North German gas fields, commonly have Biot-Willis coefficients <1 (e.g. 0.65-0.9, Zimmerman 1991, Wang 2000, Trautwein & Huenges 2005).

Derivation of the Biot-coefficient from existing material options uses the following statement in the *ABQ (2016) Theory guide* (2.8.3):

$$\frac{\rho_g}{\rho_g^0} \approx 1 + \frac{1}{K_g}\left(P_f + \frac{\bar{\sigma}}{1-n}\right) \qquad 6.1$$

ρ_g: density of solid phase ρ_g^0: density of solid phase in the reference state $\bar{\sigma}$: Mean pressure

Equation 6.1 describes the local mechanical response to a mean stress $\bar{\sigma}$, acting in the solid matter. K_g is a property of the solid grain material and is much stiffer than the bulk soil material (*ABQ 2016 Theory guide 2.8.3*). This description matches the micromechanical concept of the Biot-coefficient (cp.

section 3.3.2). The poroelastic parameter α can thus be prescribed by first deriving the drained bulk modulus from Young's modulus and Poisson's ratio

$$K_d = \frac{E_d}{3(1-2\nu)} \qquad 6.2$$

and then by computing the single grain compressibility $1/K_g$ according to the given Biot-coefficient:

$$1/K_g = \left(\frac{K_d}{1-\alpha}\right)^{-1}. \qquad 6.3$$

6.1.2 A full set of poroelastic constants for ABAQUS

For a complete description of poroelastic material, four independent constitutive parameters are required. Complete sets are represented for example by: {*G, K_u, α, M*} (Cheng 2016); {*B, G, ν, ν_u*} (Kümpel 1991); {*G, α, ν, ν_u*}, {*K_d, K_u, ν, ν_u*} (Detournay & Cheng 1993); where ν_u is the undrained Poisson's ratio.

The material parameters specified in ABAQUS are: Drained Young's modulus *E*, the drained Poisson's ratio *ν*, dry rock density ρ_{dry}, the Biot-coefficient α (section 6.1.1), hydraulic conductivity k_f, bulk modulus of the fluid $1/K_f$, and void ratio *e*.

Here the proposition of Cheng (2016) is used, stating the shear Modulus *G*, the undrained bulk modulus K_u, the Biot-coefficent α and the Biot modulus *M*. In order to derive the undrained bulk modulus from the ABAQUS set of drained soil mechanical parameters, Gassmann's equation is rearranged according to (Altmann et al. 2010[1], Cheng 2016, Fjaer 2008):

$$K_u = \frac{K_g + K_d\left(\phi\frac{K_g}{K_f} - \phi - 1\right)}{\left(1 - \phi - \frac{K_d}{K_g} + \phi\frac{K_g}{K_f}\right)} \qquad 6.4$$

then Skempton's coefficient *B* is computed according to (Eq. 3.74 Wang 2000):

$$B = -\frac{\left(\frac{K_d}{K_u} - 1\right)}{\alpha} \qquad 6.5$$

At last, the Biot Modulus is (Eq. 2.27 Wang 2000):

$$M = \frac{BK_u}{\alpha} \qquad 6.6$$

[1] the + sign is missing in Altmann's definition

6.2 Effective stress in ABAQUS

During the duration of this project, the effective stress output of ABAQUS underwent a change from Terzaghi to Biot-Willis effective stress in newer releases of the software. While at closer look, both effective stresses are physically valid including the case $\alpha<1$, inconvenience arose from the lack of total stress output and the lack of documentation. Moreover, it turned out at a later stage, that in agreement with experimental observations and the theory (cp. Section 3.4.2), failure and contact slip pertained to be governed by Terzaghi effective stress, resulting in a mismatch of displayed effective stress and background failure stress. Figure 6-23 illustrates the chronology of the issue that severely slowed down the progress of the project.

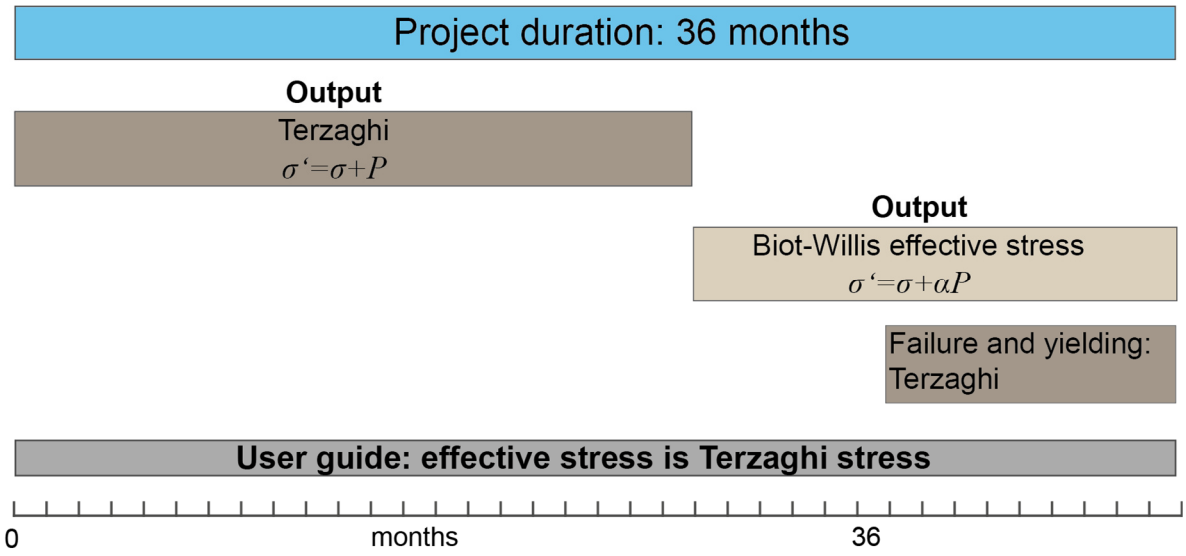

Fig. 6-23: Timeline of the project and available effective stress output. Biot-Willis effective stress was implemented in a recent ABAQUS version. In the ABAQUS user guide, the effective stress concept is currently stated inconsistently, as Terzaghi effective stress.

While at first glance it seems counterintuitive that two different effective stress concepts are associated to the same elastic strain, the consideration of total stress allows resolving this apparent contradiction as illustrated in the following of this section.

First the stress-strain relation for different load cases in terms of Terzaghi and Biot-Willis effective stress are applied on a single-element model in ABAQUS. Figure 6-24 shows the stress and strain response of a single poroelastic element to different loading conditions. The evaluated stress quantity of the single element along with its material definition is varied from left to right according to:

a) E=7.85 GPa, ν=0.17, drained conditions at 10 MPa pore pressure, α=0.7, Biot-Willis effective stress

b) E=7.85 GPa, ν=0.17, drained conditions at 10 MPa pore pressure, α=0.7, Terzaghi effective stress

c) *E*=7.85 GPa, *v*=0.17, dry material

First a displacement load is applied to determine the (effective) stress response of the three elements to an imposed strain. The results confirm that for the given loading condition, the Biot-Willis effective stress is identical to the solid stress of the dry model, Terzaghi effective stress is significantly smaller in magnitude.

As commonplace, effective stress is considered to 'cause' deformation as an 'internal' stress of the rock skeleton. Apart from initial stress conditions, there is however no direct loading condition, neither in numerical simulations nor in the laboratory to impose such an effective stress.

Only in the dry model the stress caused by the displacement load causes an identical strain if applied as a pressure load (Fig. 6-24 f). That is because in the drained models, the elevated pore pressure contributes to the overall resistance to loading (cp. section 3.4.1).

In turn, using total stress as a pressure load, all three elements show identical strains (Fig. 6-24 g-i). In conclusion, the commonly taught concept of (new) effective stress governing strain is misleading. Instead, the total stress and pore pressure govern the stress-strain relation of the drained case of poroelasticity.

Pore pressure depletion is in fact a case where effective stress constitutes the driving force for deformation. Thereby only new effective stress describes the strain-stress relationship correctly in terms of the drained elastic moduli. For Terzaghi effective stress applied in ABAQUS, a decomposition of strain applies that is further explained in section 6.4.4.

In reality, porosity, fluid compressibility and permeability influence the stress-strain response as a function of the loading condition, problem size, process time and drainage condition (cp. section 3.3.1). In the quasi-static one-way coupled approach of Figure 6-24 these variables are entirely represented by pore pressure. The effects of the mentioned parameters are exclusively reflected by the magnitude of the reactive fluid volume flowing into- or out of the model, given the constant pore pressure condition.

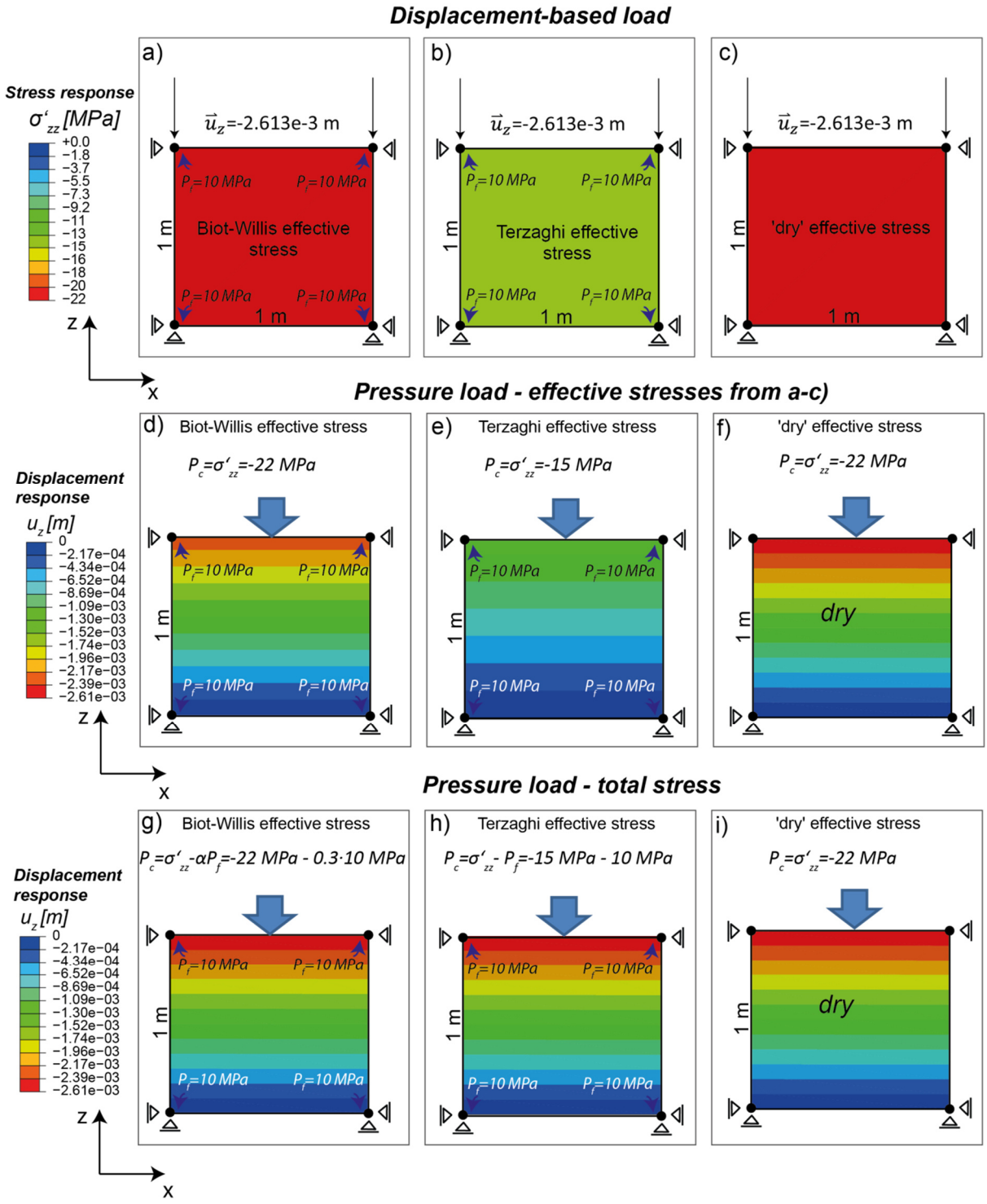

Fig. 6-24: a-c) Displacement based load on two identical poroelastic elements and a dry element, whereby the poroelastic model is evaluated in terms of Biot-Willis (a) and Terzaghi effective stress (b). The poroelastic elements are assigned a constant pore pressure boundary condition of 10 MPa in order to simulate drained boundary conditions. Using the computed effective stress as pressure load naturally results in three different displacement magnitudes (d-e). In spite of the identical 'effective' stress, this applies also between the Biot-Willis element and the dry element (e,f). After determining the total load from (a-c), the application of this total stress as a pressure load results in identical strain for all three models (g-i).

6.3 Validation issues for the Biot-coefficient and effective stress

In retrospect, the derivation and implementation of the Biot-coefficient is a straight-forward operation. Note however that only effective stresses and pore pressure are output in ABAQUS and the user has to determine whether αP_f or P_f are added to effective stresses in the computation of total stress.

The bottleneck in the implementation and validation of the Biot-coefficient was the lack of awareness of the coefficient's role as bulk poroelastic modulus (cp. section 3.3), the quasi-static nature of the transient procedure in ABAQUS and the link of the FE method to the total Cauchy-stress tensor instead of the effective stress tensor (cp. sections 5.1.2 and 6.5).

Moreover, the focusing on the coefficient's role in the effective stress law, that is stated as Terzaghi's law in ABAQUS, obscured the fact that the case α<1 does not render Terzahgi's law incorrect, but merely unable to directly reproduce the stress-strain relationship in terms of the drained moduli. In consequence, the poroelastic modulus α affects the total stress state and strain field whereby total stresses can be decomposed into pore pressure and Terzaghi or Biot-Willis effective stresses equally.

6.4 Terzaghi vs Biot-Willis stress – analytic comparison

6.4.1 Biot-Willis concept

As shown experimentally by Nur & Byerlee (1971) the stress-strain-relation for the drained case can be expressed by Biot-Willis effective stress and the dry elastic moduli. Biot & Willis originally provided the following formulation (Eq. 29, Biot & Willis 1957):

$$\sigma_{ij} = 2G\varepsilon_{ij} - \delta_{ij}\lambda\varepsilon_{kk} + \delta_{ij}\alpha P_f \qquad 6.7$$

where the term marked in yellow corresponds to Hooke's law of linear elasticity. Subtracting pore pressure from total stress of Equation 6.7 shows the compliance of Biot-Willis effective stress and the drained moduli:

$$\sigma'_{ij} = 2G\varepsilon_{ij} - \lambda\varepsilon_{kk} \qquad 6.8$$

However, in their publication, Biot-Willis 1957 (Eq. 42) state the 'effective stress' according to the formulation of Terzaghi (Eq. 3.1) and define it as the "superposition of pore pressure and a residual stress in the solid matrix". Inserting Terzaghi's effective stress (Eq. 3.1) into Equation 6.7 yields an

expression that connects the drained deformation to Terzaghi's effective stress (Eq. 43, Biot & Willis 1957):

$$\sigma'_{ij} - (1-\alpha)P_f = 2G\varepsilon_{ij} - \lambda\varepsilon_{kk} \qquad 6.9$$

6.4.2 ABAQUS Terzaghi-approach

The ABAQUS approach superposes strain from the applied loading of the solid skeleton, referred to as effective strain ε', and a strain component exerted by pore pressure on the single grains expressed by $P/3K_g$ (cp. Eq. 2.8.3-6 *ABQ 2016 Theory Guide 2.83*):

$$\boldsymbol{\varepsilon} = \boldsymbol{\varepsilon'} - \frac{\boldsymbol{P}}{\boldsymbol{3K_g}} \qquad 6.10$$

$\boldsymbol{\varepsilon}$: total strain [-]

Expressing the effective strain by means of the basic stress-strain relationship (e.g. Eq. 2.23), Equation 6.10 can be reformulated for instance in terms of the vertical principal strain component according to:

$$\varepsilon_{zz} = \frac{\sigma'_{zz\_Terz}}{E} - \nu\frac{\sigma'_{xx\_Terz}}{E} - \nu\frac{\sigma'_{yy\_Terz}}{E} - \frac{P}{3K_g} \qquad 6.11$$

Replacing effective stress by the superposition of total stress and pore pressure, Equation 6.11 becomes

$$\varepsilon_{zz} = \frac{\sigma_{zz}}{E} - \frac{\nu}{E}(\sigma_{xx} + \sigma_{yy}) + \left(\frac{1}{3K} - \frac{1}{3K_g}\right)P_f\,. \qquad 6.12$$

Using the transformation of the poroelastic moduli stated in Equation 3.2, renders the total vertical strain computed in ABAQUS identical to the constitutive equations of poroelasticity (e.g. Eq. 2.13, Wang 2000), for instance in vertical direction:

$$\varepsilon_{zz} = \frac{\sigma_{zz}}{E} - \frac{\nu}{E}(\sigma_{xx} + \sigma_{yy}) + \frac{1}{H}P_f \qquad 6.13$$

Using Biot-Willis effective stress, the pore pressure effect on the single constituents $P/3K_g$ is already accounted for in the effective stress definition yielding the following equation:

$$\varepsilon_{zz} = \frac{\sigma'_{zz\_Biot}}{E} - \nu\frac{\sigma'_{xx\_Biot}}{E} - \nu\frac{\sigma'_{yy\_Biot}}{E} \qquad 6.14$$

Replacing again effective stress by the superposition of total stress and pore pressure leads to equation 6.15

$$\varepsilon_{zz} = \frac{\sigma_{zz}}{E} - \frac{\nu}{E}\left(\sigma_{xx} + \sigma_{yy}\right) + \left(1 - \frac{K}{3K_g}\right)\frac{1}{3K}P_f \,. \qquad 6.15$$

In consequence, both effective stress concepts produce an identical total strain for the same confining pressure.

6.4.3 Horizontal effective stress

While for the gravity-based, vertical load, the two effective stress concepts result in two effective stresses whose magnitude differs simply by α, the derivation of horizontal effective Terzaghi stress is more complex.

In the direct solution of the uniaxial strain approach, vertical stress σ'_{zz} is predefined by the overburden load (Eq. 7.2) which is in a first order approach independent of the material's elastic properties. Expressing the vertical strain as a function of Terzaghi effective stress yields the following equation related to Young's modulus and Poisson's ratio:

$$\varepsilon_{zz} = \frac{\sigma'_{zz\_Terz}}{E} - \nu\frac{\sigma'_{xx\_Terz}}{E} - \nu\frac{\sigma'_{yy\_Terz}}{E} - \frac{P}{3K_g} \qquad 6.16$$

Horizontal stress $\sigma_{xx} = \sigma_{yy}$ can be determined by setting the lateral strain to zero $\varepsilon_{xx} = \varepsilon_{yy} = 0$.

$$\varepsilon_{xx} = \varepsilon_{yy} = \frac{\sigma'_{zz\_Terz}}{E} - \nu\frac{\sigma'_{xx\_Terz}}{E} - \nu\frac{\sigma'_{yy\_Terz}}{E} - \frac{P}{3K_g} = 0 \qquad 6.17$$

Solving for lateral effective stress yields:

$$\sigma'_{xx\_Terz} = \sigma'_{yy\_Terz} = \frac{\nu}{1-\nu}\sigma'_{zz\_Terz} + \frac{EP_f}{(1-\nu)3K_g} \qquad 6.18$$

The single grain modulus K_g decreases with a decreasing Biot-coefficient. The horizontal effective stress expressed by Terzaghi effective stress becomes thus comparatively small for the case *α<1*.

Biot-Willis effective stress on the other hand assumes a known expression (e.g. Eaton 1969)

$$\sigma'_{xx\_Biot} = \frac{\nu}{1-\nu}\sigma'_{zz\_Biot} \qquad 6.19$$

for the ratio of horizontal to vertical effective stress that depends on Poisson's ratio. The transformation of horizontal Terzaghi into Biot-Willis effective stress is stated in appendix B.

6.4.4 Effective stress and strain during depletion

Pore pressure reduction under a constant confining stress within a reservoir causes a transfer of the overburden load from pore pressure to the solid (Hettema et al. 1998 Hettema et al. 2000, Chan & Zoback 2002). As a consequence of the increased compressive effective stress, the reservoir deforms in vertical direction, reducing the thickness of the reservoir. This concept is congruent with the common perception of (Biot-Willis) effective stress causing deformation.

This direct stress-strain relationship does obviously not apply in ABAQUS, using Terzaghi effective stress as failure and original output quantity. Instead the identical strain for both effective stress laws arises from the concept of strain superposition. The two strain components, effective strain and 'single grain' strain have opposite signs. That means a pore pressure reduction allows the internal structure or single grains to expand whereby the strain of the grains is governed by reducing the pore pressure load on the stiffness element K_g. Effective strain on the other hand is governed by the compressive stress in the solid rock skeleton, expressed in terms of Terzaghi effective stress and acting on the stiffness component K_d. It is obvious that the two strains are opposite in their effect on volumetric deformation, whereby the relative influence is weighted by the Biot-coefficient ($\alpha = 1 - \frac{K_d}{K_g}$). Because effective strain and the internal 'single grain' strain are functions of two different stiffnesses, the pore pressure change produces also for Terzaghi effective stress a change in total strain while the total stress remains in fact constant. In conclusion, Terzaghi effective stress 'causes' an identical strain as Biot-Willis effective stress during depletion.

6.5 Benchmark Rudnicki's solutions

In order to benchmark poroelastic material and stress changes in ABAQUS, results of Rudnicki's (1986) full space solution were compared to ABAQUS results. Rudnicki's analytic model states the pore pressure changes as a function of time and distance to the well according to (Eq. 25 Rudnicki 1986)

$$\Delta P(x,t) = \frac{q}{\rho_0 c}\frac{1}{4\pi r}\left[\frac{(\lambda_u - \lambda)(\lambda + 2G)}{\alpha^2(\lambda_u + 2G)}\right]\operatorname{erfc}\left(\frac{1}{2}\beta\right) \qquad 6.20$$

where c denotes the hydraulic diffusivity (Eq. 12 Rudnicki 1986)

$$c = \frac{\kappa(\lambda_u - \lambda)(\lambda + 2G)}{\alpha^2(\lambda_u + 2G)}. \qquad 6.92$$

The change in total stress as a function of time and distance to the sink or source is (Eq. 26 Rudnicki 1986)

$$\Delta\sigma_{ij}(x,t) = \frac{q}{\rho_0 c}\frac{(\lambda_u-\lambda)G}{4\pi r\alpha(\lambda+2G)}\left\{\delta_{ij}\left[\operatorname{erfc}\left(\frac{1}{2}\beta\right)-2\beta^{-2}g(\beta)\right]\right.$$
$$\left.+\left(\frac{x_i x_j}{r^2}\right)\left[\operatorname{erfc}\left(\frac{1}{2}\beta\right)+6\beta^{-2}g(\beta)\right]\right\} \qquad 6.21$$

using the sub-functions (Eq. 19 Rudnicki 1986)

$$g(\beta) = \operatorname{erf}\left(\frac{1}{2}\beta\right)-\pi^{-\frac{1}{2}}\beta\exp\left(-\frac{1}{4}\beta^2\right) \qquad 6.22$$

and

$$\beta = \frac{r}{\sqrt{ct}}. \qquad 6.23$$

In order to transform variables used by Rudnicki into ABAQUS variables, the equations of section 6.1.2 are completed by the undrained first Lamé parameter and the undrained Poisson's ratio. The undrained second lame's constant is derived by (Eq. 4.24 Wang 2000)

$$\lambda_u = \frac{2G\nu_u}{(1-2\nu_u)} \qquad 6.24$$

where ν_u is the undrained Poisson's ratio according to (Eq. 3.34 Wang 2000)

$$\nu_u = \frac{3\nu+\alpha B(1-2\nu)}{3-\alpha B(1-2\nu)}. \qquad 6.25$$

Hydraulic and rock mechanical properties expressed in Rudnick's notation are listed in Table 2.

Tab. 2: Input parameters for the benchmark of ABAQUS vs Rudnicki's (1986) solution. The mobility coefficient used in Rudnicki's model is derived from an intrinsic permeability of 10 mD.

Variable	**Magnitude**
Fluid density ρ_f [kg/m^3]	243
Pumping rate q [m^3/s]	0.005
Undrained 1st Lamé parameter λ_u [GPa]	2.32
Drained 1st Lame parameter λ [GPa]	1.72
Drained 2nd Lamé parameter G [GPa]	3.33
Drained bulk modulus K_d [GPa]	3.94
Bulk modulus of solid grains K_g [GPa]	13.13
Mobility coefficient κ *[m/s]*	$3.4\cdot10^{-10}$
Production time *t [days]*	164
Bulk modulus gas K_f [GPa]	0.12

In 3D, looking along the x-axis of the spherical full space, the radial component corresponds to $\Delta\sigma_{rad} = \Delta\sigma_{11}$ and the tangential components constitute $\Delta\sigma_{tan} = \Delta\sigma_{22} = \Delta\sigma_{33}$.

Figure 6-25 illustrates the match of the analytic Rudnicki (1986) solution with stresses and pore pressures computed in ABAQUS. The variation of the Biot-coefficient in both the numerical simulation as well as in Rudnicki's solution confirmed the influence of the Biot-coefficient on volumetric strain and effective stresses in ABAQUS. As Rudnicki's solution refers however to total stresses, it does not have implications on the correctness of the implemented effective stress law. In fact the results are only consistent for old ABAQUS releases as in newer releases, the user is confronted with a documentation of Terzaghi's law and numerical results issued as Biot-Willis effective stress, rendering total stresses a mismatch.

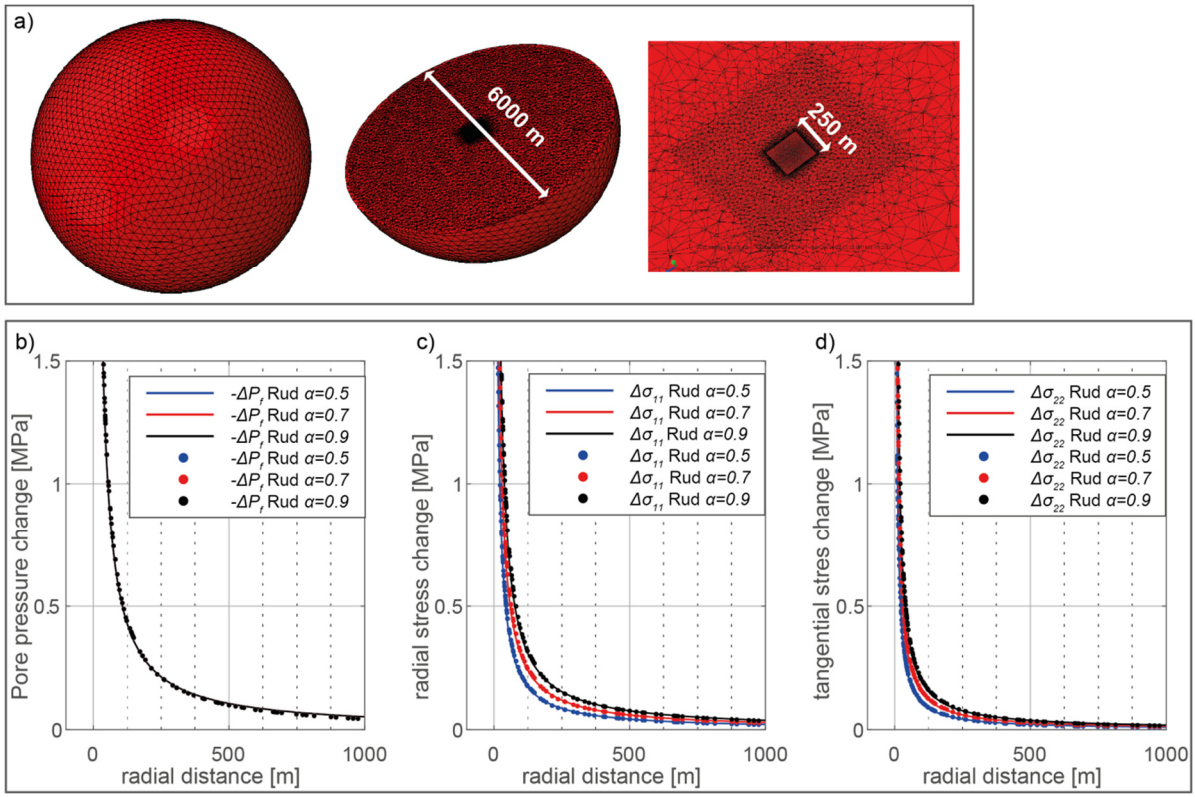

Fig. 6-25: a) Model geometry and discretization for the benchmark of the FE vs the analytic Rudnicki (1986) solution. b) Analytic vs numerical results of the pore pressure change for different Biot-coefficients. c) Analytic vs numerical results for the total radial stress change d) Analytic vs numerical results for the total tangential stress change.

7 Preliminary studies and general workflow

Previous sections dealt with analytic solutions and the retrieval of expected stresses and stress changes in the FE-software ABAQUS. This section presents preliminary studies for the case-specific numerical models, providing insight into relevant parameters of the modelling approach. The numerical models are based on typical properties of North German gas fields but have strong generic character with respect to geometry, material properties, pore pressure field and the lack of stress data. The data-limited modelling thereby reveals a strong variability of results for different model properties that have to be implemented into the numerical model, based on general assumptions. In the following, appropriate numerical approaches for the pre-production stress state, the fault and the pore pressure field are investigated. At last the pre- and post-processing workflow and the used software applications are presented and potential enhancements for a more efficient workflow are discussed.

7.1 Initial stress state

As a preliminary step to the transient simulation of pore pressure changes, the establishment of an initial stress state serves for the equilibration of the model with respect to the applied loading by gravitational and tectonic forces. Given the virtual absence of tectonic seismic events and based on the extensional stress state below the Zechstein salt, as implied by Cornet & Röckel (2012), the pre-production stress state is assumed to comprise non-critically stressed faults in a normal faulting stress regime.

7.1.1 Theoretical approach for horizontal stress at depth

The general procedure in geomechanical reservoir modelling, in science as well as industry is the derivation of a total overburden load, and the subsequent assignment of horizontal stresses in agreement either with available stress data (e.g. Hudson et al. 2003) or with frictional constraints of the given stress regime (Sibson 1974). In a normal faulting stress regime, the frictional equilibrium on potential faults is ensured as long as the following identity applies (Eq. 4.43 Zoback 2007):

$$K' = \frac{\sigma_h{}'}{\sigma_V{}'} > \left[(\mu_s{}^2 + 1)^{\frac{1}{2}} + \mu_s \right]^{-2} \qquad 7.1$$

The concept bases on Terzaghi effective (Zoback 2007) stress and requires a ratio *K'<0.32* to guarantee the stability of an optimally oriented fault of frictional strength μ_s*=0.6.*

Zoback (2007) reviews different approaches for estimating horizontal stress in sedimentary basins. Two of the approaches are validated for the application in this study:

1. Uniaxial strain – the horizontal stress is a function of Poisson ratio
2. Frictional equilibrium –the horizontal stress fulfils condition 7.1 for an assumed frictional strength μ_s=*0.6*

The vertical, overburden load is computed from depth integration of the dry rock density (Tab. 3) plus the density of the fluid fraction within the pore space (*ABQ 2016 Analysis guide 6.8.2*):

$$\sigma_V(z) = \int_z^{z_0} [\rho_{dry}(z)g + \phi\rho_{fl}(z)g]\, dz \qquad 7.2$$

ϕ: porosity [-] ρ_{dry}: dry density [kg/m^3] ρ_{fl}: fluid density [kg/m^3] g: Gravitational acceleration [m/s^2]

This overburden load, corresponding to the total vertical stress is partly counteracted by the pore pressure within the interconnected pore space. The vertical effective stress is thus given by

$$\sigma'_V(z) = \int_z^{z_0} [\rho_{dry}(z)g + \phi\rho_{fl}(z)g]\, dz - [\![\alpha]\!]\rho_{fl}gz \qquad 7.3$$

where $[\![\alpha]\!]$ applies for the computation of Biot-Willis effective stress.

According to the project partner, an overpressure condition prevails within the reservoir and below the reservoir. At the top of the reservoir, the abnormal pore pressure magnitude is 64.5 MPa.

In order to consider the overpressure below a depth of z_{ovp}= -4800 m in the computation of vertical effective stress, Equations 7.2 and 7.3 were extended to

$$\sigma'_{V_{ovp}}(z) = \left[\sigma_V(z_{ovp}) + \int_{z_{ovp2}}^{z_{ovp1}} [\rho_{dry}(z)g + \phi\rho_{fl}g]\, dz\right] + [\![\alpha]\!]P_{fovp} - [\![\alpha]\!]\rho_{fl}g(z - z_{ovp}). \qquad 7.4$$

Figure 7-26 shows the computed stress-depth profiles of the uniaxial strain approach using equations 7.3, 7.4 for the vertical and 6.18, 6.19 for the horizontal stress, given the material properties stated in (Tab. 1, section 8.2.2). The results are plotted in terms of both, Terzaghi and Biot-Willis effective stress. Given the large pore pressure and the low Poisson's ratio, effective stress becomes very small (Fig. 7-26). The Terzaghi formulation even produces tensile horizontal effective stresses (cp. section 6.4.3).

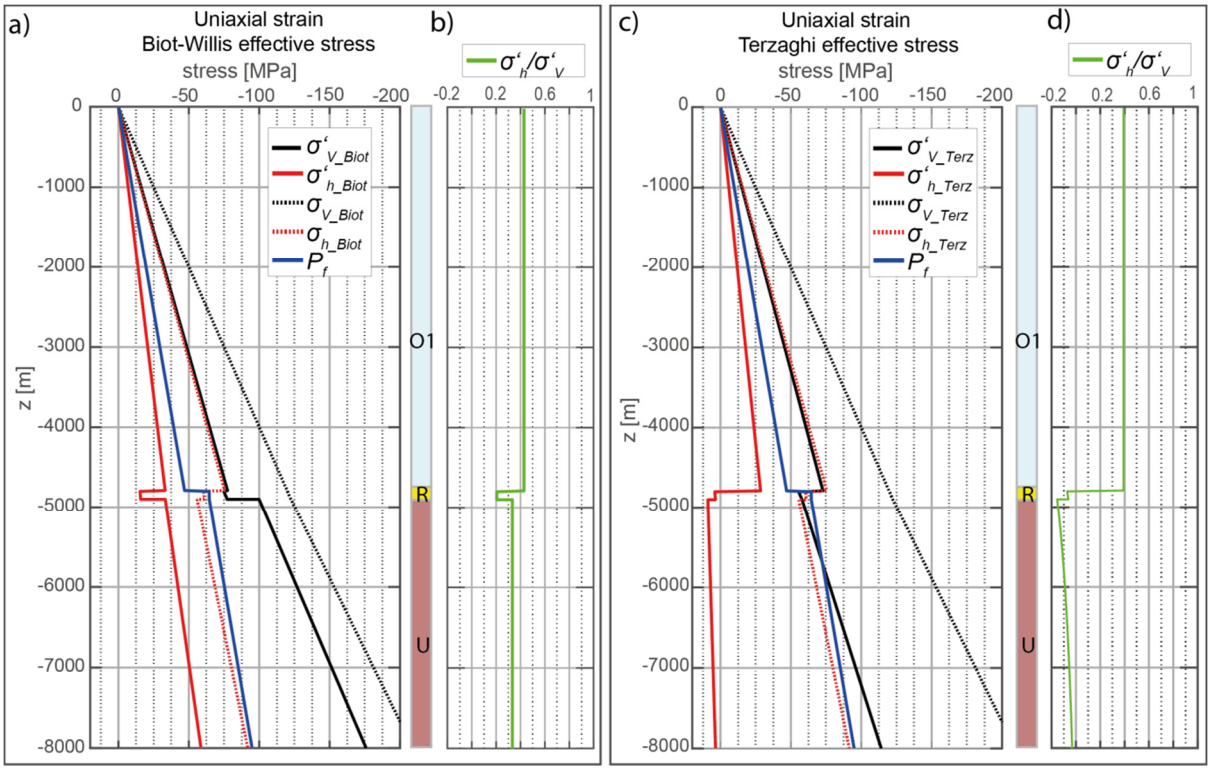

Fig. 7-26: a) Computed theoretical stress – depth profile of the uniaxial strain approach, using Biot-Willis effective stress. b) Ratio of Biot-Willis effective horizontal to vertical stress. c) Computed theoretical stress – depth profile of the uniaxial strain approach, using Terzgahi effective stress. d) Ratio of Terzaghi effective horizontal to vertical stress.

In the second approach a fixed ratio *K'*=0.32 that ensures fictional equilibrium according to Equation 7.1 is imposed. The resulting stress profiles are illustrated in Figure 7-27. Unstable conditions arise below the reservoir, as pore pressure is larger than the minimum principal stress (Fig. 7-27 a). Given the overpressure condition, the concept of frictional equilibrium fails and *K'* must be chosen large as 0.42 in order to ensure the minimum total horizontal stress to exceed the pore pressure magnitude.

As illustrated in this section, common prediction methods for the horizontal stress fail to provide a consistent initial stress state for the overpressured section of the northern German Rotliegend gas fields. Breckels & van Ekelen 1981 proposed an empirical, depth-dependent relation for horizontal stresses, based on a data compilation from the Gulf of Mexico. Their equations predict an increase of minimum horizontal stress and its approximation to the magnitude of the vertical stress component within the overpressured sections. Results of the Breckels & van Ekelen (1981) model, using material properties of Table 3 are shown in Appendix C (Fig. 13-60). Given the issues in stress initialization for material properties α<1 (section 7.1.2), this approach was not further pursued.

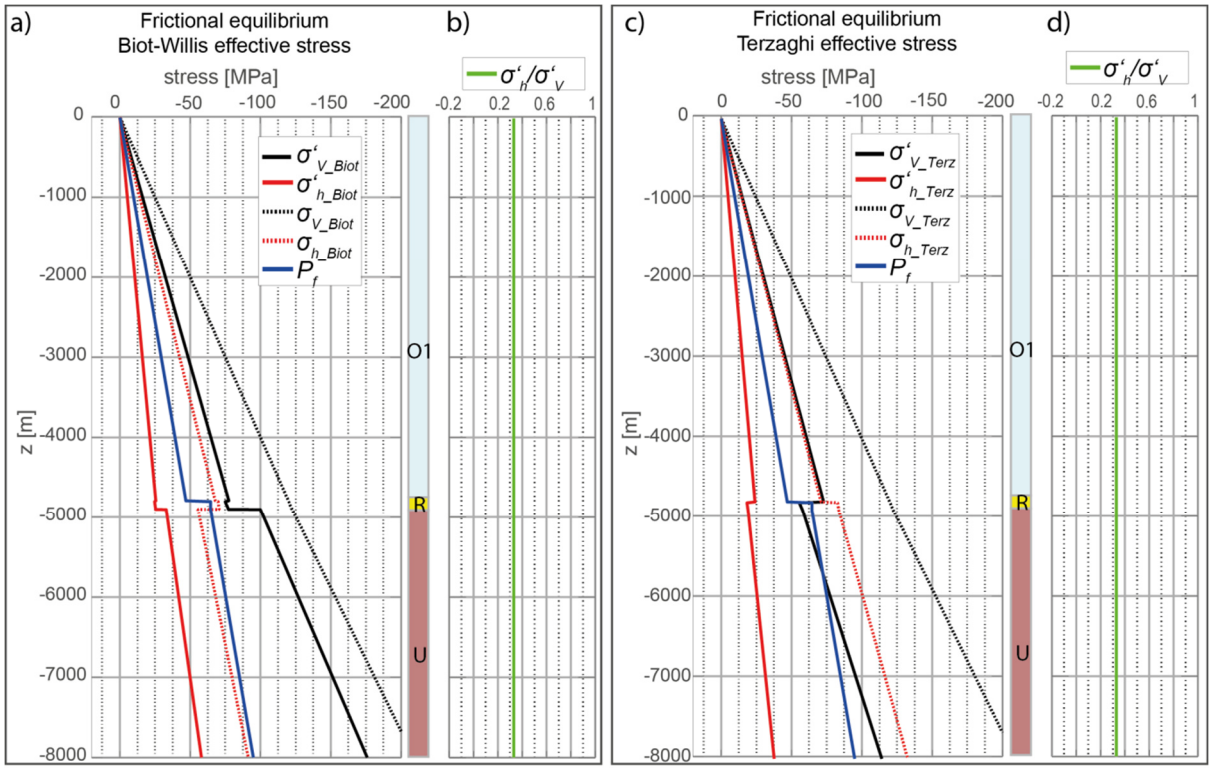

Fig. 7-27: a) Computed theoretical stress – depth profile for the frictional equilibrium approach, using Biot-Willis effective stress. b) Ratio of Biot-Willis effective horizontal to vertical stress. c) Computed theoretical stress – depth profile for the frictional equilibrium approach, using Terzgahi effective stress. d) Ratio of Terzaghi effective horizontal to vertical stress.

7.1.2 Iterative procedure to initialize stress

In order to impose a user-specified initial stress state that provides equilibrium with respect to the applied loads, an iterative procedure can be applied in ABAQUS that accepts initial stress conditions as triplets of depth, vertical effective stress and stress ratio *K'*. Equilibrium in vertical direction is given by Eq. 7.4. For an overpressured, non-homogeneous model, the correct stress state on stiffness contrasts is difficult to estimate in advance, moreover, it must be reconciled with a homogeneous ratio *K'* all over the model. In this case the iterative procedure gradually deforms the model in order to impose the prescribed stresses within a user defined deformation tolerance. While the iterative procedure originally aims at the limitation of deformation during the prestressing of geotechnical structures, such as dams or tunnels, here, the iterative procedure poses an option to establish a consistent, non-critical stress ratio *K'*, serving as a common initial stress state for different parameter variations.

The major issue with respect to the iterative procedure is the ambiguity in effective stress for $\alpha<1$. Stress input can be either Biot-Willis or Terzaghi effective stress, whereby the first is justified with

respect to the stress-strain relationship, the second needs to be considered for stability of the deterministic fault. Stress output can be either Biot-Willis or Terzaghi effective stress, depending on the applied ABAQUS version. Herein, the aim is simply the accurate enforcement of a consistent stable initial stress state.

In order to assess the procedure's accuracy, the model deformation and the *SSR* value (section 8.3) on the fault are assessed. The ratio $K' = \frac{\sigma'_3}{\sigma'_1} = \frac{\sigma'_h}{\sigma'_V} = 0.5$ can be rearranged to a target *SSR*-value of 0.346 using equations 2.17 and 2.18. Aiming at the enforcement of accurate stress rather than constrain the model deformation, the displacement tolerance was set to an arbitrarily large value. Table 5 and Table 6 in the Appendix A summarize the benchmarking results of the iterative procedure for the consideration of models of increasing complexity that come with increasing issues in terms of stiffness contrasts, varying Biot-Willis coefficients and overpressure.

For a Biot-coefficient of 1 and hydrostatic pore pressure, the enhanced iterative procedure returns accurate stresses, accompanied by negligible deformations. Considering Biot-Willis coefficients inferior to 1, prescription of Biot-Willis effective stress returns smaller deformations compared to the specification of Terzaghi effective stress. Moreover, the combination of Biot-Willis input and output yields the best approximation of the prescribed stress conditions.

Figure 7-28 shows the pre-production stress state on the fault after applying the enhanced iterative procedure to the reference model described in section 9.1.1. In- and output of Biot-Willis effective stress yields a satisfactory reproduction of the target value *SSR* = 0.346 (Fig. 7-28 b). Terzaghi effective stress on the other hand fails to reproduce the aspired values in any approach.
Major issues arise in the combination of the iterative procedure with faults represented by contact (section 7.2). First, fault slip is governed by Terzaghi effective stress and second, the iterative procedure enhances slip during the considerable deformation of the model, necessary to impose the prescribed stresses.
Because of the issue of Terzaghi effective stress being output until late 2016 and the critical initial stress observed for Biot-Willis effective stress below the reservoir (Fig. 7-28 d), stress initialization by means of the enhanced iterative procedure was prematurely discarded.

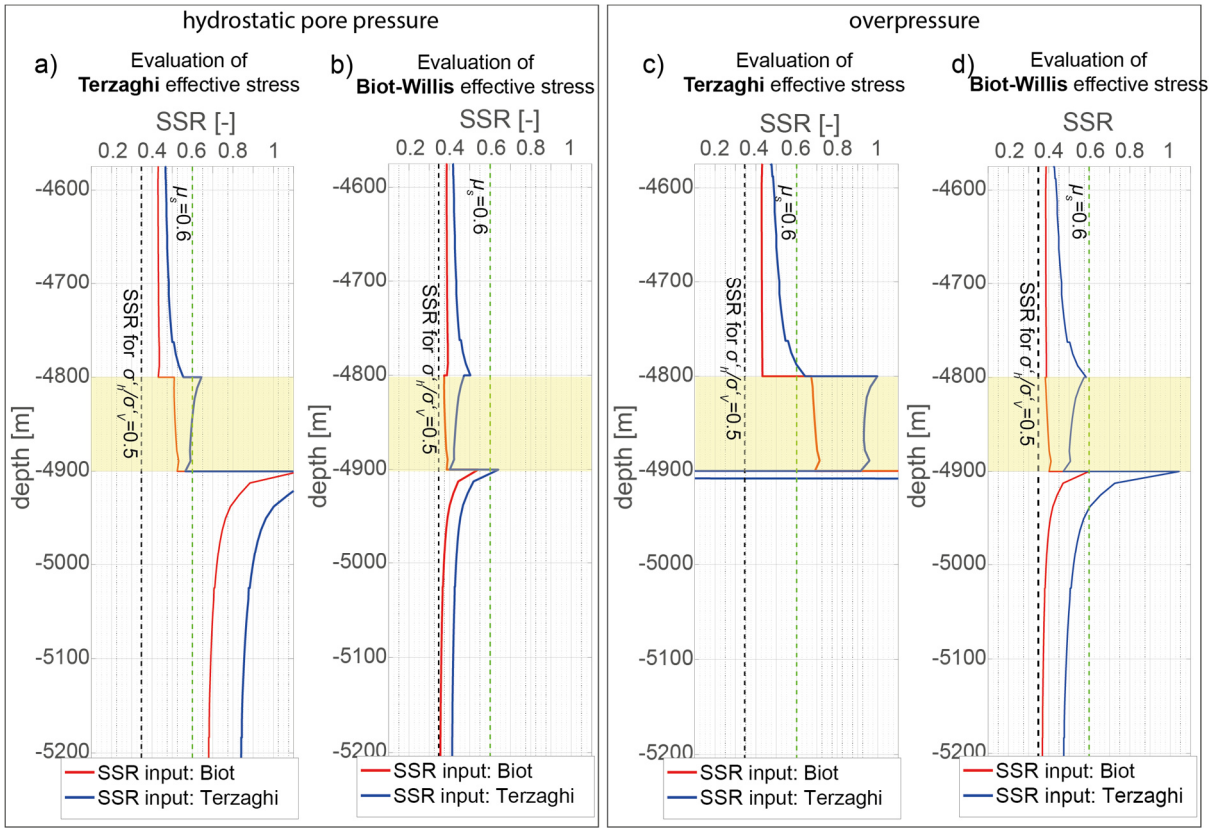

Fig. 7-28: Results of the enhanced iterative procedure expressed in terms of the *SSR* value on the reservoir-bounding fault of the reference model (section 8.2.2). The targeted value *SSR* = 0.346 indicates the accurate establishment of the prescribed stresses. a),b) Hydrostatic pore pressure condition and evaluation of: a) Terzaghi effective stress output and b) Biot-Willis effective stress output. c),d) Overpressured reservoir and underburden and evaluation of: c) Terzaghi effective stress output and d) Biot-Willis effective stress output.

7.1.3 Gravity and Displacement-based initial stress

Earthquakes have long been known to occur as slip on pre-existing planes of weakness (e.g. Townend & Zoback 2000). In consequence, the focus shifted to implementing a stable stress state on the deterministic model fault rather than attempting to impose a model-wide generic stress ratio. In order to increase the horizontal stress component with respect to the purely gravity-related uniaxial stresses (cp. Fig. 7-26), a constant horizontal confinement was applied to the lateral model boundaries (Fig. 7-29 a). For a unique lateral displacement magnitude, horizontal stress naturally increases as a function of depth and Poisson's ratio due to the increasing overburden load with increasing depth.

A displacement magnitude of 3 m yielded a stable initial stress state in terms of Biot-Willis effective stress on the fault of the reference model (Fig. 7-29 a,b), assuming a frictional fault strength of $\mu_s = 0.6$. As a reference displacement, this lateral confinement was applied to all model variations of model series I and II (sections 8.2.2, 8.2.4)

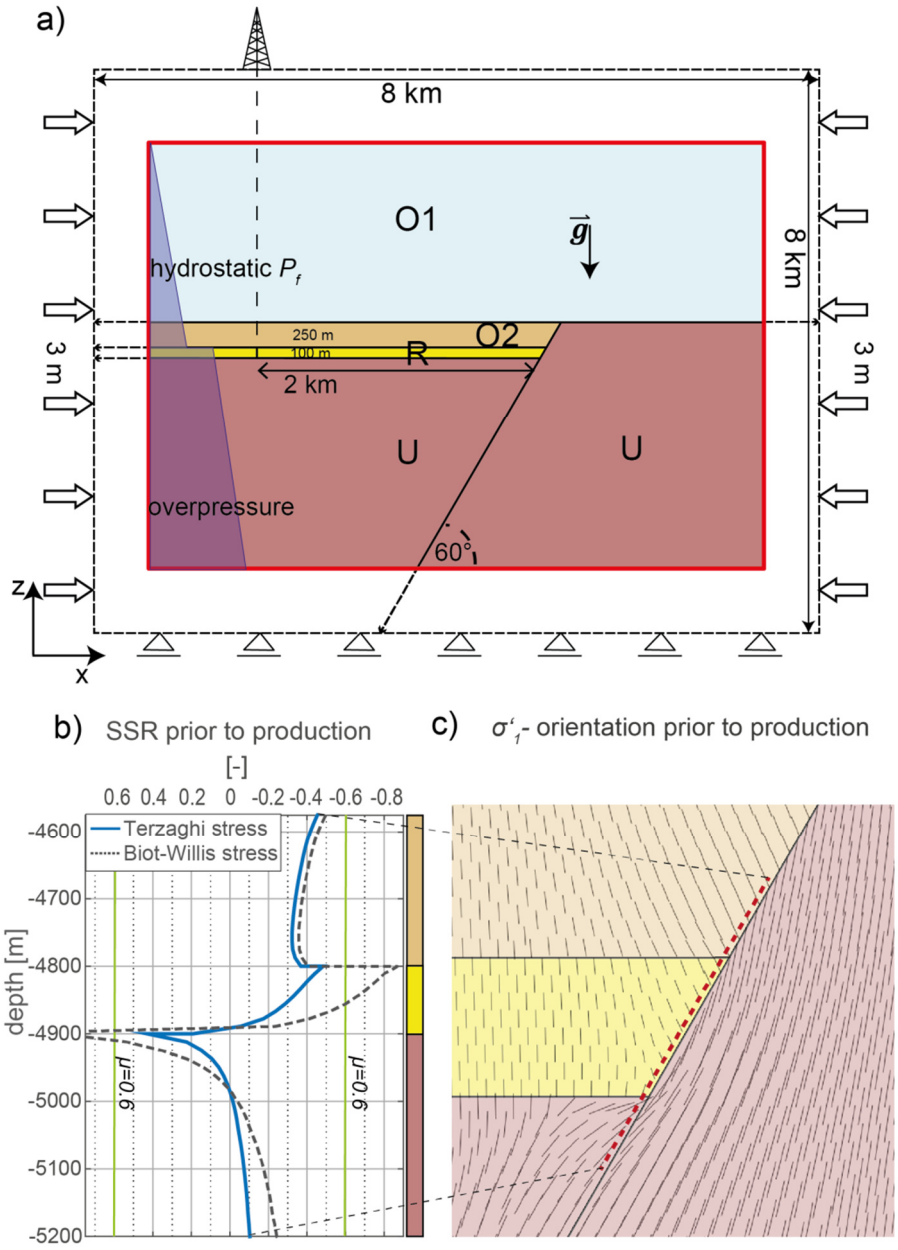

Fig. 7-29: a) schematic sketch of the reference model and its displacement boundary conditions. The model is introduced in detail in section 8.2.2. b) *SSR* value to evaluate the loading on the fault for both, Terzaghi and Biot-Willis effective stress. c) Pre-production orientation of the maximum principal stress that is commonly considered to be vertical.

Evaluating Terzaghi effective stress for the same total stress tensor, the fault domain at the upper reservoir boundary becomes critically stressed (Fig. 7-29 b). Additional lateral confinement would reduce the criticality in the upper reservoir fault-section but also enhances the already severe tendency towards reverse faulting below the lower reservoir boundary (Fig. 7-29 b).

Fig. 7-29 c) shows observed rotations of the first principal stress during the gravity and displacement based pre-stressing. As commonplace in geosciences, one principal stress within the earth's crust is assumed to be vertical, accounting for the shear-free surface of the earth (Zang & Stephansson 2010).

At depth, deviations of the principal stress orientation from the vertical direction are reported for example from the vicinity of salt domes (Dusseault et al. 2004, Koupriantchik et al. 2005, Luo et al. 2017). The stress state derived from gravity and displacement based loading within this study implies that strong stress rotations may also occur on the Permian graben topography, whose upper part consists widely of stiff volcanic rock (Fig. 7-29 c) facing a soft sedimentary graben filling and cover.

7.2 Implementation and impact of the reservoir-bounding fault

Due to the internal complexity of fault zones (e.g. Faulkner et al. 2010, Shipton et al. 2006) and poorly constrained subsurface hydromechanical fault properties (e.g. van Hulten 2010, Guglielmi et al. 2008, Manzocchi et al. 2008, Ter Heege & Bruin 2013, van Hulten 2010), the representation of faults in numerical geomechanical models is a major challenge (e.g. Cappa & Rutqvist 2011). This section deals primarily with the build-up of stress on discontinuities during pore pressure depletion. Thereby, compartmentalizing faults of northern German Rotliegend gas fields are assumed to have sealing properties (Mauthe 2003, pers. comm. DEA). That is, inflow from other compartments or sideburden does not mitigate the depletion magnitude and associated stress changes that arise from the bottomhole pore pressure decrease within single compartments.

7.2.1 Contact fault and contact permeability

In order to account for the assimilation of brittle compaction-strain, contact is a promising way to represent faults in the numerical model (e.g. Hergert et al. 2015, Reiter & Heidbach 2014). It represents an actual discontinuity in the mesh and allows therefore for the simulation of frictional constraints and relative displacements of the contact surfaces.

The methodology introduces however some constraints into the fully coupled simulation if the contact permeability is assumed very low. That is, a pore pressure gradient builds up across an interface of zero-thickness:

- In approach I the contact permeability in ABAQUS was varied arbitrarily between $K_i = 1E\text{-}7$ and $K_i = 0$, resulting in a slight lateral expansion of the reservoir (Fig. 7-30 a) that contradicts Segall & Fitzgerald's (1998) model of depletion-induced reservoir contraction (cp. Fig. 4-17). As this study addresses impermeable faults, the contact permeability of $K_i = 0$ within approach I, is in following sections referred to as *impermeable fault*.
- In approach II, fluid flow into and within the contact were constrained to zero. This sealing fault produces a stress and strain field that is in qualitative agreement with predictions of Segall & Fitzgerald (1998) (cp. Fig. 4-17). Approach II uses the same minimum contact

permeability as approach I ($K_i = 0$), but due to the impeded leak-off it shows a different mechanical behaviour. This fault is in following sections referred to as *sealing fault*

The observed strain fields can be explained as follows. In static equilibrium, prior to production, effective and total stress are both continuous across a contact fault of arbitrary permeability. With decreasing fault permeability and a different pore pressure evolution on either side of the fault, the pore pressure gradient across the zero-thickness contact interface increases. At the same time effective stresses within the depleting reservoir become more compressive while under drained conditions, the undepleted fault-juxtaposed sideburden undergoes total stress changes at constant pore pressure. In consequence, either effective normal or total normal stress across the impermeable fault can be continuous.

Approach I introduces the local condition of continuity in effective normal stress. Approach II maintains continuity in total normal stress. The latter is in agreement with theoretical considerations (e.g. Segall & Fitzgerald 1998) and the FE continuum approach. Approach I and II invoke two distinct production-induced stress states (Fig. 7-30) on the fault.

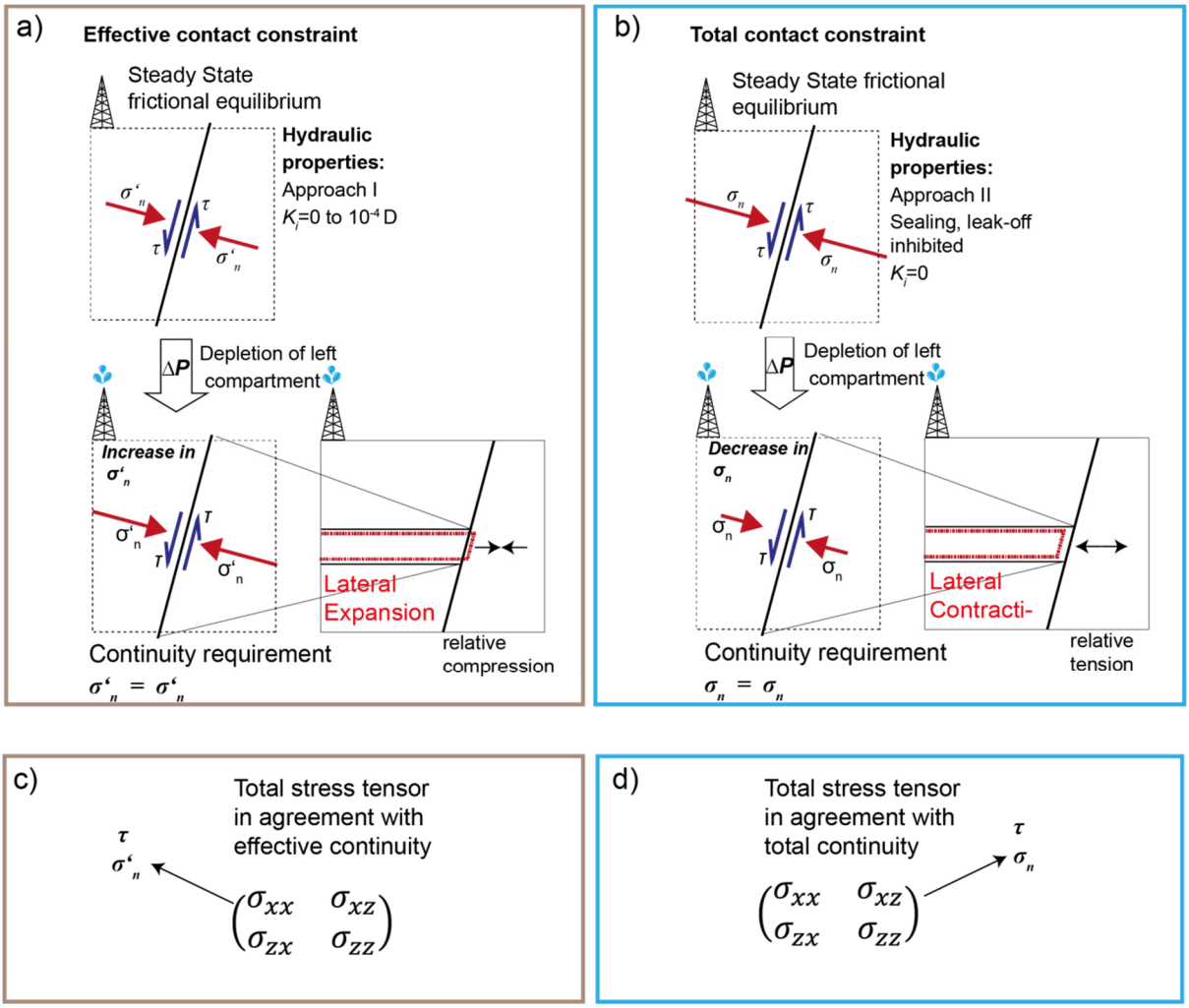

Fig. 7-30: a-b) Different permeability definitions to simulate an impermeable contact fault. In the fully coupled procedure two different continuity conditions arise from the hydraulic behaviour of the contact fault. Out of the two resulting strain fields, variant b) is more plausible with respect to analytic and tectonic considerations. c,d) The two different continuity conditions and corresponding strain fields result in different stress states on the fault further illustrated in section 7.3.

7.2.2 fault vs contact fault

The previous section has introduced two stress continuity conditions, associated to two approaches for the permeability definition of the contact fault. The continuity condition of stress arises from the requirement of a balanced normal stress on either side of the contact discontinuity. In this section, the stress and pore pressure field across a 30 m wide fault zone are investigated for different permeability values and compared to the stress and pore pressure field across contact faults. Material properties of the model are homogeneous and the fault is chosen vertical so σ_{xx} corresponds to the normal stress along the profile (Fig. 7-31)

For large fault permeabilities, total and effective stresses are continuous and recharge from the sideburden mitigates pore pressure depletion within the reservoir (Fig. 7-31 b, i). With decreasing permeability a gradient in both, pore pressure and stress builds up across the volumetric fault (Fig. 7-31 c) and total normal stress is roughly balanced on either side of the fault. An even lower fault permeability results in numerical oscillations (Fig. 7-31 d,e)

Using a contact representation and permeability approach I, low fault permeabilities result in a significantly different stress pattern compared to the volumetric representation (Fig. 7-31 c). As depletion causes effective reservoir stresses to become more compressive, the horizontal effective stress in the sideburden is forced to also become more compressive in order to maintain continuity in normal effective stress.

Approach II (Fig. 7-31 l) renders the contact fault sealing and the effective normal stress on either side of the sealing fault is decoupled. The stress pattern corresponds to the large-scale pattern of the impermeable volumetric fault.

In this investigation, the sideburden is attributed a constant hydrostatic pore pressure condition as combinations of low permeable sideburden and decreasing fault permeability caused numerical oscillations within the sideburden. In general, the simulation of impermeable fault properties in the fully coupled simulator is circumstantial and future studies should aim on using a pore pressure field from an external flow simulation, corresponding to a one-way coupled approach (section 5.2).

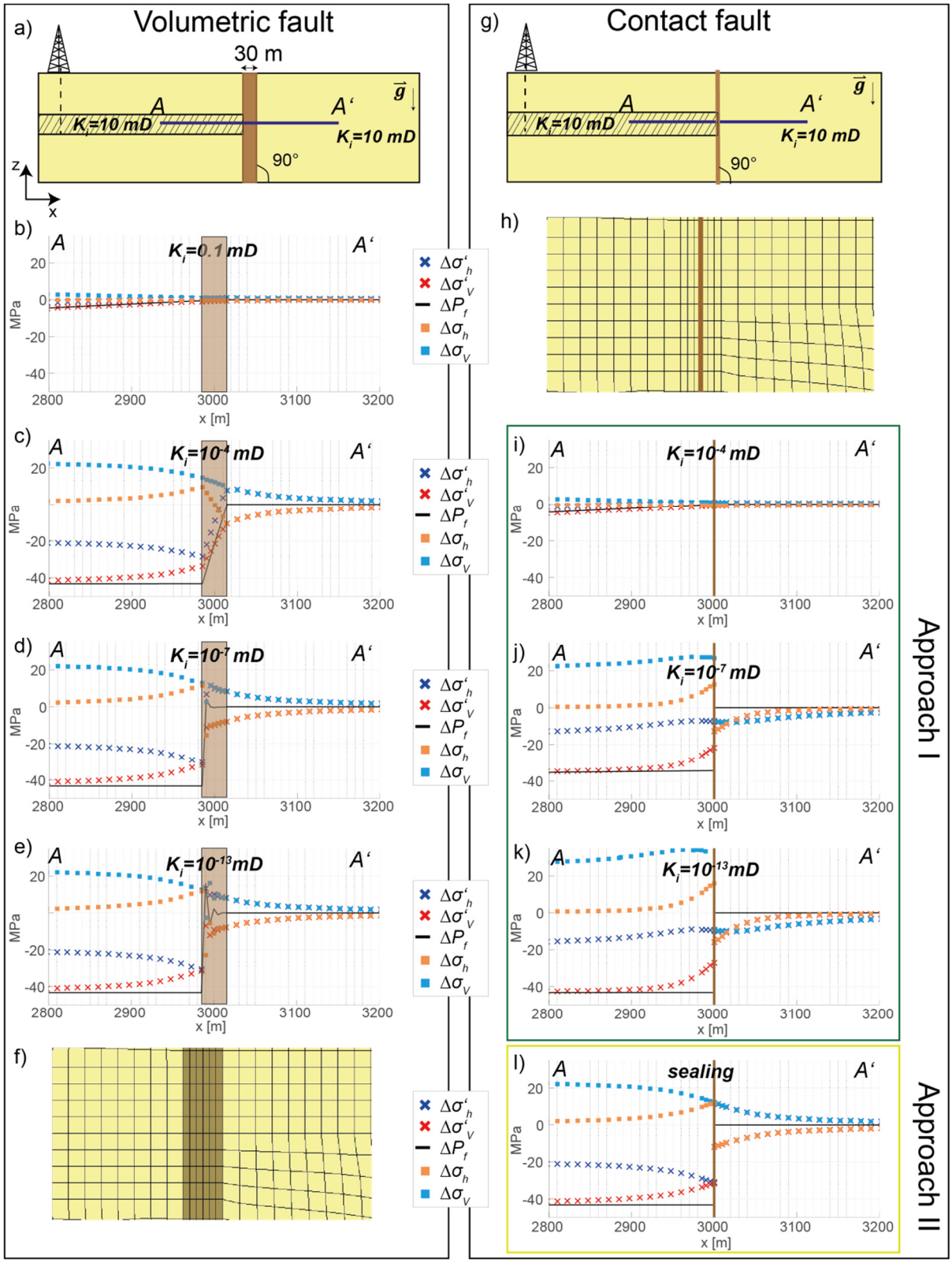

Fig. 7-31: a-f) Representation of the fault as a 30 m wide, finely meshed volumetric zone. Variation of the permeability of the fault produces strong gradients within the fault zone. For a permeability of K_i=1E-7 (c) the stress and pore pressure field are continuous and yet inflow is sufficiently impeded in order to yield full depletion of the reservoir. For unrealistically low permeabilities, numerical oscillations occur within the fault zone. g-l) Representation of the fault by contact. Using Approach I (section 7.2.1) produces continuous effective normal stresses and a significantly different overall stress pattern (i-k). Implementing permeability according to

approach II (I) results in continuous total normal stresses, a decoupling of effective normal stresses and a similar large-scale stress pattern as for the impermeable volumetric approach (c).

7.2.3 Contact fault and reactivation

In the course of this study, a mismatch between ABAQUS contact variables and effective stress at adjacent integration points was observed. The contact variables σ'_n, τ provided by ABAQUS govern sticking and slipping as a function of the frictional strength of the contact. According to the ABAQUS documentation, failure is evaluated in terms of effective stress if elements on both sides of the contact have pore pressure degrees of freedom. This was however proven incorrect in the simulations. Figure 7-32 a,b) shows the model setup for the verification of surface output variables and the shear and normal stress governing reactivation of the contact fault. The two approaches are tested for an identical lateral confinement and a coefficient of static friction $\mu_s = 0.4$.

- In Approach I effective normal stress determines the stability of the fault (Fig. 7-32 c,d) and this is Terzaghi effective stress. In consequence, the fault starts slipping prior to production due to the critical initial stress state (cp. section 7.1) and the low friction coefficient.
- In approach II, total normal stress determines the stability of the fault (Fig. 7-32 e,f). ABAQUS switches to a total stress definition as the gradient across the zero-thickness sealing fault becomes infinitely large.

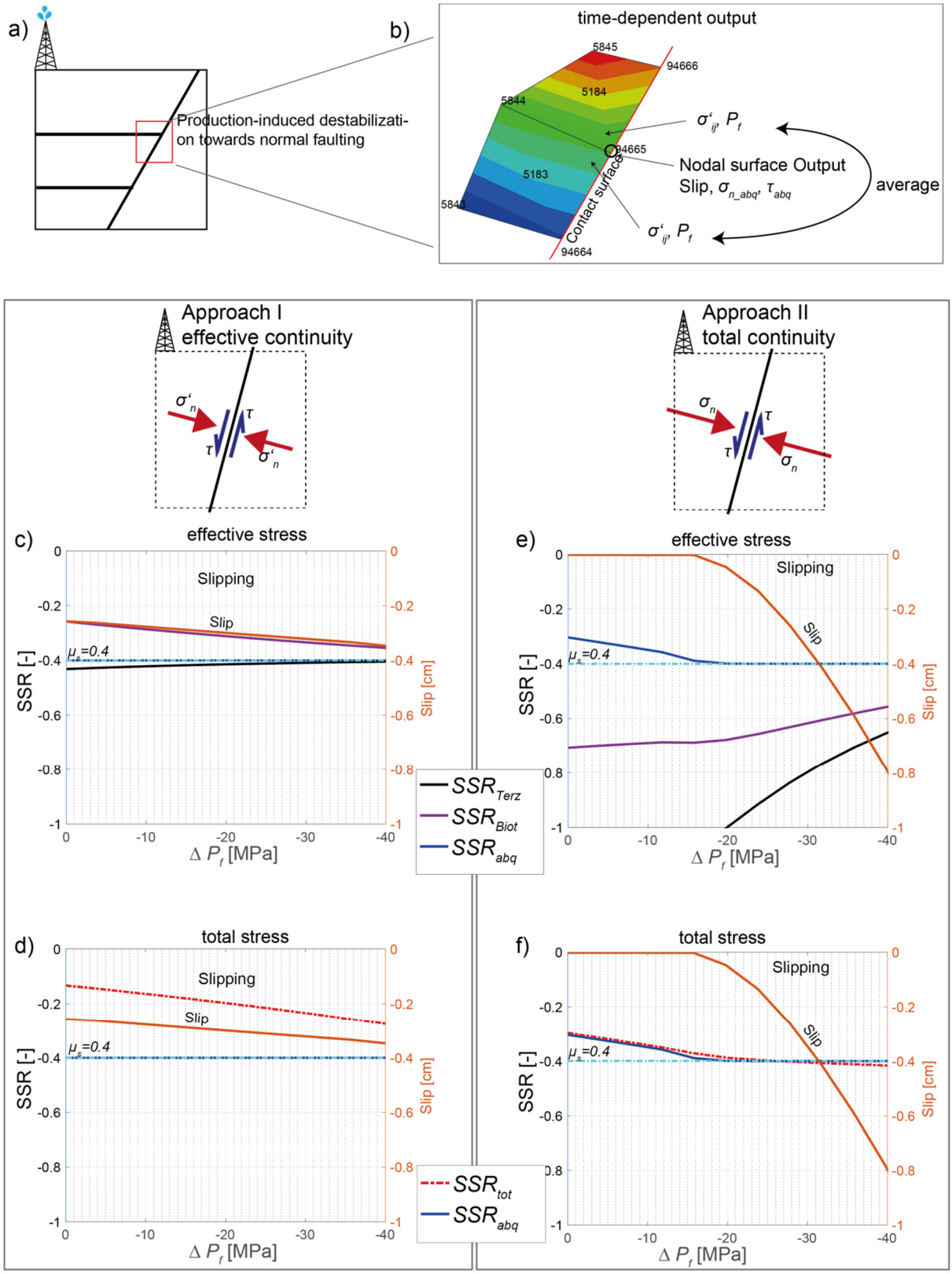

Fig. 7-32: a),b) Model approach for the verification of contact variables in the fully coupled simulation. c),d) Steady nodal slip on the contact fault, across which the effective normal stress is continuous. ABAQUS evaluates Terzaghi effective stress in this case. e),f) For continuity in total stress, invoked by permeability approach II, fault reactivation occurs in terms of total stress and slip initiates after approximately 16 MPa pore pressure depletion. Note that further stress build-up is limited by the strength of the fault and continuing ideal-plastic slip requires

further depletion-induced loading. The fault-loading parameter *SSR* is introduced in section 8.3. Subscripts in this figure. refer to the consideration of Terzaghi effective, Biot-Willis effective or total normal stresses and pre-defined ABAQUS surface output quantities.

7.3 Comparison of production-induced stress build-up on contact faults

Two basic continuity conditions arise in the modelling of impermeable contact faults that are accompanied by different total stress states. Moreover, the continuity condition invokes reactivation either in terms of total or Terzaghi effective stress. In the following, fault-loading for both continuity conditions is expressed in terms of the three stress concepts, Biot-Willis, Terzaghi and total stress, and their implications on fault loading are comparatively evaluated along a fault-parallel profile (Fig. 7-33 a,b). In order to avoid stress perturbations from slip, the contact fault is locked in this investigation.

Shear stresses on the fault depend on the total stress state and show hence a different pattern for the two continuity conditions. For continuity in effective stress, the pore pressure decrease causes an increase in shear stress along the reservoir fault section (Fig. 7-33 c). For continuity in total stress, the shear stress increases at the upper reservoir boundary and decreases at the lower reservoir boundary (Fig. 7-33 h). It is important to note that shear stresses are identical for total stress, Terzaghi effective and Biot-Willis effective stress.

The continuity condition in effective normal stress across the fault (Fig. 7-33 b) is associated to the following loading tendencies, normal effective Terzaghi stress increases along the reservoir fault with production (Fig. 7-33 d), Biot-Willis effective normal stress decreases slightly and the total normal stress decreases significantly. In consequence, Terzaghi effective stress implies a stabilization of the fault section along the reservoir (Fig. 7-33 e). The same stress state evaluated in terms of total and Biot-Willis effective stress implies a destabilization of the reservoir fault section.

In the case of continuity in total normal stress (Fig. 7-33 g), both, Terzaghi and Biot-Willis effective normal stresses increase with production. Total normal stress on the other hand decreases on the reservoir fault section and increases above the reservoir Fig. 7-33 i). In combination with the shear stress change, both effective stress concepts stabilize the reservoir fault section but destabilize the overburden fault section (Fig. 7-33 j). Evaluating the the total load on the fault reveals changes towards criticality on the upper reservoir section and above the reservoir (Fig. 7-33 j).

In summary, this section illustrates that the incorporation of contact faults within the fully coupled procedure produces significantly different model results for different assumptions on the permeability of the fault and the inevitable occurrence of two different effective stress laws, one for failure, one

for deformation (cp. sections 3.4.1, 3.4.2, 10.2). Note that detailed loading tendencies differ in models of non-homogeneous material properties (e.g. Fig. 9-44 c)

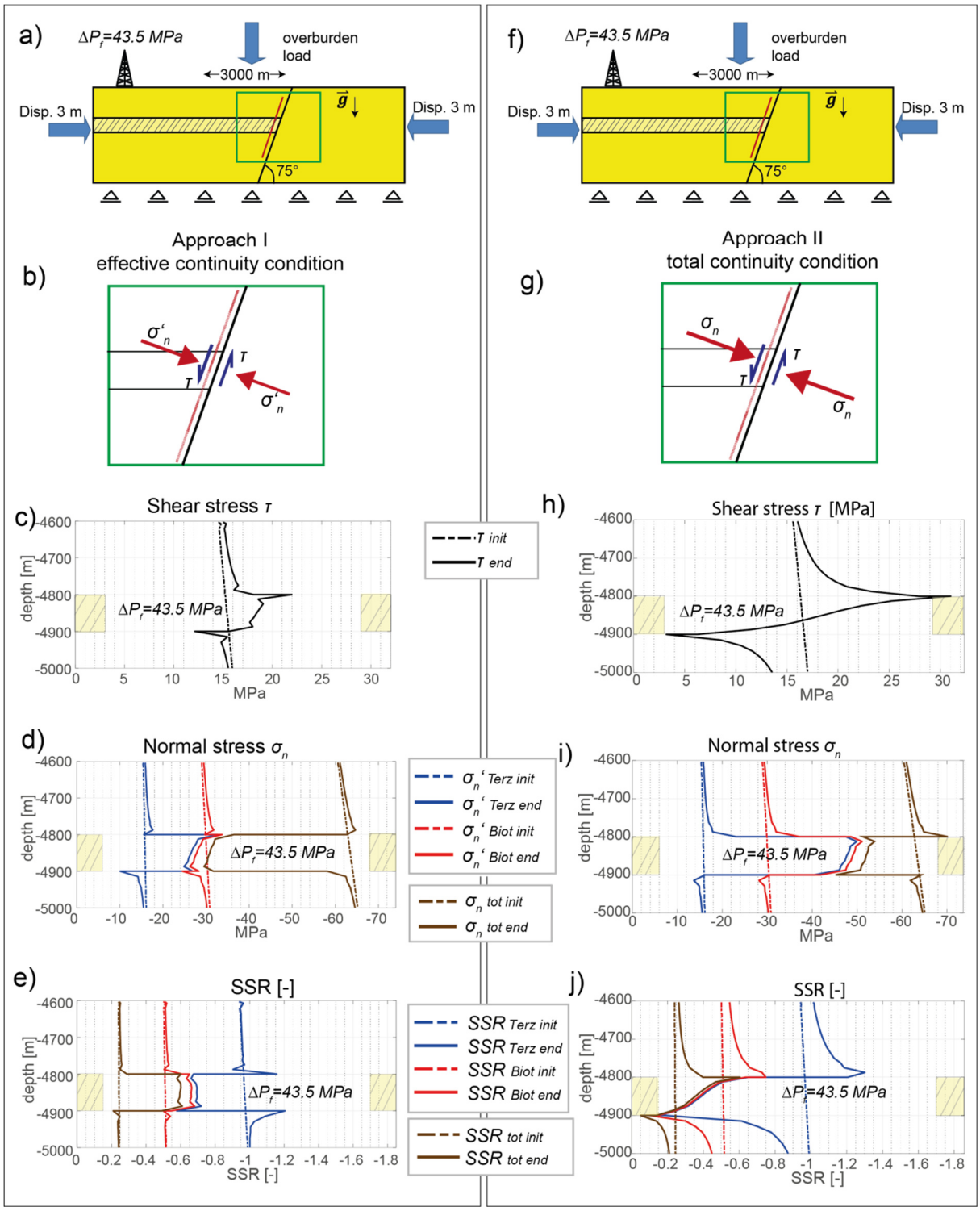

Fig. 7-33: a),b) Illustration of the modelling setup and the effective continuity condition. c) With production, shear stress increases along the reservoir fault section. d) Normal stresses show a different evolution for the evaluation of either Terzaghi, Biot-Wills effective and total stress (i). As shear stress is identical for all stress concepts, differences in fault-loading arise from normal stresses. f),g) Sketch of the modelling setup and the total continuity condition. f) Reservoir depletion leads to an increase in shear stress at the reservoir's top

boundary and decreases at the reservoir's bottom boundary. h) Normal stresses increase in terms of effective and decrease in terms of total stress. j) Production-induced loading occurs above the reservoir and within the reservoir in terms of Biot-Willis and and total stress. The dashed lines in this Figure represent initial stresses on the fault and the solid lines the loading of the fault after 43.5 MPa pore pressure depletion. Note that the apparent convergence of Biot-Willis and Terzaghi effective stresses derives from the comparably large pore pressure decrease with respect to the hydrostatic initial pore pressure.

7.4 Hydraulic model properties

The pore pressure field determines the change of the stress and the strain field in time. In this section, the implementation of a simplified pore pressure field and the modelling of depletion, based on a bottomhole pressure magnitude are explained. Detailed information on recharge and the rise of the gas-water contact, which would produce a more complex pore pressure field, were not available and these effects were indicated to be negligible by the project partner.

7.4.1 Flow in the Reservoir

Fluid flow in this study is simulated according to Darcy's law and comprises a single fluid phase of natural gas within the reservoir. Isothermal compressibility of the gas is computed using the z-factor according to Trube (1957) (Eq. 11):

$$c_g = \frac{1}{p} - \frac{1}{Z}\left(\frac{dZ}{dP}\right) \qquad 7.5$$

c_g: Isothermal gas compressibility [1/Pa] *P*: gas pressure [Pa] *Z*: compressibility factor for the deviatoric behaviour of real gases with respect to ideal gases [-]

Based on a pressure dependent *Z*-factor, provided by the project partner, isothermal gas compressibility within the reservoir is $c_g = 8.4 \ \ [\frac{1}{GPa}]$.

For the simulation of a bottomhole pore pressure decrease by 43.5 MPa over 22 years in all models (section 8.2.1), a ramped pore pressure boundary condition is applied. With respect to the fully coupled simulation, this means that the volumetric flow rate is deduced from pore pressure. Imposing on the other hand a production rate would have meant that the pore pressure is the deduced quantity. Because pore pressure is the mechanically effective variable and bottomhole pore pressure data was available, the flow within in the reservoir is based on the ramped bottomhole magnitude. This results on the other hand in a volumetric outflow from the model that can be predicted by Equation 7.6 (e.g. Segall & Lu 2015):

$$\Delta m = \alpha \rho_0 \left[\varepsilon_{kk} + \frac{\alpha P_f}{(\lambda_u - \lambda)} \right] \quad 7.6$$

Equation 7.6 implies that the fluid mass loss of the model depends among others on mechanical properties of the reservoir such as Lamé's first constant and the Biot-coefficient. Changes of mass are nevertheless negligible because the effect of fluid mass is entirely covered by the constant pore pressure load outside and the changing pore pressure load inside the reservoir.

7.4.2 Local pore pressure field

The initial pore pressure field, comprising the onset of overpressure of 64.5 MPa at 4800 m depth was computed as follows:

$$P_{fOVP\_R} = 64.5MPa - (z_{RT} - z)\rho_{gas} g \quad 7.7$$

$$P_{fOVP\_U} = P_{fOVP\_R} - (z_{RB} - z)\rho_{water} g \quad 7.8$$

P_{fOVP_R}: Overpressure reservoir P_{fOVP_U}: Overpressure underburden z: depth

z_{RT}: depth of reservoir top z_{RB}: depth of reservoir bottom.

The overpressure is a non-equilibrium condition that tends to dissipate during steady state prestressing. Consequently all nodes needed to be constrained by a pore pressure boundary condition during prestressing (Fig. 7-34 b), allowing for in- and outflow on the constrained nodes, but inhibiting dissipation of pore pressure along intra-model gradients.

Given the lack of input data, two general approaches for the constraining of the pore pressure field are conceivable:

1. Let ABAQUS compute the pore pressure field, based on a given bottomhole pressure, permeability distribution and hydrostatic pore pressure conditions on the model boundaries.
2. Constrain the pore pressure field manually.

With regard to the first approach, a model based on two pieces of information, bottomhole pore pressure and a low permeability of the reservoir surroundings constitutes an underdetermined flow model. Specific values for the caprock permeability were not provided and its variation yielded partial caprock depletion for K_{icap} = 0.1 mD (Fig. 7-34 c) and numerical oscillations for lower permeabilites, such as K_{icap} = 1E-4 mD (Fig. 7-34 d).

In the second approach, non-reservoir nodes are attributed a constant pore pressure condition and fully coupled flow is only modelled within the reservoir. However, the reservoir shares common nodes

with caprock and underburden and a pressure drop below ambient pore pressure leads to inflow into the reservoir, impeding the attainment of the prescribed depletion magnitude (Fig. 7-34 e). Releasing the constant pore pressure condition from the shared nodes, reveals an interpolation issue between integration point stresses and nodal pore pressure values. On lithological boundaries, the shared pore pressure degree of freedom enters the Biot-Willis effective stress computation at the integration points. A pore pressure value is thus weighted by α_{Ovbrdn} in the lowest integration point of the overburden whereby the uppermost integration point of the reservoir weights the identical pore pressure by the coefficient α_{Res} (Fig. 7-34 f).

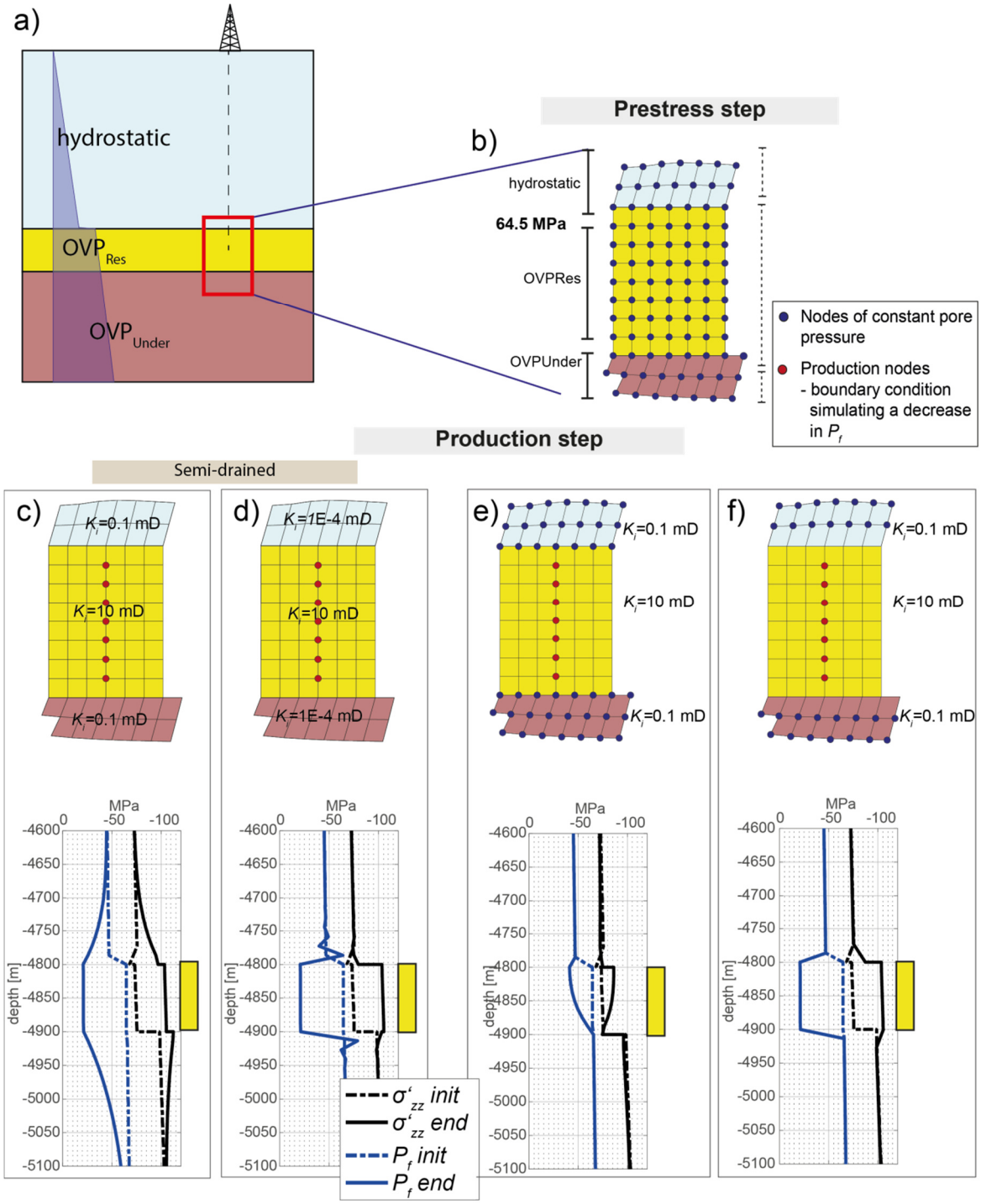

Fig. 7-34: a) Schematic sketch illustrating the vertical pore pressure profile. b) Detailed view of the reservoir section showing the assignment of pore pressure boundary conditions for hydrostatic and overpressure conditions during prestressing. Due to the continuum approach, differently pressurized formations share common nodes. c-e) Alternative approaches for the assignment of pore pressure boundary conditions during production. Red nodes indicate production nodes that control the depletion of the reservoir. The vertical profiles show vertical stresses and pore pressure prior to and after depletion. c),d) The semi-drained condition refers to the prescription of a constant pore pressure boundary condition on the model edges, excluding reservoir nodes. This approach yields numerical oscillations for low caprock permeabilites (d), and partial depletion of the caprock for increasing its permeability (c). In a second approach, the reservoir surrounding nodes are assigned

a constant pore pressure condition (e,f). For the hydrostatic condition on shared nodes, the reservoir is recharged once the reservoir pressure drops below the ambient pressure (e). Omitting the constant pore pressure boundary condition on the shared nodes cannot solve the small interpolation issue arising from different Biot-coefficients within different rock formations (f).

The interpolation issue could be solved by detaching the reservoir nodes from the surrounding units and attributing an impermeable tie constraint to the interface (Fig. 7-35). Furthermore, the detachment enables the oscillation-free simulation of undrained pore pressure and stress changes in the sideburden (see Figure 9-48, section 9.1.1).

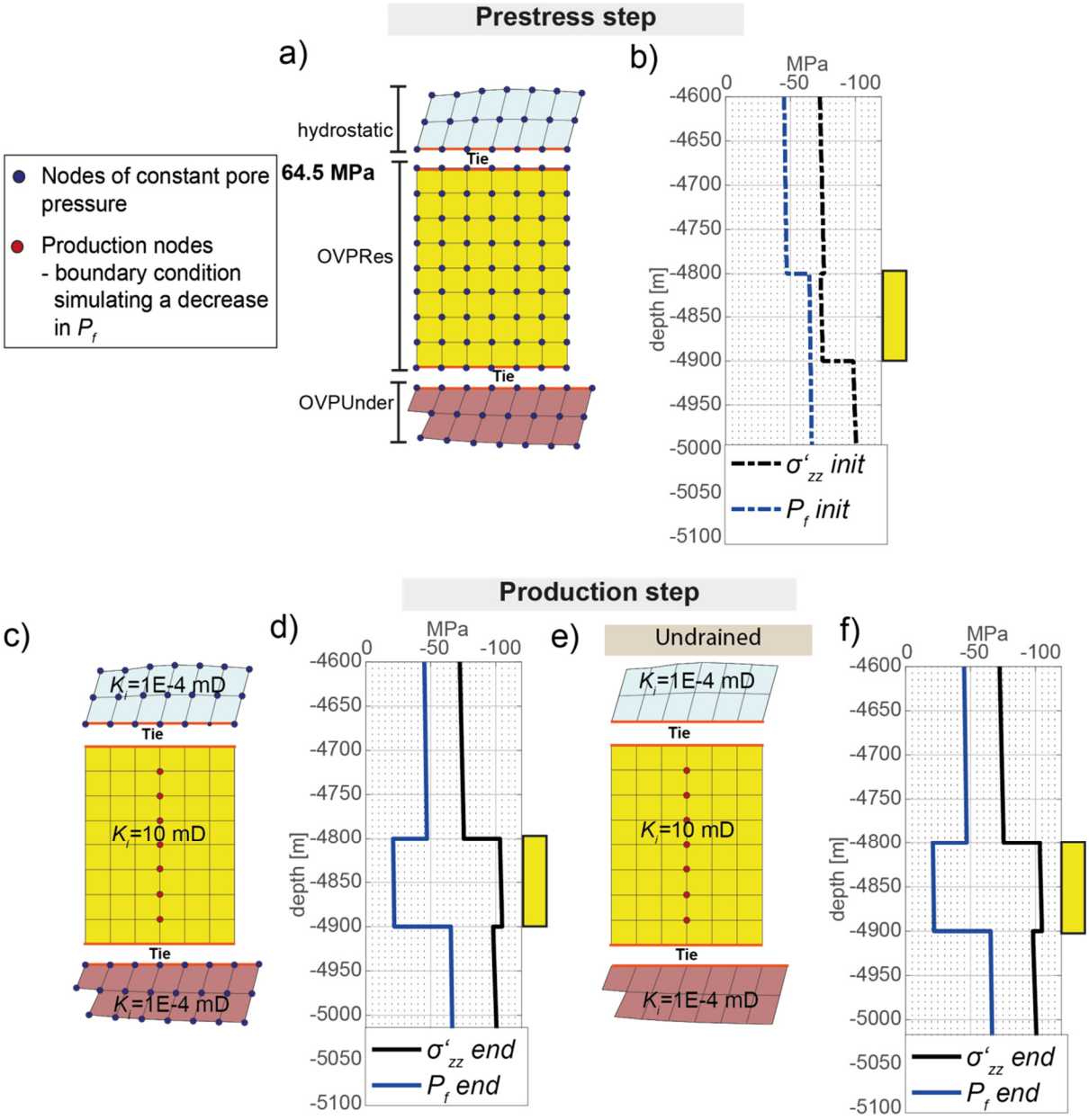

Fig. 7-35: a) Pore pressure boundary conditions during the prestressing step and the duplication of nodes as a prerequisite for the implementation of the impermeable tie constraint. b) Depth profile of effective stress vs pore pressure prior to production. c) Boundary conditions during depletion and d) resulting pore pressure-stress

profiles. e) Introducing the tie constraint allows furthermore for the computation of oscillation-free undrained stress changes in the over- and underburden, that are however negligible for the present consideration of stresses above and below the reservoir centre. See section 9.1.2 for the undrained loading of the fault-bound caprock.

7.5 Software applications

Different pre- and post-processing steps and limited plot capacities of ABAQUS led to the employment of various software applications and scripting languages. The generation of the FE mesh was carried out in the pre-processing software *Hypermesh* from which the mesh information was exported as *.inp* file. The input files were completed with ABAQUS-specific model definitions and simulations were carried out in ABAQUS standard employing the server of the working group. Several pre-processing and analysis steps, such as creating the pore pressure field and writing specific output quantities into the results file and export them, were automatized using the *Python* scripting interface of ABAQUS. Data plotting, analytic modelling and further post-processing operations were done in *Matlab*.

Figure 7-36 shows the employment of the different software applications and ABAQUS modules in this study. Due to the local framework conditions, the effective stress issue in combination with steady time pressure, numerous initiatives on enhancing the workflow and methodology had to be abandoned prematurely, rendering the workflow widely inefficient:

- Meshing and analysis in separate applications could have been summarized in an all- *Python* -scripting-based workflow. Given the ultimate geometric simplicity of the models, the employment of *Hypermesh* was cumbersome. The limited plot capacities of the ABAQUS viewer were overcome by installing the python module *Matplotlib*, that was however never employed due to the author's familiarity with *Matlab*.
- The in-house post-processing workflow, using *Tecplot* and the *Geostress*-addon, was incompatible with 2D models and the recent ABAQUS releases that had to be employed to yield Biot-Willis effective stress output.
- User subroutines in *Fortran* provide the modeller with a wide range of options to manipulate the solution procedure, specify solution- and field- dependent variables and have user-defined variables directly written into the output database file. Intel's *Fortran* compiler embedded in Intel's *Parallel Studio*, and *Microsoft Visual Studio* were installed and subroutines were successfully run in ABAQUS, but the failure to submit batch jobs lead to the ultimate dismissal of this option.

- Outsourced efforts to establish a one-way coupling scheme between ABAQUS and the FD-flow simulator ECLIPSE did not return any benefit.

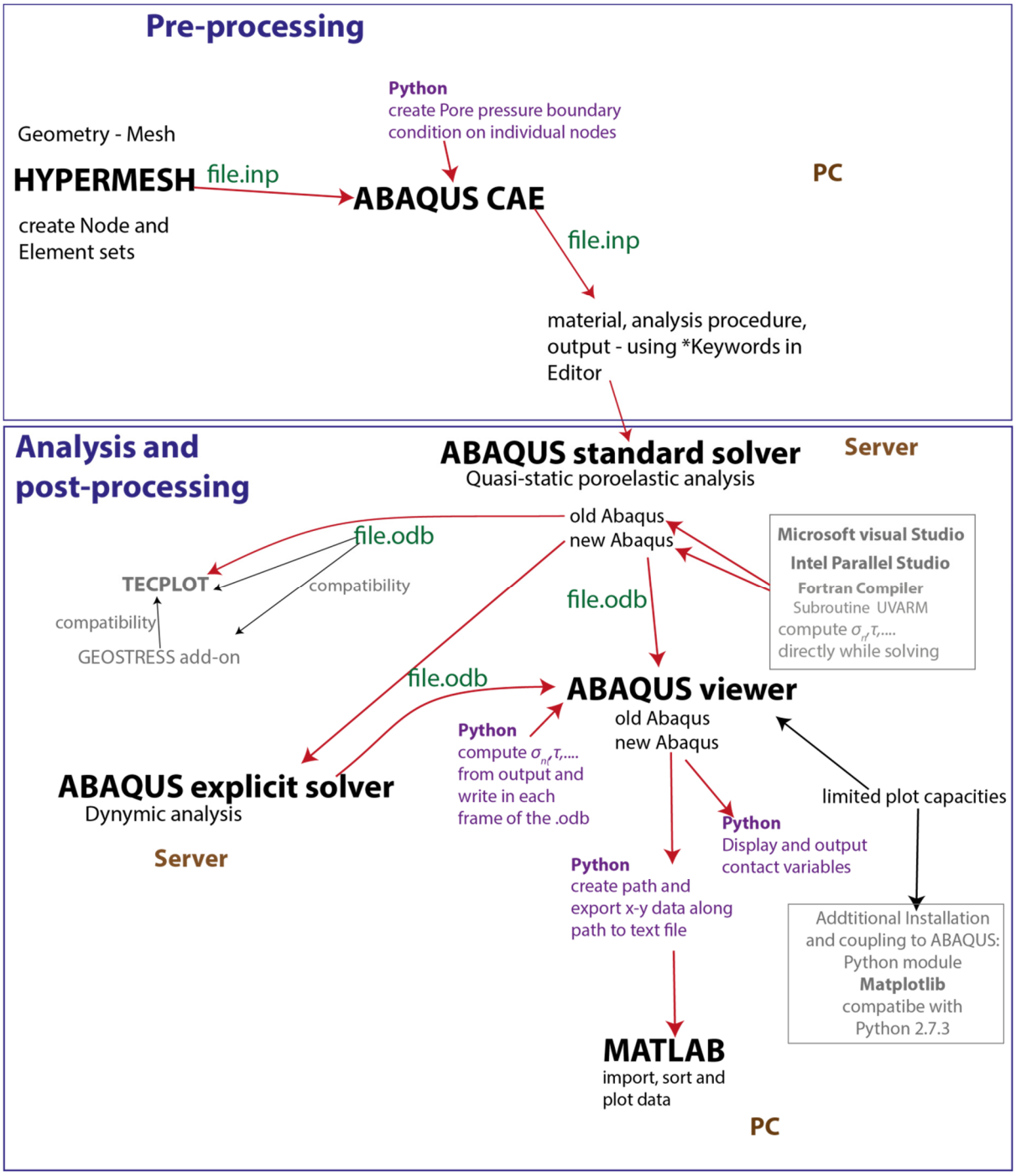

Fig. 7-36: Overview of different software applications and their utilization in the modelling workflow. Greyed-out applications were tested but ultimately discarded.

8 Geological setting and modelling approach

8.1 Geological setting and model abstraction

The northern German hydrocarbon province is located in the centre of the European Southern Permian Basin (ESPB) that represents a part of the Central European basin system (CEBS). The ESPB extends NW – SE from Poland to the North Sea (Fig. 8-37 a) and comprises several sub-basins and graben systems that formed during a complex multi-stage deformation history. The basin system initiated during late Carboniferous times, supposedly as dextral-transtensional basin (Lohr et al. 2007) superimposing on the upper carboniferous, Variscan foreland basin whose buried and coalified sediments became the most important source rock for natural gas in the area (e.g. Pasternak 2005). During early Permian, thermal subsidence coincided with the deposition of Rotliegend clastics, and strong volcanic activity resulting in wide-spread volcanic extrusions (Fig. 8-37 b). According to Kockel (2000) and Gast (1991) the formation of a N-S trending graben fan in the study area (Fig. 8-37 b) occurred during an intensive late Permian rifting phase and is accompanied by deposition of fanglomerates and dune sandstones of high reservoir potential within the grabens. During the following Zechstein, several kilometres of sediments were deposited (Lohr et al. 2007). The thick evaporite layers associated to cycles of transgression and regression render the sub-Zechstein seismic structural resolution poor (Scheck-Wenderoth & Lamarche 2005).

Kley et al. (2008) differentiate four further stages of structural evolution throughout the Mesozoic, E-W extension during the Triassic period, NE-SW extension during late Jurassic to early Cretaceous, and contraction during late Cretaceous to Palaeocene accompanied by basin-wide inversion processes. The recent stage comprises complex intraplate kinematics associated to the Alpine orogeny. According to Mohr et al. (2005) and Kukla et al. (2008) major activity of salt tectonics occurred during two stages in Triassic times while a third stage of salt deformation is associated to the compressional phase in Cretaceous times.

The Mesozoic structural evolution comprises changes in stress regime and the reactivation of major pre-existing faults. The latter created unconformities and lead to an individual structural evolution of different sub-areas (Mazur & Scheck-Wenderoth 2005). During late Jurassic the Pompeckj Block was uplifted while the Lower Saxony Basin (LSB) underwent differential subsidence. During transpressive tectonics of Cretaceous times, the fault systems on the LSB margin became reactivated and the sedimentary fill of the LSB was thrust over the stable Pompeckj block that is characterized by a dominant N-NNW strike of faults (Lohr et al. 2007). Figure 8-37 c) shows the location of the producing northern German gas fields and in particular the Rotliegend gas fields north of the river Aller.

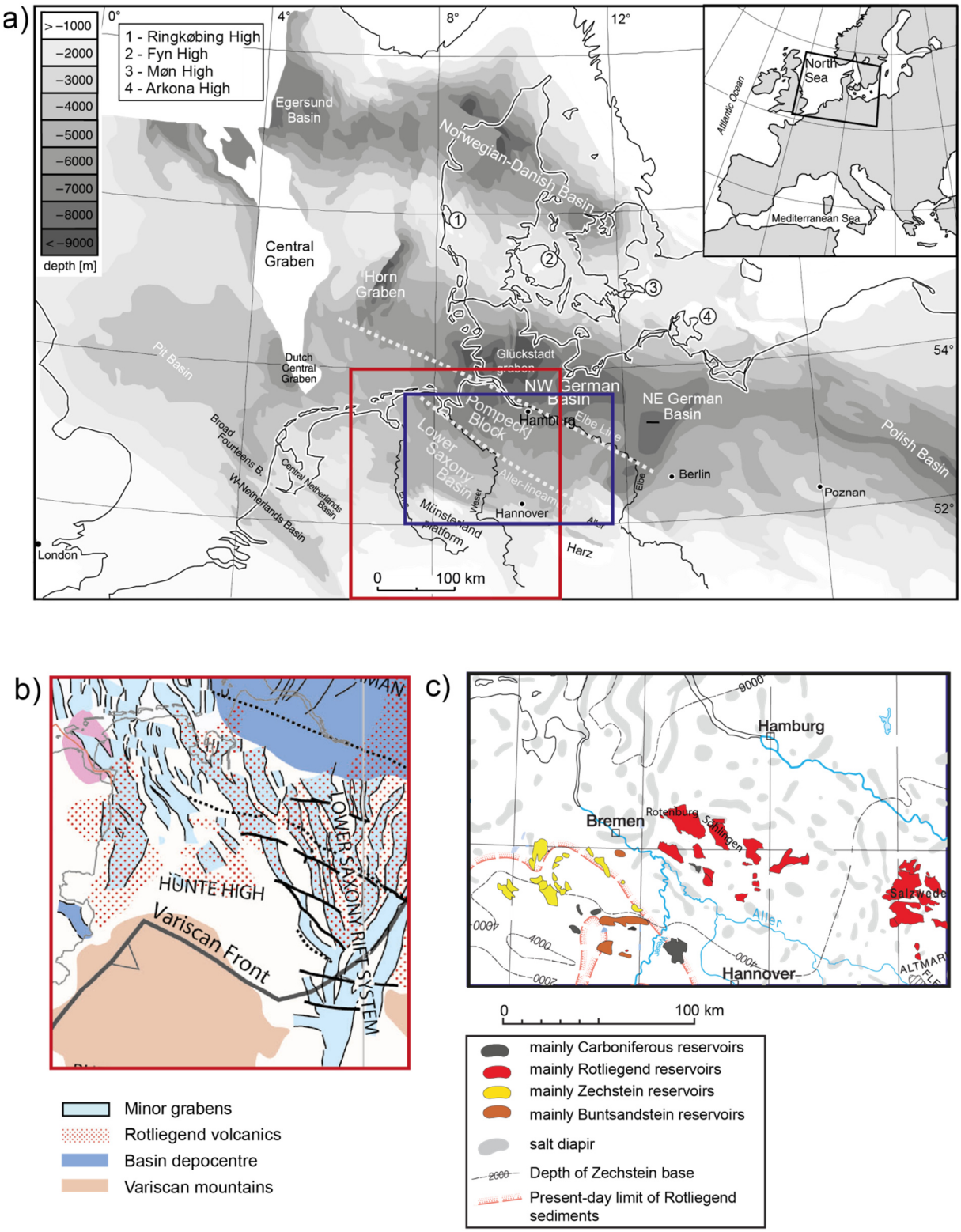

Fig. 8-37: a) Location of the Pompeckj block, hosting the Rotliegend gas reservoirs, within the ESPB (modified after Lohr et al. 2007). b) Zoom on the roughly north-south trending Rotliegend graben system and the distribution of Rotliegend volcanics (modified after Doornenbal & Stevenson 2010). c) Overview of gas fields of the Pompeckj Block and the Lower Saxony Basin associated to different stratigraphic units. The distribution of diapiric salt structures in the area of the gas fields is indicated by light-grey shapes (modified after LBEG 2016, Bischoff et al. 2017).

Economically important Rotliegend reservoirs of the Pompeckj Block are hosted in Permian Elbe and Havel subgroups of the upper Rotliegend. The reservoirs comprise sequences of aeolian sandstones and fluvial sandstones with intercalated clay-rich rocks loosely referred to as shales of varying thickness (Gast 1991).

The sedimentary reservoir rocks reside upon volcanic rocks of the lower Rotliegend that extruded during the initial stage of basin evolution (Gast & Gundlach 2006, Scheck-Wenderoth & Lamarche 2005). Atop, the gas-bearing clastic Rotliegend sequence terminates approximately 200 to 300 m above the economic reservoirs at the base of Zechstein shales, carbonates, and regional-scale evaporite layers with pronounced salt diapirism (Kukla et al. 2008, Lohr et al. 2007). The evaporites and shales constitute the regional impermeable caprock (Doornenbal & Stevenson 2010, Mueller & Scholz 2004) and the latter is generally not crosscut by Paleozoic structures (Baldschuhn et al. 2001) (Fig. 8-38 a).

Typical geological features of northern German Rotliegend gas fields (Fig. 8-38) are depicted in three different model set-ups: Reservoirs bounded by a graben-fault (Fig. 8-38 a), reservoirs situated below a viscoelastic salt diapir (Fig. 8-38 b) and reservoir compartments offset by intra-field faults (Fig. 8-38 c). The generic model set-up for the numerical investigation of production-induced stress changes and fault-loading is based on the geological setting of Rotliegend gas fields of North Germany, but no exact match to a particular field is intended.

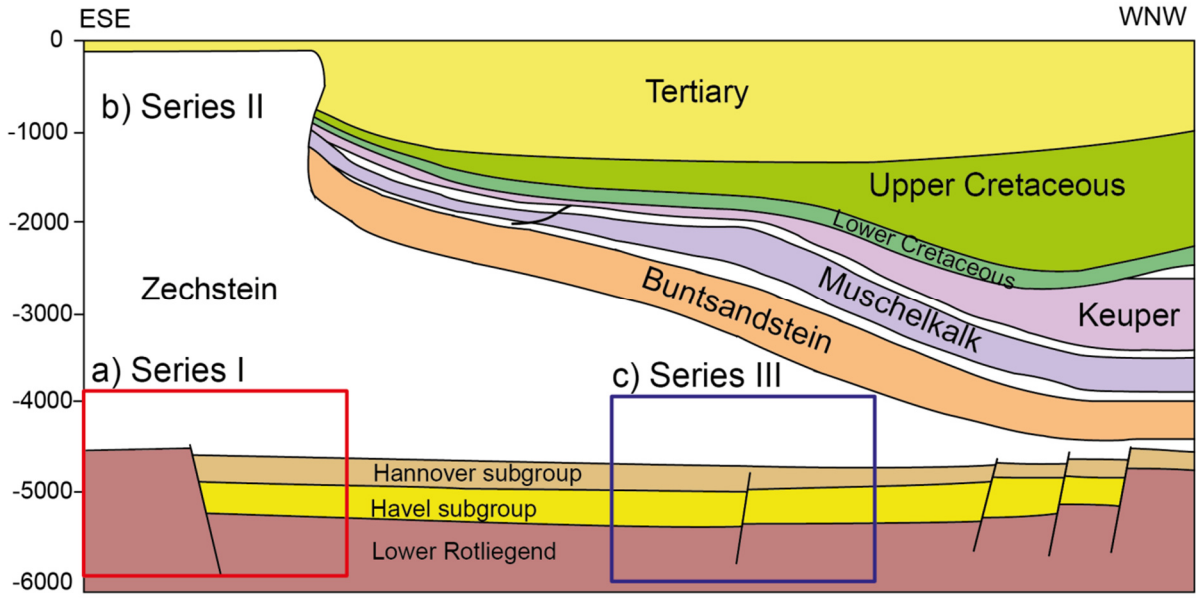

Fig. 8-38: Schematic geological section through a typical Rotliegend gas field in the North German basin located next to a main graben-bounding normal fault. The red frame (a) indicates the template for the graben-fault model (section 8.2.2) the blue frame (c) serves as template for the compartment-fault model (section 8.2.3) model. The diapiric shape of mobile salt layers in the North German basin (b) is addressed by an individual model series in section 8.2.4.

8.2 Modelling approach

Building upon the expertise gathered in the preliminary studies of chapter 7, this section addresses the representation of geologic features and the assessment of production-induced fault-loading in a series of 2D plane strain models. Production–induced fault-loading is investigated in a parameter space for reservoir depth, reservoir thickness, reservoir and host rock properties and compartment geometries typically observed in North German gas fields. For all model variants a roughly 100 m thick sandstone reservoir at 4800 m depth located in a graben setting is considered a reference scenario for the comparison of different parameters.

8.2.1 General model features

Economic reservoir horizons in Northern Germany are commonly bounded by graben faults (Fig. 8-38 a) or offset along intra-field faults (Fig. 8-38 c) which are considered to isolate the compartments hydraulically (Mauthe 2003). In the herein presented fault-loading model series, faults are represented by tied zero-thickness contact surfaces (cp. section 5.3 and 10.3) that inhibit fluid flow between the separated blocks and sustain continuity in total normal stresses (cp. section 7.2). The size of the 2D numerical model series is chosen sufficiently large (Figs. 8-39 a, 8-40 a, 8-41) in order to minimize boundary effects on the salt diapir (Model series II, Fig. 8-38 b) and in the area of interest close to the fault. An adaptive mesh with an increasing mesh resolution towards the reservoir layer is employed. In the area of interest, the edge length of the elements is about 10 m. A total number of 95000 first order quadrilateral plane strain elements with displacement and pore pressure degree of freedom (CPE4P) discretize the graben and compartment models, for the salt diapir models, the FE mesh comprises a combination of pore pressure (CPE4P) and ordinary displacement elements (CPE4) adding up to 130000 elements.

Above the reservoir, a hydrostatic pore pressure gradient is assumed. The reservoir itself is isolated hydraulically by an impermeable tie constraint from the surrounding formations (section 7.4.2). Overpressure starts at the top of the reservoir and has a magnitude of 64.5 MPa at a reference depth of 4800 m. Below the reservoir, a pore pressure increase following a hydrostatic gradient is assumed (cp. section 7.4.2). The initial state of stress in the models is created by the gravity and displacement method (section 7.1.3). In all models, a 2D normal faulting stress regime in and around the reservoir as implied by Cornet & Röckel (2012) for the North German basin is assumed.

The elastic graben and compartment models are simulated in two analysis steps, the viscoelastic modelling requires an intermediate step to relax shear stresses associated to the viscoelastic rheology.

In the first step, the models are allowed to settle under the gravitational load, and a horizontal displacement is applied. The graben and compartment models are prescribed a lateral confinement of 3 metres on either model boundary (Fig. 8-39), creating a non-critical stress state $K' = \sigma_{zz} > \sigma_{xx}$ on the fault of the graben reference model (Fig. 7-29). The horizontal confinement of 3 m respectively is then applied to all graben and compartment models representing the basin-wide initial (far-field) stress state. The lateral displacement for the salt diapir model is extrapolated to 9.75 m according to its larger size.

Prior to the production step, a vertical effective stress of 74 MPa and horizontal effective stress of 21 MPa ($K' = \sigma'_{xx}/\sigma'_{zz} = 0.28$) prevail in the centre of the hanging wall reservoir horizon of the graben (Fig. 8-39) and compartment models (Fig. 8-41). Mentioned stress magnitudes vary slightly for the variation of mechanical reservoir and host rock properties and the reservoir geometry in section 9.1.2. In the salt diapir model (Fig. 8-40), the initial ratio $K' = \sigma'_{xx}/\sigma'_{zz}$ within the reservoir varies laterally with respect to the shape of the diapir (Fig. 9-51 c).

In the analysis step, production from the reservoir is simulated by a linear decrease in pore pressure at reservoir nodes at 2 km distance from the fault (Figs. 8-39, 8-41). Pore pressure is considered to decrease linearly by 43.5 MPa during a hypothetical production time of 22 years.

8.2.2 Model Series I: Graben-fault models

In the graben-fault models the reservoir horizon is located at the graben edge (Fig. 8-38 a), bounded by a normal fault that renders the reservoir juxtaposed to stratigraphically older rocks with contrasting mechanical properties. A reference model with typical rock properties and boundary conditions (Fig. 8-39, Tab. 3) is defined as a starting point. Then, a series of models is calculated to evaluate the impact of rock mechanical parameters, as well as fault and reservoir geometries on production-induced stress redistribution and fault-loading (section 9.1.2).

In the last parameter variation, the regional caprock O1 (Fig. 8-39) has viscoelastic properties (Tab. 4). In order to account for the varying thickness of the upper Rotliegend sand-shale succession and the younger Zechstein evaporites constituting the sedimentary filling of the graben, the thickness of layer O2 (Fig. 8-39) intercalated between the reservoir and the salt layer is varied. This renders the reservoir horizon at a varying distance to the viscoelastic salt. A detailed description of the modelling approach for the implementation of viscoelastic rheology follows in section 8.2.3.

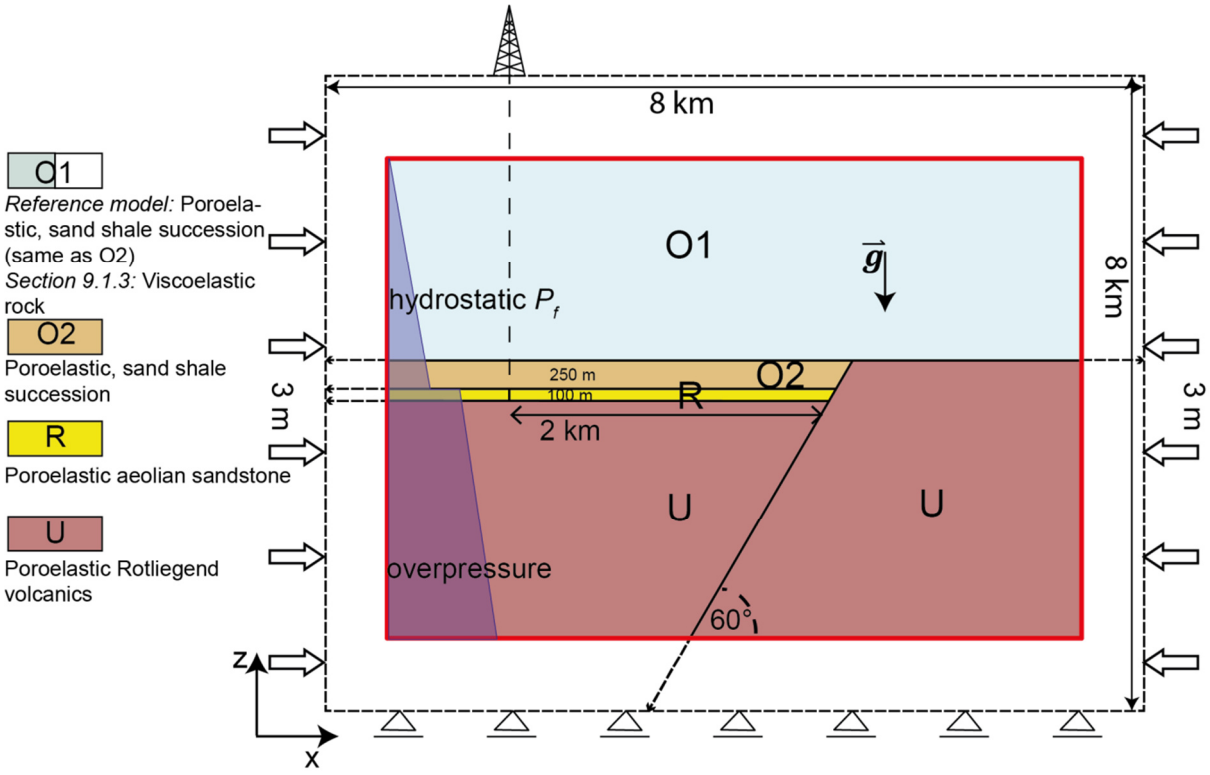

Fig. 8-39: Detail of the reference model representing the graben boundary. The boundary conditions are applied to the model frame of 8 x 8 km size.

Tab. 3: Material and hydraulic properties of the reservoir and surrounding rock in the reference model

Lithology	**Overburden O1,O2**	**Reservoir R**	**Underburden U**
Drained Young's modulus *E* [GPa]	10	7.5	50
Drained Poisson's ratio *v* [-]	0.3	0.17	0.25
Undrained bulk modulus K_u [GPa]	19.2	4.54	37.45
Biot modulus *M* [GPa]	13.4	1.2	33.7
Dry rock density ρ_{dry} [kg/m^3]	2400	2450	2700
Wet rock density ρ_{dry} [kg/m^3]	2530	2472	2747
Biot-coefficient α [-]	0.9	0.7	0.35
Intrinsic permeability K_i [mD]	1E-8	10	1E-8
Bulk modulus gas K_f [GPa]	-	0.12	-
Bulk modulus water K_f [GPa]	2	-	2
Porosity ϕ [-]	0.13	0.09	0.05

8.2.3 Model Series II: Viscoelastic diapir models

The second model series addresses the diapiric Upper Permian (Zechstein) caprock commonly found above economic Rotliegend reservoirs in North Germany and mainly consisting of rock salt. The mechanical impact of rock salt on stresses in surrounding formations is based on the two following rock mechanical properties. First, rocks mainly composed of halite reveal densities close to 2000 kg/m^3, which is significantly less than the typical rock densities of approximately 2400 kg/m^3. Second, low effective viscosities of rock salt even under upper-crustal conditions prevent support of shear stresses induced by gravitational loading or production from underlying reservoirs. A similar relaxation of shear stresses is not expected in any other types of sedimentary rocks atop of reservoirs.

In a first model, the stress state in a laterally extensive, depleting reservoir below a salt diapir of 3.5 km height and 14 km base width is investigated. Therefore, a viscoelastic diapiric layer with a constant effective Newtonian viscosity of 3x10^{17} Pa s (van Keken et al. 1993) and a constant density of 2000 kg/m^3 (Tab. 4) is incorporated into the layer O1 (Fig. 8-40). The lateral position of the graben-bounding fault is varied in this setting to investigate the effect of a laterally changing salt thickness (Fig. 8-40 b).

All viscoelastic models were run in three steps. In the first step, the gravitational load, horizontal displacement and the pore pressure boundary conditions are applied. The second step serves to relax shear stresses resulting from the modelled load to the salt shape. In order to determine the required time to degrade shear stresses, stress changes in the second step are monitored. shear stresses are considered to be relaxed, once the *von Mises* stress change drops to 1 kPa during a time-increment of 100 years. This minimum stress change is reached in less than 2000 years for all considered salt shapes (Figs. 9-50, 9-51, 9-52). If the material response of adjacent formations is simply poroelastic, the relaxation of the viscoelastic layers induces unrealistically large shear stresses (Luo et al. 2012). To prevent build-up of such unrealistic stresses, a linear Mohr-Coulomb poroelasto-plasticity model is employed (Tab. 4) with a cohesion of 5 MPa, an angle of internal friction of ψ=30°, and a dilatancy angle of χ=15° that allows for larger deformation at limited stress.

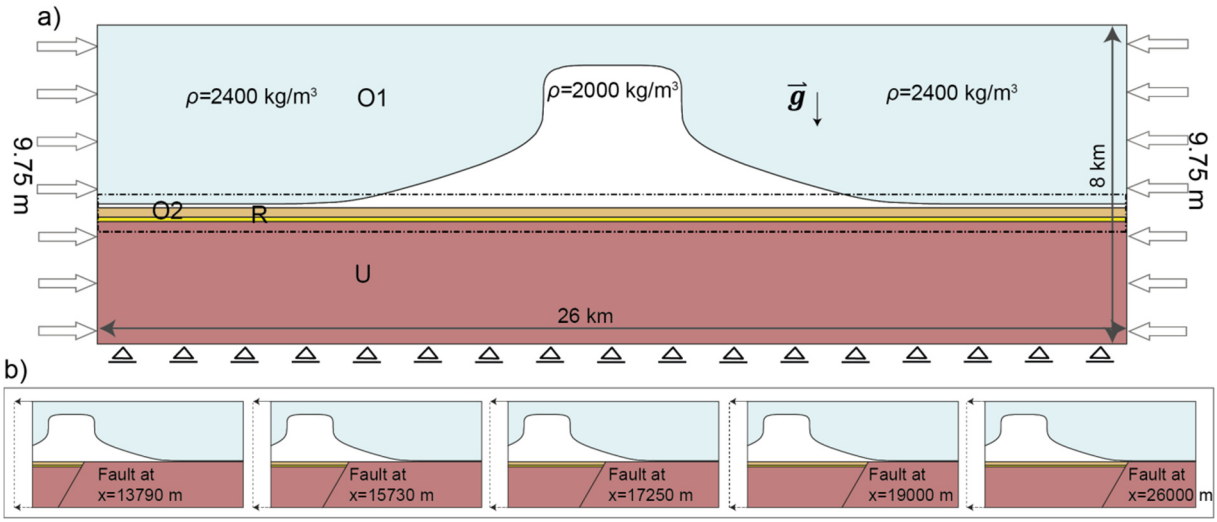

Fig. 8-40: a) Model geometry and mechanical boundary conditions of the 2D diapir model. Pore pressure is decreased homogeneously throughout the reservoir in all models of this series. b) Fault at different locations below the salt diapir.

Tab. 4: Material and hydraulic properties of the models including a viscoelastic layer.

Lithology	**Salt layer**	**Overburden O1,O2**	**Reservoir R**	**Underburden U**
(Drained) Young's modulus E [GPa]	10	10	7.5	50
Viscosity η [Pa s]	$3 \cdot 10^{17}$	-	-	-
(Drained) Poisson's ratio ν [-]	0.3	0.3	0.17	0.25
Undrained bulk modulus K_u [GPa]	-	19.2	4.54	37.45
Biot modulus M [GPa]	-	13.4	1.2	33.7
Friction angle[1] ψ [deg]	-	30	-	30
Dilatancy angle[1] χ [deg]	-	15	-	15
Cohesion[1] C [MPa]	-	5	-	5
Dry rock density ρ_{dry} [kg/m^3]	2000	2400	2450	2700
Wet rock density ρ_{wet} [kg/m^3]	-	2530	2472	2747
Biot-coefficient α [-]	-	0.9	0.7	0.35
Intrinsic permeability K_i [mD]	-	1E-8	10	1E-8
Bulk modulus gas K_f [GPa]	-	-	0.12	-
Bulk modulus water K_f [GPa]	-	2	-	2
Porosity ϕ [-]	-	0.13	0.09	0.05

[1] elastoplastic behaviour during salt relaxation step

8.2.4 Model Series III: Compartment- fault models

A second reservoir compartment is added to the reference graben-fault model (Fig. 8-41 a) to simulate effects of fault dip and offset along the fault loaded by three depletion scenarios summarized in Figure 8-41 b). Scenario 1 assumes production from the hanging wall compartment, the footwall compartment remains undepleted. Scenario 2 simulates simultaneous production from both compartments at identical rates. Scenario 3 assumes production exclusively from the footwall compartment, the hanging wall compartment remains undepleted. Initial conditions, material properties and loading conditions correspond to those used in the reference graben model (Fig. 8-39, Tab. 3).

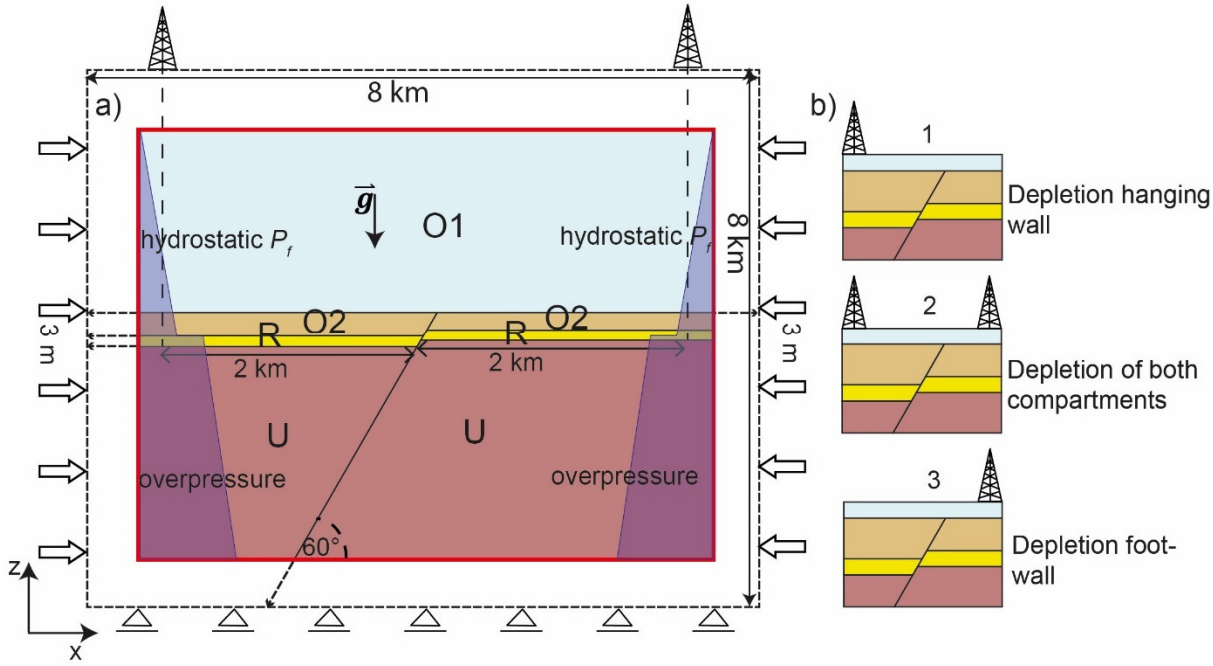

Fig. 8-41: a) Sketch of the compartmentalized model representing a reservoir horizon offset by an impermeable fault. Boundary conditions are applied to the 8 x 8 km model frame. b) Depletion scenarios for the compartmentalized model.

8.3 Assessment of fault-loading

Absolute criticality and critical stress development on the fault plane are evaluated using the Shear Stress Ratio, *SSR*

$$SSR = \frac{\tau}{\sigma_n'} \qquad 8.1$$

which is similar to the concept of slip tendency (Morris et al. 1996), although *SSR* is not limited by an assumed frictional strength of the fault plane (Fig. 8-42 a). Since the frictional strength of the faults at

depth is poorly constrained (cp. section 2.8.2), *SSR* is preferred over slip tendency. Shear stresses and effective normal stresses on the fault are computed from the effective 2D stress σ'_{ij} according to Eq. 2.17 and 2.18.

Figure 8-42 c) shows the sign convention for the tangential shear stress τ. Shear stress is positive for left lateral fault displacements i.e. normal faulting and negative for right lateral, i.e. reverse reactivation tendencies. Along with negative compressive normal stress, *SSR* is negative for normal faulting and positive for reverse faulting (Fig. 8-42 c).

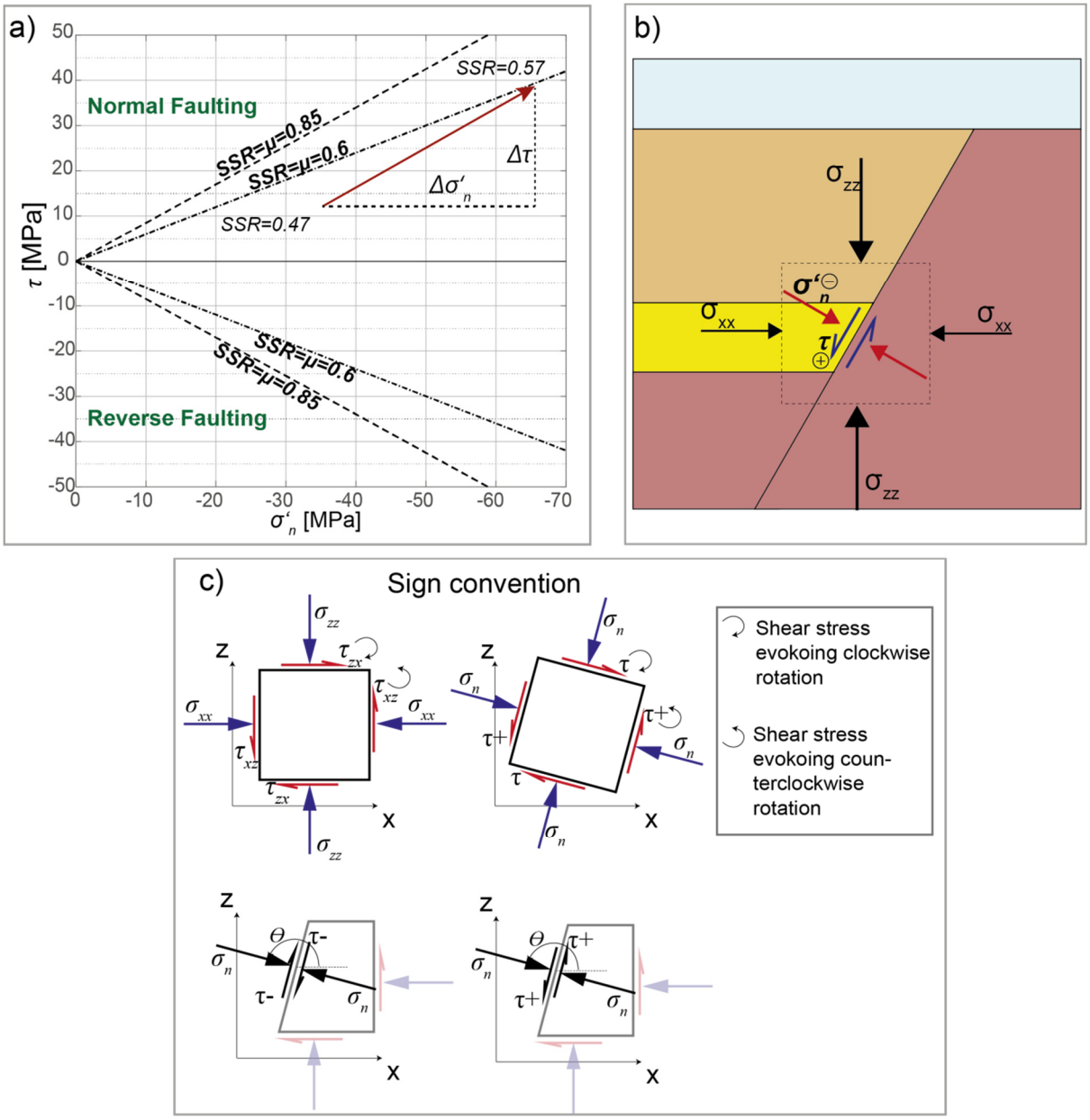

Fig. 8-42: a) SSR plot depicting shear vs effective normal stress during depletion on the normal fault of the reference model. The inclined dashed lines represent failure lines for typical values of frictional strength after Zoback (2007). b) Zoomed view on normal and shear stress at the graben-bounding fault. c) Sign convention for shear stresses in this study.

SSR values are computed along a path in 0.5 m distance to the fault that intersects the reservoir and parts of the over- and underburden (Fig. 9-44 a). The impermeable tied contact ensures that total normal stress across the fault is continuous but effective normal stresses build up in a decoupled manner.

Note that simple friction models cannot predict the mechanical response of a complex fault zone (e.g. Faulkner et al. 2010, Shipton et al. 2006). Here *SSR* is used as a measure of the fault-loading state. For this reason, the models are not capable to predict the onset of fault rupture, i.e. seismicity, and most important, cannot be used to predict magnitudes of induced seismicity. For this, far more sophisticated rheological models of fault mechanical behaviour (e.g. Scholz 1998) are required (cp. section 2.9 and 9.2). Irrespectively, *SSR* = 0.6 is here regarded as the threshold between a stable (*SSR* < 0.6) and an unstable (*SSR* > 0.6) fault, which corresponds to Zoback's (2007) lower limit of fault friction (*SSR* ≈0.6).

8.4 Perspective: Assessment of dynamic fault rupture and fault slip

In the assessment of fault-loading described in the previous section, the loading of the fault is hypothetically limited by a frictional strength but the tied contact fault can in fact be loaded infinitely. This approach was chosen to compare the loading of the fault between different model variations after 43.5 MPa depletion, sailing around the issue that the depletion magnitude to failure depends predominantly on the initial stress state and the coefficient of friction. This section addresses the effect of different fault-loading patterns on the post-failure, i.e. dynamic slip behaviour of the fault, shedding light on slip magnitudes and propagation of rupture for the different critical model variations.

As discussed in section 7.2, contact slip in the poroelastic ABAQUS procedure is strongly affected by the continuity condition. Continuity of total normal stresses across a compartmentalizing fault during production constitutes the case in accordance with tectonic considerations, and leads to fault reactivation in terms of total stresses (cp. section 7.2.3). For fault reactivation in terms of effective stress, fault slip in ABAQUS is evaluated by Terzaghi effective stress that is incompatible with a stable initial stress state for given material properties (cp. section 7.1) and contradicts the continuity condition of total stresses (cp. section 7.2.1).

In order to evaluate the dynamic response to the poroelastic loading of the fault and sail around the mentioned issues of the poroelastic contact model, Biot-Willis effective stress is transferred to a dynamic stress displacement analysis in ABAQUS explicit to simulate the dynamic rupture of the fault.

The dry rupture modelling in ABAQUS explicit allows furthermore to consider and dissipate the decoupled, production-induced effective stresses on either side of the contact fault, that arise from its sealing properties (cp. section 7.2.2 and 10.3). The dynamic analysis in ABAQUS explicit considers the temporal derivatives of stress (*ABQ 2016 Analysis guide 6.3.1*) and includes the effect of inertia on the slipping fault. ABAQUS explicit has been successfully applied in earthquake simulations (e.g. Templeton et al. 2009) and the forward stepping integration scheme is particularly efficient for short modelling times (*ABQ 2016 Analysis guide 6.3.1*), such as the rupture time of small seismic events (Frankel & Kanamori 1983, Tomic et al. 2009).

The herein introduced workflow for the modelling of dynamic fault rupture is illustrated in Figure 8-43. It comprises the assessment of fault stability in ABAQUS standard and the transfer of Biot-Willis poroelastic stresses to the dry contact model in ABAQUS explicit.

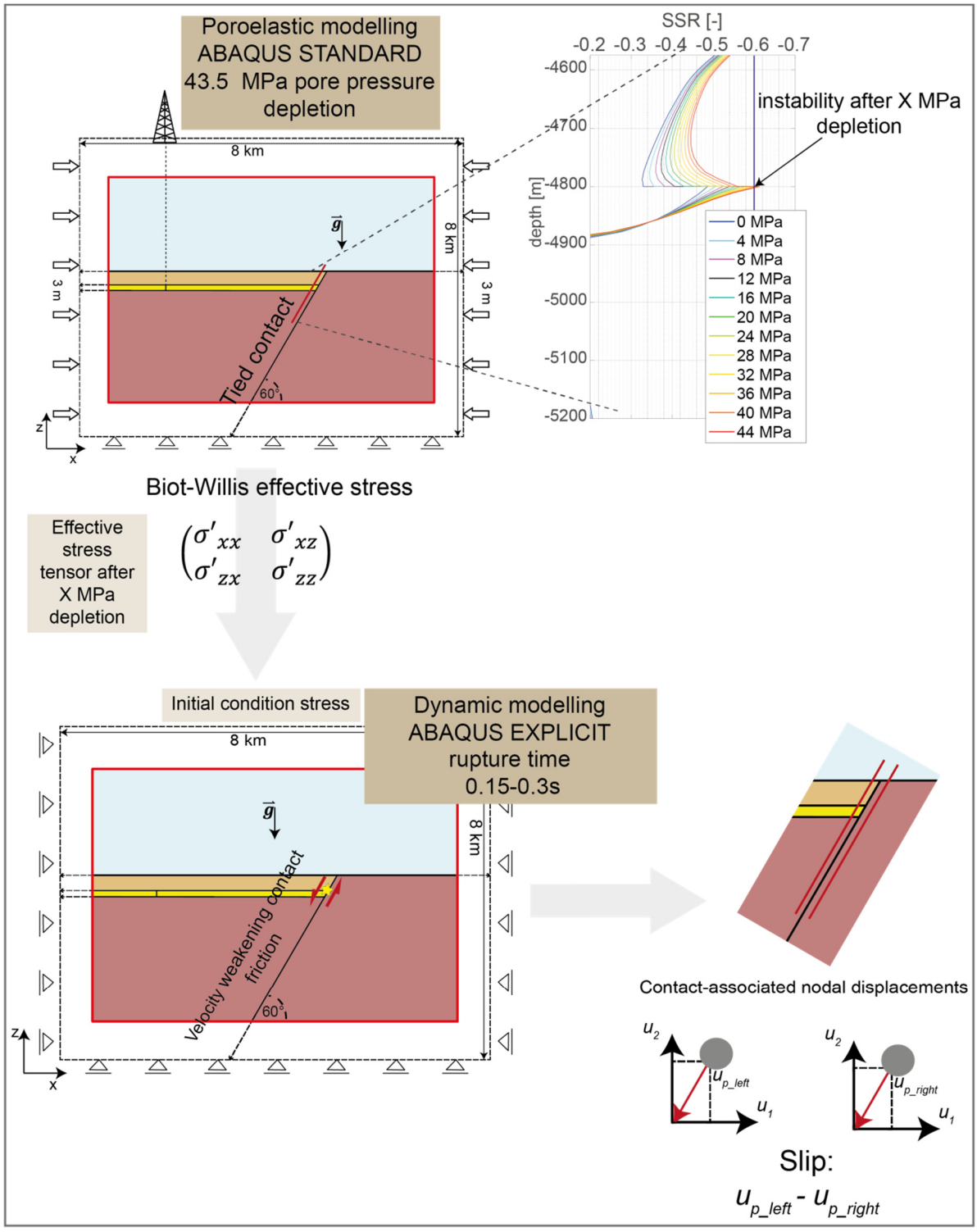

Fig. 8-43: Workflow for the modelling of dynamic rupture in ABAQUS. Fault criticality in the poroelastic model is evaluated during steps of 4 MPa of depletion. The critical effective stress state in terms of Biot-Willis effective stress is then used as initial condition to evaluate the faults dynamic response to the depletion-induced loading during a time period of 0.15-0.3 s in ABAQUS explicit. Contact slip is computed as differential displacements of contact-associated nodes. Therefore, nodal displacements on either side of the fault are first projected onto the fault, before differential displacements are externally translated into slip.

SSR values of model series I and III are evaluated during depletion steps of 4 MPa with respect to their fault-loading state. At the onset of criticality, i.e. *SSR*=0.6, the stress state of the respective increment of the poroelastic procedure is used as initial stress condition for the instantaneous dynamic fault slip analysis. On the contact fault, the frictional resistance to sliding is considered to weaken as an exponential function of slip velocity according to:

$$\mu = \mu_d + (\mu_s - \mu_d)e^{-d \cdot vs} \qquad 8.2$$

μ_d: dynamic coefficient of friction μ_s: static coefficient of friction *d*: decay coefficient *vs*: slip velocity [m/s]

The dynamic coefficient of friction is assumed to be 0.25 (Zbinden et al. 2017).The decay coefficient *d = 0.5* is chosen in order to simulate a full drop of frictional resistance to its dynamic value (Eq. 8.2) at slip velocities between 10-15 m/s, experimentally observed for instance by Daub & Carlson (2010) and Rubino et al. (2017). The simulation time of 0.15 -0.3 sufficed to yield saturation of rupture propagation. That is, the increase in rupture length slowed significantly down before this simulation time terminated. ABAQUS explicit provides only reduced first order quadrilateral elements, leading to a slight reduction in the resolution of stresses with respect to the discretization of the poroelastic model.

The modelling of dynamic rupture in ABAQUS aims on investigating the effect of different loading patterns associated to criticality of model variations presented in sections 8.2.2 and 8.2.4. The heterogeneous stress state in the reservoir and its surroundings, arising from production-induced stresses, has recently been shown to have significant impact on rupture propagation in models of the Groningen gas field (Buijze et al. 2017). In opposition to previous static models of fault slip (e.g. Mulders 2003, Orlic & Wassing 2013, section 7.2.3 of this study) the dynamic modelling of rupture accounts for propagation of slip from unstable fault sections to conditionally stable fault sections when dynamic stresses and slip acceleration are sufficiently large with respect to the frictional resistance.

The dynamic rupture simulation returns a slip length and a 1D distribution of the slip magnitude. Thereby the seismic moment is a measure of earthquake size and can be computed from rupture area, mean slip and the shear modulus (Kanamori & Anderson 1975). In this study, the focus lies on the propagation of slip associated to loading patterns of different model variations that experience a critical fault-loading during depletion (cp. results sections 9.1.1-9.1.3 and 9.1.5). Slip length and slip magnitude are compared in a quantitative manner but the deduction of earthquake magnitudes from the seismic moment (e.g. Kanamori 1977, Wells & Coppersmith 1994) is not intended (see discussion in section 10.5).

9 Results

9.1 Results: Fault-loading Model Series I-III

9.1.1 Model series I: Reference model

Fault-loading in the reference model, before and after production is expressed by *SSR* in Figure 9-44 b). Prior to production, *SSR* magnitudes are below 0.6 rendering the fault in a non-critical initial stress state. Depletion induces a slight increase in *SSR* at the upper termination of the fault and immediately above the reservoir top. Principal stresses rotate in counter-clockwise and clockwise direction above and below the reservoir respectively (Fig. 9-44 e,d).

Beneath the reservoir, *SSR* becomes negative due to the large contrasts in stiffness between the relative compliant reservoir sandstones and the stiff Rotliegend volcanic rocks in the footwall of the fault (Fig. 9-44 b). The stiffness contrast results in an initial sub-horizontal orientation of σ_1 below the reservoir (Fig. 9-44 c). A decrease in the stiffness contrast results in higher values for *SSR*, indicating a less pronounced tendency to reverse faulting (Fig. 9-46 a). The loading of the fault on the upper reservoir boundary increases linearly over the 22 years production time (Fig. 9-44 c). Nonlinear loading may arise from semi-permeable properties of the fault (e.g. Zbinden et al. 2017).

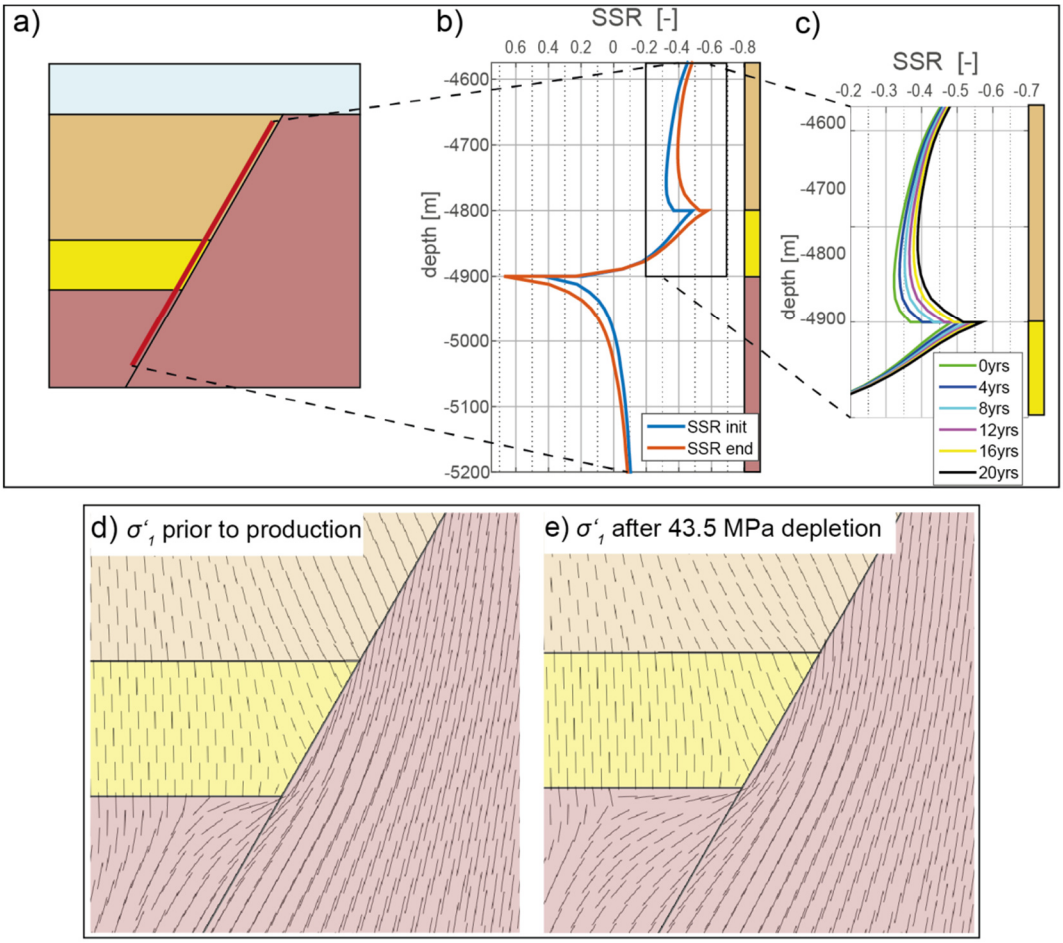

Fig. 9-44: a) Observation line in 0.5 m distance to the graben-bounding fault from which the calculated stresses are extracted for the determination of *SSR*. b) *SSR* prior to production and after pore pressure depletion of 43.5 MPa. *SSR* increases in the upper part of the reservoir and above the reservoir top. The decrease below the reservoir signifies a reduced tendency for normal faulting and an increased tendency for reverse faulting. c) The Effective principal stresses σ'_1 in the vicinity of the graben-bounding fault differ from the expected sub-vertical orientation because of the stiffer Rotliegend volcanics. d) Pore pressure drawdown results in a counter-clockwise rotation of the effective maximum principal stress above and clockwise rotation below the reservoir.

9.1.2 Model series I: Parameter study of Reservoir properties and geometry

Figure 9-45 summarizes the impact of reservoir depth (Fig. 9-45 a), reservoir thickness (Fig. 9-45 b), fault dip (Fig. 9-45 c), the value of the Biot-coefficient α (Fig. 9-45 d), the density of the overburden (Fig. 9-45 e), and the magnitude of the remote stress (Fig. 9-45 f) on *SSR* values at the end of the production period, and relative to the reference model (Fig. 9-45 b). The impact of contrasts in elastic properties between the reservoir and its surroundings are summarized in Figure 9-46. *SSR* values in Figures 9-45 and 9-46 depict fault loading only on the upper reservoir and the overburden fault section in accordance with reservoir compaction and the prevailing normal faulting stress regime. Note that

the results presented in the following account for a static, i.e. non-slipping fault, local stress redistribution related to fault slip are not modelled.

Reservoir depth and reservoir thickness

SSR values decrease slightly with increasing reservoir depth (Fig. 9-45 a). Criticality with respect to the arbitrary threshold of *SSR* = 0.6 is only obtained for the reservoir at 4600 m depth (Fig. 9-45 a), *SSR* values obtained for deeper reservoirs stay below the threshold (Fig. 9-45 a). An increase in reservoir thickness results in increasing *SSR* values (Fig. 9-45 b) and a higher risk of fault failure respectively.

Fault dip

SSR values increase with fault dip, and show invariantly highest values for faults dipping > 75° (Fig. 9-45 c). This is in obvious contrast to faults loaded by far-field tectonic forces, for which fault dips of ~60° are expected to show highest criticality in normal-faulting environments (e.g. (Sibson 1974)). The difference to tectonic faulting arises from initial and production-induced stress rotations, and fault-loading caused by reservoir compaction, resulting from the increase in effective stresses during pore pressure reduction (Eq. 4.4). In the tectonic case, preservation of layer thickness is assumed.

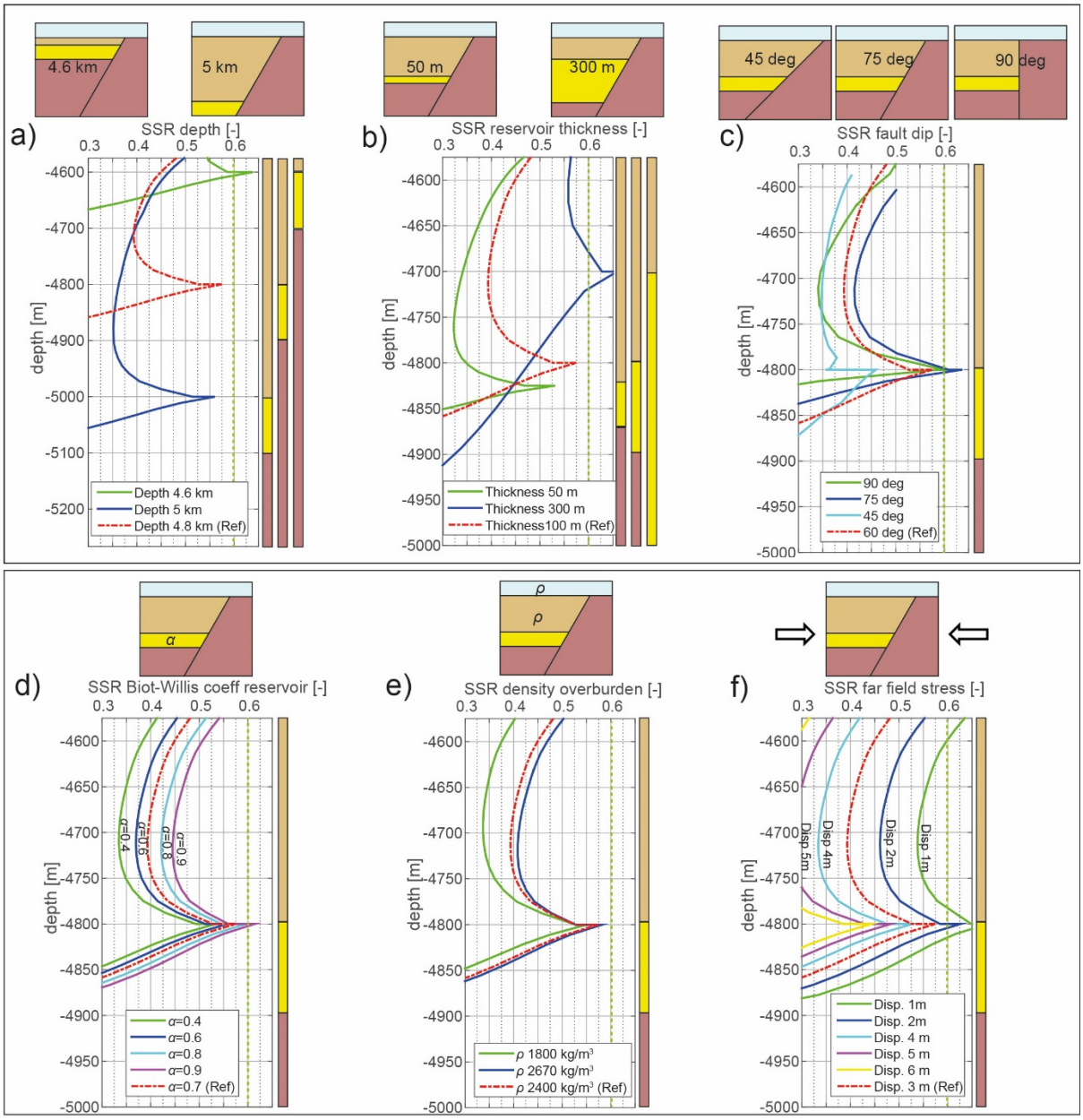

Fig. 9-45: *SSR* value on the upper reservoir- and overburden fault section after pore pressure depletion of 43.5 MPa for various parameter variations: a) reservoir depth 4600 m vs 5000 m, b) reservoir thickness 50 m vs 300 m, c) fault dip 45,75,90°, d) Biot-Willis coefficient α=0.4-0.9, e) overburden density 1800 vs 2670 kg/m^3, f) horizontal stresses are varied by different displacement magnitudes. The dashed red line represents the reference model which is considered to be representative for a Rotliegend graben setting in the North German Basin.

Biot-coefficient of reservoir

Large Biot-coefficients are more favourable for fault reactivation as *SSR* values increase for higher coefficients (Fig. 9-45 d). This is because larger Biot-coefficients imply that the magnitude of stress which during depletion is transferred from the pore pressure to the solid rock's skeleton increases.

Larger effective vertical stress enhances compaction of the reservoir, which in turn leads to stronger stress arching effects in the surroundings of the reservoir.

Density of overburden

The average overburden density and, hence, the lithostatic load on the reservoir can be heterogeneous in the North German basin due to laterally varying thicknesses of salt layers which have a relatively low density. The variation of the average overburden density (Fig. 9-45 e) shows that the fault is stressed slightly stronger for the larger density of the overburden units O1 and O2 compared to the lower density variant. The absolute influence of the overburden density variation is small however.

Far-field stresses

Production-induced fault-loading and eventual rupture result from superposition of a pre-production tectonic stress field by local poroelastic stress changes. The numerical results show that the changes in stress are independent of the initial stress field but absolute values of *SSR* clearly depend on the pre-production state of stress (Fig. 9-45 f). Given the overpressured reservoir horizon and the low Poisson's ratio of the reservoir, the window for a stable initial stress state is narrow. For weak horizontal compression, the fault is initially reactivated as a normal fault, for large horizontal compression the reverse tendency on the reservoir bottom increases beyond frictional strength. However, an increasing horizontal compressive stress counteracts normal faulting (Fig. 9-45 f) so that the impact of production on fault criticality is reduced.

Young's modulus of reservoir, over- and underburden

Differences in Young's moduli of different rock types and units result in stiffness contrasts between the reservoir and its surrounding rocks. Such stiffness contrasts have been reported to be of key importance for production-induced fault reactivation in the Netherlands (van Eijs et al. 2006). Results of this study are as follows. First, a decrease in Young's modulus of the horizon directly below the reservoir reduces the tendency for reverse faulting significantly (Fig. 9-46 a) and favours normal faulting at the reservoir top. Second, reduction of reservoir Young's moduli to values significantly less than the overburden layer O2 results in a concentration of *SSR* along the fault in the O2 layer (Fig. 9-46 b). A large stiffness of the O2 layer reveals a wide but subcritical loading of the fault in the O2 layer, a significantly lower stiffness of the overburden compared to the reference reservoir stiffness results in a substantial concentration of critical *SSR* values on the upper level of the reservoir fault section (Fig. 9-46 c). In either case, the concentration of *SSR* in the O2 layer reduces when the contrast in Young's moduli between the reservoir and the O2 layer is reduced.

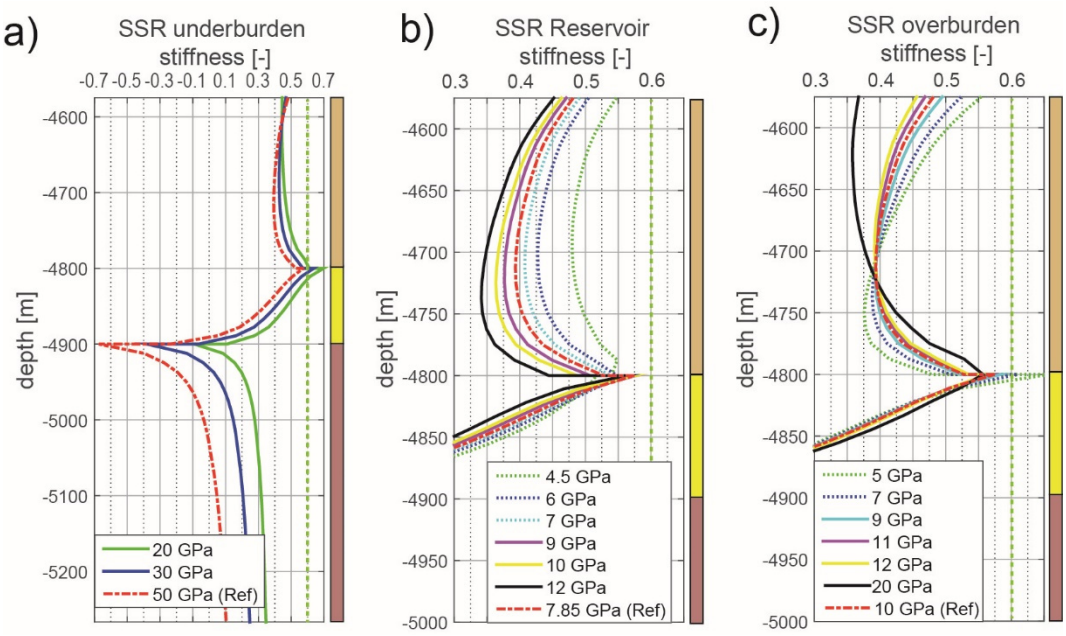

Fig. 9-46: *SSR* values for the variation of the stiffness of different lithological units after 43.5 MPa depletion. a) underburden stiffness, b) reservoir stiffness, c) overburden stiffness. The dotted lines represent stiffnesses which are smaller than the reference stiffness respectively.

Reservoir permeability

The permeability of the reservoir controls the spatio-temporal evolution of pore pressure and associated loading of the fault by effective stress changes. Large permeabilites of $K_i \geq 10$ mD lead to an almost homogeneous pore pressure depletion throughout the compartment while lower permeabilities (Fig. 9-47, c) result in a distinct depression cone. Apart from the direct effect of depletion-induced loading of the fault (Eq. 4.4 and 4.5), the pore pressure depletion cone governs the bulk compaction of the reservoir (Fig. 9-47 d,e). For instance, widespread compaction associated to the high reservoir permeability induces a stronger loading of the fault above the reservoir (Fig. 9-47 a). Within the reservoir, the direct effect of the permeability variation on pore pressure and fault loading is smaller than expected (Fig. 9-47 a-c), but may be overprinted by the effect of the different strain fields (Fig. 9-47 d,e)

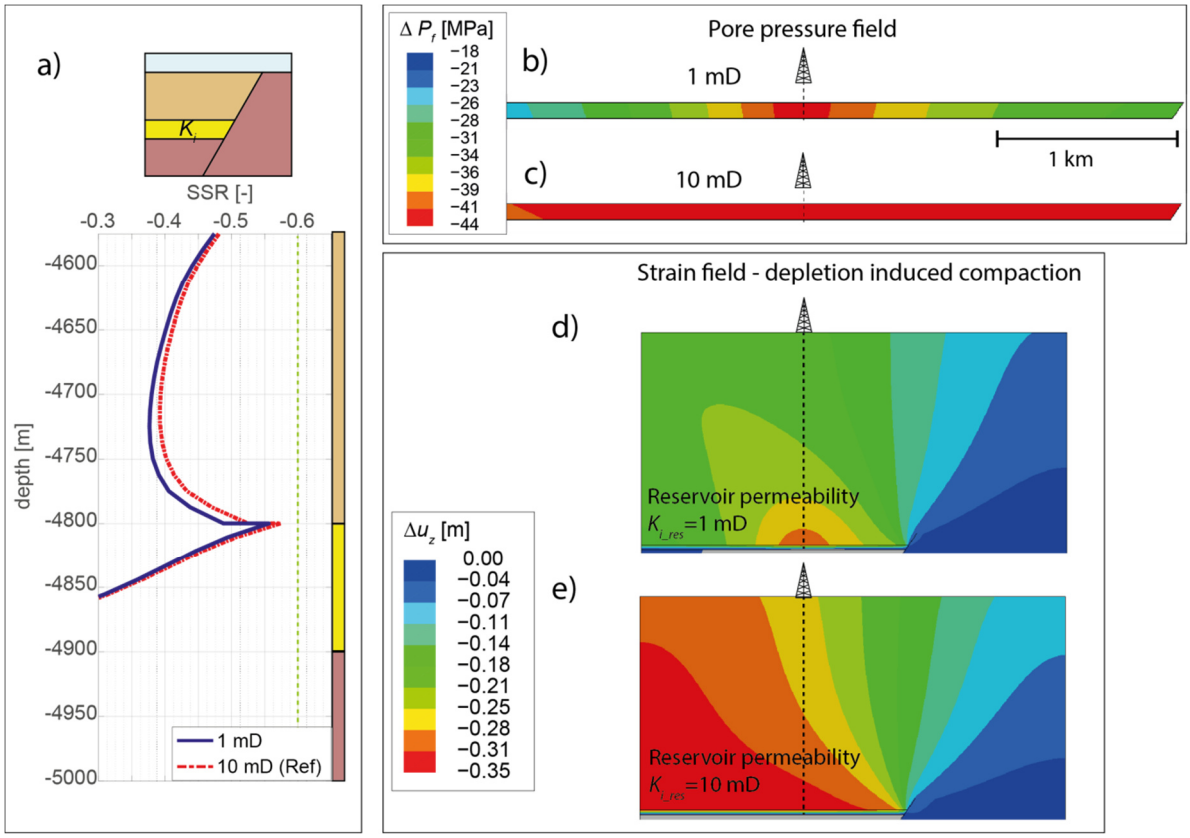

Fig. 9-47: a) Fault-loading for different reservoir permeabilities. The full depletion magnitude of 43.5 MPa extends over the entire reservoir for a permeability of K_i = 10 mD (b) while lower permeabilities result in a distinct depression cone (c). The different extend of the pore pressure perturbation results in significantly different strain fields (d,e).

Undrained conditions

Depletion of the reservoir and the associated tendency of the reservoir to contract, causes compatibility stresses, i.e tension and compression in the reservoir surroundings according to the stress arching effect (cp. Fig. 4-17). If this loading occurs too fast with respect to the medium's permeability and thus its capacity to dissipate pore pressure perturbations, compressive stresses cause a localized increase in pore pressure. Technically, the simulation of undrained conditions in the fully coupled procedure corresponds to the omission of fixed pore pressure boundary conditions in the low permeable over- and underburden (cp. section 7.4.2). Figure 9-48 a,b) shows the undrained pore pressure changes in the reservoir surrounding rocks for different burden permeabilities. Low permeability of the sand-shale caprock succession leads to a pore pressure build-up on the fault section above the reservoir Figure 9-48 c,d), reducing normal stress and leading to a slight enhancement of fault-loading, that does however not question fault integrity.

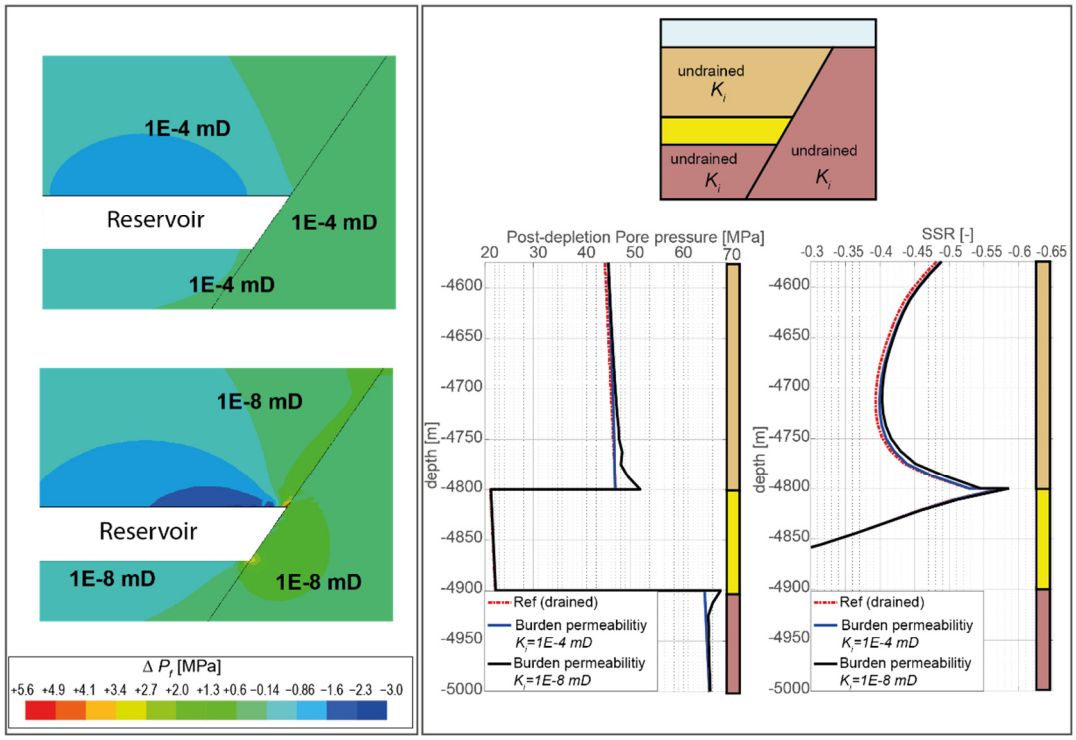

Fig. 9-48: a-b) Pore pressure changes in the burden associated to depletion induced reservoir strain, scaling with the permeability of the burden. a) Relative tension above a wide area of the reservoir result in a relative relaxation of pore pressure that dissipates as a function of permeability. b) Relative compression in the caprock close to the fault locally increases pore pressure. c-d) Effect of undrained burden conditions on the pore pressure and loading along the fault.

Summary parameter study

Figure 9-49 shows a summary of the parameter study, evaluating the maximum *SSR* value after 43.5 MPa pore pressure depletion for a range of parameter magnitudes that can be considered typical for the North German basin. The arrows point to the parameter variation that is more favourable for fault reactivation than the parameter magnitude located on the origin of the arrows. A low Biot-coefficient of the reservoir for instance results in a lower loading compared to the larger coefficient variation. The thickness of the arrow on the other hand indicates the relative impact of the parameter variation, fault-loading in the thick reservoir model variant for example is much stronger than in the less thick reservoir variant. For the dip of the fault a steeper orientation than predicted from classic tectonic considerations (e.g. Anderson 1951, Sibson 1985) is preferential but the rotation of principal stresses renders also a vertical fault unfavourable. The variation of the reservoir and overburden stiffnesses encompasses both, variations of the caprock with respect to the reservoir and the variation of the reservoir stiffness with respect to the burden. In Figure 9-49 the variation of stiffness is expressed by stiffness ratios as the modelling results infer critical load concentrations on the reservoir and adjacent fault sections as a function of relative, rather than absolute stiffness values.

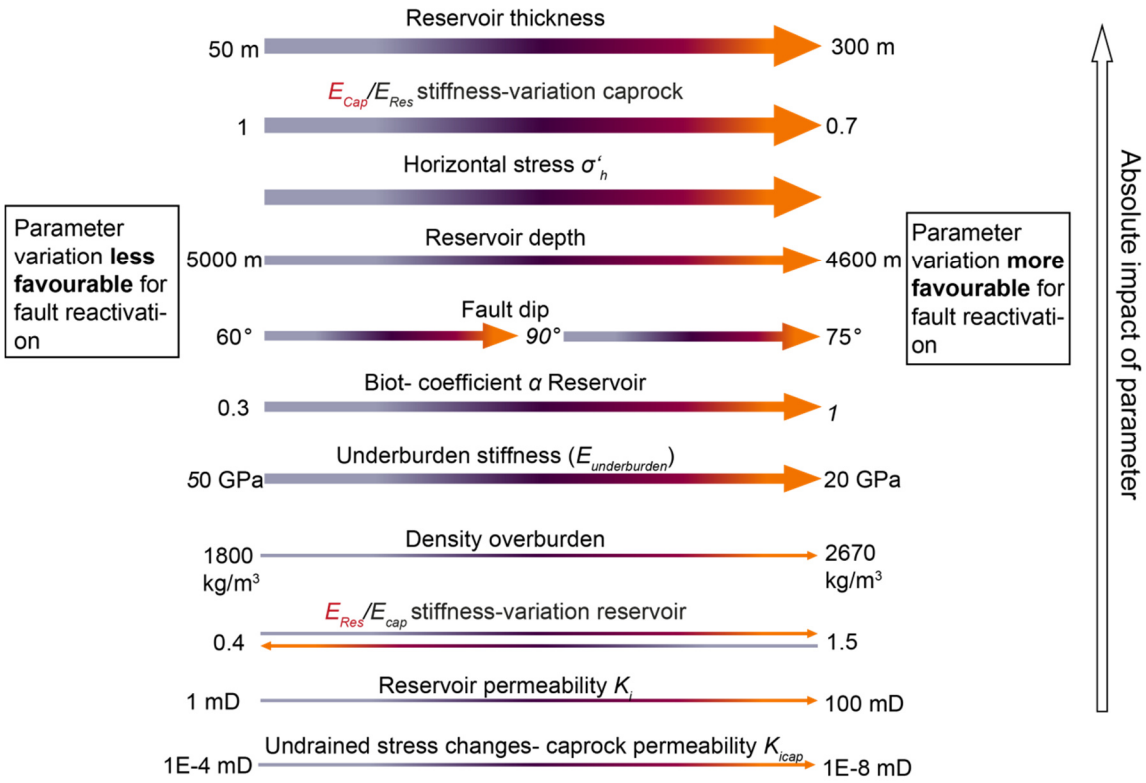

Fig. 9-49: Summary of the modelling results illustrating the impact of different parameter variations on fault-loading in single, graben fault-bounded reservoirs. The arrow points towards the parameter magnitude that shows a relatively larger tendency towards normal fault reactivation, the less favourable magnitude is indicated at the origin of the arrow. The thickness of the arrows indicates the relative impact of the parameter variation within the parameter space. The displayed parameters and magnitudes are evaluated with respect to their maximum *SSR* value after 43.5 MPa pore pressure depletion.

9.1.3 Model series I: Effect of viscoelastic overburden on production-induced stress changes

Figure 9-50 a) illustrates the modifications to the reference graben model in order to simulate the varying thickness of viscoelastic salt in the sedimentary sequence of the graben filling. First, the results indicate that production-related stress changes induced in the overburden are almost completely balanced by loading of the elastic O2 layer, stress changes within the viscous O1 layer are negligible for all tested thicknesses of layer O2 (Fig. 9-50 b,c). Second, the top of the O2-layer experiences a reduction of horizontal stress on the fault section (Fig. 9-50 b) that results in significantly increased *SSR* values above the reservoir at the interface to the salt (Fig. 9-50 c). The maximum of *SSR* decreases with increasing distance of the rock salt base to the top of the reservoir (Fig. 9-50 c).

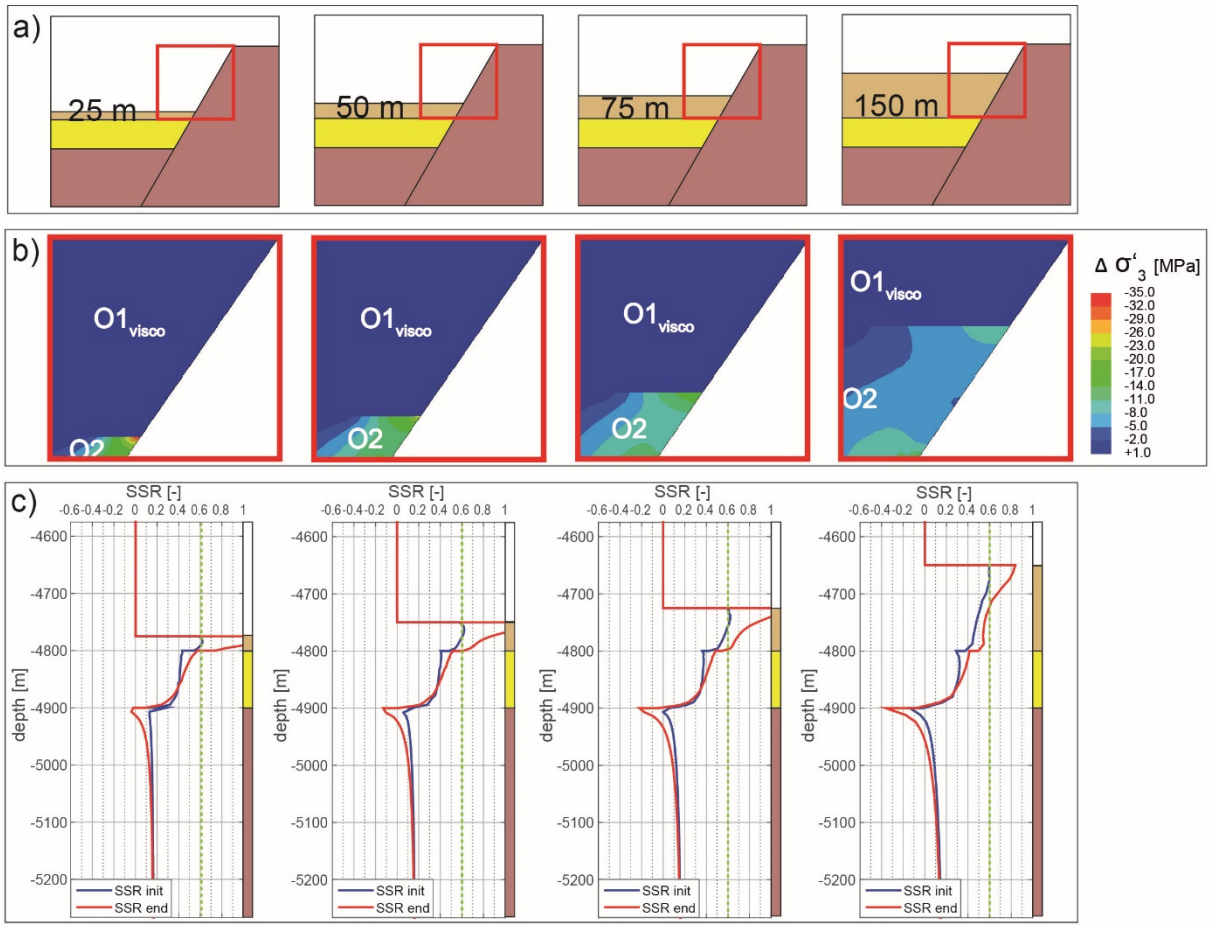

Fig. 9-50: a) Variation of the distance between the top of the reservoir and the base of the salt layer. b) Zoomed view on the production-induced change of the sub-horizontally oriented minimum principal stress σ'_3 within the intercalated layer O2 and the adjacent salt layer. c) *SSR* before and after depletion of 43.5 MPa for different distances of the reservoir top to the base salt layer. Within the salt layer the stress state remains isotropic (*SSR*=0).

9.1.4 Model Series II: Diapir models

Prior to production and after shear stresses in the salt have been relaxed during the second simulation step, the effective vertical stresses beneath the salt dome and the diapir flanks do not show significant lateral variation (Fig. 9-51 b,c), despite the simulated contrasts in density (Tab. 4). This results from overpressure in the salt diapir induced by stress transfer from the diapir flanks into the diapir centre (Fig. 9-51 a) as recently described by Heidari et al. (2017). As a result, the simulated vertical stress σ_{zz} in the salt diapir exceeds the theoretically calculated (Eq. 7.2) vertical stress σ_V (Fig. 9-51 d)

The diagrams in Fig. 9-51 d-g) document the mismatches between σ_V (Eq. 7.2), the modelled total vertical stress σ_{zz} and the total maximum principal stress σ_1. Accordingly, Equation (7.2) overestimates the vertical stress underneath the diapir flanks (Fig. 9-51 e,f), and underestimates it

below the centre of the diapir and beneath the transition zone of diapir flank and source layer (Fig. 9-51 d,g). The mismatch between σ_{zz} and σ_1 illustrated in Fig. 9-51 d-g) results from stress rotation along the almost shear stress-free salt diapir flank.

Effective vertical stresses σ'_{zz} are larger below the transition zone of source layer to diapir flank, compared to a position underneath the dome. This results in a concentration of differential stress beneath the transition zone, as indicated by local minima in the $K' = \sigma'_{xx}/\sigma'_{zz}$ curve in Figure 9-51 b). Small values of $K' = \sigma'_{xx}/\sigma'_{zz}$ mark an elevated reactivation potential towards normal faulting, in consequence, the models indicate a more critical state of stress beneath the diapir flanks and below the transition of flanks to source layer compared to positions at some distance to the diapir flanks (Fig. 9-51 b,c).

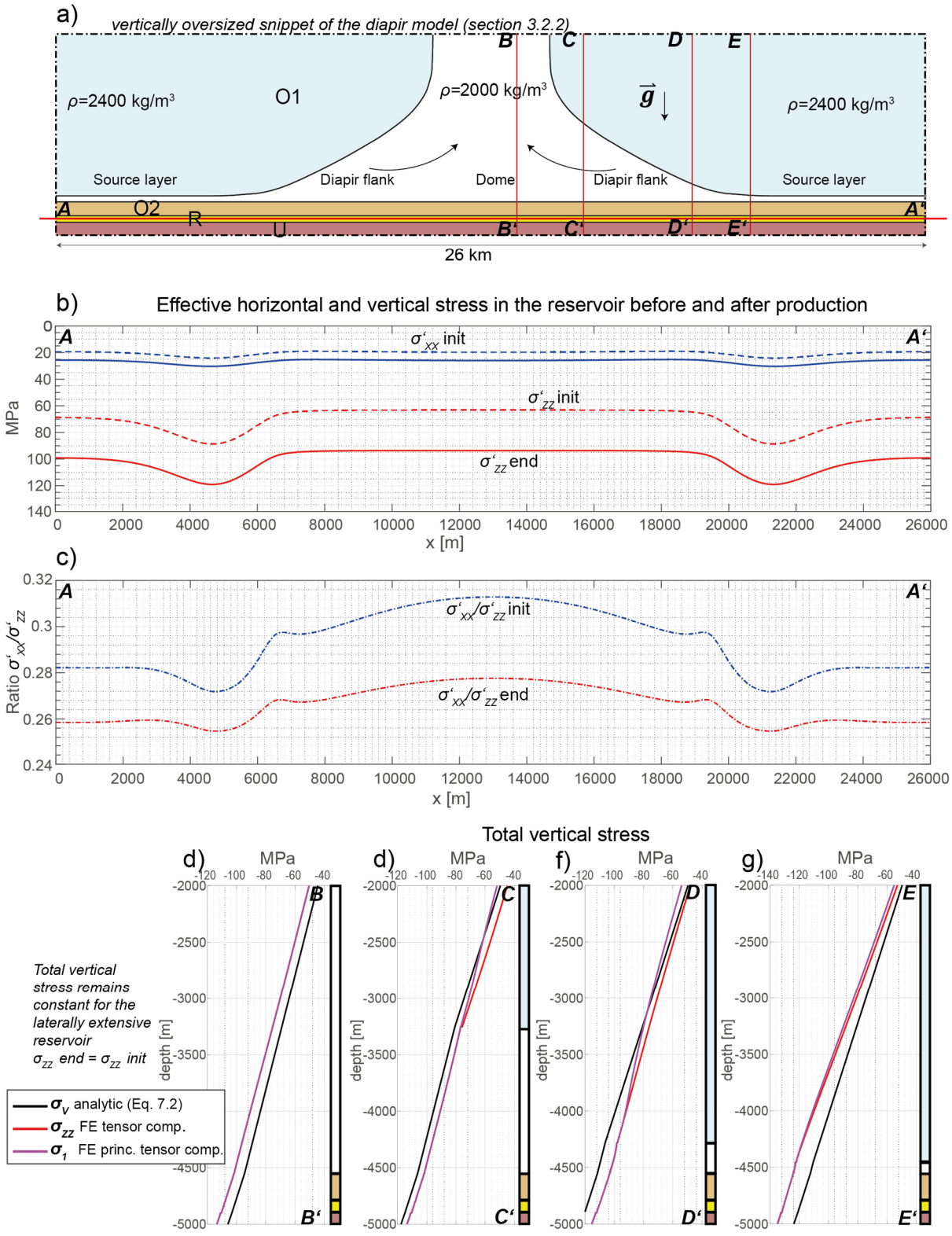

Fig. 9-51: a) Vertically oversized snippet of the reservoir underneath the diapir and the source layer. Arrows indicate the stress transfer from the diapir flanks and source layer to the diapir dome. b) Effective vertical and horizontal stress prior to and after pore pressure depletion of 43.5 MPa on a horizontal profile through the reservoir. c) Lateral variations of the effective vertical and horizontal stress result in a reduced ratio $K' = \sigma'_{xx}/\sigma'_{zz}$ beneath the flanks and an even lower ratio $K' = \sigma'_{xx}/\sigma'_{zz}$ below the transition zone of source layer to diapir flank. e-g) Vertical stress profiles, piercing different salt thicknesses, reveal a mismatch between predicted vertical

stress from depth integration of rock density and computed vertical stress magnitudes considering the viscoelastic diapir.

Analysis of stresses along normal faults located at different positions with respect to the salt diapir flanks (Fig. 9-52 a) confirms an elevated reactivation potential for fault segments beneath diapir flanks and the transition zone of diapir flanks to source layer compared to fault segments located at other positions (Fig. 9-52 b,c).

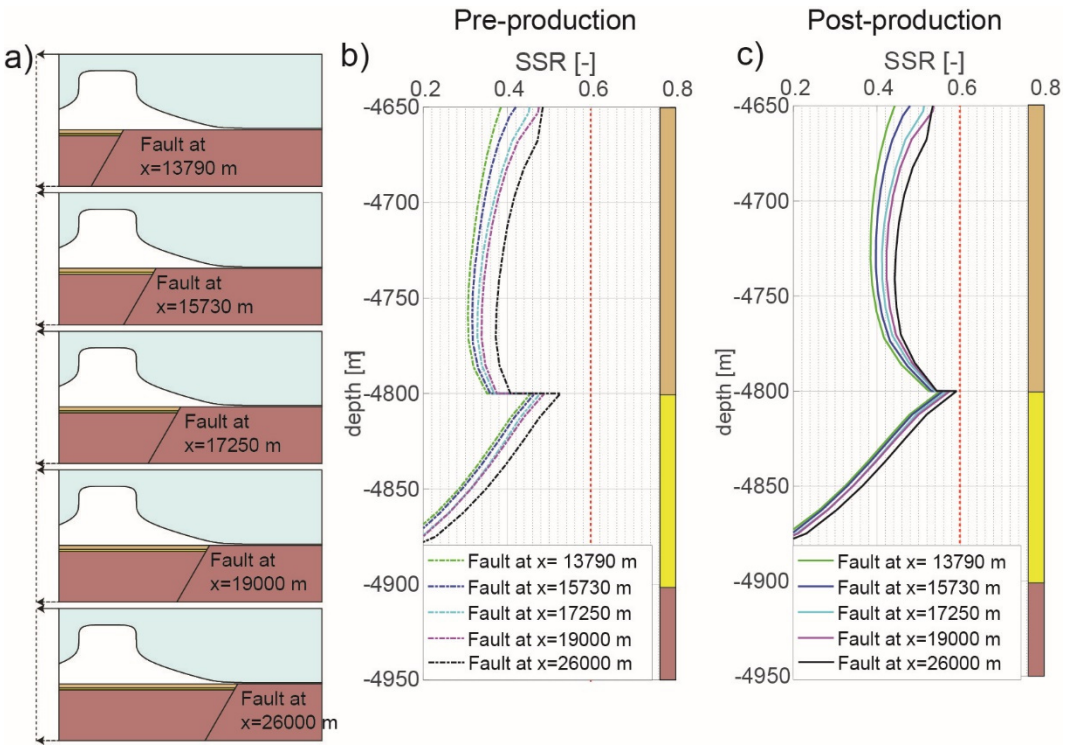

Fig. 9-52: a) Fault at different locations below the salt diapir. b) *SSR* along the fault prior to production, and c) *SSR* after pore pressure depletion of 43.5 MPa for different positions of the graben-bounding faults underneath a salt diapir.

Note that this model series provides first insight into the states of stress beneath diapiric salt layers in two dimensions. Accordingly, the presented plane strain approximation cannot account for complexities in stress fields expected to prevail beneath irregularly shaped salt domes in three dimensions.

9.1.5 Model Series III: Offset compartments

The results summarized in Figure 9-53 provide insights into how interference of production-induced stress redistributions in two offset compartments affect loading of the fault towards normal displacement of the hanging wall block. The following observations are important. (1) For a fault offset of less than the reservoir thickness (i.e. the reservoirs are partly juxtaposed), maximum fault-loading

is achieved when production is restricted to the footwall compartment. Overall, maximum *SSR* values are obtained for the case that fault throw is half of the reservoir thickness and production is exclusively from the footwall (Fig. 9-53 a-c). (2) If the fault throw is larger than the reservoir thickness, production from both compartments and from the footwall compartment result in similar *SSR* values along the fault (Fig. 9-53 a,b). (3) Production restricted to the hanging wall compartment always results in lowest *SSR* values, irrespective of fault throw (Fig. 9-53 c). (4) The depletion scenario most favourable for normal displacement of the footwall block depends on the fault dip (Fig. 9-53 d-f). Strongest loading occurs for a vertical fault if production is restricted to the hanging wall block. For depletion scenarios 1 and 2, the most favourable fault for reactivation dips at 75°. With decreasing offset, the strong loading from depletion scenarios 2 and 3 becomes relatively smaller Fig. 9-53 b).

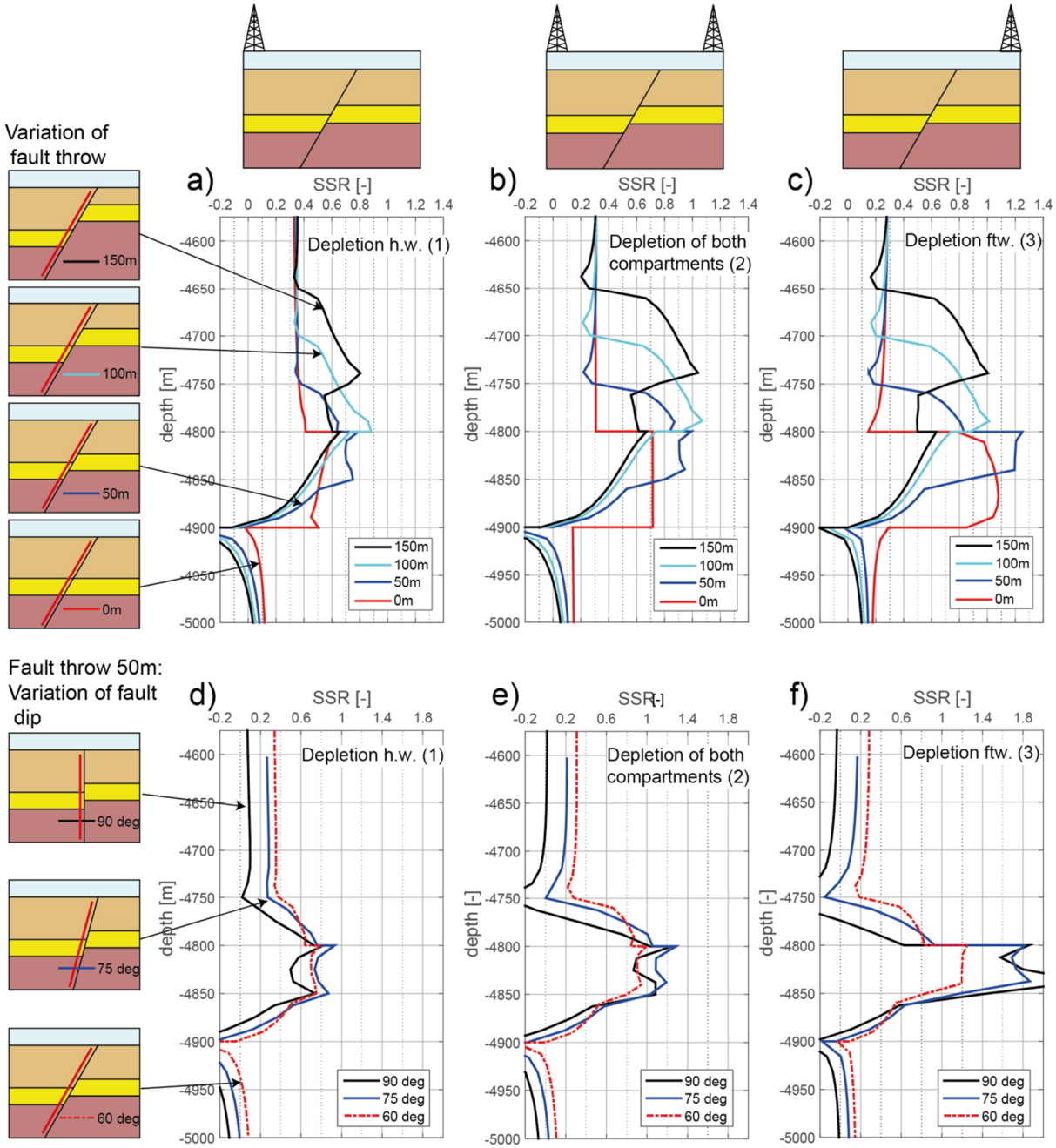

Fig. 9-53: Results of compartmentalized models. a-c): *SSR* value in the hanging wall block, varying fault throw and simulating 3 scenarios of 43.5 MPa pore pressure reduction. a) Depletion restricted to the hanging wall block (1), b) depletion of both compartments (2), c) depletion restricted to the footwall block (3). d-f) *SSR* values simulating 3 depletion scenarios on faults of varying dip.

9.2 Perspective: Fault Rupture in Model Series I and III

This section presents the results of the dynamic rupture investigation on critical stress states obtained in the simulation of production-induced fault-loading (section 9.1). The investigation is restricted to model series I and III as the distinct loading below the thinning flanks of the salt diapir of model series II (section 9.1.4) did not result in failure. In the fault-loading series, a constant lateral model confinement of 3 m (Fig. 8-39) was assumed as basin-wide far-field, i.e. initial stress state. For the juxtaposed compartments of model series III however, this lateral confinement renders the fault in an unstable stress state prior to production. In the assessment of fault-loading this initial criticality was negligible because the fault was not assigned a finite strength. For the dynamic fault rupture analysis however, fault strength is assumed to be μ_s=0.6 and a lateral push of 10 m is applied to provide a stable pre-production stress state for the identification of a critical depletion magnitude (cp. Fig. 8-43).

9.2.1 Model Series I

Figure 9-54 shows three potential rupture points in model series I and the influence of the decay parameter *d* (Eq. 8.2) on the propagation of slip. Negative slip magnitudes represent normal faulting and positive slip indicates fault reactivation in reverse mode. For illustration purposes, the stress state of the reference model after a depletion of 43.5 MPa is used in Figure 9-54. The reference model does in fact not reach criticality so the coefficient of friction was reduced to μ_s = 0.55. Results of slip propagation emphasize the strong influence of the velocity dependant decay of frictional resistance on the resulting rupture length (Fig. 9-54 b,d). The reduction in frictional resistance is accompanied by a shear stress drop during sliding (Fig. 9-54 c,e). At some distance to rupture point 2 and 3 (Fig. 9-54 a) the change in shear stress below the slip patch is partly associated to equilibrium computations during the dynamic procedure. That is, the initial prescribed stresses are not entirely balanced with respect to the undeformed model and applied loads. The disequilibrium is however considered negligible compared to the loading constituted by production-induced stresses.

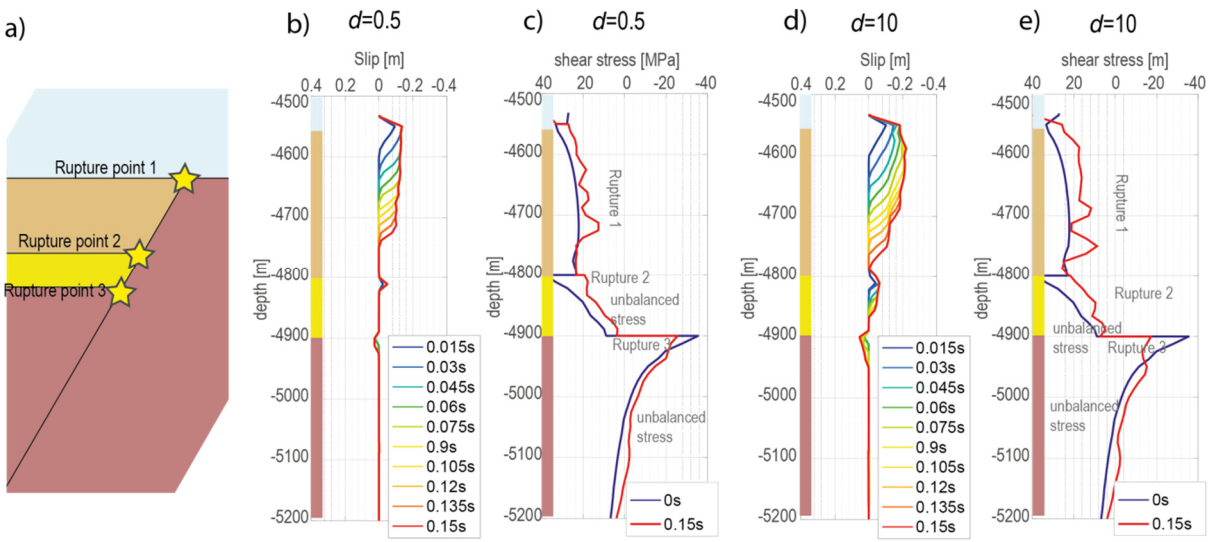

Fig. 9-54: a) Localization of three potential rupture points in the dynamic analysis. b) Dynamic fault slip for a decay coefficient of 0.5 and downward propagation of slip from rupture point 1. From rupture point 2, slip does not propagate. Negative slip magnitudes are associated to normal faulting; positive slip magnitudes indicate reverse faulting. b) Co-seismic shear stress drop along the slip path and shear stress changes associated to equilibrium computations. d) Downward slip is facilitated by the larger decay coefficient allowing the slip to propagate also from rupture point 2. e) Larger slip events result in larger magnitudes of the shear stress drop.

The three potential rupture points (Fig. 9-54 a) are in agreement with the modelling of fault-loading in section 9.1.2. The most prominent rupture occurs at the upper termination of the fault. Criticality here cannot be clearly allocated to either initial stress, production-induced stress and strain or the numerical issue of a terminating contact. From a geological point of view, the upper fault tip of the graben fault may well undergo syn-compactional stressing, but a nucleation at the fault tip is considered improbable. Subsequently, faults of the graben models were assigned a larger static friction coefficient μ_s=0.55 in direct vicinity to the graben edge, to prevent nucleation and downward propagation from the upper fault tip. Production-induced fault slip is associated predominantly to rupture point 2 and partly to reverse reactivation at rupture point 3 (Fig. 9-54 a).

Figure 9-55 shows dynamic fault slip of parameter variations that underwent critical stressing in the fault-loading analysis of model series I (section 9.1.2). The critical pore pressure depletion magnitude is indicated in Figure 9-55 for each model variation. Except for the two models covering the large reservoir Biot-coefficient and addressing low far-field stress, slip is propagating predominantly downwards (Fig. 9-55 a,f). The mentioned two parameters show a large rupture length but small slip magnitudes. This can be explained by a comparatively small load at rupture initiation but a homogeneous stress state on the fault that favours rupture propagation, i.e. low far field stresses exert low normal stresses on wide sections of the fault. For the steeply dipping 75° fault, rupture does not propagate and for the low overburden stiffness nucleation cannot be observed (Fig. 9-55 b,e). The

model variations addressing the thick reservoir horizon and the distance of 150 m between salt and reservoir exhibit particularly large events (Fig. 9-55 c,i).

The proximity of the reservoir top-boundary to the stress perturbation on the edge of the graben significantly influences the initiation of rupture above the reservoir; this applies for the model variants of the thick reservoir horizon and the shallow reservoir position (Fig. 9-55 c,d). Above the thick reservoir variant, a second rupture initiates that superposes with the slip of the first rupture (Fig. 9-55 c). The event proceeds during a relatively longer time period of 0.3s and the rupture length implies that the stress state within the thick reservoir does not pose a significant resistance to slip propagation (Fig. 9-55 c). Downward propagation is limited in all cases by the reverse tendency below the reservoir. The variation of the caprock thickness, controlling the distance of the reservoir to the salt layer showed similar loading patterns (Fig. 9-50) and two geometric settings, a distance of 50 m and 150 m, are shown as an example(Fig. 9-55 h,i). Herein, large horizontal stresses within the salt entirely damp out any upward propagation through the fault section that is faced by the salt.

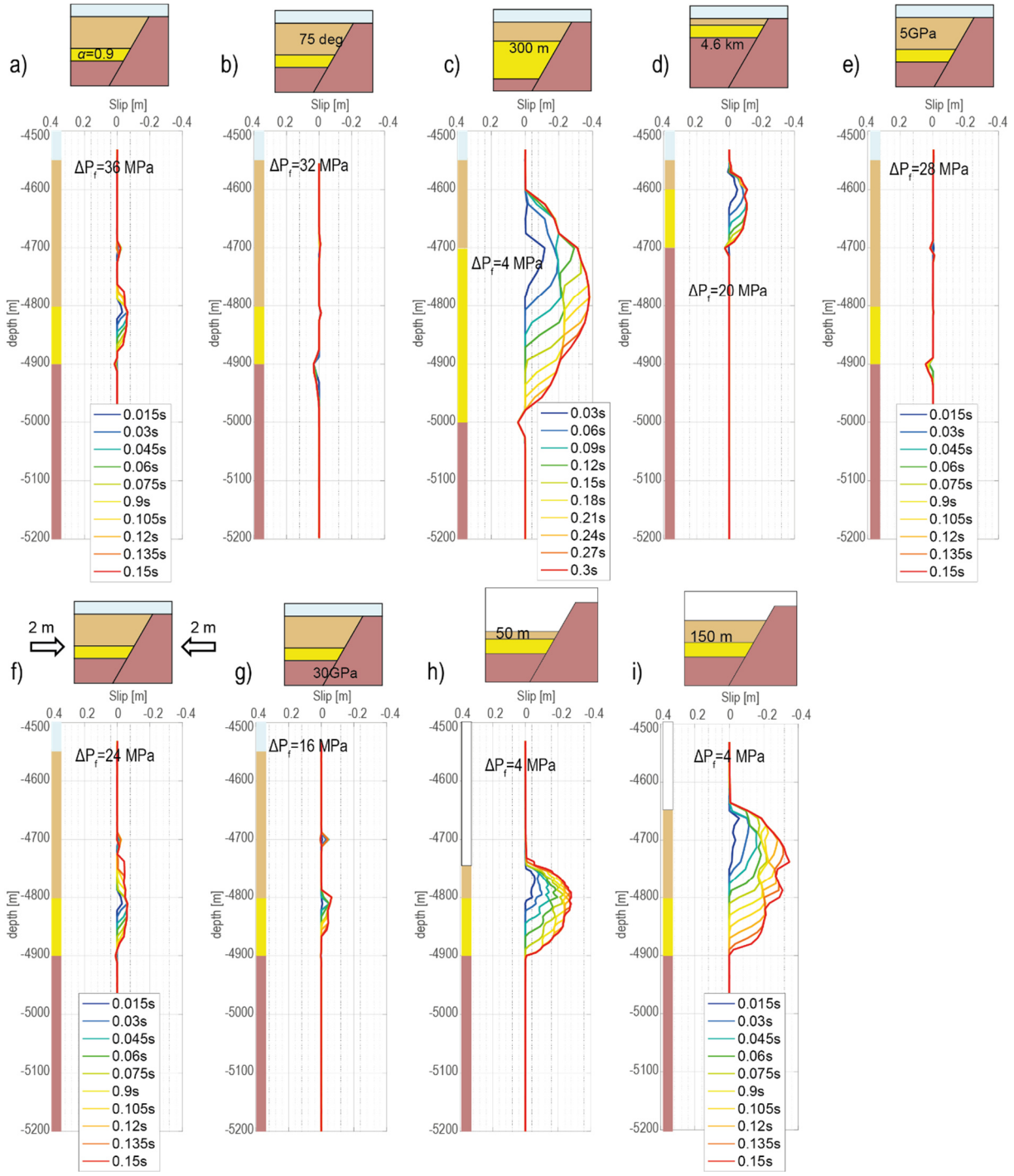

Fig. 9-55: Rupture propagation for different loading patterns, associated to critical stress states that were determined in the fault-loading analysis (section 9.1.2). The propagation of rupture reaches saturation after approximately 0.15 s in all model variations except for the combined rupture within and above the thick reservoir horizon (c). Negative slip magnitudes are associated to normal faulting; positive slip magnitudes indicate reverse faulting. The pore pressure depletion magnitude, indicating criticality in the poroelastic modelling, is annotated in all plots and marks the associated stress state that was used for the dynamic analysis.

9.2.2 Model Series III

Fault-loading investigations of section 9.1.5 revealed a strong impact of the production scheme on fault-loading and criticality. Thereby the production scenario primarily controls the required pore pressure drawdown to failure. However, the evaluation of corresponding slip, illustrated in Figure 9-56 reveals only slight differences in the rupture pattern for different production schemes (Fig. 9-56, e.g. c-e). Overall, largest seismic events can be observed for offsets of 50 and 100 m (Fig. 9-56 c-e, i-k).

For the compartment model of 50 offset, the rupture pattern is characterized by a wide initial rupture patch and large slip magnitudes, while the final length of rupture is comparatively limited (Fig. 9-56 c-e). The geometric setting of 100 m fault offset between hanging- and footwall compartment reveals a wide propagation of slip and a distinctive maximum slip magnitude for production scenario 3 (Fig. 9-56 k). In general, the intra- field setting exhibits the initiation of rupture on the lower level of the fault section that bounds the footwall block. From there, rupture propagates both, up- and downwards.

In the fault-loading analysis, the dip of the fault was previously varied for the setting of 50 m compartment-offset as this geometry returned the strongest loading in model series 3 (Fig. 9-53 d-f). Steeply dipping faults have shown an increased reactivation tendency in model series I and III compared to the theoretically favourable 60° dip. Simulated seismic events are however significantly smaller on the steep fault (Fig. 9-56 f-h), in accordance with results of the steep graben-bounding fault (Fig. 9-55 b) in the previous section.

The intra-field setting that considers a fault throw of 150 m (Fig. 9-56 l,m) exhibits comparatively larger reverse faulting events below the hanging wall compartment, supposedly as a consequence of the large horizontal push that was required to ensure non-criticality on the faults of the other compartment models, prior to production. The results show that the reverse reactivation of the fault below the reservoir propagates to a maximum depth of roughly 150 m below the reservoir (Fig. 9-56 m). At the same time, the extend of the rupture patch is restricted to the fault section bounding the footwall compartment and the fault section between the compartments remains stable (Fig. 9-55 h,m). This implies that the maximum rupture length can probably be assumed smaller than the fault throw between two depleting reservoir horizons.

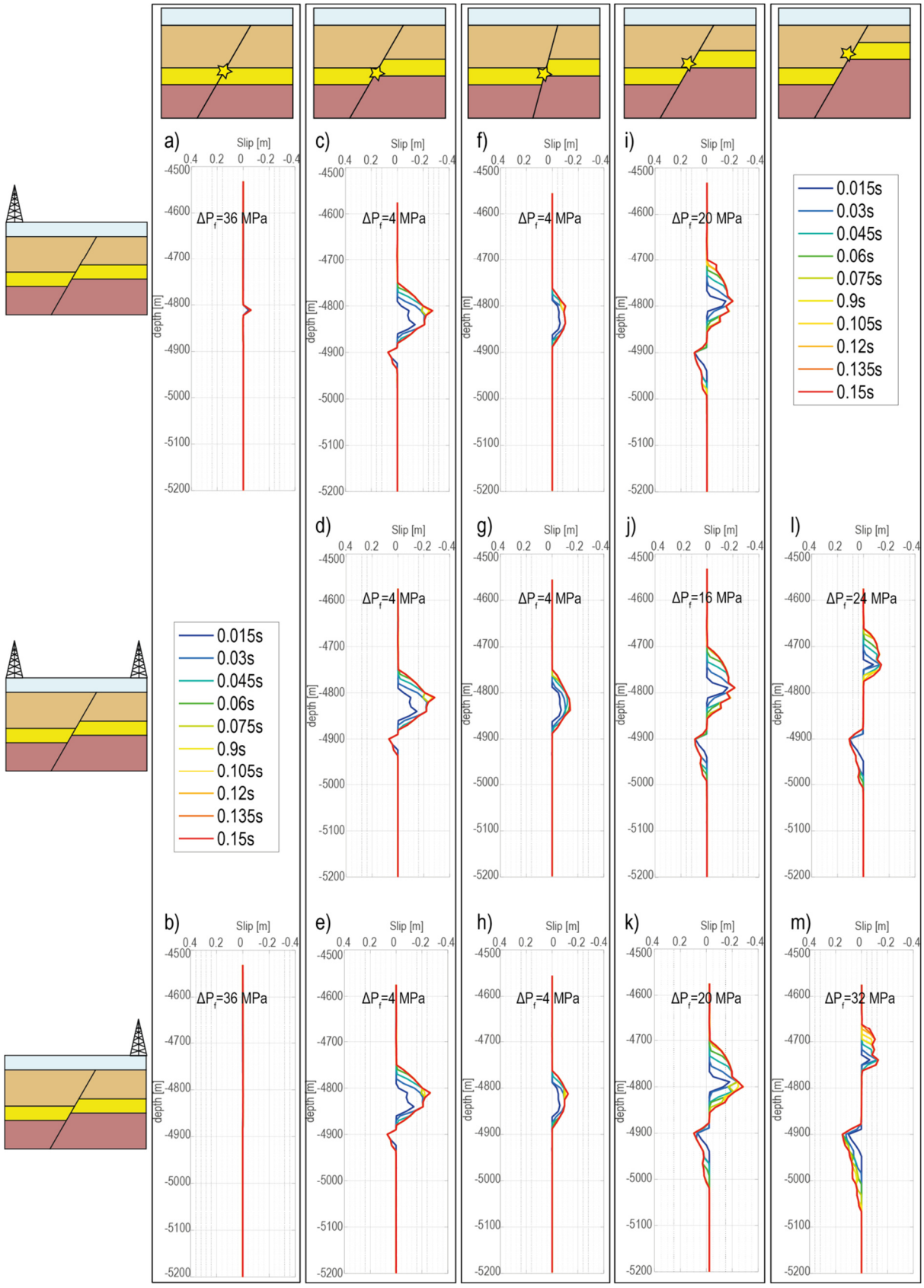

Fig. 9-56: Rupture length and slip magnitudes of the dynamic rupture analysis addressing the intra-field setting. The pore pressure depletion magnitude, indicating criticality in the poroelastic modelling, is annotated in all plots and marks the associated stress state that was used for the dynamic analysis. Model variations that did

not produce criticality during the depletion of 43.5 MPa are not shown. Negative slip magnitudes are associated to normal faulting; positive slip magnitudes indicate reverse faulting.

9.2.3 Long-term depletion effect

Prior to production, some models exhibit an initial stress state that is more proximate to failure than for other model variants. These models require hence only small pore pressure depletion magnitudes (4 MPa) to reach criticality (e.g. Fig. 9-55 c,h,I; Fig. 9-56 c-e, f-h). This section investigates the effect of depletion on dynamic rupture for model variants that showed an early reactivation of their fault. In consequence, the stress state after a pore pressure depletion of 43.5 MPa is applied in the dynamic analysis aiming to capture the effect of actual depletion over the impact of the initial stress state. From a geological point of view this approach considers either a locked fault or the occurrence of stable sliding (cp. section 2.9) during most of the depletion time. The results of this dynamic rupture analysis are illustrated in Figure 9-57 and show only small changes in the maximum slip magnitude as a function of ongoing depletion and almost identical final rupture lengths compared to fault reactivation at lower depletion magnitudes. As the effect of depletion is clearly reflected by the larger width and larger slip magnitude of the initial rupture patch (Fig. 9-57), the final rupture length seems to be predominantly governed by either geologic limits or a dominant influence of the far-field stress state on the propagation of rupture.

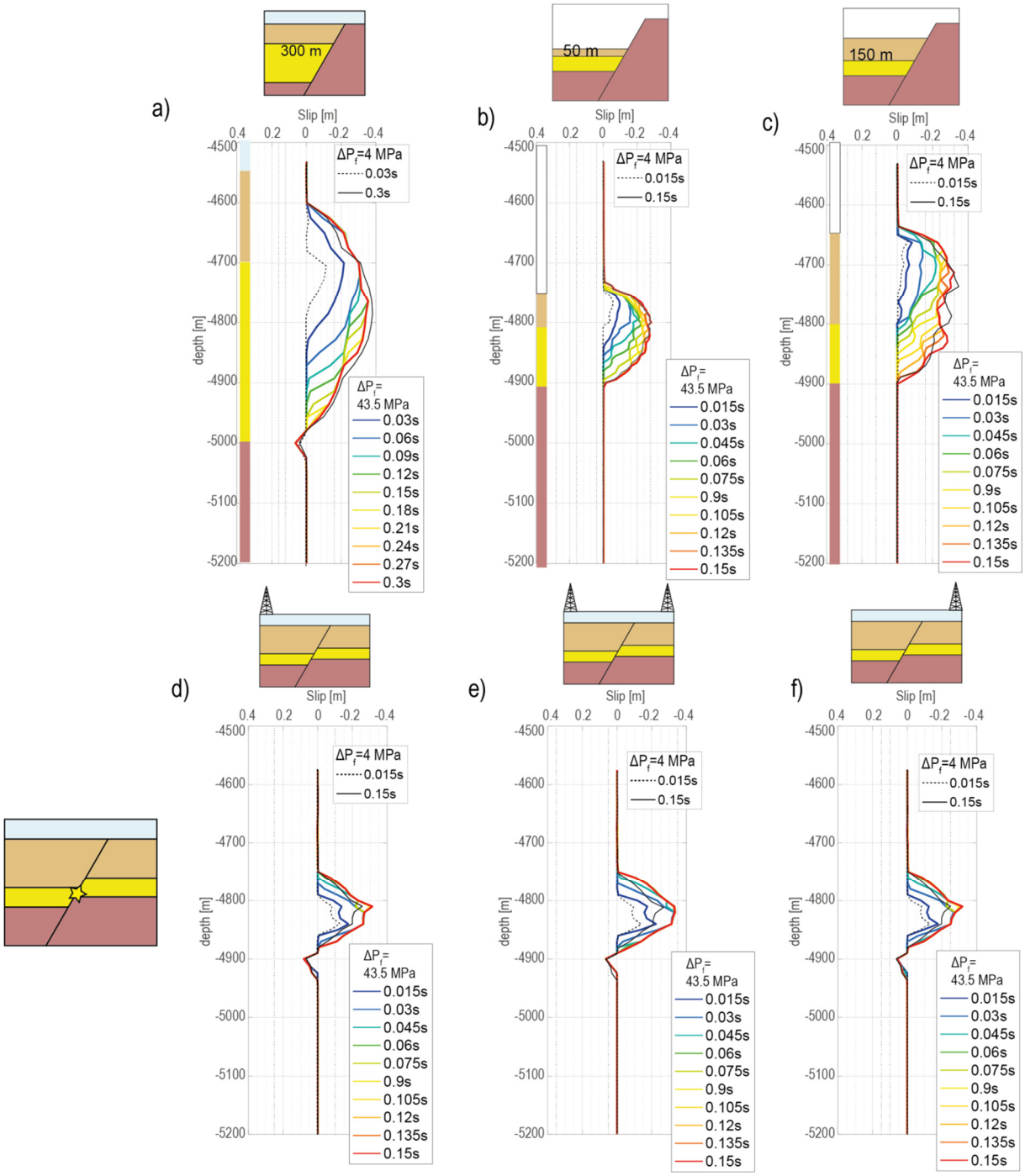

Fig. 9-57: Dynamic rupture after 43.5 MPa depletion of pore pressure for model variations that have otherwise shown criticality at a comparatively early stage of depletion (after 4 MPa) (cp. Figs. 9-55, 9-56). The initial rupture and final slip length associated to rupture after 4 MPa of depletion are indicated by a dashed and solid black line in order to compare the influence of depletion magnitudes and schemes on the pattern of seismic rupture.

10 Summary and Discussion

10.1 Summary of results

In this study, a series of 2D geomechanical FE models was created, inspired by Rotliegend gas reservoirs of the North German basin, to investigate stress changes and potential fault reactivation arising from the decrease of pore pressure within the reservoir horizon. The tendency towards normal fault reactivation was investigated for a parameter space of reservoir depth, reservoir thickness, mechanical and hydraulic reservoir and host rock properties, and compartment geometries, aiming to improve the understanding of production-induced seismicity and to identify geological parameters that may favour the occurrence of seismicity in North German Rotliegend gas fields. Three different settings were investigated in order to capture distinct features of the local geology such as varying thickness of evaporites in the overburden, and compartmentalized reservoir horizons offset by sealing faults.

A graben setting served as a reference scenario. Herein different parameters were varied within a range considered typical for north German gas fields, to evaluate their influence on production-induced stresses and fault-loading. A particular loading of the graben-fault was observed for thick reservoir horizons, steeply dipping faults, low reservoir depths, a large Biot-coefficient of the reservoir, low magnitudes of the horizontal far-field stress (Fig. 9-45 a-d,f), a large stiffness contrast between reservoir and caprock, and a reduced stiffness of the volcanic underburden rocks (Fig. 9-46 a,c). Moreover the fault section along the caprock of the reservoir takes up a significant loading, when the production-induced redistribution of stresses is limited by shear-free viscoelastic salt in vertical proximity to the reservoir (Fig. 9-50 a-c). The incorporation of an idealized viscoelastic salt diapir into the model revealed favourable locations for production-induced fault reactivation below the transition of the diapir flanks to the thinning source layer (Figs. 9-51, 9-52).

In a second setting, reservoir compartments offset along impermeable intra-field faults were investigated. For a large range of parameter variations the graben fault bounding a single reservoir (Fig. 8-38 a) experiences a much smaller loading compared to the intra-field fault (Fig. 8-38 c). Especially short offsets (equal or less than reservoir height), rendering the compartments partly juxtaposed, and production schemes that deplete either the footwall or both compartments pose favourable scenarios for fault reactivation. An important finding from both, graben and compartment models is the pronounced loading of steeply dipping faults.

In order to translate critical fault-loading patterns into coseismic slip and account for the effective decoupled loading along sealing faults, a second modelling approach was introduced (Fig. 8-43).

Reaching a respective critical depletion magnitude, the poroelastic stresses were transferred into a dynamic analysis, simulating fault slip on a contact fault whose resistance to sliding weakened as a function of slip velocity.

Three potential rupture points were identified whereby the production-induced loading reactivates the fault at the upper boundary of the compacting reservoir (Fig. 9-54 a). Rupture propagates either downwards or in both directions, i.e. up and downwards, depending on the given parameter variation and reservoir geometry (Fig. 9-54). The corresponding rupture area and the maximum slip magnitude depend on the parameter-specific critical load, the stress state along the fault and its modifications by production that altogether may result in an inhibition or enhancement of rupture propagation. For instance, the fault section along the thick reservoir model variant poses little resistance to sliding and produces a large seismic event (Fig. 9-55 c). Low horizontal far field stresses allow for a wide upward propagation of slip but expose small absolute slip magnitudes (Fig. 9-55 f). Thereby geologic boundaries for the propagation of slip could be identified, deriving from large horizontal stresses within the salt above the reservoir (Fig. 9-55 h,i), and a reverse tendency of slip below the reservoir(Fig. 9-55 c).

In the intra-field setting, rupture initiates in the lower part of the fault section that bounds the footwall compartment and propagates up- and downwards (Fig. 9-56). The slip pattern is shown to be rather dominated by the overall stress state and the compartment offset than by either one of the tested production scenarios (Figs. 9-56, 9-57). For offsets larger than the reservoir height, slip does not propagate along the intermediate fault section that seperates the two compartments (Fig. 9-56 l,m), rendering potentially large events that scale with compartment offset improbable.

10.2 **Controversy on effective stress**

For reasons of simplicity, the Biot-coefficient in geomechanical studies is often assumed to be one. This is justified for high-porosity sediments (e.g. Ingraham et al. 2017) but reservoir sandstones commonly exhibit Biot-coefficients smaller than one (e.g. Zimmerman 1991). This study considers Biot-coefficients inferior to one, leading to a less critical but more realistic stress evolution within the reservoir during production.

The consideration of Biot-Willis effective stress in the FE-software ABAQUS and the evaluation of two alternative effective stress concepts for fault-loading addresses an issue that has so far gone widely unnoticed in modelling. The commonly taught concept of Biot-Willis effective stress applying for Biot-coefficients $\alpha < 1$ and Terzaghi effective stress for coefficients $\alpha = 1$ was presumed at the beginning of

the project. In consequence, the original mismatch of stress output with both effective stress formulations, encountered in earlier ABAQUS versions, led to major confusion.

The procedure used in ABAQUS originally addresses soil mechanical problems. Soil mechanics deals with granular materials that have a low bulk stiffness compared to their single grain constituents, expressed by a Biot-coefficient α = 1 (cp. section 6.1.1). Solid rocks on the other hand encompass similar compressibilites of their rock skeleton $1/K_d$ and their single grain constituents $1/K_g$. This results in a load decomposition between the two compressibilities (cp. section 6.4.4) and a reduced influence of the fluid pressure on the solid stress, expressed by coefficients $\alpha < 1$.

The Biot-Willis effective stress has been shown to correctly express the elastic stress-strain relationship of rocks subjected to a confining and pore pressure (cp. section 3.4.1 and 6.2). However, experimental studies have evidenced that failure of fluid infiltrated rock is governed by Terzaghi effective stress (e.g. Lade & Boer 1997, Garg & Nur 1973). In the simplest case the Biot-coefficient of the investigated rock is unity and the Biot-Willis and Terzaghi effective stress laws assume identical values. At first glance irritating, Terzaghi effective stress is not limited to the initially presumed case α=1 but defines also the yield and failure stress of rocks that exhibit smaller Biot-coefficients. As the Biot-coefficient affects the bulk deformation behaviour, Terzaghi effective stresses also scale with the Biot-coefficient (cp. section 6.4 and 6.5) but their magnitude is different than for the Biot-Willis concept that considers α directly.

Examples of computing the reservoir strain according to a given Biot-coefficient $\alpha < 1$ and evaluating Terzaghi effective stress for failure are *reservoir stress path* studies and the inclusion model of Segall & Fitzgerald (1998). In its original context, the *reservoir stress path* (e.g. Goulty 2003, Hettema et al. 1998, Ozan et al. 2011, Teufel et al. 1991) addresses the failure of porous sediments under large confining pressures. This refers to their nonlinear deformation associated to pore collapse and shear-enhanced compaction (cp. section 3.4.2). Similarly, experimental studies, promoting Terzaghi effective stress for failure investigate macroscopically intact rock (e.g. Dropek et al. 1978, Garg & Nur 1973, Handin et al. 1963). Two experimental studies by Byerlee (1967, 1975) indicate that the 'wet' frictional strength of discontinuities plots on the Coulomb failure line $\tau = c_0 + 0.6(\sigma_n - P_f)$ (cp. section 2.8.2) which considers an effective normal stress according to Terzaghi's law. However, this finding encompasses first, assumptions on frictional fault strength and second, the deviation of data from the ideal failure line may correlate with stresses associated to large Biot coefficients (e.g. α = 0.8). Simultaneously, the author omits to state the Biot-coefficient of the tested specimens. In the light of little evidence that Terzaghi effective stress governs the reactivation of faults and because of the incompatibility of Terzaghi effective stress with various technical aspects of the

modelling, (cp. section 7.1.2) macro-scale processes of fault reactivation are associated to Biot-Willis effective stress in this study. While on the macro-scale fault reactivation is assumed to scale with deformation, the processes on a smaller scale, within the fault wear, may be governed by the irreversible loss of porosity that is appropriately described by Terzaghi effective stress.

For the multiphysics tool ABAQUS the deployment of a particular fault reactivation mechanism is clearly out of scope and the software cannot cover and document any specific application. However, changing the effective stress output and maintaining Terzaghi's law for failure while omitting any update or clarification of this in the User guide poses a rather inconsistent approach to the issue of effective stress.

10.3 Constraints on the numerical fault

Stress build-up across the fault, induced by the depletion of different compartments depends strongly on the hydraulic properties of the fault (e.g. Vilarrasa et al. 2016) and its representation in the numerical model (e.g. Rutqvist et al. 2016). It is known from field observations that despite varying thicknesses of damage zones (e.g. Faulkner et al. 2010, Mitchell & Faulkner 2009) the major portion of strain and displacement is cumulated in a fault core of several centimetres of width (Sibson 2003). This suggests that the representation of faults by discrete contact surfaces, allowing for relative displacements within the model, is an appropriate numerical approach. However, acting as a fluid baffle, the mesh discontinuity produces also a discontinuous pore pressure field between depleted and undepleted compartments. At the same time, the normal constraint on the contact fault requires an approximate balance of contact pressures on either side of the contact interface (cp. section 7.2.1). From a geologic point of view, tectonic stresses are total stresses and the total normal stress should be continuous on a large scale across faults (e.g. Segall & Fitzgerald 1998).

The continuum based FE modelling provides a continuous total stress field (e.g. Lewis & Schrefler 1999), serving as an explanation for the significantly different slip and loading patterns when the effective continuity condition applies (cp. section 7.2.3), (Fig. 10-58 b,c). While the constraint on normal stress continuity arises from the representation of the fault by contact, the mechanism of faulting is in the literature clearly associated to effective stresses (e.g. Zoback 2007). In conclusion, the contact fault should provide continuity in total stress and reactivation in terms of effective stress. Figure 10-58 illustrates the dilemma of the fault representation by contact graphically. The sealing fault maintains continuity in total stress (Fig. 7-31) and is reactivated in terms of total stress (Fig. 7-32). The impermeable contact fault that sustains effective continuity is reactivated in terms of Terzaghi effective stress which is incompatible with a stable initial stress state for the given model

properties (cp. section 7.1). For the evaluation of total stress (Fig. 10-58 b), fault slip occurs within the reservoir as a consequence of the depletion-induced reduction of total horizontal stress (cp. section 4.2). For effective stress, compaction-induced slip occurs predominantly above the reservoir (Fig. 10-58 c) as the reservoir fault section, subject to direct effective stress changes, has been shown a tendency to stabilize, when evaluated in terms of Terzaghi effective stress (cp. Fig. 7-33). It is important to note that the different results do not only arise from the distinction between (Terzaghi) effective stress and total stress but from the dependency of the local stress state on the continuity condition of the contact fault during depletion.

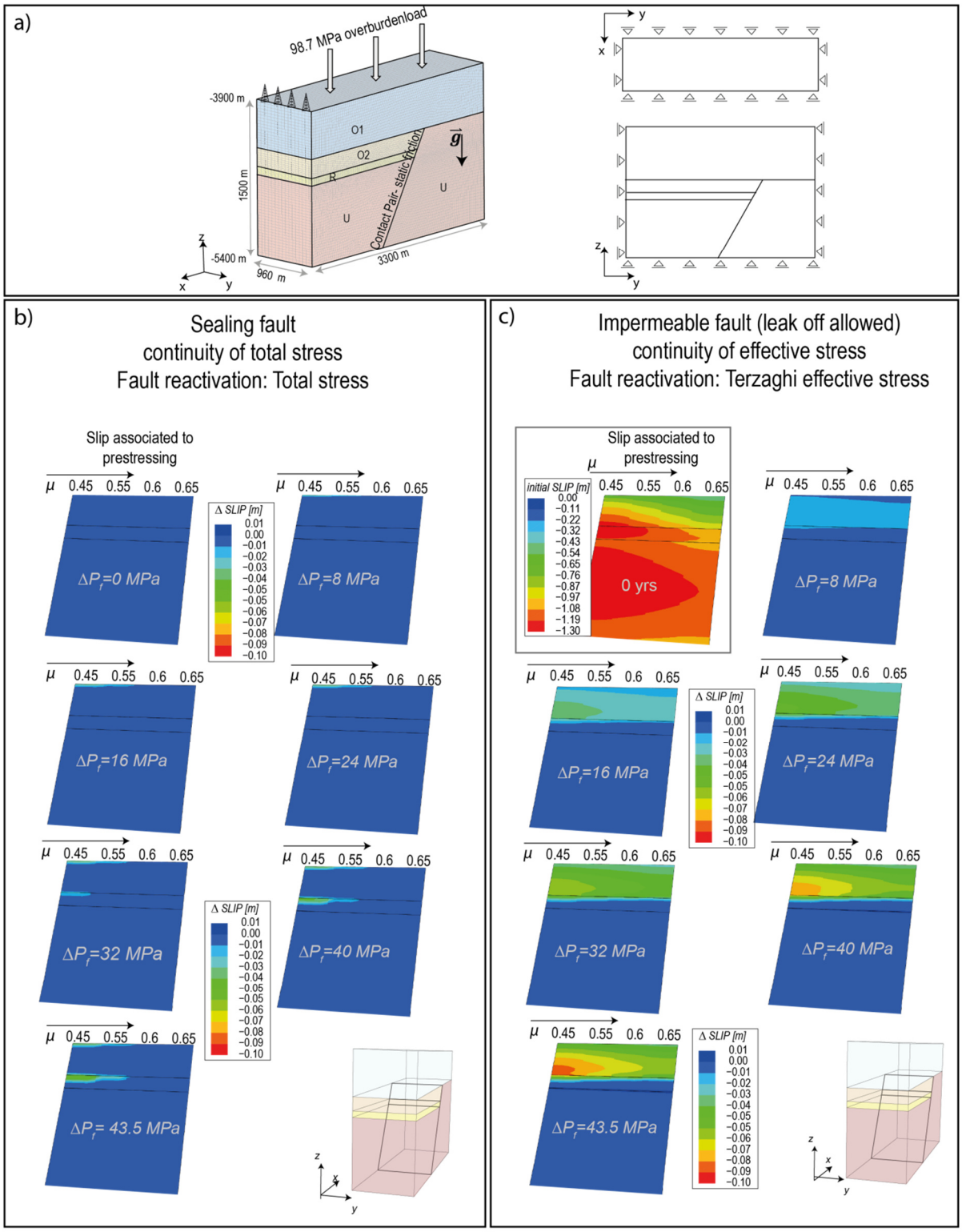

Fig. 10-58: a) Schematic sketch of the 3D contact model and its boundary conditions. The frictional constraint on the fault is represented by a constant coefficient of static friction whose magnitude is varied along the strike of the fault. b) Resulting contact slip in terms of total stress on the sealing fault. The fault slip is a function of pore pressure depletion and the frictional strength of the fault. In the presented case, the fault is reactivated after 34 MPa pore pressure depletion. c) Contact slip governed by Terzaghi effective stress leads to an initially unstable stress state on the fault. Production causes a reactivation of the fault section above the reservoir after negligible depletion magnitudes. Both models encompass the same total pre-production stress state as their

boundary conditions are identical. After production starts, the stress state on the contact is affected by the respective continuity condition for normal stresses.

In order to sail around the incompatibility of effective fault reactivation and a continuous total stress field, the sealing contact fault was locked and the evolution of shear and normal effective stresses were evaluated along the hanging wall fault plane, using the Biot-Willis concept of effective stress (Fig. 9-44 a,b). The sealing contact fault thereby allows for the decoupled build-up of effective stress on opposite sides of the fault. That is, normal effective stresses are discontinuous and induce moments on the fault that are not accounted for in the assessment of normal displacements of the footwall block. Confronted with the same issue in the modelling of fault slip on FE discontinuities, Jha & Juanes (2014) introduced a '*first come first serve'* principle, stating that whatever side of the fault becomes critical first, determines the stability of the fault. Figure 10-59 exemplarily shows the evaluation of this principle for the intra-field model of 100 m compartment offset. Production from the hanging wall compartment (scenario 1) produces unstable stresses on the footwall-side first, depletion of either both compartments (scenario 2) or the right compartment (scenario 3) result in critical stresses on the hanging wall-side of the fault.

All offset models were investigated with respect to criticality on either side of the fault. This investigation revealed that the assessment of criticality on the hanging wall side of the fault is justified for production scenario 2 and 3 while in scenario 1, the footwall block experiences a stronger loading. As production scenario 1 affects the fault stability significantly less than scenarios 2 and 3, the evaluation of the hanging wall block as displayed in Figure 9-53 captures essential fault-loading tendencies.

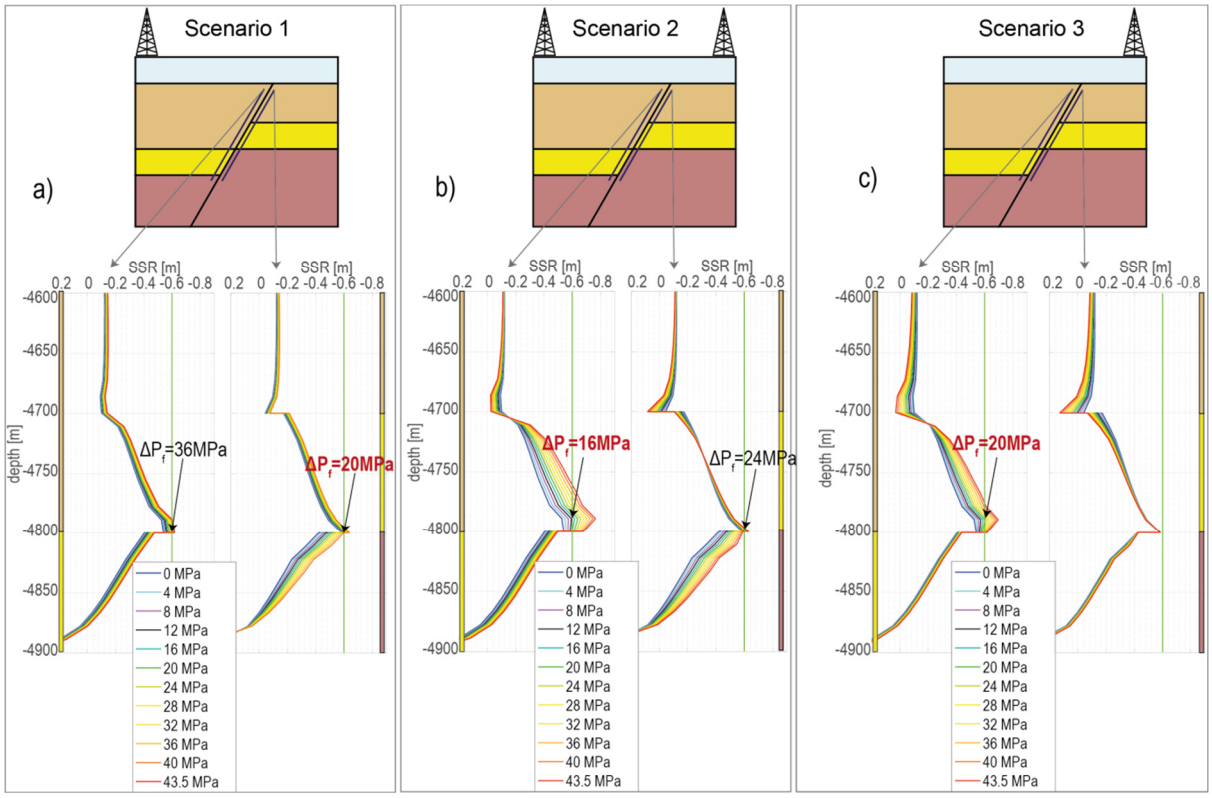

Fig. 10-59: Evaluation of *SSR* in terms of Biot-Willis effective stress on a locked sealing fault that exhibits a compartment offset of 100 m. a) Production scenario 1, the depletion of the hanging wall block induces a critical fault-loading first within the footwall block. b) Production scenario 2, the depletion of both compartments equally leads to preferred reactivation in the hanging wall block. c) Production scenario 3, the depletion of the footwall block results in criticality in the hanging wall block only.

The decoupled loading of a discontinuity is incompatible with the physical Coulomb model for two dry surfaces in frictional contact. Instead, the decoupling reflects the modelling of an impermeable contact fault that maintains continuity in total normal stress and thereby avoids the reactivation in terms of Terzaghi effective stress. The occurrence of the decoupled loading sheds particular light on the major issue of representing (sealing) faults and their scale-dependant properties in geomechanical models appropriately.

In order to evaluate the complex loading pattern of the intra-field fault, the effect of decoupled loading is captured by transferring the Biot-Willis effective stress state to a dry dynamic contact model that allows for the release of the unbalanced loading in terms of dynamic fault slip (section 8.4).

The issues of decoupled stresses and the requirement of continuity in total stress across sealing contact faults have been successfully addressed in section 7.2.2, by representing the fault as a volumetric body instead of a discrete plane. If failure and slip were however to be evaluated in terms of plastic yielding in this approach, reactivation would again be governed by Terzaghi effective stress and would lack a defined slip localisation with respect to the thickness of the fault zone. Emerging

from previous experiences in the coupling of the mechanical simulator *FLAC3D* and the flow code *TOUGH2* (e.g. Rutqvist & Tsang 2002), Zbinden et al. (2017) consider a semipermeable volumetric fault zone comprising a fault core of *ubiquitous joint elements* that allows for localized directional slip, whereby the pore pressure field across the fault is computed in the external flow simulator. This strategy constitutes a sophisticated approach that should be considered for future modelling.

10.4 Discussion of fault-loading results

A critical stress state on a distinct fault that may lead to its reactivation arises from the superposition of man-made production-induced stress changes and an initial stress state, resulting from gravitation, the far-field tectonic stress field and its perturbations on faults and material contrasts (e.g. Yale 2003, Zang & Stephansson 2010, Zoback 1992).

For the implementation of initial stresses a horizontal confinement (Figs. 8-39, 8-40, 8-41) was applied, in opposition to other authors (e.g. Buijze et al. 2017, Jeanne et al. 2017, Orlic & Wassing 2013, Rinaldi et al. 2014, van Wees et al. 2014) who impose a fixed ratio of effective horizontal to effective vertical stress. The synthetic ratio $K' = \sigma'_{xx}/\sigma'_{zz}$ is an assumption that cannot account for realistic mechanical stratigraphies. This study sheds hence light on the strong stress perturbations that arise from the stiffness contrast of soft sediments and the stiff volcanic rock that constitutes the upper unit of the subsurface graben and horst topography. Here, the displacement of the lateral model boundaries is calibrated to non-criticality of the fault in the reference model and this displacement magnitude is used as far-field stress for all models, serving as a starting point for the parameter variations.

The presence of salt structures in vicinity to the producing reservoir horizons and their significant thickness variation could explain the focussing of production-induced seismicity to particular locations within the North German gas fields. Due to locally increased vertical stress (Fig. 9-51 b-e) the stress state below the transition of a salt diapir's flanks to its source layer is favourable for fault reactivation. Salt diapirism is also prominent in the Dutch part of the North German basin. For example Roest & Mulders (2003) report a small earthquake in the Eleveld gas field below the thinning flank of a salt diapir and van Eijs et al. (2006) discuss a correlation between active diapirism and seismicity.

In the area of investigation, variations in thickness of the sandstone-shale caprock succession control the distance of the reservoir horizon to the viscoelastic evaporite layers. Viscoelastic rock-salt and the intercalated sandstone-shale succession are attributed an identical instantaneous stiffness, yet production-induced stress changes do not propagate into the viscoelastic layer resulting in a

concentration of the stress redistribution within the elastic caprock as a function of its thickness (Fig. 9-50 a,b). In consequence, a pronounced loading of the fault section along the elastic caprock is observed for a relatively short distance (< 150 m) between the top of the reservoir and the base of the salt layer (Fig. 9-50 c). In supplementation to earlier studies that considered viscoelastic salt in the overburden and reported unstable conditions prior to production (e.g. Orlic & Wassing 2013, Wassing et al. 2017), the stressing of salt-adjacent layers during relaxation was in this study limited by Mohr-Coulomb plasticity. This rendered the pre-production stress state non-critical and accounts for the large strain imposed on adjacent layers during the diapiric rise of salt. During the comparatively short production time, all non-viscous layers were re-assigned elastic properties. In sum, the pore-elastoplastic approach allowed to better capture production-induced stress changes that have otherwise been overprinted by initial slip of the fault.

The stiffness contrast between reservoir and surrounding rocks governs the distribution of the production-induced loading and the degree of rotation of the principal stresses being favourable or unfavourable for fault reactivation. For the graben setting, the stiff graben shoulder impedes normal faulting compared to a lower stiffness that may be associated to softer volcanic rocks, following the extrusions that constitute the underburden to the model reservoir (Figs. 8-37 b, 9-46 a). Investigating stiffness contrasts of the sedimentary graben filling, the loading of the fault concentrates within the respectively stiffer formation. A particularly strong loading of the fault occurs on the upper fault section of the reservoir if the overburden stiffness is inferior to the reservoir stiffness (Fig. 9-46 b,c).

Reservoir compaction and the assimilation of strain on normal faults can serve as a first-order explanation for production-induced fault reactivation and associated seismicity (e.g. van Thienen-Visser & Breunese 2015). For instance, the depletion of thick reservoir horizons results in a stronger fault-loading (Fig. 9-45 b) with respect to the depletion of less thick variants. This finding can be explained by a combination of two effects. First, similarly to the shallow reservoir variation (Fig. 9-45 a), the proximity of the upper boundary of the thick reservoir to the stress perturbation on the stiff graben shoulder renders the respective model faults more prone to fault reactivation. Second, the thick reservoir undergoes an absolutely larger vertical displacement, i.e. compaction compared to the less thick variation, given an identical decrease of pore pressure. In order to depict reservoir compaction appropriately, parameters for the modelling of potentially nonlinear deformation of the affected reservoir sandstone have to be retrieved by rock mechanical testing. The strain-hardening plastic deformation of porous reservoir sediments (e.g. Zoback 2007) may thereby result in a different loading pattern of the reservoir-bounding fault, associated to the modified bulk deformation of the reservoir (e.g. Boutéca et al. 2000, Ozan et al. 2011, Hettema et al. 1998).

In accordance with analytic poroelastic inclusion models (e.g. Segall & Fitzgerald 1998, Soltanzadeh & Hawkes 2008), the numerical results indicate a distinct loading pattern of the rocks surrounding the reservoir. In reality, stress arching and caprock loading may be partly compensated by fluid flow and pore pressure changes that cannot be resolved by the simple flow model of the herein presented simulations. The variation of reservoir permeability reveals the correlation between reservoir permeability, the extent of the pore pressure depression cone and resulting compaction-strain. Widespread compaction leads to a stronger loading of the fault section above the reservoir compared to a localized depression cone (Fig. 9-47). Here future models should either consult sophisticated reservoir simulations or apply production rates in place of the bottomhole pore pressure boundary condition. Production rates are the input parameter that can be directly manipulated in the operation of hydrocarbon fields and the pore pressure boundary condition returns different production rates, i.e. extracted fluid volumes, for different material properties, permeabilities and reservoir geometries.

Varying a large range of parameters, the single reservoir, bounded by a graben fault experiences a significantly smaller loading than the intra-field compartmentalizing fault, tested for different depletion schemes. For both model series, graben and compartment models, the pronounced loading of steeply dipping faults (Figs. 9-45 c, 9-53 d-f) is an important finding and can be explained by a dominant contribution of compaction-strain, and depletion-induced rotations of the principal stresses to the loading of the fault. Consequently, pore pressure depletion may reactivate faults that are considered unfavourable for reactivation in the prevailing tectonic stress field as identified for example by means of slip tendency analysis (e.g. Moeck et al. 2009). Moreover, the preferred reactivation of steeply dipping faults is in clear contrast to tectonic faulting and injection-induced fault reactivation (Vilarrasa et al. 2016) for which an inclination of approximately 30° with respect to the maximum principal stress represents the most favourable fault orientation.

For the intra-field setting, the production from either both compartments or the footwall compartment yield a relatively stronger loading than a depletion scheme limited to the hanging wall compartment. For these two critical production scenarios stress arching effects and their interference govern the critical loading of the fault. Particular loading occurs for a an offset geometry that considers partly-juxtaposed reservoir compartments (Fig. 9-53), a finding in general agreement with previous studies by Orlic & Wassing (2013) and van den Bogert (2015). For the partly juxtaposed compartments, depletion of the footwall compartment exerts a stress-arching-related vertical load to the overpressured hanging wall compartment. This load would partly be compensated by an increase of vertical and horizontal effective stresses within the hanging wall compartment if pore pressure decreased there as well. The effect of the corresponding depletion of both compartments is strongly geometry-dependent. Because hanging and footwall compartment compact equally for identical

production rates, differential compaction arises from the geometric offset. A decreasing compartment offset towards the configuration of entirely juxtaposed reservoir horizons results thus in a decreasing geometry-related loading. In the extreme case of negligible offset, production from both compartments results in congruent compaction of both compartments and differential compaction does not occur (cp. Fig. 9-53 a-c). For this case, the sealing properties of the fault are questionable (e.g. Knipe 1997), and criticality of the permeable fault could simply be derived from the *reservoir stress path* parameter.

In conclusion, the results from different parameter variations and the intra-field models point out that simple analytic or pointwise measured stress path parameters (e.g. Zoback & Zinke 2002) have very limited applicability and cannot be considered as characteristic field parameter for the assessment of field-wide seismic hazard in hydrocarbon production.

10.5 Discussion of dynamic rupture results

Earlier numerical investigations of fault slip considered a constant static coefficient of friction (Fig. 9-52) (e.g. van Wees et al. 2014). At failure, the fault showed ideal plastic behaviour, requiring additional loading, i.e. depletion, to extend the rupture (Buijze et al. 2017), (Fig. 7-32, this study). In the simulation of sudden earthquake ruptures, linear slip and cohesion-weakening friction have recently been introduced into the numerical assessment of production-induced seismicity (e.g. Buijze et al. 2017, Zbinden et al. 2017, Wassing et al. 2017). This approach encompasses a drop in shear stress and slip-dependant decrease of friction during sliding. In this study, an exponential decrease of static to dynamic friction is assumed (section 8.4). The exponential velocity-dependent weakening of friction poses a novel approach to the modelling of dynamic rupture in production-induced seismicity and addresses the velocity dependent nature of friction in earthquakes (cp. section 2.9). Furthermore, the dynamic modelling procedure in ABAQUS explicit accounts for the temporal derivatives of stresses (*ABQ 2016 Analysis guide 6.3*) and depicts effects of inertia on the acceleration of slip and slip propagation.

Investigation of post-failure fault slip on the graben-fault returned a selection of potential rupture points in agreement with critical fault sections of the preliminary fault-loading investigation (Fig. 9-54). Production-induced slip nucleates at the upper reservoir boundary and is observed to propagate either down or both, up- and downwards. The final rupture length depends on the acceleration of slip at rupture and the overall stress state on the fault that may inhibit or facilitate slip propagation.

For instance, in the model series investigating fault-loading as a function of the vertical distance between salt and reservoir, the viscoelastic salt poses an effective barrier to upward propagation of slip. Here, rupture initiates directly below the salt and propagates exclusively downwards as the pre-defined slip surface above the rupture point faces significantly larger normal stresses deriving from the isotropic stress state within the salt.

While isotropic stresses in the salt pose an ultimate limit for upward propagation of slip, downward propagation is impeded directly below the reservoir. Here the observed tendency for reverse faulting represents a potential location for the initiation of dextral slip, propagating to a maximum depth of about 150 m below the reservoir (Fig. 9-56 m). The observed reverse faulting tendency (Fig. 9-44 b-e) is enhanced by the large stiffness contrast between reservoir and underburden and may partly be associated to the removal of fluid mass that cannot be balanced by recharge of the reservoir. However, in the discussion on deep reverse faulting earthquakes below producing hydrocarbon fields, Segall (1985) demonstrated that the impact of mass removal on the subsurface stress state is negligible compared to poroelastic stresses at reservoir scale. In agreement with focal mechanisms (Uta 2017) and the normal faulting stress regime (Cornet & Röckel 2012), seismicity is driven by reservoir compaction questioning fault stability in terms of normal fault slip at the upper reservoir boundary and the reverse faulting tendency is neglected.

The onset of rupture at the upper fault tip (Fig. 9-54 a) cannot be clearly attributed to either production, the stress perturbation on the tapered, stiff graben shoulder or the numerical issue of terminating contact surfaces, and requires further investigation. While the elastic coupling of overburden sediments to the compacting reservoir may load the tip of the graben fault and rupture can extend the fault plane by propagating fractures at the fault tip (Cowie & Scholz 1992), the actual nucleation of a seismic events at the tip is considered unlikely and this rupture point is hence disregarded.

The previous study of production-induced fault-loading on compartmentalizing faults (sections 9.1.5) revealed significant differences in fault-loading between different production schemes and compartment offsets. The results of the dynamic rupture investigation however imply a merely small effect of the production scheme on the location and size of induced events. In order to enlighten the effect of depletion on rupture length and slip magnitude, model variations that experienced an early reactivation were allowed to rupture after a full depletion magnitude of 43.5 MPa. The results indicate a comparatively larger initial nucleation patch and a slightly increased maximum slip magnitude. The ultimate slip pattern however, is very similar for fault reactivation at small and large depletion magnitudes. This finding can be explained by two hypotheses. First the rupture decay coefficient (Eq.

8.2) is overestimated and thus insensitive to production. That is, the rupture at small depletion magnitudes, characterized by small initial rupture patches, results ultimately in the maximum rupture length as the decay coefficient facilitates propagation. The final rupture patch thus reflects the absolute maximum rupture length determined by the geological setting. Alternatively, magnitudes and distribution of the induced events may be dominated by the initial and locally modified far-field stress state that overprints the effect of depletion magnitude and scheme. The second statement is supported by a study of Dieterich et al. (2015) who draws a similar conclusion from the modelling of injection-induced earthquakes. With respect to the first hypotheses, an evolution of event magnitude, i.e. increasing magnitudes for delayed reactivation should be observed as ongoing depletion renders increasing fault patches in a stress state favourable for rupture propagation (e.g. Buijze et al. 2017). This effect may however be obscured by the mentioned overestimated propagation of slip, and the diverse, parameter-specific, initial stress state (cp. section7.1.2). Future works will address this issue by systematically investigating the decay and dynamic friction coefficient and by comparing the slip at different critical depletion magnitudes, based on a generic initial stress state (cp. section 7.1.2), to the observations of this study.

Because the onset of failure is an absolute prerequisite to earthquake rupture, the results of the fault-loading series have a relatively higher significance. For instance the finding that steep faults are more favourable for compaction-induced fault reactivation should be considered of higher relevance for seismic hazard assessment than the finding that rupture propagation along the steep fault was negligible. At this point, the dynamic rupture modelling still features several methodological limitations, along with a friction model that is poorly constrained.

Transferring Biot-Willis effective stress to the dry contact model produces a small loss of accuracy in the previously computed critical stresses. First, stresses are transferred from a poroelastic model that considers a decoupled stress field on a tied contact to a dry contact model that enforces contact constraints. Second, ABAQUS explicit provides only first-order reduced integration elements, leading to a decreased resolution of the previously computed stresses. Third, the rock densities implemented into the dry model produce a slight misfit between overburden-load and the Biot-Willis effective stresses. At last, the assessment of criticality in the fault-loading series has a poor resolution of 4 MPa depletion steps. In spite of these inaccuracies, the workflow captures essential characteristics of the seismic dissipation of production-induced stresses for the investigated scenarios.

Continuing studies on dynamic rupture should include the effect of nonlinear geometry in the evaluation of fault slip and benchmarking of the frictional model by means of literature, field and numerical studies. For the stress transfer from ABAQUS standard to explicit, the effect of rock density

has to be systematically assessed and compensated for in the dry model. Technically, the resolution of the FE mesh requires a higher resolution and moreover, a coupling of ABAQUS standard to explicit should be implemented in order to evaluate dynamic rupture at any time during the poroelastic procedure. For the computation of the seismic energy release and seismic moment, the modelling condition that all slip-associated strain energy is radiated as seismic energy must be further assessed.

.

11 Conclusions

Induced seismicity is an issue of very high topicality (e.g. Foulger et al. 2018, van der Baan & Calixto 2017). Production-induced seismicity in the populated area of the Groningen gas field has driven particular scientific attention to the issue during the last three years (e.g. Zbinden et al. 2017, Zöller & Holschneider 2016, Wassing et al. 2017, Ter Heege et al. 2018, van Wees et al. 2017, Buijze et al. 2017, Candela et al. 2018). This study presents a first numerical investigation of production-induced seismicity in North Germany and addresses geological characteristics of the Lower Saxony Rotliegend gas fields. For instance the large depth of reservoir horizons, strong overpressure therein, the stiff volcanic underburden rock, strong lateral variations of salt thickness and in particular the sealing properties of compartmentalizing faults are novel aspects of this study.

Fault-loading and post-failure slip were investigated in 2D FE models based on North German gas fields, addressing a parameter range considered typical for the given geological setting. Based on the modelling results, the production-induced fault reactivation potential is highest at the upper reservoir level and a narrow interval above the reservoir. For viscoelastic salt considered in the overburden, fault-loading is strongest directly below the viscoelastic layer but upward propagation of rupture is impeded by the isotropic stress state and the relaxation of shear stresses in the salt. At the lower reservoir level and directly below the reservoir a similar loading does not occur, instead a reduction in *SSR*, indicating a tendency towards reverse faulting is observed but considered incompatible with detected focal mechanisms and the prevailing extensional tectonic stress regime.

A single dominant parameter that could serve as input parameter for a seismic hazard analysis could not be identified. Several parameters influence the production-induced stress state and may interfere in an enhancing or damping manner. Generally, the tested parameters affect the loading state of the fault within a stress regime that is predominantly governed by a complex interplay of fault strength, depletion magnitude and the pre-production stress state.

Nevertheless, for a large range of parameter variations the graben-fault bounding a single reservoir experiences a much smaller loading compared to the intra-field fault, leaving seismic events at the field boundary less likely compared to events on compartmentalizing faults. Here, production of either both compartments or the footwall compartment along with a compartment offset that renders the depleting horizons partially juxtaposed result in a particularly strong loading of the fault. Intra-field seismic events were identified to nucleate at the lower level of the fault section bounding the footwall compartment. Evaluating different intra-field depletion schemes, the modelling results imply, that prioritized production from hanging wall compartments may constitute a strategy to slow down the loading rate on compartmentalizing faults. While the pore pressure field clearly drives stress changes

and fault reactivation, the modelled seismic events show a dominant imprint of far–field and initial stresses rather than reflecting the depletion magnitude or production scheme. The Propagation of fault slip is thereby inhibited by local geological factors that predefine a maximum rupture length.

Correlating the modelling results to actual geological features and the suggested distribution of seismicity (Uta 2017, Bischoff et al. 2017), the active salt-diapirism posing a non-homogeneous overburden load to the reservoir horizon can serve as an explanation for the restriction of seismic events to certain fields and particular compartments herein. Future work should aim on correlating the model parameters identified favourable for fault reactivation to actual field properties and earthquake locations.

Investigations of deep subsurface operations are generally data-limited problems. The subsurface is accessible in a direct manner only by pointwise drilling and on a larger scale by indirect methods of geophysical prospecting. The latter comprises particularly large uncertainties if the target layer is buried below thick evaporite layers. Furthermore, the localization and kinematic resolution of earthquakes comes with a large uncertainty that scales with the development of the monitoring network (e.g. Grigoli et al. 2017, BVEG 2017). Given these uncertainties, geomechanical modelling allows for the investigation of scenarios, the estimation of control factors and the definition of limiting cases (e.g. Aruffo et al. 2014, Juanes et al. 2016). The parameter variation of this study could significantly increase the understanding of fault-loading and seismicity in North German Rotliegend gas fields. However, in order to provide more detailed prediction models for production-induced seismicity, 3D field data, i.e. structural data, stress data, the pore pressure field and material properties should be depicted in more detail. Nevertheless, fundamental uncertainties such as the detailed geometry of the fault plane, hydraulic and mechanical fault properties, the pre-production stress state within the reservoir and on the fault, stress magnitudes, stress orientation and the pore pressure field remain major challenges in the data-limited modelling of geomechanical problems.

Basic mechanisms of production-induced seismicity comprise the bulk compaction of the reservoir, potentially compensated by reactivation of low strength boundary faults, and the effective, direct poroelastic stressing of faults. Here, the compaction-strain has been shown to be equally expressible by two effective stress laws that have different implications on the local loading state of the fault. In spite of the *reservoir stress path* being evaluated by Terzaghi effective stress, Biot-Willis effective stress returned more plausible results in the numerical modelling. Furthermore, the continuity condition of normal stresses across sealing faults, separating compartments of differential pore pressure evolution, had a strong impact on the modelling results. Inspired by the encountered ambiguities within this study, future numerical investigations should clearly state their mechanism-

specific effective stress concept and reveal the detailed hydro-mechanical properties of their model faults in order to assure the comparability of modelling results.

This study successfully introduces a two-step strategy for the assessment of production-induced seismicity. First, fault criticality is evaluated in a quasi-static poroelastic model and once production-induced loading jeopardizes fault integrity, the stress state is transferred to a dynamic analysis in ABAQUS explicit. In this second step, the complex loading pattern is dissipated by slip on a contact fault, whereby the implemented velocity-weakening friction model and the consideration of dynamic stresses captures basic characteristics of coseisimic slip and rupture propagation. The presented workflow can be applied in the planning and licensing of field operations, to first identify critical faults and then define upper-bounds on possible earthquake magnitudes. Furthermore, the assessment of rupture propagation constitutes a useful tool to assess caprock integrity of underground gas storage operations.

12 Literature

ABQ (2016): ABAQUS 2016 Analysis User's Guide. Documentation, Dassault Systèmes Simulia Corporation, Providence, Rhode Island

ABQ (2016): ABAQUS 2016 Theory Guide. Documentation, Dassault Systèmes Simulia Corporation, Providence, Rhode Island

ABQ (2016): ABAQUS 2016 Benchmark Guide. Documentation, Dassault Systèmes Simulia Corporation, Providence, Rhode Island

Addis M.A. (1997): The Stress-Depletion Response of Reservoirs. *SPE Annual Technical Conference and Exhibition, 5-8 October 1997, San Antonio, Texas.*

Adey R.A., Pusch R. (1999): Scale dependency in rock strength. *Engineering Geology* 53 (3-4), pp. 251–258. DOI: 10.1016/S0013-7952(99)00041-1.

Alassi H., Li L., Holt R.M. (2006): Discrete Element Modeling of Stress and Strain Evolution Within and Outside a Depleting Reservoir. *Pure appl. geophys.* 163 (5-6), pp. 1131–1151. DOI: 10.1007/s00024-006-0067-5.

Altmann J.B., Müller B., Müller T.M., Heidbach O., Tingay M., Weißhardt A. (2014): Pore pressure stress coupling in 3D and consequences for reservoir stress states and fault reactivation. *Geothermics* (52), pp. 195–205.

Altmann J.B., Müller T.M., Müller B., Tingay M., Heidbach O. (2010): Poroelastic contribution to the reservoir stress path. *Int. J. Rock Mech. Min. Sci.* 47 (7), pp. 1104–1113. DOI: 10.1016/j.ijrmms.2010.08.001.

Ampuero J.-P., Rubin A.M. (2008): Earthquake nucleation on rate and state faults – Aging and slip laws. *J. Geophys. Res.* 113 (B1), p. 1987. DOI: 10.1029/2007JB005082.

Anderson E.M. (1951): The Dynamics of Faulting and Dyke Formation with Applications to Britain. 2nd ed., Oliver and Boyd. Edinburgh, p. 206.

Angelier J. (1990): Inversion of field data in fault tectonics to obtain the regional stress-III. A new rapid direct inversion method by analytical means. *Geophys. J. Int.* 103 (2), pp. 363–376. DOI: 10.1111/j.1365-246X.1990.tb01777.x.

Aruffo C.M., Rodriguez-Herrera A., Tenthorey E., Krzikalla F., Minton J., Henk A. (2014): Geomechanical modelling to assess fault integrity at the CO2CRC Otway Project, Australia. *Aust. J. Earth Sci.* 61 (7), pp. 987–1001. DOI: 10.1080/08120099.2014.958876.

Baldschuhn R., Binot F., Fleig S., Kockel F. (2001): Geotektonischer Atlas von Nordwest-Deutschland und dem deutschen Nordsee-Sektor. *Geol. Jahrb. Reihe A, Heft 153*, p. 87.

Baranova V., Mustaqeem A., Bell S. (1999): A model for induced seismicity caused by hydrocarbon production in the Western Canada Sedimentary Basin. *Can. J. Earth Sci.* 36 (1), pp. 47–64.

Bardainne T., Dubos-Sallée N., Sénéchal G., Gaillot P., Perroud H. (2008): Analysis of the induced seismicity of the Lacq gas field (Southwestern France) and model of deformation. *Geophys. J. Int.* 172 (3), pp. 1151–1162. DOI: 10.1111/j.1365-246X.2007.03705.x.

Beeler N.M., Tullis T.E., Weeks J.D. (1994): The roles of time and displacement in the evolution effect in rock friction. *Geophys. Res. Lett.* 21 (18), pp. 1987–1990.

Biot M.A. (1941): General Theory of Three-Dimensional Consolidation. *J. Appl. Phys.* 12 (2), pp. 155–164.

Biot M.A. (1962): Mechanics of Deformation and Acoustic Propagation in Porous Media. *J. Appl. Phys.* 33 (4), pp. 1482–1498.

Biot M.A., Willis D.G. (1957): The Elastic Coefficients of the Theory of Consolidation. *J. Appl. Mech.*, pp. 594–601.

Bischoff M., Bönnemann C., Fritz J., Gestermann N., Plenefisch T. (2012): Untersuchungsergebnisse zum Erdbeben bei Völkersen (Landkreis Verden) am 22.11.2012. Seismologische Auswertung. *Bericht LBEG-BGR*, p. 60.

Bischoff M., Gestermann N., Plenefisch T., Viola S., Fritz J. (2017): Characteristics of seismicity induced by gas production in Northern Germany. *Poster, Schatzalp workshop on Induced Seismicity, 14-17th march 2017, Davos, Switzerland*. Available online at http://www.seismo.ethz.ch/export/sites/sedsite/research-and-teaching/.galleries/pdf_schatzalp/P1-01_Bischoff.pdf.

Bizzarri A., Cocco M., Andrews D.J., Boschi E. (2001): Solving the dynamic rupture problem with different numerical approaches and constitutive laws. *Geophys J Int* 144 (3), pp. 656–678. DOI: 10.1046/j.1365-246x.2001.01363.x.

Bommer J.J., van Elk J. (2017): Comment on "The Maximum Possible and the Maximum Expected Earthquake Magnitude for Production-Induced Earthquakes at the Gas Field in Groningen, The Netherlands" by Gert Zöller and Matthias Holschneider. *Bull. Seismol. Soc. Am.* 107 (3), pp. 1564–1567. DOI: 10.1785/0120170040.

Bostrom B. (2009): Development of a Geomechanical Reservoir Modeling Workflow and Simulations. *SPE Annual Technical Conference and Exhibition, 4-7 October 2009, New Orleans, Louisiana*.

Bostrom B., Skomedal E. (2004): Reservoir Geomechanics with ABAQUS. *2004 ABAQUS User conference, 25-27 May 2004, Boston, Massachusetts*, pp. 117–131.

Bourne S.J., Oates S.J., van Elk J. (2018): The exponential rise of induced seismicity with increasing stress levels in the Groningen gas field and its implications for controlling seismic risk. *Geophysical Journal International* 213 (3), pp. 1693–1700. DOI: 10.1093/gji/ggy084.

Boutéca M.J., Sarda J.-P., Vincké O. (2000): Constitutive Law for permeability Evolution of Sandstondes during Depletion. *SPE 2000 International Symposium on Formation Control, 23-24 February 2000, Lafayette, Louisiana*.

Brace W.F., Byerlee J.D. (1966): Stick-slip as a mechanism for earthquakes. *Science* 153 (3739), pp. 990–992. DOI: 10.1126/science.153.3739.990.

Brandes C., Steffen H., Steffen R., Wu P. (2015): Intraplate seismicity in northern Central Europe is induced by the last glaciation. *Geology* 43 (7), pp. 611–614. DOI: 10.1130/G36710.1.

Breckels I.M., van Ekelen H. (1981): Relationship Between Horizontal Stress and Depth in Sedimentary Basins. *SPE 56the Annual Fall Technical Conference, 5-7 October 1981, San Antonio, Texas*, pp. 2191–2199.

Buijze L., van den Bogert P.A., Wassing B.B., Orlic B., Veen J. ten (2017): Fault reactivation mechanisms and dynamic rupture modelling of depletion-induced seismic events in a Rotliegend gas reservoir. *Neth. J. Geosci.* 96 (5), 131-148. DOI: 10.1017/njg.2017.27.

BVEG (2017): Bürgerinfo Seismisches Messsystem. BVEG. Available online at http://www.seis-info.de/, checked on 11/10/2017.

Byerlee J.D. (1967): Frictional characteristics of granite under high confining pressure. *J. Geophys. Res.* 72 (14), pp. 3639–3648. DOI: 10.1029/JZ072i014p03639.

Byerlee J.D. (1975): The fracture strength and frictional strength of Weber Sandstone. *Int. J. Rock Mech. Min. Sci. Abstracts* 12 (1), pp. 1–4. DOI: 10.1016/0148-9062(75)90736-6.

Byerlee J.D. (1978): Friction of Rocks. *Pure Appl. Geophys* 116, pp. 617–625.

Candela T., Wassing B., Ter Heege J., Buijze L. (2018): How earthquakes are induced. *Science* 360 (6389), pp. 598–600. DOI: 10.1126/science.aat2776.

Capasso G., Mantica S. (2006): Numerical Simulation of Compaction and Subsidence using ABAQUS. *2006 ABAQUS User Conference, 23-25 May 2006, Boston, Massachussetts*, pp. 125–144.

Cappa F., Rutqvist J. (2011): Modeling of coupled deformation and permeability evolution during fault reactivation induced by deep underground injection of CO2. *Int. J. Greenh. Gas Con.* 5 (2), pp. 336–346. DOI: 10.1016/j.ijggc.2010.08.005.

Cappa F., Rutqvist J. (2012): Seismic rupture and ground accelerations induced by CO2 injection in the shallow crust. *Geophys. J. Int.* 190 (3), pp. 1784–1789. DOI: 10.1111/j.1365-246X.2012.05606.x.

Chan A.W., Zoback M.D. (2002): Deformation Analysis in Reservoir Space (DARS): A Simple Formalism for Prediction of Reservoir Deformation with Depletion. *SPE/ISRM Rock Mechanics Conference, Irving, Texas* 20-23 October.

Cheng A.-D. (2016): Poroelasticity. Theory and Applications of Transport in Porous Media, Springer International Switzerland, p. 877.

Cornet F.H., Röckel T. (2012): Vertical stress profiles and the significance of “stress decoupling”. *Tectonophysics* 581, pp. 193–205. DOI: 10.1016/j.tecto.2012.01.020.

Cornet H.C. (2014): Elements of Crustal Geomechanics, Cambridge University Press. Cambridge United Kingdom, p. 461.

Cowie P.A., Scholz C.H. (1992): Physical explanation for the displacement-length relationship of faults using a post-yield fracture mechanics model. *J. Struct. Geol.* 14 (10), pp. 1133–1148.

Dahm T., Kruger F., Stammler K., Klinge K., Kind R., Wylegalla K., Grasso J.-R. (2007): The 2004 Mw 4.4 Rotenburg, Northern Germany, Earthquake and Its Possible Relationship with Gas Recovery. *Bull. Seismol. Soc. Am.* 97 (3), pp. 691–704. DOI: 10.1785/0120050149.

Daub E.G., Carlson J.M. (2010): Friction, Fracture, and Earthquakes. *Annu. Rev. Condens. Matter Phys.* 1 (1), pp. 397–418. DOI: 10.1146/annurev-conmatphys-070909-104025.

Dean R.H., Gai X., Stone C.M., Mnkoff S.E. (2006): A Comparison of Techniques for Coupling Porous Flow and Geomechanics. *SPE Reservoir Simulation Symposium, 3-5 February 2006, Houston*, pp. 132–140.

DeDontney N., Gans C., Burnett W.A., Burch D., Garzon M.J., Gist G. et al. (2016): Maximum Magnitude of Induced Earthquakes in the Groningen Gas Field. Report ExxonMobil Upstream Research Company, p. 65.

Deng K., Liu Y., Harrington R.M. (2016): Poroelastic stress triggering of the December 2013 Crooked Lake, Alberta, induced seismicity sequence. *Geophys. Res. Lett.* 43 (16), pp. 8482–8491. DOI: 10.1002/2016GL070421.

Detournay E., Cheng A.-D. (1993): fundamentals of poroelasticity. In: C. Fairhurst (Ed.): Chapter 6 Comprehensive Rock Engnineering: Principles, Practice and projects, Vol. II, Analysis and Design Method: Pergamon Press, 113-171.

Dieterich J.H., Keith B.R.-D., Kroll K.A. (2015): Modeling Injection-Induced Seismicity with the Physics-Based Earthquake Simulator RSQSim. *Seismol. Res. Lett.* 86 (4), pp. 1102–1109. DOI: 10.1785/0220150057.

Doornenbal H., Stevenson A. (2010): Petroleum Geological Atlas of the Southern Permian Basin Area, EAGE Publications bv. Houten, p. 354.

Doornhof D., Kristiansen T.G., Nagel N.B., Pattillo P.D., Sayers C. (2006): Compaction and Subsidence. *Oilfield Rev.* 18 (3), pp. 50–68.

Doser D.I., Baker M.R., Mason D.B. (1991): Seismicity in the War-Wink gas field, Delaware Basin, west Texas, and its relationship to petroleum production. *Bull. Seismol. Soc. Am.* 81 (3), pp. 971–986.

Dropek R.K., Johnson J.N., Walsh J.B. (1978): The influence of pore pressure on the mechanical properties of Kayenta sandstone. *J. Geophys. Res.* 83 (B6), p. 2817. DOI: 10.1029/JB083iB06p02817.

Dusseault M.B., Maury V., Sanfilippo F., Santarelli F.J. (2004): Drilling Around Salt: Risks, Stresses and Uncertainties. *Gulf Rocks 2004, 6th North American Rock Mechanics Symposium, 5-9 June 2004, Houston, Texas*.

Eaton B.A. (1969): Fracture gradient prediction and its application in ooilfield operations. *J. Pet. Tech.* 246, pp. 1353–1360.

Ellsworth W.L. (2013): Injection-induced earthquakes. *Science* 341 (6142), p. 1225942. DOI: 10.1126/science.1225942.

Engelder T. (1994): Deviatoric Stressitis: A Virus Infecting the Earth Science Community. *EOS, Trans. Amer. Geophys. Union* 75 (18), pp. 209–218.

Engelder T., Lacazette A. (1990): Natural hydraulic fracturing. In: N. Barton, O. Stephansson (Eds.): Rock Joints. Rotterdam: AA. Balkema, pp. 35–44.

Evans K.F., Zappone A., Kraft T., Deichmann N., Moia F. (2012): A survey of the induced seismic responses to fluid injection in geothermal and CO2 reservoirs in Europe. *Geothermics* 41, pp. 30–54. DOI: 10.1016/j.geothermics.2011.08.002.

Faulkner D.R., Jackson C., Lunn R.J., Schlische R.W., Shipton Z.K., Wibberley C., Withjack M.O. (2010): A review of recent developments concerning the structure, mechanics and fluid flow properties of fault zones. *J. Struct. Geol.* 32 (11), pp. 1557–1575. DOI: 10.1016/j.jsg.2010.06.009.

Ferronato M., Gambolati G., Janna C., Teatini P. (2008): Numerical modelling of regional faults in land subsidence prediction above gas/oil reservoirs. *Int. J. Numer. Anal. Meth. Geomech.* 32 (6), pp. 633–657. DOI: 10.1002/nag.640.

Fischer K., Henk A. (2013): A workflow for building and calibrating 3-D geomechanical models - a case study for a gas reservoir in the North German Basin. *Solid Earth* 4 (2), pp. 347–355. DOI: 10.5194/se-4-347-2013.

Fjaer E. (2008): Petroleum related rock mechanics. 2nd ed., Elsevier. Amsterdam, Boston In: Developments in petroleum science, 53, p. 514.

Fokker P.A., van Thienen-Visser K. (2015): Inversion of double-difference measurements from optical levelling for the Groningen gas field. *Proc. IAHS* 372, pp. 375–378. DOI: 10.5194/piahs-372-375-2015.

Foulger G.R., Wilson M.P., Gluyas J.G., Julian B.R., Davies R.J. (2018): Global review of human-induced earthquakes. *Earth-Sci. Rev.* 178, pp. 438–514. DOI: 10.1016/j.earscirev.2017.07.008.

Frankel A., Kanamori H. (1983): Determination of Rupture Duration and Stress Drop for Earthquakes in Southern California. *Bull. Seismol. Soc. Am.* 73 (6), pp. 1527–1551.

Frohlich C., DeShon H., Stump B., Hayward C., Hornbach M., Walter J.-I. (2016): A Historical Review of Induced Earthquakes in Texas. *Seismol. Res. Lett.* 87 (4), pp. 1022–1038. DOI: 10.1785/0220160016.

Garg S.K., Nur A. (1973): Effective Stress laws for Fluid-saturated porous rocks. *J. Geophys. Res.* 78 (26), pp. 5911–5921.

Gast R. (1991): The Perennial Rotliegend Saline Lake in NW Germany. *Geol. Jahrb.* 119, pp. 25–59.

Gast R., Gundlach T. (2006): Permian strike slip and extensional tectonics in Lower Saxony, Germany. *Z. Dtsch. Ges. Geowiss.* 157 (1), pp. 41–55. DOI: 10.1127/1860-1804/2006/0157-0041.

Gawehn W., Funk S. (2017): Finite Elemente Methode - FEM-Grundlagen zur Statik und Dynamik. 3rd ed., Books on Demand. Osnabrück, p. 295.

Gheibi S., Holt R.M., Vilarrasa V. (2017): Effect of faults on stress path evolution during reservoir pressurization. *Int. J. Greenh. Gas Con.* 63, pp. 412–430. DOI: 10.1016/j.ijggc.2017.06.008.

Goebel T., Weingarten M., Chen X., Haffener J., Brodsky E.E. (2017): The 2016 Mw5.1 Fairview, Oklahoma earthquakes. Evidence for long-range poroelastic triggering at >40 km from fluid disposal wells. *Earth Planet. Sci. Lett.* 472, pp. 50–61. DOI: 10.1016/j.epsl.2017.05.011.

Goulty N.R. (2003): Reservoir Stress path during depletion of Norwegian chalk oilfields. *Pet. Geosci.* 9, pp. 223–241.

Grasso J.-R. (1992): Mechanics of Seismic Instabilities Induced by the Recovery of Hydrocarbons. *Pure Appl. Geophys* 139, pp. 507–534.

Grigoli F., Cesca S., Priolo E., Rinaldi A.P., Clinton J.F., Stabile T.A. et al. (2017): Current challenges in monitoring, discrimination, and management of induced seismicity related to underground industrial activities. A European perspective. *Rev. Geophys.* 55 (2), pp. 310–340. DOI: 10.1002/2016RG000542.

Grünthal G., Stromeyer D., Bosse C., Cotton F., Bindi D. (2018): Correction to: The probabilistic seismic hazard assessment of Germany-version 2016, considering the range of epistemic uncertainties and aleatory variability. *Bull. Earthq. Eng.* 16 (10), pp. 4397–4398. DOI: 10.1007/s10518-018-0398-5.

Guglielmi Y., Cappa F., Amitrano D. (2008): High-definition analysis of fluid-induced seismicity related to the mesoscale hydromechanical properties of a fault zone. *Geophys. Res. Lett.* 35 (6), p. 207. DOI: 10.1029/2007GL033087.

Gutierrez M.S., Lewis R.W. (2002): Coupling of Fluid Flow and Deformation in Underground Formations. *J. Eng. Mech.* 128 (7), pp. 779–787. DOI: 10.1061/(ASCE)0733-9399(2002)128:7(779).

Haimson B., Rudnicki J.W. (2010): The effect of the intermediate principal stress on fault formation and fault angle in siltstone. *J. Struct. Geol.* 32 (11), pp. 1701–1711. DOI: 10.1016/j.jsg.2009.08.017.

Haimson B.C., Cornet F.H. (2003): ISRM Suggested Methods for rock stress estimation—Part 3. Hydraulic fracturing (HF) and/or hydraulic testing of pre-existing fractures (HTPF). *Int. J. Rock Mech. & Min. Sci.* 40 (7-8), pp. 1011–1020. DOI: 10.1016/j.ijrmms.2003.08.002.

Handin J., Hager R.V., Friedman M., Feather J.N. (1963): Experimental Deformation of sedimentary rocks under confining pressure: Pore pressure tests. *AAPG Bulletin* 47 (5), pp. 717–755.

Haug C., Nüchter J.-A., Henk A. (2018): Assessment of geological factors potentially affecting production-induced seismicity in North German gas fields. *Geomech. Energy Env.*, pp. 15–31. DOI: 10.1016/j.gete.2018.04.002.

Hauksson E., Göbel T., Ampuero J.-P., Cochran E. (2015): A century of oil-field operations and earthquakes in the greater Los Angeles Basin, southern California. *The Leading Edge* 34 (6), pp. 650–656. DOI: 10.1190/tle34060650.1.

Haupt M. (1991): A Constitutive Law for Rock Salt based on Creep and Relaxation Tests. *Rock Mech. Rock Eng. (Rock Mechanics and Rock Engineering)*, pp. 197–206.

Heidari M., Nikolinakou M.A., Flemings P.B., Hudec M.R. (2017): A simplified stress analysis of rising salt domes. *Basin Res.* 29 (3), pp. 363–376. DOI: 10.1111/bre.12181.

Hergert T., Heidbach O., Reiter K., Giger S.B., Marschall P. (2015): Stress field sensitivity analysis in a sedimentary sequence of the Alpine foreland, northern Switzerland. *Solid Earth* 6 (2), pp. 533–552. DOI: 10.5194/se-6-533-2015.

Hettema M., Schutjens P., Verboom B., Gussinklo H.J. (1998): Production-Induced Compaction of Sandstone Reservoirs: The Strong Influence of Field Stress. *SPE European Petroleum Conference, 20 - 22 October 1998, The Hague*.

Hettema M., Schutjens P., Verboom B., Gussinklo H.J. (2000): Production-Induced Compaction of a Sandstone Reservoir: The Strong Influence of Stress Path. *SPE Res. Eval. Eng.* 3 (4), pp. 342–347.

Hoek E., Brown E.T. (1997): Practical estimates of rock mass strength. *Int. J. Rock Mech. & Min. Sci.* 34 (8), pp. 1165–1186. DOI: 10.1016/S1365-1609(97)80069-X.

Holt R.M., Flornes O., Li L., Fjaer E. (2004): Consequences of Depletion-Induced Stress Changes on Reservoir Compaction and Recovery. *Gulf Rocks 2004, 6th North America Rock Mechanics Symposium (NARMS), 5-9 June 2004, Houston, Texas*.

Hough S.E., Page M. (2016): Potentially Induced Earthquakes during the Early Twentieth Century in the Los Angeles Basin. *Bull. Seismol. Soc. Am.* 106 (6), pp. 2419–2435. DOI: 10.1785/0120160157.

Hudson J.A., Cornet F.H., Christiansson R. (2003): ISRM Suggested Methods for rock stress estimation—Part 1. Strategy for rock stress estimation. *International Journal of Rock Mechanics and Mining Sciences* 40 (7-8), pp. 991–998. DOI: 10.1016/j.ijrmms.2003.07.011.

Ingraham M.D., Bauer S.J., Issen K.A., Dewers T.A. (2017): Evolution of permeability and Biot coefficient at high mean stresses in high porosity sandstone. *Int. J. Rock Mech. & Min. Sci.* 96, pp. 1–10. DOI: 10.1016/j.ijrmms.2017.04.004.

Inoue N., Da Fontoura A.B. (2009a): Answers to Some Questions About the Coupling Between Fluid Flow and Rock Deformation in Oil Reservoirs. *SPE/EAGE Reservoir Characterization and Simulation Conference, 19-21 October 2009, Abu Dhabi, UAE*.

Inoue N., Da Fontoura A.B. (2009b): Explicit Coupling Between Flow and Geomechanical Simulators. *Int. Conf. on Computational Methods for Coupled Problems in Science and Engineering, 21-23 May 2009, Ischia Islands, Italy*.

Jaeger J.C., Cook N., Zimmerman R.W. (2007): Fundamentals of Rock Mechanics. Fourth edition, Blackwell Publishing, p. 488.

Jeanne P., Rutqvist J., Dobson P.F. (2017): Influence of injection-induced cooling on deviatoric stress and shear reactivation of preexisting fractures in Enhanced Geothermal Systems. *Geothermics* 70, pp. 367–375. DOI: 10.1016/j.geothermics.2017.08.003.

Jha B., Juanes R. (2014): Coupled multiphase flow and poromechanics. A computational model of pore pressure effects on fault slip and earthquake triggering. *Water Resour. Res.* 50 (5), pp. 3776–3808. DOI: 10.1002/2013WR015175.

Juanes R., Jha B., Hager B.H., Shaw J.H., Plesch A., Astiz L. et al. (2016): Were the May 2012 Emilia-Romagna earthquakes induced? A coupled flow - geomechanics modeling assessment. *Geophys. Res. Lett.* 43 (13), pp. 6891–6897, p. 7. DOI: 10.1002/2016GL069284.

Kanamori H. (1977): The energy release in great earthquakes. *J. Geophys. Res.* 82 (20), pp. 2981–2987. DOI: 10.1029/JB082i020p02981.

Kanamori H., Anderson D.L. (1975): Theoretical Basis of some Empirical Relations in Seismology. *Bull. Seismol. Soc. Am.* 65 (5), pp. 1073–1095.

Katzenbach R., Bachmann C., Gutberlet C., Gutwald J., Leppla S., Ramm H. et al. (2012): Anwendung der FEM in der Geotechnik, Geotechnik TU Darmstadt. Darmstadt. Available online at https://www.geotechnik.tudarmstadt.de/media/institut_und_versuchsanstalt_fuer_geotechnik/studiumundlehre_1/musterloesungen/fem_skript/Skript-_FEM_in_der_Geotechnik.pdf, p.170.

Khan M., Teufel L.W., Zheng Z. (2000): Determining the Effect of Geological and Geomechanical Parameters on Reservoir Stress path through Numerical Simulation. *SPE Annual Technical Conference and Exhibition, 1-4 october, Dallas, Texas*.

Kley J., Franzke H.J., Jähne, F., Krawczyk, C., Lohr T., Reicherter K. et al.: Strain and Stress. In: Littke R, Bayer U, Gajewski U, Nelskamp S, eds. Dynamics of Complex Intracontinental Basins - The Central European Basin System: Springer-Verlag Berlin Heidelberg, pp. 97–124.

Knipe R.J. (1997): Juxtaposition and Seal Diagrams to Help Analyze Fault Seals in Hydrocarbon Reservoirs. *AAPG Bulletin* 81 (1997). DOI: 10.1306/522B42DF-1727-11D7-8645000102C1865D.

Kockel F. (2000): Rifting processes in NW-Germany and the German North Sea Sector. *Neth. J. Geosci.* 81 (2), pp. 149–158.

Kohli A.H., Zoback M.D. (2013): Frictional properties of shale reservoir rocks. *J. Geophys. Res. Solid Earth* 118 (9), pp. 5109–5125. DOI: 10.1002/jgrb.50346.

Koupriantchik D., Hunt S., Boult P., Meyers A. (2005): Geomechanical modeling of salt diapirs: Generic shapes and a 3D salt structure from the Officer Basin, South Australia. In: G. Barla, M. Barla (Eds.): Proceedings of the 11th International Conference on Computer Methods and Advances in Geomechanics. Bologna: Patron Editore, pp. 27–34.

Kroll K.A., Richards-Dinger K.B., Dieterich J.H. (2017): Sensitivity of Induced Seismic Sequences to Rate-and-State Frictional Processes. *J. Geophys. Res. Solid Earth* 122 (12), 10,207-10,219. DOI: 10.1002/2017JB014841.

Kukla P.A., Urai J.L., Mohr M. (2008): Dynamics of salt structures. In: Littke R, Bayer U, Gajewski U, Nelskamp S, eds. Dynamics of Complex Intracontinental Basins - The Central European Basin System: Springer-Verlag Berlin Heidelberg, pp. 291–306.

Kümpel H.-J. (1991): Poroelasticity: Parameters reviewed. *Geophys. J. Int.* 105 (3), pp. 783–799. DOI: 10.1111/j.1365-246X.1991.tb00813.x.

Labuz J.F., Zang A. (2012): Mohr–Coulomb Failure Criterion. *Rock Mech Rock Eng* 45 (6), pp. 975–979. DOI: 10.1007/s00603-012-0281-7.

Lade P.V., Boer R. de (1997): The concept of effective stress for soil, concrete and rock. *Géotechnique* 47 (1), pp. 61–78.

Lautenschläger C., Righetto G.L., Inoue N., da Fontoura S. (2013): Advances on Partial coupling in Reservoir Simulation: A New Scheme of Hydromechanical Coupling. *SPE North Africa Technical Conference & Exhibition, 15-17 April 2013*.

Lawn B.R., Marshall D.B. (1998): Nonlinear stress-strain curves for solids containing closed cracks with friction. *J. Mech. Phys. Solids* 46 (1), pp. 85–113. DOI: 10.1016/S0022-5096(97)00036-7.

LBEG (2016): Erdöl und Erdgas in der Bundesrepublik Deutschland. Jahresbericht, p. 73.

Lee M.Y., Ehgartner B. (2001): Laboratory Evaluation of Damage Criteria and Creep parameters of Tioga Dolomite and Rock Salt from Cavern Well No. 1. *SANDIA REPORT, SAND2001-0918, p.* 94.

Lele S., Hsu S.-Y., Garzon J.L., DeDontney N., Searles K., Gist G. et al. (2016): Geomechanical Modeling to Evaluate Production-Induced Seismicity at Groningen Field. *Abu Dhabi International Petroleum Exhibition & Conference, 7-10 November 2016, Abu Dhabi*.

Lewis R.W., Schrefler B.A. (1999): The Finite Element Method in the Static and Dynamic Deformation and Consolidation of Porous Media. 2nd edition, Wiley. Chichester, p. 508.

Li S.-Y., Urai J.L. (2016): Rheology of rock salt for salt tectonics modeling. *Pet. Sci.* 13 (4), pp. 712–724. DOI: 10.1007/s12182-016-0121-6.

Lohr T., Krawczyk C.M., Tanner D.C., Samiee R., Endres H., Oncken O. et al. (2007): Strain partitioning due to salt. Insights from interpretation of a 3D seismic data set in the NW German Basin. *Basin Res.* 19 (4), pp. 579–597. DOI: 10.1111/j.1365-2117.2007.00338.x.

Longuemare P., Mainguy M., Lemonnier P., Onaisi A., Gérard C., Koutsabeloulis N. (2002): Geomechanics in Reservoir Simulation: Overview of Coupling Methods and Field Case Study. *Oil & Gas Sci. and Technol.* 57 (5), pp. 471–483.

Lund B., Townend J. (2007): Calculating horizontal stress orientations with full or partial knowledge of the tectonic stress tensor. *Geophys. J. Int.* 170 (3), pp. 1328–1335. DOI: 10.1111/j.1365-246X.2007.03468.x.

Luo G., Hudec M.R., Flemings P.B., Nikolinakou M.A. (2017): Deformation, stress, and pore pressure in an evolving suprasalt basin. *J. Geophys. Res. Solid Earth* 122 (7), pp. 5663–5690. DOI: 10.1002/2016JB013779.

Luo G., Nikolinakou M.A., Flemings P.B., Hudec M.R. (2012): Geomechanical modeling of stresses adjacent to salt bodies. Part 1—Uncoupled models. *AAPG Bulletin* 96 (1), pp. 43–64. DOI: 10.1306/04111110144.

Majer E.L., Baria R., Stark M., Oates S., Bommer J., Smith B., Asanuma H. (2007): Induced seismicity associated with Enhanced Geothermal Systems. *Geothermics* 36 (3), pp. 185–222. DOI: 10.1016/j.geothermics.2007.03.003.

Manzocchi T., Heath A.E., Palananthakumar B., Childs C., Walsh J.J. (2008): Faults in conventional flow simulation models: a consideration of representational assumptions and geological uncertainties. *Pet. Geosci.* 14, pp. 91–110.

Marketos G., Spiers C.J., Govers R. (2016): Impact of rock salt creep law choice on subsidence calculations for hydrocarbon reservoirs overlain by evaporite caprocks. *J. Geophys. Res. Solid Earth* 121 (6), pp. 4249–4267. DOI: 10.1002/2016JB012892.

Marone C. (1995): Fault zone strength and Failure criteria. *Geophy. Res. Let.* 22 (6), pp. 723–726.

Marone C. (1998): Laboratory-derived friction laws and their application to seismic faulting. *Annu. Rev. Earth Planet. Sci.* 26, pp. 643–696.

Mauthe G. (2003): Sealing Faults Due to Cataclasis in Rotliegend Sandstones (Lower Permian) of NW-Germany. *Erdöl, Erdgas, Kohle* (1), pp. 12–17.

Mazur S., Scheck-Wenderoth M. (2005): Constraints on the tectonic evolution of the Central European Basin System revealed by seismic reflection profiles from Northern Germany. *Neth. J. Geosci.* 84, pp. 389–401.

McClure M.W., Horne R.N. (2011): Investigation of injection-induced seismicity using a coupled fluid flow and rate/state friction model. *Geophysics* 76 (6), pp. 181–198. DOI: 10.1190/GEO2011-0064.1.

McGarr A., Simpson D., Seeber L.: Case histories of induced and triggered seismicity. In: Lee WHK, Kanamori H, Jennings PC, Kisslinger C, eds. International Geophysics, 81 Part A: Academic Press, pp. 647–661.

Merkel M., Öchsner A. (2010): Eindimensionale Finite Elemente - Ein Einstieg in die Methode, Springer Berlin Heidelberg. Berlin, Heidelberg, p. 428.

Mitchell T.M., Faulkner D.R. (2009): The nature and origin of off-fault damage surrounding strike-slip fault zones with a wide range of displacements. A field study from the Atacama fault system, northern Chile. *J. Struct. Geol.* 31 (8), pp. 802–816. DOI: 10.1016/j.jsg.2009.05.002.

Moeck I., Kwiatek G., Zimmermann G. (2009): Slip tendency analysis, fault reactivation potential and induced seismicity in a deep geothermal reservoir. *J. Struct. Geol.* 31 (10), pp. 1174–1182. DOI: 10.1016/j.jsg.2009.06.012.

Mohr M., Kukla P.A., Urai J.L., Bresser G. (2005): Multiphase salt tectonic evolution in NW Germany. Seismic interpretation and retro-deformation. *Int J Earth Sci (Geol Rundsch)* 94 (5-6), pp. 917–940. DOI: 10.1007/s00531-005-0039-5.

Mohr M., Warren J.K., Kukla P.A., Urai J.L., Irmen A. (2007): Subsurface seismic record of salt glaciers in an extensional intracontinental setting (Late Triassic of northwestern Germany). *Geol* 35 (11), p. 963. DOI: 10.1130/G23378A.1.

Mokelke G., Heinrich Z., Sick B., Häfner R., Walter M., Blascheck P., Joswig M. (2016): Recent seismicity in the northern German gas fields - induced and tectonic? *Poster, Schatzalp workshop on Induced Seismicity, 14-17th march 2017, Davos, Switzerland*. Available online at http://www.seismo.ethz.ch/export/sites/sedsite/research-and-teaching/.galleries/pdf_schatzalp/P1-13_Mokelke.pdf.

Monaco S., Capasso G., Datye D., Mantica S., Vitali R. (2011): Field Scale Geomechnical Modelling Using a New Automated Workflow in Abaqus. *2011 SIMULIA Customer Conference, May 17-19 2011, Barcelona*.

Morris A., Ferrill D.A., Henderson D.B. (1996): Slip-tendency analysis and fault reactivation. *Geology* 24 (3), pp. 275–278. DOI: 10.1130/0091-7613(1996)024.

Mueller E., Scholz T. (2004): Application of geochemistry in the evaluation and development of deep Rotliegend dry gas reservoirs, NW Germany. *Geol. Soc. London Spec. Publ.* 237 (1), pp. 221–230. DOI: 10.1144/GSL.SP.2004.237.01.13.

Mulders F. (2003): Modelling of stress development and fault slip in and around a producing gas reservoir. Dissertation, p. 272.

Munson D.E. (1997): Constitutive Model of Creep in Rock Salt applied to underground room closure 34 (2), pp. 233–247.

Muntendam-Bos A.G., Roest J.P.A., Waal J.A. de (2015): A guideline for assessing seismic risk induced by gas extraction in the Netherlands. *The Leading Edge* 34 (6), pp. 672–677, p. 5. DOI: 10.1190/tle34060672.1.

Nagel N.B. (2001): Compaction and subsidence issues within the petroleum industry. From Wilmington to Ekofisk and beyond. *Phys. and Chem. of the Earth, Part A: Solid Earth and Geodes.* 26 (1-2), pp. 3–14. DOI: 10.1016/S1464-1895(01)00015-1.

Nagelhout A., Roest J.A. (1997): Investigating Fault Slip in a Model of an Underground Gas Storage Facility. *Int. J. Rock Mech. & Min. Sci.* 34 (3-4).

Nur A., Byerlee J.D. (1971): An Exact Effective Stress Law for Elastic Deformation of Rock with Fluids. *J. Geophys. Res.* 76 (26), pp. 6414–6419.

Odonne F., Ménard I., Massonnat G.J., Rolando J.-P. (1999): Abnormal reverse faulting above a depleting reservoir. *Geology* 27 (2), pp. 111–114.

Orlic B., Wassing B.B.T. (2013): A Study of Stress Change and Fault Slip in Producing Gas Reservoirs Overlain by Elastic and Viscoelastic Caprocks. *Rock Mech. Rock Eng.* 46 (3), pp. 421–435. DOI: 10.1007/s00603-012-0347-6.

Ozan C., Brudy M., van der Zee W. (2011): Fault Reactivation due to Fluid Production and Injection in Compacting Reservoirs. *45th American Rock Mechanics / Geomechanics Symposium, 26-29 June, San Francisco, California*.

Pasternak M. (2005): Exploration und Produktion von Erdöl und Erdgas in Deutschland 2004. *Erdöl, Erdgas, Kohle* 121 (7/8).

Pennington W.D., Davis S.D., Carlson S.M., Dupree J., Ewing T. (1986): The Evolution of Seismic Barriers and Asperities caused by the depressuring of Fault Planes in Oil and Gas Fields of South Texas. *Bull. Seismol. Soc. Am.* 76 (4), pp. 939–948.

Pratt W.E., Johnson D.W. (1926): Local Subsidence of the Goose Creek oil field. *J. Geol.* 34 (7), pp. 577–590.

Raleigh C.B., Healy J., Bredehoeft J.D. (1976): An Experiment in Earthquake Control at Rangely, Colorado. *Science* 191, pp. 1230–1237, p. 8, checked on 9/22/2017.

Reiter K., Heidbach O. (2014): 3-D geomechanical–numerical model of the contemporary crustal stress state in the Alberta Basin (Canada). *Solid Earth* 5 (2), pp. 1123–1149. DOI: 10.5194/se-5-1123-2014.

Rinaldi A.P., Jeanne P., Rutqvist J., Cappa F., Guglielmi Y. (2014): Effects of fault-zone architecture on earthquake magnitude and gas leakage related to CO 2 injection in a multi-layered sedimentary system. *GREENH. GASES* 4 (1), pp. 99–120. DOI: 10.1002/ghg.1403.

Roest J., Mulders F. (2000): Overview Modelling Gas Production-Induced Seismicity Mechanisms. In: Deutsche Gesellschaft für Geotechnik (Ed.): Tagungsband des 14. Nationalen Symposiums für Felsmechanik und Tunnelbau. Eurock 2000, 27 - 31 March, Aachen. Aachen, pp. 333–340.

Rozhko A.Y. (2010): Role of seepage forces on seismicity triggering. *J. Geophys. Res.* 115 (B11), 10311. DOI: 10.1029/2009JB007182.

Rubin A.M., Ampuero J.-P. (2005): Earthquake nucleation on (aging) rate and state faults. *J. Geophys. Res.* 110 (B11), p. 1. DOI: 10.1029/2005JB003686.

Rubino V., Rosakis A.J., Lapusta N. (2017): Understanding dynamic friction through spontaneously evolving laboratory earthquakes. *Nat. Comms. (Nature Communications)* 8, p. 15991. DOI: 10.1038/ncomms15991.

Rubinstein J.L., Mahani A.B. (2015): Myths and Facts on Wastewater Injection, Hydraulic Fracturing, Enhanced Oil Recovery, and Induced Seismicity. *Seismol. Res. Lett.* 86 (4), pp. 1060–1067, p. 8. DOI: 10.1785/0220150067.

Rudnicki J.W. (1986): Fluid Mass Sources And Point Forces In Linear Elastic Diffusive Solids. *Mech. Matter.* 5, pp. 383–393.

Rueda J.C., Noreña N.V., Oliveira M.F.F., Roehl D. (2014): Numerical models for detection of fault reactivation in oil and gas fields. *48th US Rock Mechanics / Geomechanics Symposium, 1-4 June 2014, Minneapolis, MN, USA*.

Ruina A. (1983): Slip Instability and State Variable Friction Laws. *J. Geophys. Res.* 88, pp. 10359–10370.

Ruiz-Barajas S., Sharma N., Convertito V., Zollo A., Benito B. (2017): Temporal evolution of a seismic sequence induced by a gas injection in the Eastern coast of Spain. *Sci. Rep.* 7 (1), p. 2901, p. 15. DOI: 10.1038/s41598-017-02773-2.

Rutqvist J., Birkholzer J.T., Tsang C.-F. (2008): Coupled reservoir–geomechanical analysis of the potential for tensile and shear failure associated with CO2 injection in multilayered reservoir–caprock systems. *Int. J. Rock Mech. Min. Sci.* 45 (2), pp. 132–143. DOI: 10.1016/j.ijrmms.2007.04.006.

Rutqvist J., Rinaldi A.P., Cappa F., Jeanne P., Mazzoldi A., Urpi L. et al. (2016): Fault activation and induced seismicity in geological carbon storage – Lessons learned from recent modeling studies. *J. Rock Mech. Geotech. Eng.* 8 (6), pp. 789–804. DOI: 10.1016/j.jrmge.2016.09.001.

Rutqvist J., Stephansson O. (2003): The role of hydromechanical coupling in fractured rock engineering. *Hydrogeol. J.* 11 (1), pp. 7–40. DOI: 10.1007/s10040-002-0241-5.

Rutqvist J., Tsang C.-F. (2002): A study of caprock hydromechanical changes associated with CO2-injection into a brine formation. *Env. Geol. (Environmental Geology)* 42 (2-3), pp. 296–305. DOI: 10.1007/s00254-001-0499-2.

Rutqvist J., Tsang C.-F. (2005): Coupled hydromechanical effects of CO2 injection. *Dev. Water Sci.* 52, pp. 649–679. DOI: 10.1016/S0167-5648(05)52050-1.

Salz L.B. (1977): Relationship between fracture propagation pressure and pore pressure. *52nd SPE Annual Fall Technical Conference and Exhibition, 09-12 October 1977, Denver, Colorado*.

Samier P., Onaisi A., Fontaine G. (2003): Coupled Analysis of Geomechanics and Fluid Flow in Reservoir Simulation. *SPE Reservoir Simulation Symposium, 3-5 February 2003, Houston*.

Santarelli F.J., Tronvoll J.T., Svennekjaer M., Skeie H., Henriksen R., Bratli R.K. (1998): Reservoir Stress Path: The Depletion and the Rebound. *SPE/ISRM Eurock '98, 8-10 July 1998, Trondheim, Norway*, pp. 1–7.

Sanz P.F., Lele S.P., Searles K.H., Hsu S.-Y., Garzon J.L., Burdette J.A. et al. (2015): Geomechanical Analysis to Evaluate Production-Induced Fault Reactivation at Groningen Gas Field. *SPE Annual Technical Conference and Exhibition. DOI:* 10.2118/174942-MS.

Scheck-Wenderoth M., Lamarche J. (2005): Crustal memory and basin evolution in the Central European Basin System—new insights from a 3D structural model. *Tectonophysics* 397 (1-2), pp. 143–165. DOI: 10.1016/j.tecto.2004.10.007.

Schmitt D.R., Zoback M.D. (1989): Poroelastic effects in the determination of the maximum horizontal principal stress in hydraulic fracturing tests—A proposed breakdown equation employing a modified effective stress relation for tensile failure. *Int. J. Rock Mech. Min. Sci. Abstracts* 26 (6), pp. 499–506. DOI: 10.1016/0148-9062(89)91427-7.

Scholz C. (1998): Earthquakes and friction laws. *Nature* 391, pp. 37–42. DOI: 10.1038/34097.

Scholz C.H. (2002): The Mechanics of Earthquakes and Faulting. (2nd Edition), Cambridge University Press. Cambridge.

Schutjens P., Blanton T.L., Martin J.W., Lehr B.C., Baaijens M.N. (1998): Depletion-induced compaction of an overpressured reservoir sandstone: An experimental approach. *SPE/ISRM Eurock 98, 8-10 July 1998, Trondheim, Norway*, pp. 53–62.

Schutjens P., Burrelll R., Fehmers G., Hindriks K., Collins C., van der Horst, J. (2007): On the stress change in overburden resulting from reservoir compaction: Observations from two computer models and implications for 4D seismic. *The Leading Edge* 25 (5), pp. 628–634.

Segall P. (1985): Stress and Subsidence Resuling from Subsurface Fluid Withdrawal in the Epicentral Region of the 1983 Coalinga Earthquake. *J. Geophys. Res.* 90, pp. 6801–6816.

Segall P. (1989): Earthquakes triggered by fluid extraction. *Geology* 17, pp. 942–946.

Segall P. (1992): Induced stresses due to fluid extraction from axisymmetric reservoirs. *Pure Appl. Geophys* 139 (3/4), pp. 535–560.

Segall P., Fitzgerald S. (1998): A note on induced stress changes in hydrocarbon and geothermal reservoirs. *Tectonophysics* 289, pp. 117–128.

Segall P., Lu S. (2015): Injection-induced seismicity. Poroelastic and earthquake nucleation effects. *J. Geophys. Res. Solid Earth* 120 (7), pp. 5082–5103. DOI: 10.1002/2015JB012060.

Segall P., Rice J.R. (1995): Dilatancy, compaction and slip instability of a fluid-infiltrated fault. *J. Geophys. Res.* 100, pp. 22155–22171.

Segall P., Rubin A.M., Bradley A.M., Rice J.R. (2010): Dilatant strengthening as a mechanism for slow slip events. *J. Geophys. Res.* 115 (B12), B01302. DOI: 10.1029/2010JB007449.

Segura J.M., Fisher Q.J., Crook A.J.L., Dutko M., Yu J.G., Skachkov S. et al. (2011): Reservoir stress path characterization and its implications for fluid-flow production simulations. *Pet. Geosci.* 17 (4), pp. 335–344. DOI: 10.1144/1354-079310-034.

Settari A.T., Bachman R.C., Walters D.A. (2005): How to Approximate Effects of Geomechanics in Conventional Reservoir Simulation. *SPE Annual Technical Conference and Exhibition, 9-12 October 2005, Dallas, Texas*.

Settari A.T., Sen V. (2007): The role of geomechanics in integrated reservoir modeling. *The Leading Edge* 26 (5), pp. 622–627.

Settari A.T., Walters D.A. (2001): Advances in Coupled Geomechanical and Reservoir Modeling with Applications to Reservoir Compaction. *SPE Reservoir Simulation Symposium, 14-17 April, Houston*, pp. 334–342.

Shapiro S.A. (2015): Fluid-Induced Seismicity, Cambridge University Press. Cambridge, p. 289.

Shapiro S.A., Dinske C. (2009): Fluid-induced seismicity. Pressure diffusion and hydraulic fracturing. *Geophys. Prospect.* 57 (2), pp. 301–310. DOI: 10.1111/j.1365-2478.2008.00770.x.

Shipton Z.K., Soden A.M., Kirkpatrick J.D., Bright A., Lunn R.J. (2006): How Thick is a Fault? Fault Displacement-Thickness Scaling Revisited. In: Abercrombie R, eds. Earthquakes: Radiated Energy and the Physics of Faulting: American Geophysical Union, pp. 193–198.

Sibson R.H. (1974): Frictional constraints on thrust, wrench and normal faults. *Nature* 249, pp. 542–544.

Sibson R.H. (1985): A note on fault reactivation. *J. Struct. Geol.* 7 (6), pp. 751–754.

Sibson R.H. (2003): Thickness of the Seismic Slip Zone. *Bull. Seismol. Soc. Am.* 93 (3), pp. 1169–1178.

Sijacic D., Pijpers F., Nepveu M., van Thienen-Visser K. (2017): Statistical evidence on the effect of production changes on induced seismicity. *Neth. J. Geosci.* 96 (5), 27-38. DOI: 10.1017/njg.2017.14.

Singh M., Rao K.S., Ramamurthy T. (2002): Strength and Deformational Behaviour of a Jointed Rock Mass. *Rock Mech. Rock Eng.* 35 (1), pp. 45–64. DOI: 10.1007/s006030200008.

Soltanzadeh H., Hawkes C.D. (2008): Semi-analytical models for stress change and fault reactivation induced by reservoir production and injection. *J. Pet. Sci. Eng.* 60 (2), pp. 71–85. DOI: 10.1016/j.petrol.2007.05.006.

Spiers C.J., Hangx S.J., Niemeijer A.R. (2017): New approaches in experimental research on rock and fault behaviour in the Groningen gas field. *Neth. J. Geosci.* 96 (5), 55-69. DOI: 10.1017/njg.2017.32.

Suckale J.: Induced Seismicity in Hydrocarbon Fields. In: Nielsen, S eds. Advances in Geophysics, vol. 51: Academic Press, pp. 55–106.

Templeton E.L., Baudet A., Bhat H.S., Dmowska R., Rice J.R., Rosakis A.J., Rousseau C.-E. (2009): Finite element simulations of dynamic shear rupture experiments and dynamic path selection along kinked and branched faults. *J. Geophys. Res.* 114 (B8), p. 2064. DOI: 10.1029/2008JB006174.

Ter Heege J., Osinga S., Wassing B., Candela T., Orlic B., Buijze L., Chitu A. (2018): Mitigating induced seismicity around depleted gas fields based on geomechanical modeling. *The Leading Edge* 37 (5), pp. 334–342. DOI: 10.1190/tle37050334.1.

Ter Heege J.H., Bruin G. de (2013): Discrete Element Modeling of Fault Mechanics and Permeability Evolution for Gas Production and Storage: Effect of Shale Content and Distribution. *47th US Rock Mechanics/Geomechanics Symposium, 23-26 June, San Francisco, California*.

Terzaghi K. (1925): Erdbaumechanik auf bodenphysikalischer Grundlage, Deuticke. Leipzig, Wien, p. 399.

Terzaghi K. (1936): The shearing resistance of saturated soils and the angle between the planes of shear. *First international conference on soil mechanics* 1, pp. 54–56.

Teufel L.W., Rhett D.W., Farrell H.E. (1991): Effect of reservoir depletion and pore pressure drawdown on in situ stress and deformation in the Ekofisk Field, North Sea. In: J.-C. Roegiers (Ed.): Rock Mechanics as a multidisciplinary science. Proceedings of the 32nd US Symposium. 1st Edition, pp. 63–72.

Tingay M., Heidbach O., Davies R.J., Swarbrick R.E. (2008): Triggering of the Lusi mud eruption: Earthquake versus drilling initiation. *Geology* 36 (8), pp. 639–642.

Tingay M.R.P., Hillis R.R., Morley, Christopher K., Swarbrick R.E., Okpere E.C. (2003): Pore pressure/stress coupling in Brunei Darussalam — implications for shale injection. *Geol. Soc. London Spec. Publ.* 216 (1), pp. 369–379. DOI: 10.1144/GSL.SP.2003.216.01.24.

Tomic J., Abercrombie R.E., do Nascimento A.F. (2009): Source parameters and rupture velocity of small M ≤ 2.1 reservoir induced earthquakes. *Geophysical Journal International* 179 (2), pp. 1013–1023. DOI: 10.1111/j.1365-246X.2009.04233.x.

Townend J., Zoback M.D. (2000): How faulting keeps the crust strong. *Geol* 28 (5), p. 399. DOI: 10.1130/0091-7613(2000)28<399:HFKTCS>2.0.CO;2.

Trautwein U., Huenges E. (2005): Poroelastic behaviour of physical properties in Rotliegend sandstones under uniaxial strain. *Int. J. Rock Mech. & Min. Sci.* 42 (7-8), pp. 924–932. DOI: 10.1016/j.ijrmms.2005.05.016.

Twiss R.J., Moores E.M. (2007): Structural Geology. 2nd ed., W. H. Freeman. New York, p. 736.

Urai J.L., Spiers C.J. (2007): The effect of grain boundary water on deformation mechanisms and rheology of rocksalt during long-term deformation. *Proceedings of the 6th. conference on the mechanical behaviour of salt, 'SaltMech6', 22-25 May 2007, Hannover, Germany*.

Uta P. (2017): Recent Intraplate Earthquakes in Northwest Germany. Glacial Isostatic Adjustment and/or a Consequence of Hydrocarbon Production? Dissertation, p. 199.

van den Bogert P.A. (2015): Impact of various modelling options on the onset of fault slip and the fault slip response using 2-dimensional Finite-Elmenent modelling. *NAM internal report, p.* 101.

van der Baan M., Calixto F.J. (2017): Human-induced seismicity and large-scale hydrocarbon production in the USA and Canada. *Geochem. Geophys. Geosyst.* 18 (7), pp. 2467–2485, p. 19. DOI: 10.1002/2017GC006915.

van Eijs R., Mulders F., Nepveu M., Kenter C.J., Scheffers B.C. (2006): Correlation between hydrocarbon reservoir properties and induced seismicity in the Netherlands. *Eng. Geol.* 84 (3-4), pp. 99–111. DOI: 10.1016/j.enggeo.2006.01.002.

van Hulten F.F.N. (2010): Geological factors effecting compartmentalization of Rotliegend gas fields in the Netherlands. *Geol. Soc. London Spec. Publ.* 347 (1), pp. 301–315. DOI: 10.1144/SP347.17.

van Keken P.E., Spiers C.J., Berg van den A.P., Muyzert E.J. (1993): The effective viscosity of rocksalt: Implementation of steady-state creep laws in numerical models of salt diapirism. *Tectonophysics* 225, pp. 457–476.

van Thienen-Visser K., Breunese J.N. (2015): Induced seismicity of the Groningen gas field: History and recent developments. *The Leading Edge* 34 (6), pp. 664–671. DOI: 10.1190/tle34060664.1.

van Thienen-Visser K., Fokker P.A. (2017): The future of subsidence modelling. Compaction and subsidence due to gas depletion of the Groningen gas field in the Netherlands. *Neth. J. Geosci.* 119, pp. 1–12. DOI: 10.1017/njg.2017.10.

van Wees J.D., Buijze L., van Thienen-Visser K., Nepveu M., Wassing B., Orlic B., Fokker P.A. (2014): Geomechanics response and induced seismicity during gas field depletion in the Netherlands. *Geothermics* 52, pp. 206–219. DOI: 10.1016/j.geothermics.2014.05.004.

van Wees J.-D., Fokker P.A., van Thienen-Visser K., Wassing B.B., Osinga S., Orlic B. et al. (2017): Geomechanical models for induced seismicity in the Netherlands. Inferences from simplified analytical, finite element and rupture model approaches. *Neth. J. Geosci.* 96 (5), 183-202. DOI: 10.1017/njg.2017.38.

Vilarrasa V., Makhnenko R., Gheibi S. (2016): Geomechanical analysis of the influence of CO 2 injection location on fault stability. *J. Rock Mech. Geotech. Eng.* 8 (6), pp. 805–818. DOI: 10.1016/j.jrmge.2016.06.006.

Vincké O., Boutéca M.J., Piau J.M., Fourmaintraux D. (1998): Study of the effective stress at failure: . In: J. F. Thimus, Y. Abousleiman, A.H.-D. Cheng, O. Coussy, E. Detournay (Eds.): Poromechanics-a tribute Maurice A. Biot. Rotterdam: Balkema.

Waal J.A. de, Muntendam-Bos A.G., Roest J.P.A. (2015): Production induced subsidence and seismicity in the Groningen gas field - can it be managed? *Proc. IAHS* 372, pp. 129–139. DOI: 10.5194/piahs-372-129-2015.

Walsh F.R., Zoback M.D. (2015): Oklahoma's recent earthquakes and saltwater disposal. *Sci. Adv* 1 (5), 1-9, p. 10. DOI: 10.1126/sciadv.1500195.

Wang H.F. (2000): Theory of Linear Poroelasticity. with Applications to Geomechanics and Hydrogeology, Princeton University Press. Princeton, 08540 New Jersey, p. 304.

Wassing B., Buijze L., Orlic B. (2016): Modelling of fault reactivation and fault slip in producing gas fields using a slip-weakening friction law. *50th US Rock Mechanics / Geomechanics Symposium, 26-29 June 2016, Houston, Texas, p.* 11.

Wassing B.B.T., Buijze L., Ter Heege J.H., Orlic B., Osinga S.S. (2017): The impact of viscoelastic caprock on fault reactivation and fault rupture in producing gas fields. *51st US Rock Mechanics/Geomechanics symposium, 25-28 June, San Francisco, California*.

Weijermars R., Jackson M.P.A., van Harmelen A. (2014): Closure of open wellbores in creeping salt sheets. *Geophysical Journal International* 196 (1), pp. 279–290. DOI: 10.1093/gji/ggt346.

Weijermars R., Jackson M.P.A., Vendeville B. (1993): Rheological and tectonic modeling of salt provinces. *Tectonophysics* (217), pp. 143–174.

Wells D.L., Coppersmith J.K. (1994): New Empirical Relationships among Magnitude, Rupture Length, Rupture Width, Rupture Area and Surface Displacement. *Bulletin of the seismological Society of America* 84 (4), pp. 974–1002.

Weyler R., Oliver J., Sain T., Cante J.C. (2012): On the contact domain method. A comparison of penalty and Lagrange multiplier implementations. *Computer Methods in Applied Mechanics and Engineering* 205-208, pp. 68–82. DOI: 10.1016/j.cma.2011.01.011.

Wong T.-F., David C., Zhu W. (1997): The transition from brittle faulting to cataclastic flow in porous sandstones: Mechanical deformation. *J. Geophys. Res.* 102, pp. 3009–3025.

Yale D.P. (2003): Fault and stress magnitude controls on variations in the orientation of in situ stresses. *in: Ameen, M. (Ed.), Fracture and In-Situ Stress Characterization of Hydrocarbon Reservoirs. Geological Society, London*, pp. 55–64.

Yerkes R.F., Castle R.O. (1976): Seismicity and Faulting Attributabl to Fluid Extraction. *Eng. Geol.* 10, pp. 151–167.

Zang A., Stephansson O. (2010): Stress Field of the Earth's Crust, Springer. Dordrecht, NL, p. 324.

Zbinden D., Rinaldi A.P., Urpi L., Wiemer S. (2017): On the physics-based processes behind production-induced seismicity in natural gas fields. *J. Geophys. Res. Solid Earth* 122 (5), pp. 3792–3812. DOI: 10.1002/2017JB014003.

Zhou F. (1997): Räumliche Konsolidationsberechnung nach der Methode der Finiten Elemente unter Berücksichtigung des elastoplastischen Verhaltens von bindigen Böden. Veröffentlichungen des Institutes für Grundbau, Bodenmechanik, Felsmechanik und Verkehrswasserbau der RWTH Aachen. 31st ed., Aachen: Institut für Grundbau, Bodenmechanik, Felsmechanik und Verkehrswasserbau.

Zielonka M.G., Searles K.H., Ning J., Buechler S.R. (2014): Development and Validation of Fully-Coupled Hydraulic Fracturing Simulation Capabilities. *2014 SIMULIA Community Conference, 20-22 May 2014, Providence, Rhode Island*, pp. 1–31.

Zienkiewicz O.C., Taylor R.L., Zhu J.Z. (2013): The Finite Element Method: Its Basis and Fundamentals. 7th ed., Butterworth-Heinemann.

Zienkiewicz (1982): Basic Formulation of Static and Dynamic Behaviours of Soil and other Porous Media. *Applied Mathematics and Mechanics* 3 (4), pp. 457–468.

Zilch K., Diederichs C.-J., Katzenbach R. (2013): Geotechnik. In: K. J. Beckmann (Ed.): Handbuch für Bauingenieure. p. 284.

Zimmerman R.W. (1991): compressibility of sandstones. In: G. V. Chilingarian (Ed.): Developments in petroleum science, vol. 29.

Zoback M.D. (2007): Reservoir Geomechanics, Cambridge University Press. Cambridge, p. 461.

Zoback M.D., Zinke J.C. (2002): Production-induced Normal Faulting in the Valhall and Ekofisk Oil Fields. *Pure Appl. Geophys (pageoph)* (159), pp. 403–420.

Zoback M.L. (1992): First- and Second-Order Patterns of Stress in the Lithosphere: The World Stress Map Project. *J. Geophys. Res.* 97 (11703-11728), p. 703-711.

Zöller G., Holschneider M. (2016): The Maximum Possible and the Maximum Expected Earthquake Magnitude for Production-Induced Earthquakes at the Gas Field in Groningen, The Netherlands. *Bull. Seismol. Soc. Am.* 106 (6), pp. 2917–2921. DOI: 10.1785/0120160220.

13 Appendix

A

Tab. 5: Evaluation of the initial stress state using the enhanced iterative procedure for different model configurations

Material Drained stiffness of Lithological Units (Tab. 3) $\alpha = 0.7$	Pore Pressure	Material Biot-Willis coefficient α	Input stress	Ratio $\frac{\sigma'_h}{\sigma'_V}$	Evaluated stress	Max deviation from SSR=0.346 left	Max deviation from SSR=0.346 right	Max vertical displacement [m]
Homogeneous ***R***	hydrostatic	Homogeneous 1	Terzaghi/ Biot Identical	0.5	Terzaghi/ Biot Identical	+-0.075	+-0.01	+0.03684 u_z
Heterogeneous ***R, O1, O2, U***	hydrostatic	Homogeneous 1	Terzaghi/ Biot Identical	0.5	Terzaghi/ Biot Identical	+0.075	+0.006	+0.03684 u_z
Homogeneous ***R***	hydrostatic	Homogeneous 0.7	Terzaghi	0.5	Terzaghi	+0.15	+0.15	-14.6 u_z
Homogeneous ***R***	hydrostatic	Homogeneous 0.7	Biot-Willis	0.5	Terzaghi	+0.2	+0.2	-3.55 u_z
Homogeneous ***R***	hydrostatic	Homogeneous 0.7	Terzaghi	0.5	Biot-Willis	+0.051	+0.051	-14.6 u_z
Homogeneous ***R***	hydrostatic	Homogeneous 0.7	Biot-Willis	0.5	Biot-Willis	+0.02	+0.02	-3.55 u_z

Tab. 6: Evaluation of the initial stress state using the enhanced iterative procedure for different model configurations of various Biot-coefficients

Material Drained stiffness of Lithological Units (Tab. 3) $\alpha = 0.7$	Pore Pressure	Material Biot-Willis coefficient α (Tab. 3)	Input stress	Ratio $\frac{\sigma'_h}{\sigma'_V}$	Evaluated stress	Max deviation from SSR=0.346 left	Max displacement [m]
Heterogeneous ***R, O1, O2, U***	hydrostatic	Heterogeneous ***R, O1, O2, U***	Terzaghi	0.5	Terzaghi	Fig. 7-28 a)	-31.51 u_z
Heterogeneous ***R, O1, O2, U***	hydrostatic	Heterogeneous ***R, O1, O2, U***	Biot-Willis	0.5	Terzaghi	Fig. 7-28 a)	+0.033 u_z
Heterogeneous ***R, O1, O2, U***	hydrostatic	Heterogeneous ***R, O1, O2, U***	Terzaghi	0.5	Biot-Willis	Fig. 7-28 b)	-31.51 u_z
Heterogeneous ***R, O1, O2, U***	hydrostatic	Heterogeneous ***R, O1, O2, U***	Biot-Willis	0.5	Biot-Willis	Fig. 7-28 b)	+0.033 u_z
Heterogeneous ***R, O1, O2, U***	overpressure	Heterogeneous ***R, O1, O2, U***	Terzaghi	0.5	Terzaghi	Fig. 7-28 c)	-29.56 u_z
Heterogeneous ***R, O1, O2, U***	overpressure	Heterogeneous ***R, O1, O2, U***	Biot-Willis	0.5	Terzaghi	Fig. 7-28 c)	+0.072 u_z
Heterogeneous ***R, O1, O2, U***	overpressure	Heterogeneous ***R, O1, O2, U***	Terzaghi	0.5	Biot-Willis	Fig. 7-28 d)	-29.56 u_z
Heterogeneous ***R, O1, O2, U***	overpressure	Heterogeneous ***R, O1, O2, U***	Biot-Willis	0.5	Biot-Willis	Fig. 7-28 d)	+0.072 u_z

B

The conversion of horizontal Biot-Willis effective into Terzaghi effective stress (Eq. 13.1) proceeds according to Eq. 6.9. Considering uniaxial strain conditions, the horizontal effective stress derives from the solid vertical stress. Equations. 13.2-13.5 show the equivalency of both concepts for solid stress with respect to resulting horizontal effective stresses.

$$\sigma'_{xx\_Biot} = (\sigma'_{xx\_Terz} - P_f) + \alpha P_f \qquad 13.1$$

$$\sigma'_{xx\_Biot} = \left[\frac{\nu}{1-\nu}\sigma'_{zz\_Terz} + \frac{EP_f}{(1-\nu)3K_g}\right] - P_f + \left(1 - \frac{K_d}{K_g}\right)P_f \qquad 13.2$$

Expressing vertical Terzaghi effective stress in terms of total stress:

$$\sigma'_{xx\_Biot} = \frac{\nu}{1-\nu}\left[\sigma_{zz} + P_f\right] + \frac{EP_f}{(1-\nu)3K_g} - \frac{K_d}{K_g}P_f \qquad 13.3$$

Rearranging total stress for Biot-Willis effective stress yields:

$$\sigma'_{xx\_Biot} = \frac{\nu}{1-\nu}\left[\sigma'_{zz\_Biot} - \alpha P_f + P_f\right] + \frac{EP_f}{(1-\nu)3K_g} - \frac{K_d}{K_g}P_f \qquad 13.4$$

Simplifying and using equations 3.20 and 6.20 leads to:

$$\sigma'_{xx\_Biot} = \frac{\nu}{1-\nu}\sigma'_{zz\_Biot} \qquad 13.5$$

C

Breckels & van Ekelen (1981) propose an empirical correlation between depth and stress based on data from the Gulf of Mexico. In their equations abnormal pore pressure is accounted for in the magnitude of minimum principal stress:

$$\sigma_h = 0.197\, z^{1.145} + 0.46\left(P_{fovp} - P_{fhyd}\right) \quad for\ z < 11500\ ft \qquad 13.6$$

$$\sigma_h = 1.167\, z - 4596 + 0.46\left(P_{fovp} - P_{fhyd}\right) \quad for\ z > 11500\ ft \qquad 13.7$$

P_{fovp}: overpressure P_{fhyd}: hydrostatic pore pressure

Figure 13-60 shows the computed profiles of depth vs stress from Breckels & van Ekelen 1982, converted to SI-units and evaluated in terms of the Terzaghi and new effective stress law. In this estimation of stress, the onset of overpressure is also accompanied by an increased minimum horizontal stress, approaching the total vertical stress. The disproportional increase of σ_{hmin} with

depth in sedimentary basins is also described by (Goulty 2003) as a consequence of the poisson effect with normal faulting, sediment compaction or basin-scale coupling of pore pressure to stress.

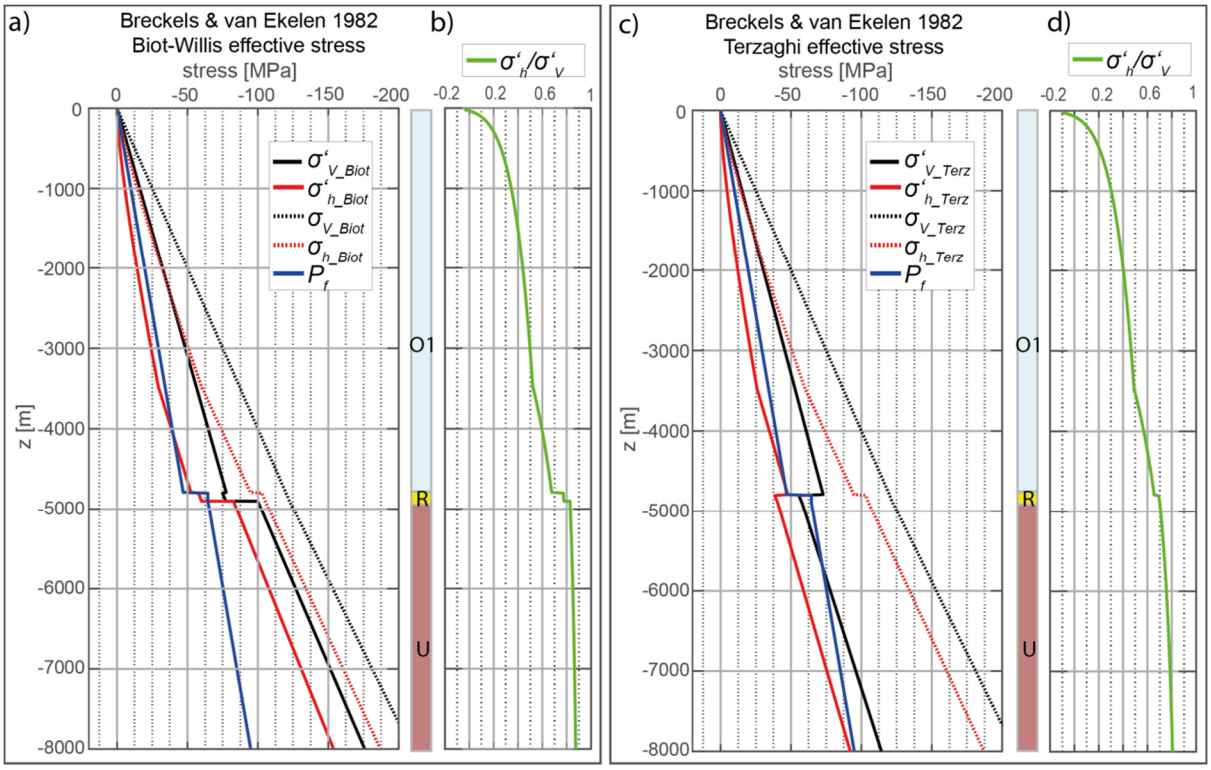

Fig. 13-60: Computed stress depth profile using properties of Table 3 and the approach of Breckels & van Ekelen (1981), addressing overpressure conditions in the Gulf of Mexico. Computed total stresses are evaluated in terms of Biot-Willis (a) and Terzaghi effective stress (b)

Statement of authorship/Erklärung

I hereby certify that this thesis has been composed by myself and describes my own work unless otherwise acknowledged in the text. All references and verbatim extracts have been quoted and all sources of information have been specifically acknowledged. This thesis has not been accepted in any previous application for a degree.

Hiermit versichere ich, dass ich die vorliegende Arbeit selbstständig und ohne Benutzung anderer als der angegebenen Hilfsmittel angefertigt habe. Stellen, die wörtlich oder sinngemäß aus anderen Schriften entnommen sind, sind als solche kenntlich gemacht. Die Arbeit ist in gleicher oder ähnlicher Form noch nicht als Prüfungsarbeit eingereicht worden.

Darmstadt, den _____Unterschrift_____